Lehrstuhl für Elektrische Energiespeichertechnik
Fakultät für Elektrotechnik und Informationstechnik
Technische Universität München

Diffraction Analysis of Anode Inhomogeneity in Lithium-Ion Batteries

Dipl.-Phys. Jörn Wilhelm

Vollständiger Abdruck der von der Fakultät für Elektrotechnik und Informationstechnik der Technischen Universität München zur Erlangung des akademischen Grades eines

Doktor-Ingenieurs (Dr.-Ing.)

genehmigten Dissertation.

Vorsitzende:		Priv.-Doz. Dr. Gabriele Schrag
Prüfer der Dissertation:	1.	Prof. Dr.-Ing. Andreas Jossen
	2.	Prof. Dr. Dirk Uwe Sauer

Die Dissertation wurde am 23.09.2020 bei der Technischen Universität München eingereicht und durch die Fakultät für Elektrotechnik und Informationstechnik am 15.02.2021 angenommen.

List of publications

Publications (lead author)

1 J. Wilhelm, S. Seidlmayer, P. Keil, J. Schuster, A. Kriele, R. Gilles, A. Jossen: Cycling capacity recovery effect: A coulombic efficiency and post-mortem study, Journal of Power Sources, 365 (2017), 327-338. *The author designed the experiment, conducted the measurements and data analysis, and wrote the manuscript.*

2 J. Wilhelm, S. Seidlmayer, S. V. Erhard, M. Hofmann, R. Gilles, A. Jossen: In situ neutron diffraction study of lithiation gradients in graphite anodes during discharge and relaxation, Journal of the Electrochemical Society, 165 (9), A1846 (2018)
The author designed the experiment, conducted the measurements and data analysis, and wrote the manuscript.

Publications (co-author)

1 S. V. Erhard, P. J. Osswald, J. Wilhelm, A. Rheinfeld, S. Kosch, A. Jossen: Simulation and measurement of local potentials of modified commercial cylindrical cells: I. Cell preparation and measurement, Journal of the Electrochemical Society, 162(14), A2707-A2719 (2015).
The author contributed to data analysis and discussion as well as the review of the manuscript.

2 P. J. Osswald, S. V. Erhard, J. Wilhelm, H. E. Hoster and A. Jossen: Simulation and measurement of local potentials of modified commercial cylindrical cells, Journal of the Electrochemical Society, 162(10), A2099-A2105 (2015).
The author built and measured a prototype of the modified cylindrical cells. The author contributed to data analysis and discussion as well as the review of the manuscript.

3 P. Keil, S. F. Schuster, J. Wilhelm, J. Travi, A. Hauser, R. C. Karl and A. Jossen: Calendar aging of Lithium-Ion cells, Journal of the Electrochemical Society, 163(9), A1872-A1880 (2016).
The author performed post mortem analysis and sample preparation. The author contributed to data analysis and discussion as well as the review of the manuscript.

4 S. V. Erhard, P. J. Osswald, P. Keil, E. Höffer, M. Haug, A. Noel, J. Wilhelm, B. Rieger, K. Schmidt, S. Kosch, F. M. Kindermann, F. Spingler, H. Kloust, T. Thoennessen, A. Rheinfeld and A. Jossen: Simulation and measurement of the current density distribution in lithium-ion batteries by a multi-tab cell approach, Journal of the Electrochemical Society, 164(1), A6324-A6333 (2017).
The author analyzed electrode material and prepared samples. The author contributed to discussion and review of the manuscript.

5 V. Zinth, C. von Lüders, J. Wilhelm, S. V. Erhard, M. Hofmann, S. Seidlmayer, J. Rebelo-Kornmeier, W. Gan, A. Jossen and R. Gilles: Inhomogeneity and relaxation phenomena in the graphite anode of a lithium-ion battery probed by in situ neutron diffraction, Journal of Power Sources, 361, 54–60 (2017). *The author contributed to writing, discussion, and review of the manuscript.*

6 A. Rheinfeld, A. Noel, J. Wilhelm, A. Kriston, A. Pfrang, A. Jossen: Quasi-isothermal external short circuit tests applied to lithium-ion cells: Part I. Measurements, Journal of the Electrochemical Society, 165(14), A3427-A3448 (2018).
The author analyzed electrode material and contributed to the discussion of the manuscript.

7 A. Rheinfeld, J. Sturm, A. Noel, J. Wilhelm, A. Kriston, A. Pfrang and A. Jossen: Quasi-isothermal external short circuit tests applied to lithium-ion cells: Part II. Modeling and Simulation, Journal of the Electrochemical Society, 166(2), A151-A177 (2019).
The author analyzed electrode material.

Conference contributions (Selection)

1 J. Wilhelm, M. Müller, C. v. Lüders, S. V. Erhard, V. Zinth, S. Seidlmayer, R. Gilles, Neutron Diffraction Measurements of Lithium-Ion Battery State of Charge Distribution, Oral presentation, 14th Ulm Electrochemical Talks 2014, Germany

2 J. Wilhelm, P. J. Osswald, S. V. Erhard, S. Gläser, A. Jossen, Current distribution and local potentials of a modified battery test-cell, Poster contribution, Kraftwerk Batterie 2015, Germany

3 J. Wilhelm, S. V. Erhard, I. Buchberger, A. Jossen, Simulation of Lithium-ion Battery Equalization Effects, MODVAL 13, Lausanne 2016, Switzerland

4 J. Wilhelm, V. Zinth, S. V. Erhard, I. Buchberger, A. Jossen, In-Situ Neutron Diffraction Study of Lithium-Ion Battery Equalization Effects, Oral presentation, ECS PRIME 2017, Honolulu USA

5 J. Wilhelm, S. Seidlmayer, R. Gilles, A. Jossen, In situ neutron diffraction study of lithium-ion batteries during operation and relaxation, Oral presentation, SNI 2018, Garching Germany

Vorwort und Danksagung

Die vorliegende Dissertation wurde während meiner Zeit als wissenschaftlicher Mitarbeiter am Lehrstuhl für Elektrische Energiespeichertechnik der Technischen Universität München erarbeitet.

An erster Stelle bedanke ich mich herzlich bei Prof. Dr. Jossen für die wissenschaftliche Betreuung und die fruchtbare Diskussion zahlreicher Ideen und Argumente im Laufe der Promotion.

Ob in Meetings, auf dem Flur oder an der Kaffeemaschine, die Zeit am EES wäre nicht halb so schön gewesen ohne meine Kollegen, denen ich allen ausdrücklich für die tolle Zeit danken möchte. Ein herzlicher Dank gilt insbesondere meinen langjährigen Kollegen Christian von Lüders, Franz Spingler und Maik Naumann für den fachlichen und persönlichen Austausch sowie die Korrektur des Manuskripts.

Die vorgestellte wissenschaftliche Arbeit wäre ohne die Unterstützung der Partnerlehrstühle des EES nicht möglich gewesen. Von den vielen Kollegen möchte ich hierbei besonders Jörg Schuster, Irmgard Buchberger sowie Fabian Linsenmann vom Lehrstuhl für Technische Elektrochemie, Nicolas Billot und Patrick Schmitz vom Institut für Werkzeugmaschinen und Betriebswissenschaften sowie Veronika Zinth und Stefan Seidlmayer vom Heinz Maier-Leibnitz Zentrum danken. Herzlich bedanken möchte ich mich zudem bei Maximilian Drexl und Korbinian Wachutka für die wertvolle Unterstützung meiner Forschungsarbeit in ihrer Zeit als Masterstudenten.

Meinen Kollegen Maik Naumann und Andreas Noel danke ich für den gelegentlichen Ausgleich und die schöne Zeit in der Natur, am Berg oder auch auf dem Spielplatz.

Abschließend möchte ich mich herzlich bei meiner Familie und meiner Frau Sabine für die Unterstützung und immerwährenden Rückhalt bedanken.

Jörn Wilhelm

München, September 2020

Kurzfassung

Das Potential einer Lithium-Ionen-Zelle wird optimal genutzt, wenn alle Bereiche der Elektroden gleichmäßig belastet werden. In einer realen Batterie kommt es jedoch aufgrund von Transporthemmnissen zu lokalen Ungleichgewichten kritischer Parameter wie der Stromdichte und des Ladezustandes. Dies kann zu gleichzeitiger lokaler Unter- sowie Überauslastung und damit einhergehenden Verlusten an Kapazität und Leistung sowie potentiell beschleunigtem Verschleiß der Zelle führen. Aufgrund der natürlichen Tendenz der Zelle ins Gleichgewicht zu streben sind lokale Ungleichgewichte flüchtig und eine Herausforderung in der Vermessung von Batterien.

Diese Arbeit präsentiert die Ergebnisse der Untersuchung lokaler Ladezustände in Graphitanoden mittels einer Kombination aus in situ und post mortem Methoden.

Die Anode kommerzieller Zellen ist gegenüber der Kathode überdimensioniert um auch bei geringen Schwankungen bei der Positionierung in der Produktion immerwährend Überlappung zu gewährleisten und Lithium-Plating zu verhindern. Die Vermessung der Randbereiche kalendarisch gealterter Rundzellen mittels Röntgendiffraktion und Kolorimetrie zeigt, dass diese Bereiche während der Lagerung lithiiert werden und als Lithium-Reservoir fungieren. Solch eine Lithiierung tritt insbesondere nach Lagerung bei hohen Temperaturen und Ladezuständen auf. Noch nach mehreren hundert Stunden Zyklisierung ist die Coulomb Effizienz der Zellen abhängig vom vorhergehenden Lagerzustand. Darüber hinaus zeigen die Messungen, dass die Randbereiche bei Batterien mit gleichem Alterungszustand temporäre Kapazitätsunterschiede von mehreren Prozent verursachen können. Aus den Ergebnissen folgt, dass Anoden-Überhangbereiche bei Coulomb-Effizienz Untersuchungen und Kapazitätsmessungen berücksichtigt werden müssen. Als Strategie hierfür wird pre-cycling vorgeschlagen.

Lithium-Reservoire können auch bei laborgefertigten Knopfzellen auftreten, wenn doppelseitige Elektroden verwendet werden. Die Untersuchung von Knopfzellen aus ein- und doppellagigen Elektroden zeigt, dass die Rückseite bis zu 70 % zusätzliche Kapazität bereitstellt und mit solchen Zellen die Materialparameter und Halbzellenprofile nicht zuverlässig vermessen werden können. Auf eine Entfernung der Rückseite bei Elektroden die post mortem aus Zellen gewonnen wurden kann daher im Laboralltag nicht verzichtet werden.

Zusätzlich zur lateralen Inhomogenität entlang von Graphit-Elektroden wird die Ausprägung orthogonaler Inhomogenität durch die Elektrodenschicht mittels in situ Neutronendiffraktion in zwei Experimenten untersucht. Die Änderung der Phasenanteile unterschiedlicher Lithiierung wird für eine kommerzielle Pouch-Zelle während der Entladung und Relaxation bei unterschiedlichen Raten und Temperaturen vermessen. Diese Untersuchung wird für speziell angefertigte Zellen mit variierender Massenbeladung der Anoden wiederholt. Darüber hinaus werden kritische Transportparameter in Materialuntersuchungen bestimmt.

Die Ergebnisse zeigen, dass sich während der Entladung eine Polarisierung der Anode in unterschiedlich stark lithiierte Segmente ausbildet. Die Ausprägung der Polarisation und die Dauer des Relaxationsprozesses in den Gleichgewichtszustand ist stark temperaturabhängig, und kann von wenigen Minuten bei Raumtemperatur bis zu mehreren Stunden bei 0 °C reichen. Basierend auf einer Core-Shell-Modellvorstellung können die langfristigen Relaxationsprozesse auf die langsamen Lithium-Diffusionsprozesse in den Partikeln zurückgeführt werden. Die im Diffraktogramm beobachteten Phasenverteilungen lassen sich hieraus ebenfalls ableiten. Die Analyse der Relaxationszeiten ergibt eine effektive Diffusionskonstante für den Lithium-Transport in niedrig lithiiertem Graphit von $1.7 \cdot 10^{-10}\ \mathrm{cm}^2\ \mathrm{s}^{-1}$ bei Raumtemperatur und $0.7 \cdot 10^{-11}\ \mathrm{cm}^2\mathrm{s}^{-1}$ bei -10 °C.

Abstract

A lithium-ion battery is most efficiently used if all electrode segments are utilized equally. However, critical parameters in a real battery such as the current density and the state of charge are inhomogeneous due to transport limitations. This results in local under-utilization and over-utilization of electrode material, which causes strain and may lead to capacity and power loss as well as accelerated aging of the battery. Due to the natural tendency of an electrochemical system to strive towards equilibrium, local inhomogeneity is transient which limits the range of experimental techniques applicable.

This work investigates lateral and orthogonal state of charge inhomogeneity in graphite anodes with in situ and post mortem methods.

In commercial lithium-ion batteries, the anode is oversized with respect to the cathode to compensate for small positioning variations during production and to reliably achieve 100 % electrode overlap. The investigation of these so-called *overhang areas* by means of X-ray diffraction and color analysis shows that these areas are lithiated during storage and function as lithium reservoirs. Consecutive cycling of cylindrical cells shows that the exchange of lithium with these reservoirs alters the cells' coulombic efficiency. This influence may persist for hundreds of hours of cycling, depending on the storage conditions. Furthermore, these reservoirs may cause temporary capacity differences of up to several percent of nominal capacity for cells of equal State of Health (SoH). The findings show that anode overhang areas need to be taken into account in the interpretation of coulombic efficiency and SoH measurements. Strategies to quantify or mitigate these effects, such as pre-cycling, are discussed.

Lithium reservoirs may also occur in the context of handmade laboratory cells if double-coated electrodes acquired through post mortem are utilized. The investigation of coin cells made from single and double-coated electrodes show that the backside coating may provide up to 70 % additional capacity which compromises the measurements of the electrode material in consideration. Removal of the backside coating for post mortem electrodes is thus highly advised.

The orthogonal inhomogeneity in electrodes is investigated by means of in situ neutron diffraction in two experiments. The phase change of the anode in a commercial pouch battery during discharge and relaxation is monitored for several discharge rates and temperatures. This approach is extended to custom-built pouch cells with varying anode loading.

The results show that during discharge the graphite in the anode is polarized into segments with different degree of lithiation. The degree of polarization and the duration of the relaxation process to an equilibrium state is found to strongly depend on temperature, ranging from minutes at room temperature to several hours below 0 °C. The long-term relaxation phenomena can be attributed to slow lithium transport within particles at low temperature based on a core-shell model approach. Analysis of the relaxation times and particle size distribution yields effective diffusion constants for lithium transport in low lithiated graphite of $1.7 \times 10^{-10}\ \mathrm{cm^2\ s^{-1}}$ at room temperature and $0.7 \times 10^{-11}\ \mathrm{cm^2 s^{-1}}$ at -10 °C.

Table of contents

Abbreviations

AC	alternating current
CC	constant current
CCCV	constant current constant voltage
CE	coulombic efficiency
CV	constant voltage
DEC	diethyl carbonate
DoD	depth of discharge
DVA	differential voltage analysis
EC	ethylene carbonate
EIS	electrochemical impedance spectroscopy
EoL	end of life
EV	electric vehicle
FWHM	full width half maximum
HEV	hybrid electric vehicle
HTT	high temperature treatment
LCO	lithium cobalt oxide
LFP	lithium iron phosphate
MCMB	mesocarbon microbeads
MLZ	Mayer-Leibnitz Zentrum
ND	neutron diffraction
NMC	lithium nickel manganese cobalt oxide
NMP	*N*-Methyl-2-pyrrolidone
OCV	open circuit voltage
p2D	pseudo 2-dimensional
SEI	solid electrolyte interphase
SEM	scanning electron microscope
SoC	state of charge
SoH	state of health
TCH	Thompson-Cox-Hasting (profile)
VC	vinylene carbonate
XRD	X-ray diffraction

1 Introduction

Lithium-ion batteries are used in a range of applications, from small batteries in portable electronics to large battery systems in electric vehicles and stationary storage. Figure 1 shows the greater than linear growth of battery sales and the broadening range of applications during the last decade. As prices continue to decrease, continuing strong growth is expected in the segment energy storage systems and electromobility as well as new applications [1].

Critical performance parameters for the continuing success of lithium-ion batteries in electromobility and other markets are: cost, discharge power, specific energy, calendar life, cycle life and low temperature capability [2]. Improvements in these parameters at cell level can be achieved through research of new materials as well as modification of cell design. With such a large quantity of yearly manufactured cells, even small optimizations in cell design will have a notable impact.

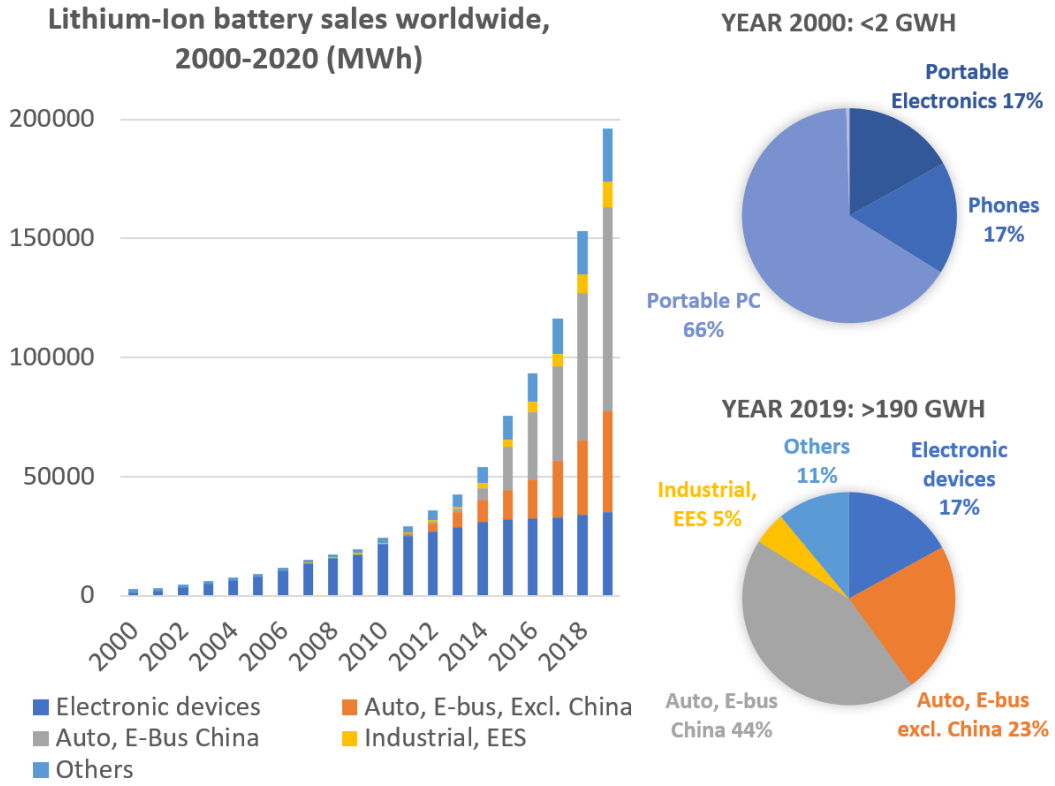

Figure 1 Lithium-ion battery sales for year 2000 up to 2020 as reported by Avicenne Energy [1].

Optimal utilization of electrode materials and thus cell performance overall is strongly dependent on cell design. Two particular ways how electrode design affects local inhomogeneity, cell aging, and low temperature performance are presented in this chapter, along with the experiments conducted to evaluate these effects and to improve upon current design of anodes. In addition, an overview of this work is given.

1.1 Motivation

A key challenge of current generation cells is to improve the aging behavior of established battery active materials, such as graphite, to achieve a longer and more predictable battery lifetime [3, 4]. Two types of studies form the basis for aging experiments: calendar aging experiments, where batteries are stored at various conditions for several months or years [5–9] and cycling studies where batteries are repeatedly charged and discharged [10–12] often replicating real use scenarios [13]. These experiments rely on precise capacity measurements to correctly distinguish between irreversible effects, such as loss of cyclable lithium, and reversible effects, such as temperature dependent rate capability. New ultra-high precision coulombic efficiency (CE) experiments may reduce the need for costly long term measurements through early detection of side reactions and better predictability of battery lifetime [14, 15]. The changes in CE due to degradation processes through parasitic reactions are very small. Thus, CE studies of these processes require precisely set currents, high precision voltage measurements as well as strictly controlled sample environments [16].

The high sensitivity of these measurements under controlled sample conditions led to the discovery of a surprising reversible capacity effect. Studies found *anomalous transient CEs* with $CE > 1$ in high-precision cycling experiments after storage [17, 18]. This behavior was linked to *anode overhang*, acting as a lithium-ion source or sink depending on the charging or discharging scenario [18]. The term anode overhang describes the areas of the anode active material without a cathode counterpart. Overhang areas occur if the negative electrode in a lithium-ion cell is designed slightly larger than the positive electrode. This is a common design feature to assure 100 % cathode-anode overlap and to avoid lithium plating at the border area of the graphite anode [19]. The analysis of 220 mAh wound pouch bag cells with 1 mm side overhangs showed a lithiation of the overhang regions after high state of charge (SoC) storage. Previous studies determined that the storage SoC affected the CE for up to 1000 h of subsequent cycling [18]. Reversible and SoC-dependent capacity increase was also observed by Lewerenz et al., who performed calendar and cyclic aging experiments with 8 Ah cylindrical cells at elevated temperatures [20]. They also attribute this effect to anode overhang areas. Understanding of the influence of overhang areas on CE, SoC, and SoH is thus crucial for the interpretation of precise measurements of aging phenomena in research as well as in operation and management of batteries in commercial applications. Advancement of aging research is important to improve cycle life of battery cells and thus reduce battery cost and entry barriers for applications such as e-mobility.

Another key challenge closely related to aging is the improvement of low temperature performance of batteries in general and graphite anodes in particular. Low temperatures may affect batteries negatively in several ways, such as: energy and power loss [21], deposition of metallic lithium (lithium plating) at the anode during charging [22], and electrode degeneration during cycling [23]. As a result, safety problems including total battery failure may occur [24]. Temperature affects battery components and processes broadly and makes isolation of a particular phenomenon difficult. For example, lithium transport through the electrolyte slows down with decreasing temperature as the electrolyte diffusivity and conductivity decrease [25, 26]. Similarly, lithium transport through the active material slows down due to decreasing solid diffusion coefficients of graphite [27, 28] and cathode materials [29]. Furthermore, the overall cell impedance increases at low temperature as shown by reference electrode experiments [30, 31]. Graphite anodes are particularly affected by low temperatures. Increased low-frequency resistances are associated with hampered charge transfer processes at the solid electrolyte interface (SEI) [32]. With the potential of lithium intercalation into graphite close to the potential of metallic lithium Li/Li^+ deposition (~ 100 mV) [33, 34], overpotentials at low temperature can quickly exceed 100 mV and prevent intercalation [35]. Additionally, the wide range of possible morphological and crystallographic configurations of graphite [36, 37] increases the complexity since transport parameters may vary for different types of graphite. For example, the transport of lithium in particles depends on the graphite crystallinity and stage of lithiation [38, 39].

Charge transfer resistance decreases with increasing graphite surface area [40]. Transport in the electrolyte depends on the tortuosity of the electrode coating which itself depends on parameters of the active material such as particle shape and radii distribution [41, 42]. Consequently, low temperature performance of graphite based anodes is generally considered to be a major obstacle in lithium-ion battery applicability [43].

With the broad impact of low temperatures on batteries, it is difficult to determine the dominating limitation in cells compared to laboratory systems. Application-oriented measurements with large format cells, preferably in situ, are needed due to the transient nature of the inhomogeneity caused by transport limitations. Measurement techniques such as Electrochemical Impedance Spectroscopy (EIS) have been successfully applied to investigate low temperature effects in several experiments [27, 32, 38, 44, 45] but the capability to localize effects is limited. More recently, neutron diffraction (ND) has been applied to lithium-ion batteries to study structure dynamics [46–48], lithium plating [22, 49], overcharge, or current depending phase evolution [50, 51]. Neutrons have excellent sensitivity towards lithium and fast in situ measurements are possible by focusing on a narrow angular range. With neutron diffraction, SoC inhomogeneity as a result of transport limitations at low temperature can be visualized. Time-resolved lithiation data provides complementary information to the capacity and EIS data, which helps to determine the dominating limitations for a given cell design and to improve it for challenging operation scenarios and environmental conditions.

1.2 Object and purpose

The focus of this thesis is the investigation of SoC inhomogeneity and accompanying transient local effects in graphite anodes, their impact on cell performance as well as the accuracy of battery measurements. Lateral inhomogeneity caused by electrode design of overhang areas is investigated by means of XRD. Electrode inhomogeneity caused by transport limitations is examined through in situ ND. In addition, post mortem and other techniques are applied.

The effect of excess anode area is examined for two variations, overhang areas in cylindrical cells and backside coating in coin cells.

Overhang areas

A set of commercial 18650-type cylindrical cells, which feature wide anode overhang areas of 2-6 cm in addition to smaller side overhang areas of 1.5 mm, were calendar aged. To examine whether these areas can be lithiated and influence the capacity measurements of cells, CE and post mortem analysis of commercial cylindrical cells was conducted after long-term storage at SoCs ranging from 0 % to 100 %. The post mortem analysis consists of a qualitative assessment of the overhang area through observation of color changes complemented by ex situ XRD for quantitative local information. Graphite shows a well-known color change upon intercalation of lithium which is used to detect lithium transport into the overhang regions [52–54]. In addition XRD is applied to measure SoC inhomogeneity in electrodes and the overhang area [55]. The purpose of this experiment is to expand knowledge on overhang areas beyond existing work in the following two aspects.

First, the lithiation of overhang areas has so far only been shown qualitatively using color analysis. However, in a top view image of an extracted electrode only the surface of the graphite particles at the surface of the electrode layer is visible. The observed surface lithiation may differ from the average electrode lithiation if lithiation gradients within particles or the layer are present [54]. In XRD measurements, the X-rays penetrate the electrode layer and active material particles. The resulting XRD diffraction pattern contains the structural information of the exposed volume. The XRD measurements thus complement and verify the color analysis with a quantitative measurement of the average lithiation of a given segment.

Secondly, previous research focuses on rather small overhang areas of 1-2 mm at the electrode sides. Additional large areas without cathode counterpart are located at the innermost and outermost winding of the jelly roll, which have not been investigated so far. These areas are also ionically connected to the lithium electrolyte reservoir. However, given that diffusion processes in batteries are slow, it is not clear whether segments several centimeters away from the cathode can also be lithiated and affect CE and capacity measurements. The investigation is thus extended to these areas.

Backside coating

Excess anode area is not limited to cylindrical cells but can also be found in pouch cells, prismatic cells as well as laboratory-made coin cells. In addition to the side overhang area, it may occur that a double-coated electrode only has a counter electrode on one side but not on the other. The area without counter electrode is referred to as backside coating. Similar to the overhang area, this coating is electrically and ionically connected to the battery. Yet, in contrast to overhang areas the coating is not a continuous extension of the active electrode area but separated by a gap. In commercial cells this may occur if the outermost layer in pouch cells is double-coated. In laboratory coin cells a backside is present if double-coated electrodes are used for half-cell measurements. Aging analysis and simulation models of commercial batteries often require detailed knowledge about electrode properties such as loading and half-cell profiles. Pre-formation electrode material is seldom available from the manufacturers which produce commercial large format cells. Thus, material for experiments needs to

be taken post mortem from batteries. Often full cells do not have single-coated electrode segments and thus one can only extract double-coated electrodes. The backside coating can be removed mechanically with or without the help of a solvent. Yet, this may damage the coating intended for use, especially in the case of brittle or aged electrodes. To the knowledge of the author, coin cells with double-coated electrodes have been used to analyze commercial cells. However, the use of double-coated electrodes in coin cells is questionable since the backside areas can potentially participate in the charging/discharging process.

The lithiation of backside coating in coin cell electrodes is investigated with single- and double-coated graphite and lithium iron phosphate (LFP) electrode material. Coin cells are made from pre-formation electrodes and from custom-made small format pouch cells using the same electrode materials. The backside coating of the post mortem electrodes is set to specific lithiation states, i.e. fully charged and fully discharged. The rate dependent capacity as well as the voltage profiles are compared for single and double-coated electrodes. The purpose of these measurements is to evaluate the impact of the backside coating on the coin cell capacity and the half-cell profiles. In particular, the question is investigated if there is a rate limit above which backside coating effects can be disregarded because the associated diffusion processes are too slow. Based on this analysis, best practice guidelines for post mortem electrodes are derived.

Electrode layer inhomogeneity

In situ neutron diffraction is performed with a commercial pouch cell as well as three custom-made pouch cells with varying anode loading. The graphite phase evolution during discharge and relaxation for a high power $LiCoO_2$/graphite pouch battery is measured by applying time-resolved in situ neutron diffraction. In addition to the ND data, information on electrode properties such as graphite particle shape and size is acquired via post mortem methods. The low temperature capacity and impedance are determined. The rate and temperature dependence of the anode phase polarization is assessed and the relaxation time is analyzed and compared to previous results obtained with cylindrical cells.

The purpose of these experiments is to test and verify previous ND results of transient graphite inhomogeneity and to expand this method to a new battery format. Previous investigations by means of ND use commercial, high energy cylindrical cells [56]. These cells are typically chosen due to their high active material weight fraction and radial symmetry, where the best data quality can be achieved in combination with a large gauge volume. However, considerable potential [57–60] and temperature gradients [44, 61–63] as well as local SoC differences [64–66] have been observed in simulations and measurements of cylindrical cells. As the difficulty to interpret the observed graphite phases increases with the number of effects contributing to SoC inhomogeneity in the gauge volume, a small-format pouch cell is selected to reduce temperature and potential gradients within the observed volume. The effect of the coating thickness on electrode inhomogeneity is isolated through variation of cell loading for otherwise equal sample cells.

The conducted experimental studies highlight the capabilities and limitations of diffraction in the investigation of local lithiation distributions. The results aid the design of future cells with minimized electrode inhomogeneity. Strategies to reduce the impact of electrode inhomogeneity in SoH and CE are derived and will enable more precise and faster aging studies.

1.3 Outline

The structure of this thesis is outlined in Figure 2. The central topic is local SoC inhomogeneity in the anode. Two particular instances of such inhomogeneity are investigated in four experiments.

Local inhomogeneity caused by excess anode areas lithiated during storage is examined in chapter 5 and 6. The transient SoC inhomogeneity in the anode due to transport limitations during use and relaxation is researched in chapter 7 and 8. The foundation for the discussion and interpretation for the experiments is built in chapter 2, 3, and 4, where the transport processes and limitations in batteries, the particular properties of graphite electrode as well as the applied experimental methods are introduced. The thesis closes with a conclusion in chapter 9.

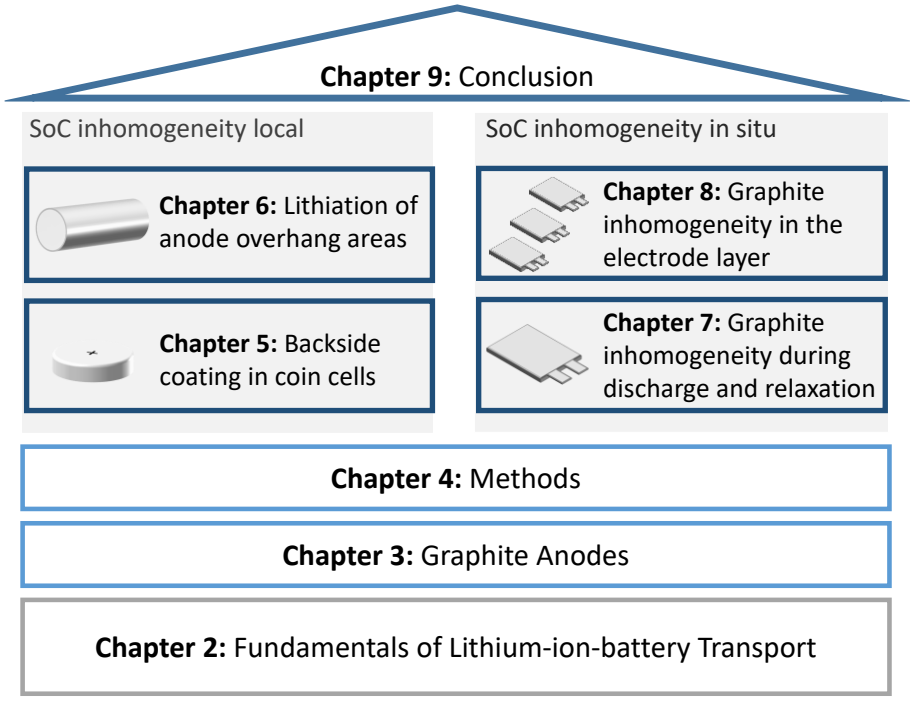

Figure 2 Structure of the thesis.

Chapter 2 discusses the transport of ions and electrons in lithium-ion batteries. After a brief introduction of the working principle of lithium-ion-batteries and popular cell designs, transport in the different domains, liquid and solid as well as the interface in between is described. In particular, limitations arising from slow solid or liquid diffusion and the temperature dependence of these material properties are highlighted. Evidence of the impact of transport limitations and anode overhang areas on cell performance and SoC inhomogeneity in state-of-the-art research publications is examined.

The material properties of active material are of great importance for the ionic and electronic transport in the anode. Despite being the most common material, transport in graphite is still not fully understood due to the phase transition the material undergoes during lithiation. **Chapter 3** discusses in detail the crystal properties of lithiated graphite as well as the competing models for stage transformation in literature. In addition, a model for diffusion driven transport is given.

Chapter 4 presents the experimental techniques and methods applied in the overhang and relaxation experiments. This includes standard procedures such as cycling tests, electrochemical impedance spectroscopy (EIS), differential voltage analysis (DVA) as well as more uncommon techniques such as color analysis of post mortem electrodes, and tortuosity analysis through SEM and EIS. Central to the experiments is the determination of the anode SoC through measuring the changes in the diffraction patterns of graphite upon lithiation. Two different forms of diffraction are utilized in the experiments;

X-ray diffraction and neutron diffraction. Both methods are compared and the techniques to analyze the raw data, such as Rietveld refinement and Pawley fits, are introduced.

Excess anode area, commonly found in commercial cells due to the oversizing of the anode compared to the cathode, may act as a lithium reservoir. While lithiation of these areas is slow, it does occur for calendar aged cells, particularly at high storage SoC and high temperatures. **Chapter 6** studies this effect quantitatively for commercial 18650 cells stored at various SoC and subsequently cycled and opened for post mortem investigation. It is shown by means of color change and XRD that small and large overhang areas are lithiated to varying extent, and that cycling processes are affected by the lithium reservoirs up to several hundred cycles after storage.

Furthermore, it was found that coated electrode backsides without cathode counterpart may also act as a lithium reservoir. In commercial pouch cells, this may occur if the outermost layer is double coated. **Chapter 5** investigates the effect of backside coating in the context of electrode analysis of commercial cells. Electrodes extracted from commercial cells for material analysis, i.e. half-cell profiles, can be brittle and thus the removal of the backside difficult to handle. The experiment finds that coin cells made from double-coated graphite and LFP electrodes utilize the backside to a high degree, resulting in up to 70 % of additional capacity. Even at high discharge rates, the backside is partially charged and discharged. This effect is reproduced qualitatively with a 2D electrochemical model of the coin cell backside.

While the previous two chapters discussed the local inhomogeneity in the vicinity of excess areas, the following chapters investigate the inhomogeneity in the electrode during use.

In **chapter 7** the emergence of multiple coexisting graphite lithiation phases in the anode of a commercial pouch cell during discharge and relaxation is examined. Analysis of the ND data of a commercial cell at various discharge rates and cell temperatures reveals the coexistence of phases at different degrees of lithiation. This coexistence persists during the relaxation process. Extent and longevity of the effect strongly depends on cell temperature and coexistence can be observed up to several hours after discharge at low temperatures of -10 °C and 0 °C. Temperature inhomogeneity, potential gradients as well as diffusivity limitations are discussed as potential origins of the inhomogeneity. An effective graphite diffusion constant is derived from the relaxation times.

Chapter 8 extends the experimental approach from the previous chapter to custom-made pouch cells with varying loading to investigate the effect of electrode thickness on the observed phase inhomogeneity. The custom-made cell performance parameters and the anode material properties, such as tortuosity and porosity, are discussed in detail. Furthermore, the preparations for the ND experiment are outlined including the DVA analysis for the optimal depth of discharge (DoD) as well as low temperature performance and neutron beam characterization. The results of the ND-data-analysis of the different graphite loadings at fixed rate and temperature finds a comparatively small effect of the electrode layer thickness on phase separation and relaxation times.

The conclusions drawn from each experiment are summarized in **chapter 9**. Overhang areas and backside coatings significantly influence the cell capacity, SoH determination, and coulombic efficiency after storage. Strategies to minimize the effect, such as pre-cycling before SoH determination, are explored. Neutron diffraction is found to be a powerful tool to visualize anode inhomogeneity. However, the graphite inhomogeneity cannot be localized without additional information about the cell.

The thesis closes with a brief outlook of potential follow-up experiments exploring the nature of the observed graphite inhomogeneity.

2 Fundamentals of lithium-ion transport

Transport phenomena in lithium-ion batteries encompass a variety of different mechanisms, such as ionic and electronic conduction processes in liquid environments, solid environments and at the interface between them. Transport processes are complex but crucial for the performance of lithium-ion batteries. Transport limitations can cause loss of battery capacity and power capability, accelerate aging processes, or safety hazards. Lithium-ion batteries are operated in a range of applications at different environmental conditions. This is a challenge for the design of a cell, because of the temperature dependence of material properties, such as conductivity and diffusivity, potentially negatively affecting the transport processes.

This chapter presents the working principle of lithium-ion batteries and the transport processes in each domain of the battery. Furthermore, the impact of transport limitations on the battery in general and the SoC distribution in particular are described.

2.1 Lithium-ion batteries

The lithium-ion battery is the dominant type of secondary battery for portable electrons and electric vehicles. A lithium-ion battery consists of one or more electrochemical cells connected in series or parallel.

2.1.1 Working principle

In the basic unit of a lithium-ion battery, the electrochemical cell, electrical energy is stored through a redox reaction of the electrode materials. The change in Gibbs energy ΔG between the charged state and the discharged state of a battery for a given pairing of electrode materials is the driving force which enables the battery to provide electrical energy to an external circuit. The choice of the electrochemical couple determines the amount of electrical energy that can be stored.

The typical setup of today's lithium-ion batteries is the so called *rocking chair* or *shuttlecock* setup [67], where both electrodes consist of lithium insertion compounds as depicted in Figure 3. The insertion of Li^+ into the intercalation compound is called *lithiation*. The removal of Li^+ from the intercalation compound is called *delithiation*. The commonly used negative electrode material is graphitic carbon. For the positive electrode material, a wide range of metal oxides is used. During operation of a lithium-ion battery the Li^+ ions are exchanged between the positive and negative electrodes. In a charging process, the cathode is oxidized. Li^+ is released into the electrolyte and an electron is transported through the current collector over an external circuit to the anode. The anode is reduced and Li^+ is intercalated. During a discharge, this process is reversed. By convention, the electrode positive during discharge is defined as the cathode and the electrode negative for discharge is defined as the anode independent from the reaction direction during charging [68].

The half-reaction at a graphitic anode side is described by

$$\mathrm{Li}_x\mathrm{C}_6 \rightleftharpoons \mathrm{C}_6 + x\mathrm{Li}^+ + x\mathrm{e}^- \ (0 \leq x \leq 1). \tag{1}$$

The half reactions at the cathode side for the cathode materials examined in the experiments of this thesis are given in equation (2)(3)(4). Here x gives the degree of lithiation of a material.

$$\mathrm{Li}_{1-x}\mathrm{CoO}_2 + x\mathrm{Li}^+ + x\mathrm{e}^- \rightleftharpoons \mathrm{LiCoO}_2 \ (0 \leq x \leq 0{,}5) \tag{2}$$

$$\mathrm{Li}_{1-x}\mathrm{FePO}_4 + x\mathrm{Li}^+ + x\mathrm{e}^- \rightleftharpoons \mathrm{LiFePO}_4 \ (0 \leq x \leq 1) \tag{3}$$

$$\mathrm{Li}_{1-x}\mathrm{Ni}_{1/3}\mathrm{Mn}_{1/3}\mathrm{Co}_{1/3}\mathrm{O}_2 + x\mathrm{Li}^+ + x\mathrm{e}^- \rightleftharpoons \mathrm{LiNi}_{1/3}\mathrm{Mn}_{1/3}\mathrm{Co}_{1/3}\mathrm{O}_2 \ (0 \leq x \leq 1). \tag{4}$$

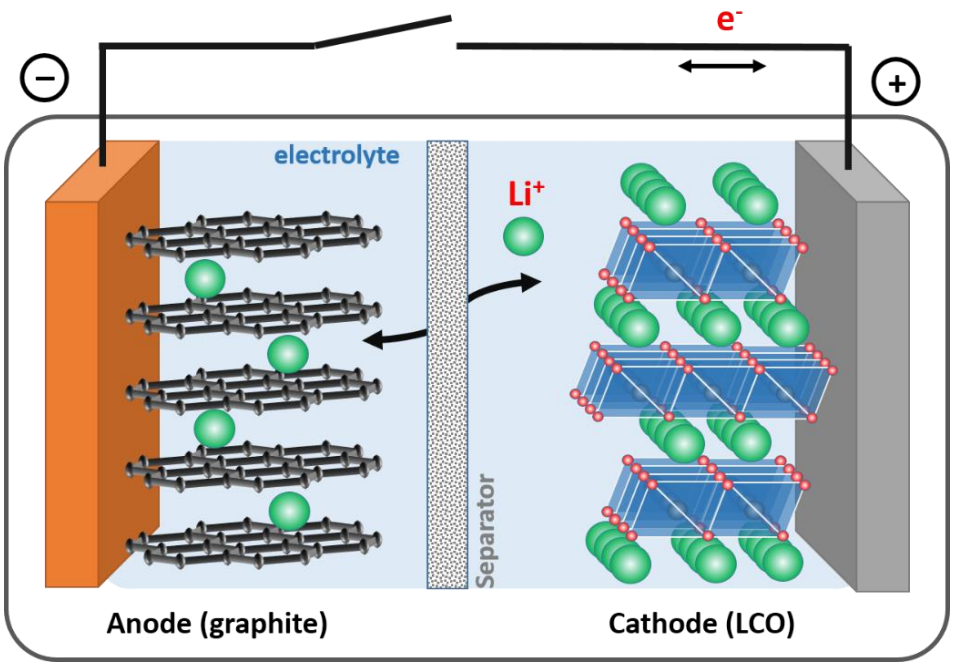

Figure 3 Schematic description of a lithium-ion battery. Lithium ions and electrons are exchanged between the positive and the negative electrodes. The Li^+ ions are transported in the electrolyte through the separator and the electrons through the current collectors and the external circuit. The depicted anode (graphite) and cathode ($LiCoO_2$) materials have a layered crystal structure. Image based on [69, 70].

2.1.2 Construction and components

The basic components of a lithium-ion battery are electrodes, separator, electrolyte, and casing. Lithium-ion cells can be built in various sizes ranging from a capacity of a few mAh up to several hundreds of Ah. Electronic and ionic transport properties depend on the materials used as well as the size and design of the cell.

Electrodes

The electrochemically active materials are mixed with a binder material to achieve mechanical stability and to attach the electrode material to the current collector. Typical binder materials are polyvinylidene fluoride (PVDF), styrene-butadiene rubber, and carboxymethylcellulose [71]. The current collector is a thin foil of about 5-25 µm thickness that transports the electrons to the terminals of the battery. The material chosen for the foil at the anode side is typically copper, at the cathode side it is aluminum. For some materials, conductive additives such as carbon black are added to improve the electronic conductivity in the electrode. The electrodes have a porous structure to increase the electrode/ electrolyte surface area and thus the rate capability of the battery.

Graphitic carbon is the most commonly used anode material in commercial lithium-ion batteries due to the low cost of the material and the excellent cycling stability that can be achieved [72]. During the first electrochemical reaction the strong reducing power of the graphite surface causes a thermodynamic instability of the electrolyte that causes a reaction of the lithium ions with electrolyte decomposition products to form a protective layer, the so-called solid electrolyte interphase (SEI) layer. This layer is electronically insulating and electrochemically inactive but permeable to Li^+ carriers. However, the formation of the SEI layer consumes lithium and causes an initial capacity loss. Alternative anode materials are Lithium Titanate $Li_4Ti_5O_{12}$ (LTO) and silicon carbon composites.

Commercially available lithium-ion cells utilize lithiated metal oxides or lithiated metal phosphates as cathode materials. The samples in this work utilize lithium cobalt oxide $LiCoO_2$ (LCO), lithium nickel manganese cobalt oxide $LiNi_{1/3}Mn_{1/3}Co_{1/3}O_2$ (NCM-111) and lithium iron phosphate $LiFePO_4$ (LFP). LCO and NCM-111 have a layered crystal structure while LFP is an olivine structure with 1D tunnels for the Li^+ to intercalate. The materials differ in their potential, specific capacity and energy. The anode composition of the sample cells as given in the material safety data sheets (MSDS) is shown in Table 1.

Table 1 Active material and binder composition for the electrodes of the sample cells. For A123 18650m1a no information was provided in the MSDS by A123. *Given as % of total weight in MSDS.

Sample	Graphite (%)	Cathode (%)	Anode Binder (PVDF CMC) (%)
SLIP 540839	15*	30*	1.5*
Custom Cells	96	84	4

Separator

The separator is a porous film of several µm thickness that isolates anode and cathode electronically but is permeable to the electrolyte and lithium ions. The materials used in commercial cells are polymers such as polyethylene (PE) and polypropylene (PP). Some cells use a trilayer separator (PP/PE/PP) instead of a single layer for increased safety. At high temperatures the PE layer melts and acts as shutdown mechanism due to the lower melting point of 135 °C compared to 155 °C of PP.

Electrolyte

Liquid lithium-ion battery electrolytes consist of lithium salts dissolved in aprotic organic solvents. Examples of commercially used lithium salts are Lithium hexafluorophosphate ($LiPF_6$) and Lithium tetrafluoroborate ($LiBF_4$). Examples of organic solvents are diethyl carbonate (DEC), ethyl methyl carbonate (EMC) and dimethyl carbonate (DMC). Electrolytes commonly utilize a mixture of multiple solvents to combine the individual properties of the materials. An example of such a commercial battery electrolyte is LP30 by BASF which contains 1.0M $LiPF_6$ in a 1:1 mixture of EC/DMC. The electrolyte composition is of great importance to the transport properties in the cell. A key parameter is the temperature and concentration dependent ionic conductivity σ_{ion}.

Design

Mass-produced lithium-ion batteries are manufactured in cylindrical, prismatic or pouch configuration shown in Figure 4. For cylindrical cells the electrodes and separator are wound with a mandrel and inserted into a gasket made from nickel plated steel or aluminum. The wound electrodes, the so-called *Jelly roll* is connected to the terminals through welded tabs. Common formats are 18650 (18 mm diameter, 65 mm height) 26650 (26 mm diameter, 65 mm height). Pouch and prismatic cell designs can use either flat wound electrodes or stacked electrodes. In the case of stacked electrodes, each electrode has an individual tab. The tabs of all electrodes are bundled together and welded to the terminal. Prismatic cells use hard casings such as the cylindrical cells while pouch cells are sealed in a flexible trilayer foil of polyamide (PA)/Al/PP that is thermally laminated. Additional safety devices such as a rupture disk/ safety vent and circuit interruption devices (CID) are found in commercial cells to protect from high currents, temperature, or pressure [73].

In addition to the various formats available, internal properties, such as the coating thickness and porosity of the electrodes, the current collector width, electrolyte composition and others are adjusted to design cells for high power or high energy capabilities. How the cell design choices and operation conditions affect the transport properties is discussed in the following chapter.

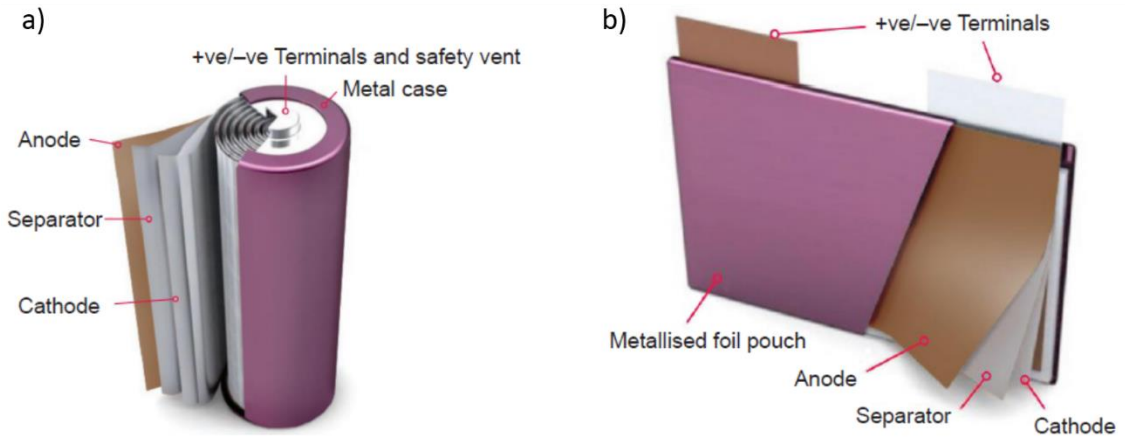

Figure 4 Cell design of a cylindrical (a) and pouch (b) cell. Image reprinted from [74] with permission from Johnson Matthey Plc. Distributed under Creative Commons BY NC ND license.

2.2 Transport processes

In a real battery electronic and ionic transport processes are not frictionless. Transport limitations cause performance loss, such as diminished power, capacity, and cycle life. Performance loss is often linked to inhomogeneity of important cell parameters such as the current density, the electrode potential or the SoC, due to which the battery capacity and rate capability is not fully utilized. The internal resistance of a cell is the sum of the ionic resistance, the electrical resistance and interfacial resistances.

In the following the electrical and ionic transport in the different domains of the battery will be discussed including the contributions of morphology and temperature. Figure 5 gives an overview of the processes and domains. Furthermore, the impact on performance is discussed with some examples from measurement and literature.

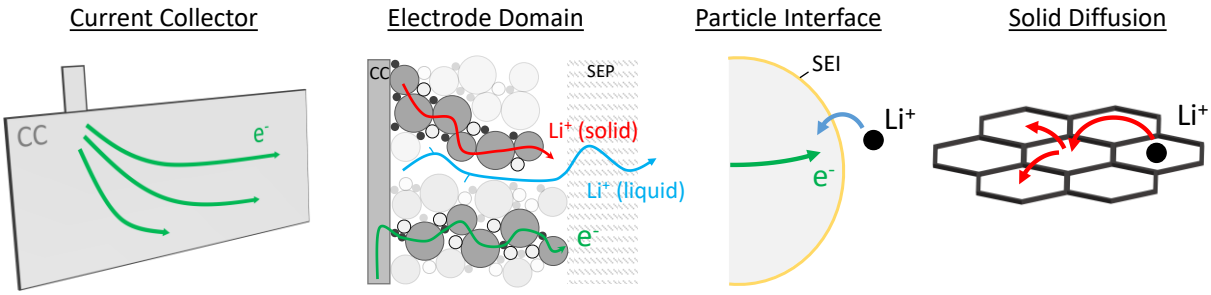

Figure 5 Schematic overview of the transport processes in the current collector and electrode domains, at the particle interface, and in the bulk active material.

2.2.1 Electrical transport

An electron traveling through a battery encounters resistance at the electrode particles, the conductive additives, the current collectors, and the electrical taps connected to the cell casing.

2.2.1.1 Current Collectors

The electrical resistance and potential distribution in the current collector and tabs can be calculated analytically for simple geometries or numerically for complicated geometries with the Poisson equation and Ohm's law [75]. Especially for cylindrical or wound prismatic cells, where the electrodes exceed lengths of 1 meter, the potential drop along the current collector foils may be considerable and result in SoC inhomogeneity [66]. Therefore, commercial high-power cells such as the A123 AMR18650m1a utilize multiple taps. An analytical description of 1D foil current and potentials for spiral wound cells with arbitrary tab configuration is given by Reimers et al. [57, 75].

2.2.1.2 Electrodes

Transport in the electrode is dependent on the material properties as well as the microstructure. Graphite is a zero bandgap semi-metal with a conductivity of $\sim 10^3\ \mathrm{S/cm}$ [29]. In comparison, cathode materials are often semiconductors with a band gap at room temperature and lower conductivity. $LiCoO_2$ and $LiFePO_4$ have band gaps of > 0.2 eV at room temperature and orders of magnitude lower conductivities $\sim 10^{-4} - 10^{-9}\ \mathrm{S/cm}$ [29]. In addition to the electronic pathway, ionic conduction contributes to conductivity in these materials. Despite the band gap and ionic contributions, conduction phenomena are commonly discussed in terms of the free electron gas concept [29]. To compensate for low conductivity the materials are covered with conductive carbon coatings [76] or conductive additives such as carbon black are added to the electrodes. The resistance an electron or ion encounters on its way to a particular position in the electrode is path dependent on the percolation network of particles and additives. The effect of the microstructure is modeled with resistor networks for the electronic transport and electrochemical fin theory for the ionic pathways [77]. In addition, covering layers on the particle-particle or particle-liquid interfaces, such as the SEI on graphite, may have a much lower ionic and electronic conductivity than the bulk electrode. Peled et al. report SEI resistances of 10-1000 $\Omega\mathrm{cm}^2$ for 10 nm SEI layers [78]. However, the composition of the SEI may vary depending on electrolyte additives and formation [79] and the thickness may grow over time [80], making the contribution of the SEI to the internal resistance difficult to determine.

Table 2 Active material properties.

	Prac. capacity (Ah/ kg)	Energy density (mAh/cc)	Density (kg/L)	Diffusivity (cm^2/s)	Conductivity (S/cm)
Graphite	360[81]	810	2.25 [72]	10^{-5} to 10^{-12}[40, 82]	10^3 [29]
NCM(111)	200[81]	940	4.7[81]	10^{-10} to 10^{-11}[83]	10^{-4} [29]
LFP	160[81]	592	3.7[81]	10^{-14} to 10^{-15}[29]	10^{-9} [29]
LCO	160[81]	808	5.05[81]	10^{-10} to 10^{-8} [29]	10^{-4} [29]

2.2.2 Solid-phase lithium transport

The ionic transport properties of active materials can be rate determining for lithium-ion batteries. Active materials such as graphite are polycrystalline and the lithium ions are transported through the bulk and along the interface between crystallites. In the following the general principle of these ionic pathways is discussed. A detailed description needs to take a material's crystallographic properties into account and is provided for graphitic carbons in chapter 3.

2.2.2.1 Bulk transport

The main transport mechanism in bulk crystals is diffusion. Fick's law of diffusion describes the ionic flux J_i and the change in concentration over time $\frac{\partial c_i}{\partial t}$.

$$J_i = -D_i \nabla c_i \tag{5}$$

$$\frac{\partial c_i}{\partial t} = \nabla(D\, \nabla c_i) \tag{6}$$

The index i describes the ionic species. D_i is the diffusion constant. Diffusion in solids can be vacancy (defect) or non-vacancy (non-defect) mediated. Given that the lithium ion is small, the dominant diffusion mechanism is thought to be the non-vacancy mediated transport through incorporation into interstitial sites of the host lattice [84][39]. Solid diffusion is temperature dependent and follows an Arrhenius type relationship (see section 2.2.6).

2.2.2.2 Grain boundaries

The grain boundary is defined as the interface between two crystals or grains [29] in a polycrystalline material. Grains can be tilted or twisted with respect to the neighbor crystallite orientation. Disorder or incomplete bonding at the grain boundary is responsible for a high defect concentration [85]. The defects mediate diffusion through Frenkel and Schottky pairs [29].

2.2.3 Liquid-phase lithium transport

A lithium ion in an organic electrolyte does not move unhindered within the electrolyte, but is subject to drag. The cations (Li^+) and anions (e.g. PF_6^-) of a dissolved lithium salt (e.g. $LiPF_6$) are surrounded by a solvation hull of solvent molecules. The electrostatic forces of the ionic surroundings and other friction mechanisms (Stokes) provide resistance for the ionic movement.

There are three transport mechanisms in electrolytes; convection, migration and diffusion. Convection is generally neglected in batteries, since the porous medium prevents the flow of the electrolyte [70]. Diffusion in liquids is described by Fick's law, similar to solid diffusion, but with a liquid diffusion constant D_i. With the Debye Hückel Onsager theory the transport properties for such non-ideal ionic solutions can be calculated.

2.2.3.1 Concentrated solutions

The concentration of lithium ions for commercial battery electrolytes is ≈ 1 mol/ L und thus exceeds the concentration limit 0.1 M to 0.01 M up until a solution can still be considered dilute [86]. For such a *concentrated solution* the assumption of local electro neutrality $\sum_i z_i c_i = 0$ does not hold and the potentiostatic interaction of the solvated ions needs to be considered. In the concentrated solution theory, the mass conservation is calculated by

$$\frac{\partial c_i}{\partial t} = -\nabla \cdot \left(-D_i \nabla c_i + \frac{i_l t_i}{z_i F}\right) + r_i. \tag{7}$$

Equation (7) contains the local source term r_i, the transference number t_i, the Faraday constant F, the electrons transferred per ion z_i, the diffusivity, D_i and the currrent density i_l. For a binary electrolyte with a single electron exchanged per ion, the concentration dependent current density is given by

$$i_l = -\kappa \nabla \varphi_l + \frac{2\kappa RT}{F}\left(1 + \frac{\partial \ln(f_\pm)}{\partial \ln(c_+)}\right)(1 - t_+)\nabla \ln(c_+) \text{ [86].} \tag{8}$$

In addition to the direct T dependence, the ionic conductivity κ is also temperature dependent. $t_+$is the transference number, F is the Faraday constant, R is the gas constant, $f_\pm$ is the molar activity. This implementation of the concentration dependent current density and mass balance is well established in physicochemical battery models.

2.2.4 Interface transport

The Butler-Volmer equation (9) describes the reaction rate at the interface between electrolyte and active material. i_n is the current density orthogonal to the interface.

$$i_n = i_0 \left(e^{\frac{a_A F}{RT}\eta} - e^{\frac{a_C F}{RT}\eta}\right) \tag{9}$$

a_A and a_C are the anodic and cathodic transfer coefficients. η is the local surface overpotential. i_0 is the exchange current density at the chemical equilibrium without net current flow. It is given by

$$i_0 = F k_C^{a_A} k_A^{a_A} \left(c_{s,max} - c_s|_{r=r_p}\right)^{a_A} \left(c_s|_{r=r_p}\right)^{a_C} \left(\frac{c_l}{1\ \text{mol/L}}\right)^{a_A}. \tag{10}$$

$k_C^{a_A}$ and $k_A^{a_A}$ are the temperature dependent cathodic and anodic reaction rates. $c_{s,max}$ is the maximum lithium concentration and $c_s|_{r=r_p}$ is the concentration at the surface of a particle with radius r_p. c_l is the concentration in the liquid and 1 mol/ L is a set reference concentration.

2.2.5 Transport in porous medium

Battery electrodes and separators are porous to increase the surface area and to allow for Li^+ transport. Its morphological properties influence the transport properties of the electrolyte. The total volume is divided into the solid domain and the liquid domain. In the case of the electrode the total volume is the sum of the volume fractions of the active material ε_s, the electrolyte ε_l and inactive electrode components such as binder and conductive carbon included as ε_{add}.

$$\varepsilon_s + \varepsilon_l + \varepsilon_{add} = 1 \tag{11}$$

Figure 6 illustrates that ions in such an environment cannot take the direct path between two points. The tortuosity is a dimensional quantity that describes the impact of this on the transport parameters.

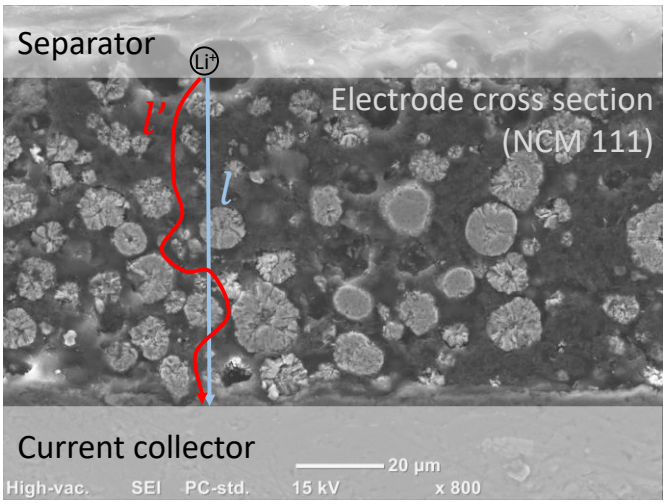

Figure 6 Schematic representation of the ionic transport effective path length. l' (red) is the diffusion length. l (blue) is the geometric length.

While the porosity is well defined and simple to measure for materials with well-known density, tortuosity is difficult to quantify. The concept of tortuosity can be approached through a microscopic or macroscopic perspective.

Microscopically, the geometric tortuosity τ_{geo} as the ratio of diffusion length l' and geometric length l (straight line between two points, i.e. electrode thickness).

$$\tau_{\text{geo}} = \frac{l'}{l} \tag{12}$$

The diffusion length is the square root of the mean square displacement $l' = \sqrt{\langle r^2(t) \rangle}$ derived from a particle performing a random walk in a *d*-dimensional space over a time t $\langle r^2(t) \rangle = 2d \cdot D \cdot t$. For an idealized geometry with spherical particles, the tortuosity can be analytically calculated to $\tau = \varepsilon^{-0.5}$. An extension of this is the well-known *Bruggeman relation*

$$\tau = \varepsilon^{-\alpha} \tag{13}$$

with the *Bruggeman exponent* α. Macroscopically, the ratio between the conductivity κ and effective conductivity κ_{eff} in a porous separator or electrode is defined as the MacMullin number.

$$N_M = \frac{\kappa}{\kappa_{\text{eff}}} \tag{14}$$

Empirically, one finds an exponential dependency on porosity with the exponent *m* without looking into individual segments or paths of ions.

$$N_M = \varepsilon^{-m} \tag{15}$$

The combination of microscopic and macroscopic approach $N_M \overset{\text{def}}{=} \frac{\tau}{\varepsilon}$ yields a nearly identical relation to the Bruggeman relation $\tau = \varepsilon^{1-m}$ with $\alpha = m - 1$. However, in this definition the tortuosity τ is not identical to τ_{geo} since it also includes effects such as variable cross-sectional areas. With this definition, the effective quantities of the ionic conductivity κ_{eff} and diffusivity D_{eff} can be expressed as

$$\kappa_{eff} = \frac{\epsilon}{\tau}\kappa_0 = \frac{1}{N_M}\kappa_0 = \varepsilon^{1+\alpha}\kappa_0 \tag{16}$$

$$D_{eff} = \frac{\epsilon}{\tau}D_0 = \frac{1}{N_M}D_0 = \varepsilon^{1+\alpha}D_0. \tag{17}$$

While MacMullin number and tortuosity are commonly used quantities, in the following solely the tortuosity will be discussed to avoid redundancy.

2.2.6 Transport and temperature

The temperature dependence of battery performance is a result of the temperature dependence of physicochemical properties $\Psi(T)$. Such a dependency can be described by the Arrhenius equation (18) [70]

$$\Psi(T) = \Psi_{ref} e^{\frac{E_{a,\Psi}}{R}\left(\frac{1}{T_{ref}} - \frac{1}{T}\right)} \tag{18}$$

where the subscript ref describes the reference value of the physicochemical property Ψ_{ref} at a reference temperature T_{ref}, the gas constant R and the activation enery $E_{a,\Psi}$ of the corresponding phase or reaction process. The activation energy is a measure of sensitivity to temperature change of the quantity $\Psi(T)$, since it is a factor in the exponent of the exponential function.

Among the properties that show an Arrhenius type temperature dependence are the conductivity of the electrolyte κ, the exchange current density i_0, the electrolyte diffusivity D_l, and solid diffusion processes D_s [24, 25, 29].

2.2.6.1 Thermal homogeneity

As described in the previous section, the temperature influences important transport parameters. An inhomogeneous temperature distribution in a battery may cause an inhomogeneous SoC distribution during lithiation or delithiation. The heat capacity of a cell is the sum of the individual specific heat capacities of its components weighted with the weight fraction in the cell.

$$C_{th,cell} = \sum_i c_{th,i} \cdot m_{\%,i} \cdot m_{cell} \tag{19}$$

Heat transport in batteries is anisotropic due to the layer structure of the electrode. Due to this, individual thermal conductivity values need to be considered for transport in parallel (‖) and orthogonal (⊥) to electrode layers. According to Chen et al. [87] thermal conductivity is calculated by

$$k_{\parallel} = \frac{\sum_i A_i \lambda_i}{\sum_i A_i} \qquad k_{\perp} = \frac{\sum_i d_i}{\frac{\sum_i d_i i}{\lambda_i}} \tag{20}$$

with the cross-sectional area A_i and thermal conductivity λ_i of the component i.

To describe temperature inhomogeneity the concept of the Biot number Bi is introduced. The Biot number is defined as the difference of the fixed body core temperature $T_{s,1}$ and surface temperature $T_{s,2}$, divided by the difference between surface temperature and the target temperature of a cooling (or heating process) T_∞. With the energy balance, this can be expressed as the ratio of the convection

heat transfer coefficient h, the thermal conductivity k and the distance L between center point and the surface.

$$\frac{T_{s,1} - T_{s,2}}{T_{s,2} - T_{\infty}} = \frac{h\,L}{k} \equiv Bi \tag{21}$$

The Biot number is a measure of the temperature homogeneity within a body during an external cooling or heating process. For $Bi \ll 0.1$ the temperature gradients within the solid are small and the body can be treated as a lumped capacitance $T(x,t) \approx T(t)$. In this case, heat transport within the solid body is faster than the transport across the fluid/solid surface layer due to convection resistance [88]. For $Bi \gg 1$ the temperture gradient within the body cannot be disregarded. Figure 7 illustrates the transient temperature distribution for each case.

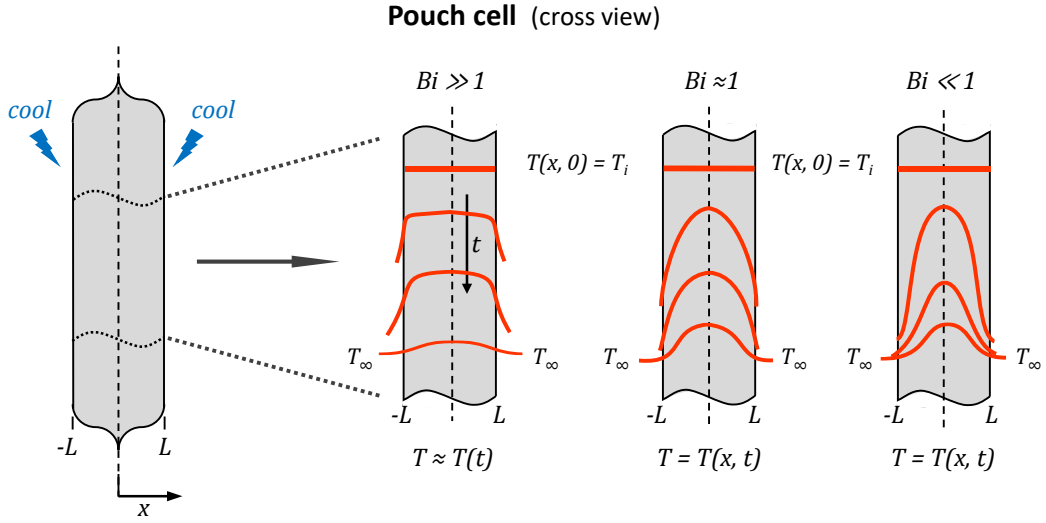

Figure 7 Schematic representation of the transient temperature distribution for different Biot numbers for a cuboid object that is symmetrically cooled by convection. Image based on [88].

2.3 Transport limitations

Transport limitations have a wide range of negative effects on a battery. Ionic and electronic transport limitations lead to lithiation gradients in cells and reduce the overall cell performance.

2.3.1 Cell performance

A battery operated under transport limitations suffers from loss of power capability, energy, and capacity. Figure 8 schematically shows the effect of ohmic-, charge-transfer- and concentration-polarization on the cell potential during discharge. The average discharge potential is reduced and the end of discharge voltage is reached earlier causing a reduction in useable capacity.

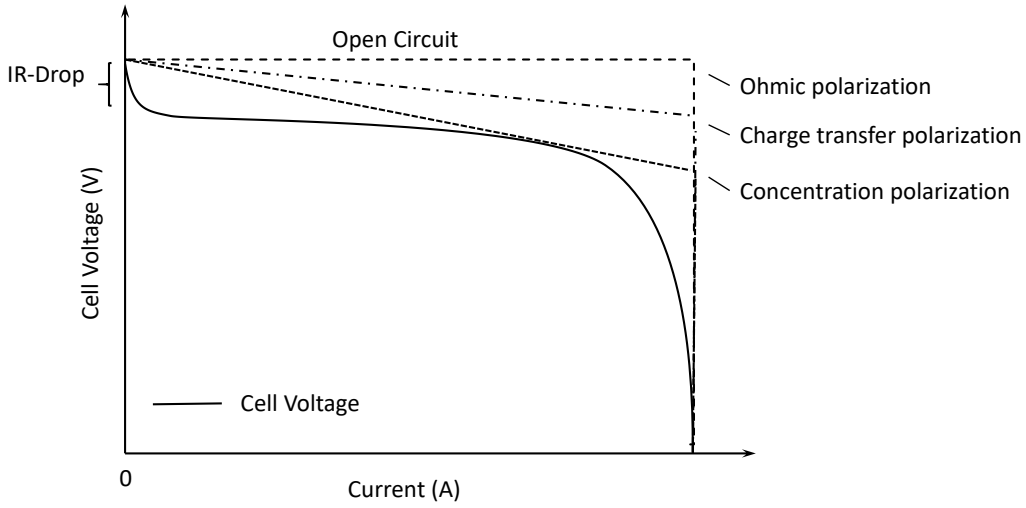

Figure 8 Cell potential as a function of operating current. Image based on [70].

The polarization is rate and temperature dependent and rate capability tests are a standard procedure in the evaluation of battery performance.

2.3.1.1 Temperature

The negative effect of low temperatures on battery performance is well established [2, 24, 43]. Ionic conductivity and diffusivity of electrolytes decreases with decreasing temperature [25] and the internal resistance increases until the electrolyte freezes and the battery seizes to function [89]. Various electrolyte salt combinations and additives are tested to lessen the negative impact on transport and to lower the point of freezing [90, 91]. Solid diffusion also decreases for materials such as graphite [27, 28]. This is particularly problematic during low temperature charging, because slow intercalation can lead to metallic lithium depositions at the anode severely damaging a cell during cycling known as lithium-plating [22, 23]. Furthermore, there is evidence that the intercalation and deintercalation processes are hampered at low temperatures causing an increase of charge transfer resistance [35].

2.3.2 State of charge inhomogeneity

Inhomogeneity in the temperature, current density, potential and ultimately in the SoC distribution is a result of transport limitations in a cell at particle, electrode and cell level. Due to the importance of such inhomogeneity on the general performance, rate limitations, and aging of cells, these effects are subject of research. Selectively, some of this research is presented to illustrate the state of the art of experimental techniques. Many experiments rely on post mortem investigations or other time consuming and destructive methods that do not allow for time resolved measurements. The interdependency of several limitations in a complete cell system is not fully understood.

2.3.2.1 Particle

The effect of particle size [92] and morphology [93] can be measured for active material powders by means of laboratory cells. Similarly, the effect of transport limitations at particle level such as plating can be measured in situ with diffraction [22] or through the effect on the cell voltage [94].

However, it is very challenging to directly measure inhomogeneity within particles caused diffusion limitations, due to the small size of particles ≈10 µm (graphite) or crystallites < 1 µm. Experiments by Umeda et al., who conducted EIS measurements on individual MCMB particles, indicate strong variation between particles with regard to the diffusion constants from $10^{-6} - 10^{-10}\ \mathrm{cm}^2/\mathrm{s}$ [95]. Levi et al. deduced the nucleation time, lateral growth rate and thickness of nucleation layers in graphite from PITT measurements of graphite coin cells [96].

The implementation of concentration gradients within particles through the introduction of a particle dimension *r* is standard in the widely used electrochemical models based on the Doyle Newman model [97, 98], despite the scarcity of experimental data on this length scale.

2.3.2.2 Electrode layer

The effect of transport limitations within an electrode layer can be measured in a straightforward way, by coating electrodes of various thicknesses or compositions and measurement of the capacity [99].

However, it is challenging to visualize or quantify the inhomogeneity resulting from transport limitations within the layer. One approach is to build a custom cell with individually contacted electrode segments. Ng et al. built a custom pouch cell with a graphite anode segmented in three parts and found vertical inhomogeneous current and SoC distribution even after several hours of relaxation [100]. Similarly, Klink et al. and Kindermann et al. found similar inhomogeneity with custom multilayer laboratory cells [101, 102]. Harris et al. utilized the color change of graphite during lithiation to visualize lithiation gradients (Figure 9) [53]. A new and promising method for 3D imaging of lithium distributions is neutron depth profiling [103–105]. However, high neutron flux is required for high resolution images [106]. The path dependence of the electrical and ionic conductivity in the electrode is subject of investigation with the resistive networks approach [107] and the electrochemical fin theory [77].

In addition to inhomogeneity in the vertical direction the cells may show inhomogeneity of potential and current distribution in lateral direction. The SoC distribution of electrodes can be mapped with XRD [55] or Raman [108]. For graphite anodes, the color distribution can also be used for SoC mapping (with certain restrictions, see section 3.4.2). However, these techniques typically rely on post mortem samples and often analyze only segments of electrodes.

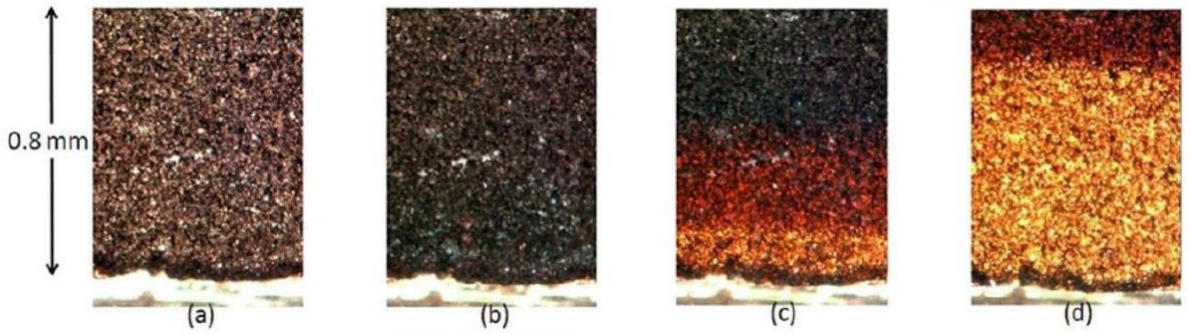

Figure 9 Optical micrographs of a graphite electrode layer cross-section during lithiation. Image reprinted from [53] with permission from Elsevier.

2.3.2.3 Cell level

Three dimensional spatially-resolved data on parameter inhomogeneity is highly thought after for design and aging optimization of commercial sized batteries. Due to the geometric complexity the possibility for analytical calculations is restricted. Reimers et al. calculated the potential distribution for cylindrical cells and found it to be strongly dependent on number and position of cell tabs [57]. The thermal transport parameters are anisotropic and differ for the direction orthogonal and parallel to electrode layers. The temperature distribution can be approximated analytically [88] or calculated in detail numerically [87, 109].

The number of experimental techniques that can be applied to local data on large format sized batteries and without disassembly of the cell is limited. In some studies, custom-built cells with segmented electrodes [110] or potential probes have been utilized and they report potential and current density gradients along electrodes. However, these publications are sparse, due to the great challenge to produce large-format custom cells with comparatively high quality to commercial cells. Thus some publications have modified commercial cells with additional voltage [59] or temperature probes. Yet, given the compactness of cell components additional reference electrodes and sensors may alter the local cell environment by locally changing the distance between anode, cathode and separator. Senyshyn et al. report SoC inhomogeneity in commercial cylindrical cells measured by means of neutron diffraction (Figure 10) [65] and neutron scattering [111, 112]. Zhou et al. have found inhomogeneous SoC distribution in neutron radiography cross-section images of single layer pouch cells [113]. Fleckenstein et al. have reported inhomogeneous SoC distributions as a result of inhomogeneous temperature locally measured [62].

In comparison to experimental data a large number of publications provide 3D simulations of cell properties of varying complexity. 3D physicochemical models as published by Gu et al. [114], Lee et al. make detailed predictions on potential, thermal and lithiation properties [64].

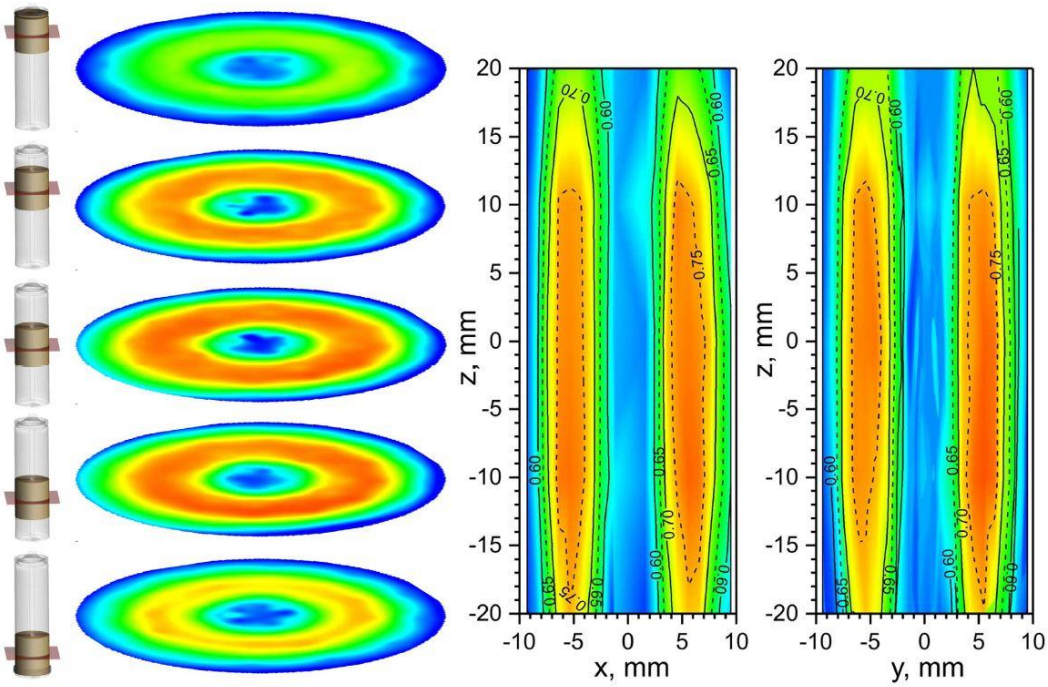

Figure 10 Lithium concentration *x* of Li_xC_6 distribution of a cylindrical LFP/graphite cell generated from local Neutron diffraction data by Senyshyn et al.. The z axis corresponds to the long axis of the cell. Figure reprinted from [65] with permission from Springer Nature. Distributed under Creative Commons CC BY license.

2.4 Lithium reservoirs

In the context of this work a lithium reservoir is defined as an electrode segment that is electronically and ionically connected to the cell but does not possess a direct counter electrode. One finds that these segments have the ability to intercalate lithium, and thus may act as a lithium sink or source despite long ionic pathways. However, the storage and release of lithium is delayed compared to the rest of the electrode. In the following, the origin of these reservoirs, as well as the impact on cell performance and cell measurements is discussed.

2.4.1 Overhang and backside areas

In commercial lithium-ion cells the negative electrodes are designed slightly larger than the positive electrodes. This is a common design feature to assure 100 % cathode-anode overlap and to avoid lithium plating at the border area of the graphite anode [19]. This “overhang” area typically is 1 mm wide at the sides of electrodes in cylindrical and pouch cells [18], but can be several centimeter at the end of the jelly roll of a cylindrical cell as shown in Figure 11. Overhang areas of commercial cells evaluated in literature had 3-10 % of the total anode size [18, 20].

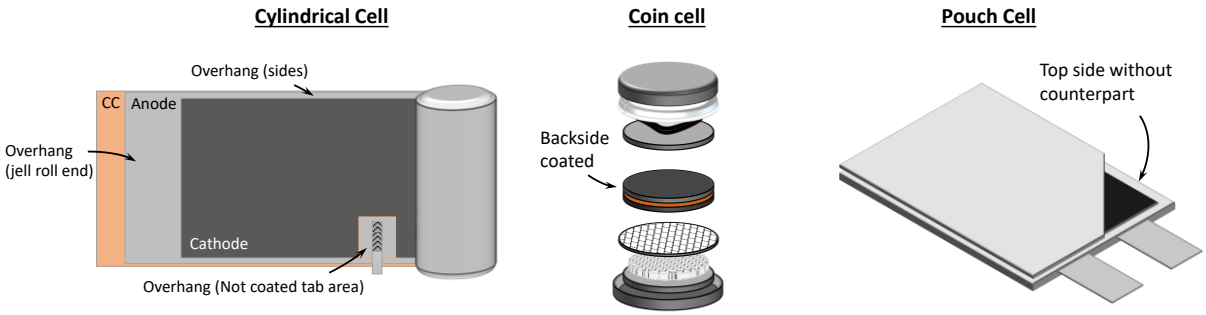

Figure 11 Electrode segments acting as lithium reservoir in commercial and laboratory cells. a) Overhang area at the side and edges of a cylindrical cell. b) Coin cell with double-coated electrode. c) Pouch cell with a double-coated electrode at the top of the electrode stack.

In some cells, e.g. A123 APR18650m1a, the anode area in opposite of the cathode current tab is coated and thus does not have a counterpart similar to the overhang area b). The anode may be covered by a non-permeable layer of electrolyte decomposition products that separates it from the cathode in aged cells (e). Such a *passivated* (Lewerenz et al.) section of the anode was also found to acts as a reservoir (Figure 13) [20] .

If a double-coated electrode is used as the outermost layer in a pouch cell, the backside electrode does not have a counter electrode. Despite the waste of active material, such a cell design can be cost efficient for a manufacturer. Depending on their coating setup, production of two types of coated material, single-coated and double-coated sheets, may cause considerable additional expenses. For example, the commercial cell SLIP 540839 and the 5 Ah pouch cells of the ExZellTUM research project use only double-coated electrodes. For a 10 layer cell the backside area of the top and bottom layer together consists of 10 % of the total electrode area.

Such an electrode backside may also occur in coin cells, especially if the coin cell is manufactured from commercial cell material from post mortem analysis. Cylindrical cells typically do not have single-coated segments and electrode material may be fragile or easily removed from the current collector complicating the mechanical removal of a backside. For such a cell the overhang area consists of 50 % of the electrode area.

2.4.2 Impact of lithium reservoirs

Some publications found an effect of lithium reservoirs on the CE in high precision measurements, SoH determination in calendar and cycling aging studies as well as structural damage to the electrode.

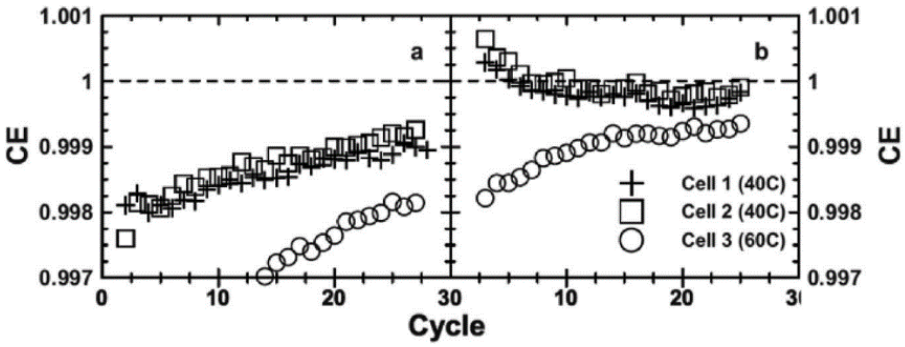

Figure 12 *CE* greater than unity observed for $LiCoO_2$/ graphite cells (a, b) in an electrolyte additive study by Burns et al.. Figure reprinted from [17] with permission from IOP Publishing, Ltd.

Gyenes et al. first discovered a reversible capacity effect in high precision coulombic efficiency measurements [18]. They found *anomalous transient CEs (Gyenes et al.)* with *CE*>1 in cycling experiments after storage [17, 18] shown in Figure 12. In the analysis of 220 mAh wound pouch bag cells with 1 mm side overhangs, they found, that the capacity of the cells nonlinearly depended on the SoC during storage prior to cycling with $CE > 1$ for high, and $CE < 1$ for low storage SoC. The storage SoC affected the *CE* for up to 1000 h of subsequent cycling [18]. From this they concluded that the effect of overhang areas is of *extreme importance (Gyenes et al.)* to practitioners of high accuracy *CE* measurements.

Lewerenz et al. found that anode overhang areas influenced the initial trend of capacity loss in their calendar aging studies of 8 Ah cylindrical cells at elevated temperatures [115]. The linear decrease in capacity was delayed for high SoC storage cells compared to low SoC storage cells. In cycling studies they found a 2-3 % capacity difference between fast and slow discharge procedures which they attribute to rate dependent overhang area lithiation [115]. The capacity difference diminishes during continued cycling which they attribute to the overhang area mechanically breaking away from the rest of the electrode due to strain between differently lithiated electrode areas and/or electrode dryout. In the same study, they also observed the formation of a deposition layer on the anode acting as a lithium reservoir in the same way as the overhang area (Figure 13).

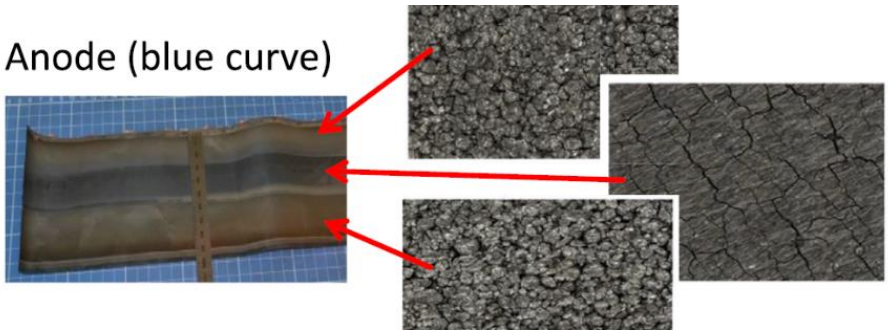

Figure 13 Deposition layer on anode surface. Image reprinted from Lewerenz et al. [115] with permission from Elsevier.

3 Graphite anodes

Graphitic carbon is the most common anode active material in commercial lithium-ion battery cells due to its low negative redox potential, long-term cycle stability, comparatively small volume change, and competitive price. The material is present in all types of cell designs ranging from coin cells to cylindrical cells and large prismatic cells for automotive use [67]. Thus, it can be expected that effects detrimental to battery performance which are caused by either intrinsic material properties or common design principle affect a wide range of batteries in use.

The objective of this thesis is to investigate SoC inhomogeneity in graphite due to lithium reservoirs in oversized electrodes and transport limitations. The fundamental properties of graphite allow for various methods to investigate the state of lithiation, such as in situ diffraction, colorimetry, and DVA, which will be explored in detail in the method descriptions in chapter 4.

In the following, the graphite properties and models fundamental to understanding these methods are outlined. This includes the crystal structure of graphite as well as the change during lithiation, theoretical models of the lithium distribution in graphite and the lithiation process.

3.1 Graphitic and non-graphitic carbon anodes

A challenge for research utilizing commercial cells is the lack of information provided by the manufacturers. This is the case for the properties of the anode material, particularly the type of graphite used. Some information needs to be deduced from cell properties or through experiment.

At the basic level the carbon atoms are connected through covalent bonds of sp^2 hybridized orbitals. From the repetition of the sp^2 bonding follow 6-ring structures and subsequently planar hexagonal (honeycomb-like) structures known as *graphene layer*. For graphitic carbons these graphene layers are stacked in a regular fashion and bonded through Van der Waals force. For non-graphitic carbons, the material is dominated by amorphous sections with three dimensionally interconnected graphitic layer segments and carbon rings. A schematic representation is shown in Figure 14 a. The majority of non-graphitic carbons are manufactured from heating organic polymer or hydrocarbon precursors. Non-graphitic carbons are further categorized in *hard* and *soft* carbons, according to their mechanical properties. Soft carbons are graphitizable through high temperature treatment (HTT).

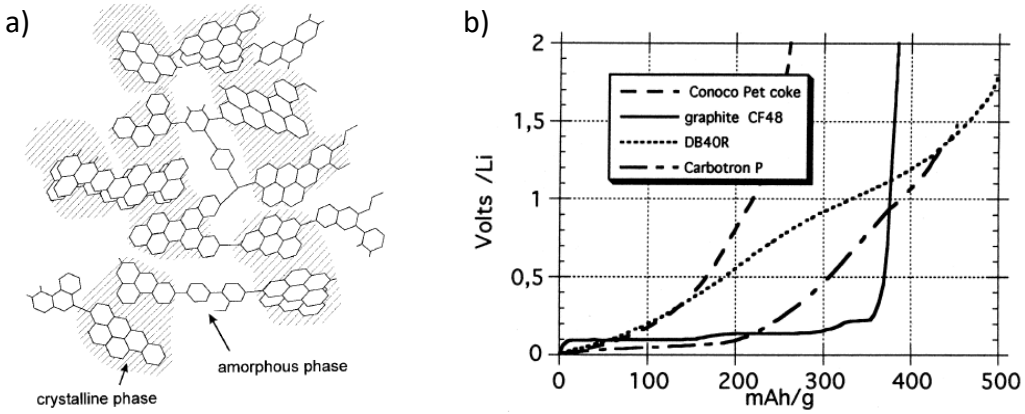

Figure 14 Schematic of interconnected ring structures in non-graphitic carbons. Cell voltage of graphite and several non-graphitic carbons upon delithiation. Figure 14a reprinted from [72] with permission from John Wiley and Sons. Figure 14 b reprinted from [37] with permission from Elsevier.

At temperatures of 1500 °C to 3000 °C the amount of randomly oriented layers is severely reduced and layers coalesce to an ordered stacking structure. Hard carbons maintain their random orientation even at high temperatures of 3000 °C. Graphite manufactured from soft carbons by means of HTT in this way is sometimes called *artificial graphite* or *synthetic graphite*. Whether a battery is utilizing graphite or non-graphitic carbons can be determined from the differences in the cell voltage Figure 14 b). Non-graphitic carbons show a rather continuous voltage increase upon delithiation and lack the characteristic voltage plateaus observed for graphite.

It needs to be determined, whether the graphite used in a commercial cell is natural graphite or graphitized soft carbons. An indication for the origin can be the particle morphology observable with SEM. Sharp edged flakes indicate natural origin, while potato or balled shaped particles can indicate graphitized carbon such as mesocarbon microbeads (MCMB) graphite. Besides the effects of the particle morphology onto active material properties such as the surface area, the origin of the graphite can also influence the bulk properties, since small segments of amorphous, non-graphitizable areas within the soft carbon may remain despite the HTT treatment, which differ in lithium diffusivity and electric conductivity from the graphitized. Such defects are in principle detectable by means of powder diffraction with high quality pure samples [116], but are indistinguishable from background noise in the presented in situ experiments and XRD measurement with post mortem material.

3.2 Crystal structure

Graphite consists of stacked layers of graphene bound by Van der Waals bonding. These layers are depicted in Figure 15. Two neighboring graphene layers are shifted by the distance of a c-c bonding. There are two idealized stacking orders, ABAB… and ABCABC, where the C layer is shifted by the distance of two c-c bondings with reference to the A layer. The ABAB… stacking has a hexagonal symmetry and belongs to the space group $P6_3/mmc$. The ABCABC… stacking has a rhombohedral symmetry and belongs to $R\bar{3}m$. In natural graphite the ABAB… stacking is dominant with approximately 95 % of the layers in hexagonal symmetry. Consequently, in all following discussions only the ABAB stacking will be considered.

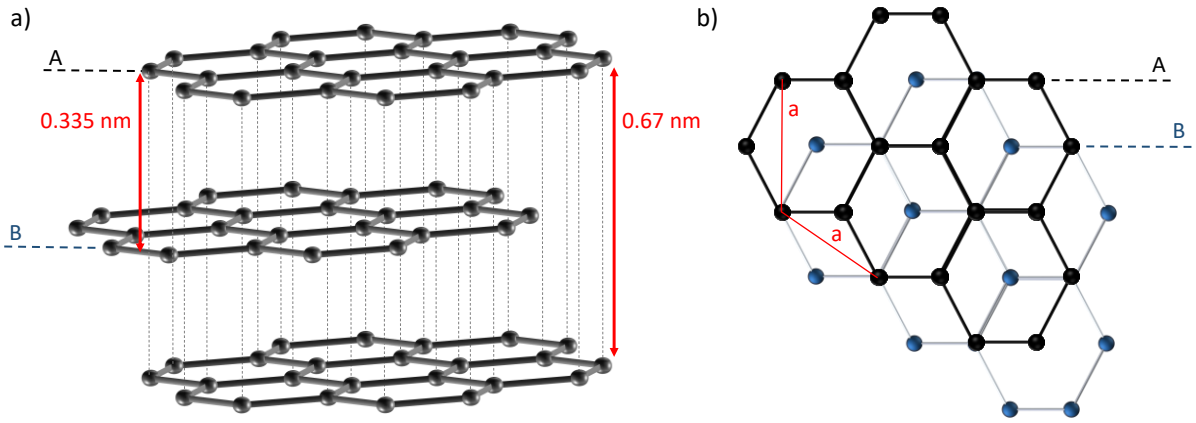

Figure 15 Graphite A and B layers in side view (a) and with marked unicell (red) top view (b). Graphical description based on data from [117, 118]. The unit cell contains two C atoms at the position 0 0 ¼ and ⅓ ⅔ ¼. The length of the *a* axis is 2.464 Å [117]. The length of the *c*-axis is 6.711 Å [117]. The spacing between layers d_{layer} is equal to half of the *c*-axis.

Natural and artificial graphite alike are typically polycrystalline with crystallite sizes ranging from nm to µm. Exceptions such as highly ordered pyrolytic graphite (HOPG) do exist, but their use is, to the knowledge of the author, currently limited to experimental research.

3.3 Lithiation

Lithium can be inserted into carbon to form a lithium carbon compound as described generally in the following redox reaction:

$$\mathrm{Li}_x\mathrm{C}_n \rightleftharpoons x\ \mathrm{Li}^+ + xe^- + \mathrm{C}_n \tag{22}$$

Typically the reaction happens within an aprotic organic electrolyte providing and transporting the Li^+ ions. If the carbon host is graphite and thus crystalline, the insertion process is called *intercalation*. The reaction is reversible. The resulting material is called lithium-graphite intercalation compound (Li-GIC). At ambient pressure, the maximum lithium content for ideally crystalline graphite is one lithium atom per six carbon host atoms ($x \leq 1$ in $\mathrm{Li}_x\mathrm{C}_6$) [72]. With this the theoretical capacity of graphite is calculated to 372 Ah/kg.

While the properties of the initial state (graphite), the 50 % SoC state (LiC_{12}) and the final fully charged state (LiC_6) of the lithium intercalation reaction are well known, the intermediate stages are subject of continuous discussion and competing models have been proposed.

3.3.1 Phenomenological staging model

The most commonly used model of the lithiation process is the so-called *staging model.* The key assertion is that a random distribution of lithium intercalants is energetically unfavorable to fully filled layers because the insertion of lithium requires more energy to widen the Van der Waals gap than is required to fill a layer with Li atoms despite the repulsive forces.

Staging describes a periodical arrangement of intercalated layers within the graphite matrix. The staging index *n* is defined as the number of graphite layers which separate two successive intercalated layers [72]. Figure 16 shows graphite and several stages of lithiation in side view. The GIC with the highest density of lithium LiC_6 is stage-I. Stage-II corresponds to LiC_{12}, stage-III to $LiC_{24,}$ and higher stages continue in this fashion. An intermediate stage LiC_{18}, that can be observed in ND-data and in the voltage profile of a cell, is described as dilute lattice-gas disordered stage II, where the lithiated layers maintain a single intermediate empty layer but these layers are less densely lithiated. At stage I and II all but the nearest neighbor sites are occupied in plane with Li atoms (Figure 16 b). At dilute stages it is less than that.

The staging model explains the major features of the voltage profile of lithiated graphite. The discussion of this model follows [33, 34, 72]. A schematic representation of this as well as early experimental data is shown in Figure 17. The voltage plateaus in the galvanostatic (peaks in the voltammetric plot) are caused by two phase regimes. The voltage plateau at about 90 mV vs. Li/Li^+ from $0.5 < x < 1.0$ is due to coexisting LiC_6 and LiC_{12} phases (Stage I + II). The plateau at $0.34 < x < 0.5$ is due to coexistence of LiC_{12} and LiC_{18} (Stage II + IIL), followed by the plateau at $0.22 < x < 0.34$ with LiC_{18} and LiC_{24} (stage IIL + lll). The voltage plateau at about 210 mV corresponds to the phases LiC_{24} and LiC_{48} (stage III + IV). The alleged voltage difference between the III/ IIL and the IIL/ ll plateaus is about 20 mV and thus fairly small. The voltage data of Ohzuku and similar measurements (Figure 17 b) is sloped and does not show plateaus conclusively. Diffraction data is similarly inconclusive as super lattice peaks observed by Dahn et al. [33] are not observed by Ohzuku et al. [34]. Reports of higher order stages are inconsistent [119].

A major drawback of the staging model is that it does not explain the significant shift in the crystal structure during lithiation. As illustrated in Figure 17 b) the stacking order of graphene layers ABAB… changes to AA upon lithiation. While it is clear, that stage I and II are AA stacked [72], it is unclear at which particular stage the transformation from ABAB.. to AA happens.

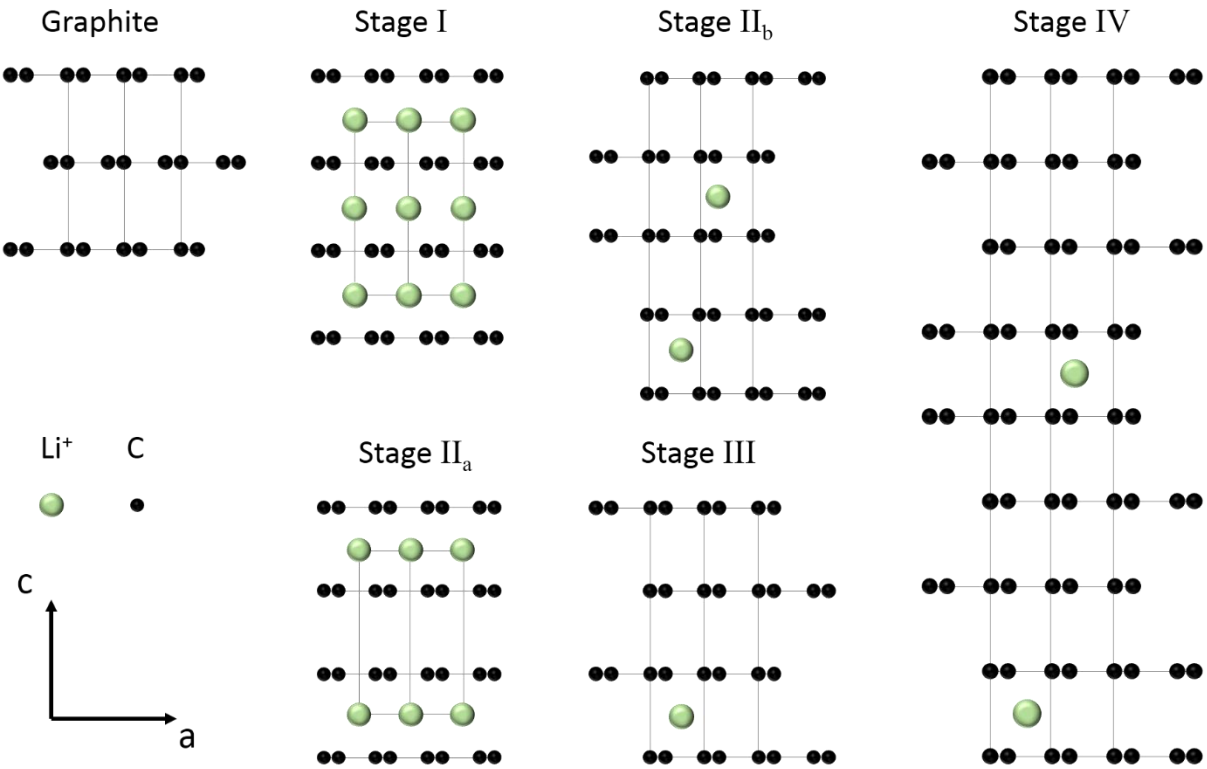

Figure 16 Side view of lithiation stages; graphite, stage IV, stage III, stage IIa, stage IIb, and stage I. Positional data taken from [117, 118].

Additionally, it is unclear how several non-lithiated layers at high staging numbers are in conformity with estimates of the electrostatic screening length. All interactions besides electrostatic forces are restricted to bounding layers (layers adjacent to intercalant layer). For graphite, Spain and Nagel estimated screening lengths of about 5 Å [120]. Given that the distance between two adjacent graphene layers is about 3 Å, one would not expect a lithium atom to be hindered in intercalating into an empty layer by an intercalant layer unless it is the neighboring layer.

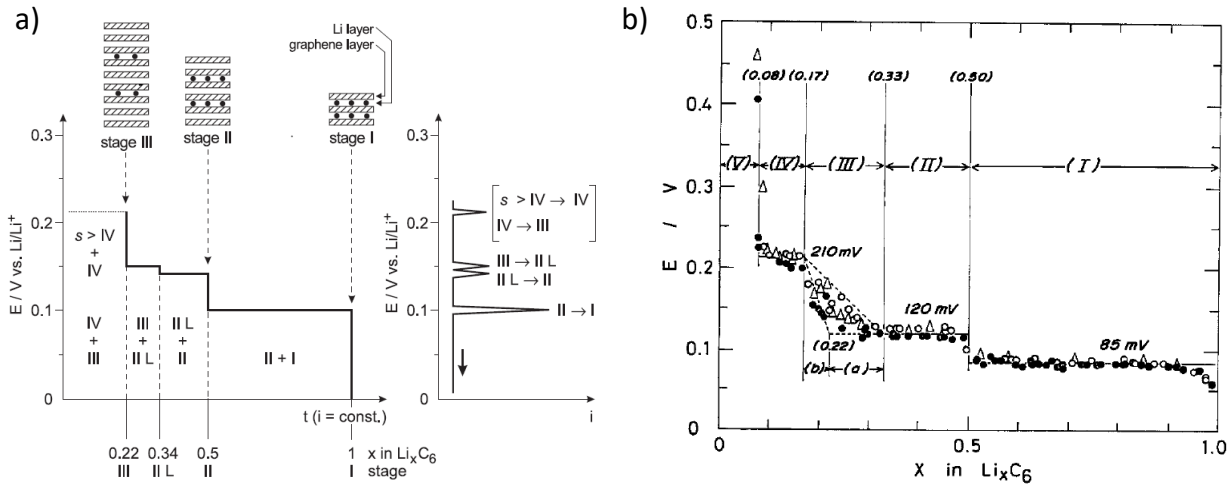

Figure 17 (a) Schematic of stage formation for lithiated graphite. Galvanostatic and voltammetric curves adopted from Winter et al. [72] reprinted with permission from John Wiley and Sons. (b) Stages attributed to experimental data of the Li-GIC vs. composition by Ohzuku et al.. Figure reprinted from [34] with permission from IOP publishing, Ltd..

3.3.2 Ab initio staging models and island formation

The staging model of Ohzuku and Dahn is predated by ab initio calculations of general solid state models of the interactions of intercalant atoms that aim to describe the phase diagram as a function of stage, temperature, chemical potential and intercalant concentration. Cahn and Hilliard derived a general expression for the free energy for a *non-uniform* system with spatial variation in one of its intensive scalar properties such as the composition or density, i.e. intercalant density as early as 1957 [121]. Based on this approach, Safran calculated a phase diagram of staged intercalation compounds with graphite intercalation compounds given as specific example [122, 123]. The phase diagram is given in Figure 18. This model uses equilibrium thermodynamics and sets the intercalants as given without considering the process of intercalation.

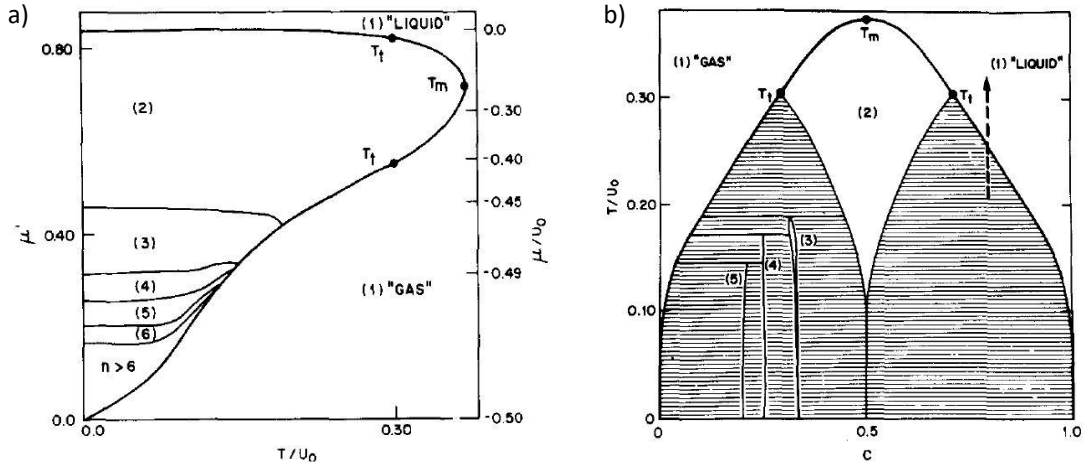

Figure 18 (a) Phase diagram of lithiated graphite plotted as a function of temperature T and chemical potential μ (a) as well as temperature and concentration c (b) as obtained by the mean field lattice gas model by Safran et al.. Reprinted from [122] with permission from the American Physical Society.

This model excludes an effect introduced by Daumas and Herold who suggested that in a staged sample the areal density of intercalants is the same for every carbon layer and thus the staggered domains exist [124]. This effect is also called *Island formation* or *Domain model* [125].It was subsequently shown that such islands form naturally in the equilibrium model if it is extended with an intercalant flux and diffusion to study time dependent kinetic processes [126] (Figure 19). The propagation of intercalation is explained through formation and migration of island intermediate stages [127].

While the in situ XRD and potential measurements by Dahn et al. and others have been seen as evidence for the staging model, notably the authors themselves have noted shortcomings in the model descriptions. The critical question is the microscopic origin of the repulsive interlayer interaction that is the root cause of staging. According to Safran et al. the occurrence of widely separated ionized intercalant layers is due to a repulsive interaction between layers due to a weak power law screening of electrostatic forces in graphite intercalation compounds [128]. The energy per intercalant $g(n) \sim (1+n)^{-5}$ for a given stage *n* monotonically decreases with number of stages. However, at the same time there is an "anti-staging" attractive interaction between intercalant layers due to in plane strain caused by the extension upon intercalation. This effect may limit the possible stages $n < n_{max}$, but the exact contribution is unclear [128].

Island formation has been shown directly for materials such as KC_{24} [129] and $FeCl_3$ [130]. Dimiev et al. observed tidal wave phase propagation and Island formation in sulfuric acid GIC. To the knowledge of the author, evidence of Island formation in lithium carbon compounds is very limited and relies on optical imaging of stage transformation [131]. Guo et al. conducted optical measurements with a lithiated graphite single crystal and found that the observed color distribution matches the lithium concentration simulated with a "checkerboard" Islands formation lithium distribution [131].

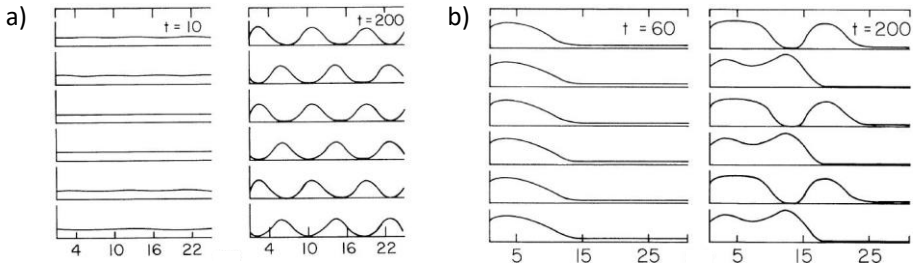

Figure 19 Formation of Daumas-Herold domains in the extended free energy model. Qualitative density profiles of six layers of graphite. a) Formation of stage 2 islands during quenching. b) Formation of stage 2 islands after intercalation. Reprinted from [126] with permission of the American Physical Society.

3.3.3 Twisted bilayer model

Graphite is prone to crystallographic errors such as shearing due to its weak van der Waals bonds between graphene layers. Based on comparatively new high resolution in situ ND data of the graphite lithiation process, Senyshyn at al. proposed an alternative model of the low lithiation states due to a modulation within the ab planes [46]. Figure 20 a) shows the graphite *d*-spacing obtained by ND during lithiation as well as the graphite phases attributed to the data in their model.

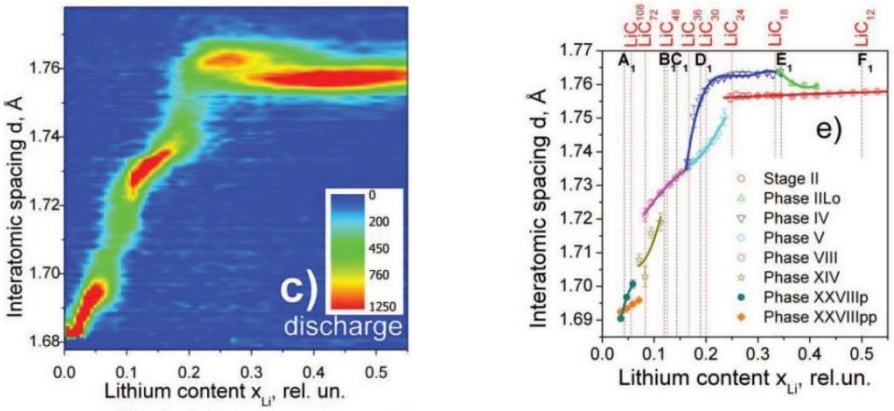

Figure 20 (left) ND data of interatomic spacing d during lithiation. (right) Model analysis of the ND data with phases attributed to data segments. Figure by Senyshyn et al. reprinted from [46] with permission from IOP Publishing, Ltd..

The proposed alternative mechanism to form theses phases is a twist in the graphene bilayers. Figure 21 shows a simulation of graphene bilayers with three different twist angles ω of 0.564°, 5.75°, and 14.4°. At non-zero twist angles periodically distributed AA stacked areas form. Instead of an immediate switch from AA to AB in the staging model, the crystal structure changes continually.

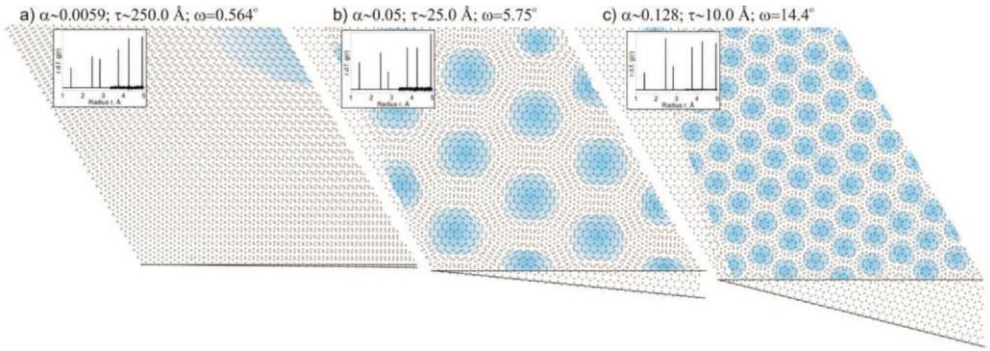

Figure 21 Schematic of twisting graphene bilayers at twist angles ω. Blue color highlights regions with AA stacking. The inlet shows the associated radial distribution functions. Figure by Senyshyn et al. reprinted from [46] with permission from IOP Publishing, Ltd..

3.3.4 Impact on XRD and ND analysis

With at least two competing models of graphite phase transformation, the established staging model (section 3.3.1) and the twisted bilayer model (section 3.3.3), multiple descriptions of the crystal structure of the intermediate stages at low degrees of lithiation exist. This uncertainty has great implications for the analysis of the diffraction data as presented in the XRD overhang and ND experiments, since it is the basis for Rietveld refinement and Pawley analysis (section 4.9).

In all three experiments lower lithiated phases than the crystallographically established LiC_{12} phase are observed. According to the staging model, the structural change would follow: C (graphite) ↔ stage 4L (LiC_{24}) ↔ stage 3L (LiC_{18}) stage 2 (LiC_{12}) [47, 132, 133]. The alternative twisted bilayer mechanism would suggest up to seven higher order phases (Phase IIL – Phase XXVIIIpp) as a result of modulation within ab-planes of graphite layers, instead of the layer ordering of the staging model [46].

Given the limited resolution and angular range of the presented XRD and ND data this work cannot contribute to the discussion of the correct transition mechanism. To circumvent the challenge to precisely identify low lithiated graphite phases a simplified picture is adopted in this thesis. Lower lithiated phases are classified qualitatively according to the shift of the *c*-axis. Phases with shifted *c*-axis below 7.040 Å are considered as $LiC_{18.}$ Phases with shifted *c*-axis below 6.900 Å are considered as $LiC_{\geq 24.}$ With this classification only relative phase ratios can be given. The amount of lithium in each phase cannot be quantified from the Rietveld refinement or Pawley fit since not all structure factors are known, with the exception of measurements where only LiC_6 and LiC_{12} are observed.

3.4 Diffusion in graphite

Lithium diffusion in graphite active material is complex because it involves multiple transport mechanisms at the bulk level and at the particle level. This is reflected in a wide range of diffusivity values found in experiments and simulation ranging from 10^{-5} cm^2s^{-1} [40] to $10^{-12}cm^2s^{-1}$ [134] However, lithium diffusion is very important since it is potentially performance limiting for anodes and thus batteries at a whole in certain use cases, such as low temperature charging and discharging.

At the bulk level, the diffusion properties depend on the degree of lithiation of the GIC. DFT calculations find that with decreasing degree of lithiation the chemical diffusivity increases for Stage II and IIL increases because of more jump paths for the Li^+ ions [39]. An increase in diffusivity at lower lithiated states of GIC was also observed experimentally [28, 135]. Furthermore, DFT calculations suggest that diffusivity depends on the DH domains in the material. A variation of 10^{-9} to 10^{-12} cm^2/s has been suggested within a single gallery (two graphene layers).

At the particle level, diffusion cannot solely be described with bulk properties since natural and artificial graphites are polycrystalline [72]. Here ions need to cross over crystallites or can travel through alternative pathways along grain boundaries [39]. Measurements of transport properties at particle level are difficult because it is hard to disentangle the impact of properties such as the surface area or electrolyte diffusivity onto intercalation and the variety of commercial graphite materials, which may explain the wide spread between diffusion parameters in literature [29].

3.4.1 Transport anisotropy

Transport in graphite is highly anisotropic as lithium ions can only change position within the gallery laterally to the graphene layers. DFT calculations find a prohibitive energy barrier of > 8 eV for lithium to cross through the graphene layer [84]. This is supported by experimental evidence. Tran et. al observed quicker lithiation through edge planes in cyclic voltammetry experiments with HOPG [136]. Persson et al. measured the direction dependent current response of HOPG crystals, and found that transport along grain boundaries is four orders of magnitude slower (10^{-11} cm^2/s) than travel in plane (≈10^{-7} cm^2/s) [39].

From this follows that lithium intercalates predominantly through edge planes in graphite active material. In the kinetic interpretation of the staging model a gallery has to be completely emptied from lithium through the edges, and another has to be completely filled with lithium through the edges before a staging transition happens.

3.4.2 Shrinking annuli model

The shrinking annuli model by Heß et al. describes the propagation of stages in a particle during lithiation and delithiation. Figure 22 shows a visualization of shrinking annuli (a) and a schematic of the phase propagation during lithiation (b). The model incorporates the DH-domains. Heß et al. find very high discharge rates up to 680 C for the liquid stages 3L and 4L for highly crystalline ≈6 µm diameter (a-b axis) flake graphite which they attribute to rapid diffusion through the solid-solution regime [133].

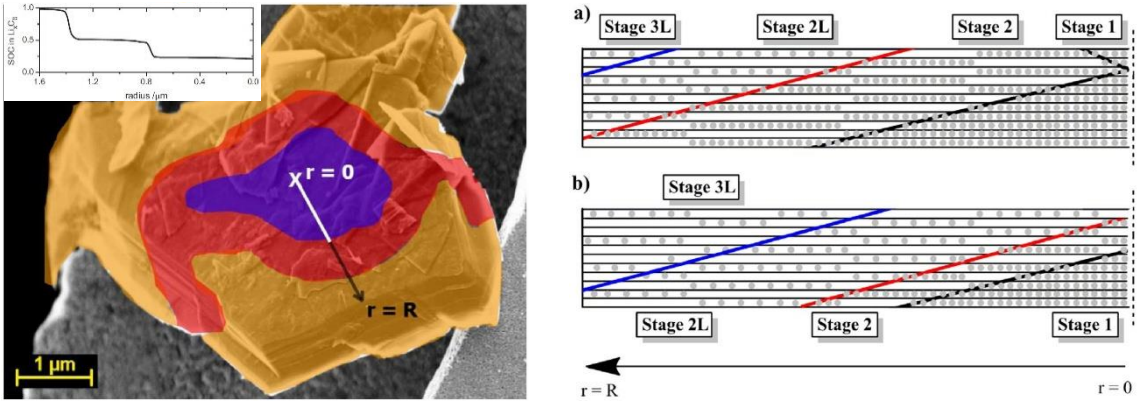

Figure 22 (left) Shrinking annuli visualized with a colored SEM image of a graphite particle. The SoC distribution is illustrated by the color segments and the radial profile in the inlay. (right) Schematic of the delithiation process according to the shrinking annuli model. Figure reprinted from [133] with permission from Elsevier.

From the shrinking annuli model follow three restrictions significant for the presented research:

1. "The diffusion coefficient cannot be extracted by applying Fick's law over the entire particle when a phase boundary is present" (Heß et al.) [133].
2. The degree of lithiation at the surface of a particle may deviate strongly from the center. From this follows that the average SoC of a particle may not be securely judged by color analysis alone.
3. As a result of (1.) all diffusion coefficients calculated from ND relaxation times and particle dimensions are treated as effective values, with time scale of the diffusion process being the result of several graphite phases with different diffusion coefficients.

4 Methods

This section describes the methods and techniques applied in the experiments conducted to investigate lithiation gradients in anodes. All experiments follow the procedures outlined in the following.

The first step is to measure the fundamental properties of the sample batteries. Cell capacity, open circuit voltage, rated performance, and internal resistance are the basis for further analysis and are required to secure sample quality and to identify outliers.

The second step is to measure material and cell properties commonly not provided by the manufacturer. This includes geometric information on the electrode overhang areas, material properties such as particle radii, electrode porosity, and tortuosity or half-cell profiles of the anode and cathode materials. These measurements require post mortem analysis of the samples.

The third step is the preparation and execution of the experiment. This includes the XRD measurements of the overhang areas and the in situ ND measurements of pouch cells during discharge and relaxation. In the case of the backside coating experiment, it includes the preparation and cycling of half-cells prepared with backside electrodes.

The last step is the data analysis. The XRD and ND data require extensive analysis using automated and manual refinement techniques. The lithium distribution in backside electrodes is simulated with an electrochemical battery model. Figure 23 gives an overview of the progression of the experiments and techniques applied at each stage.

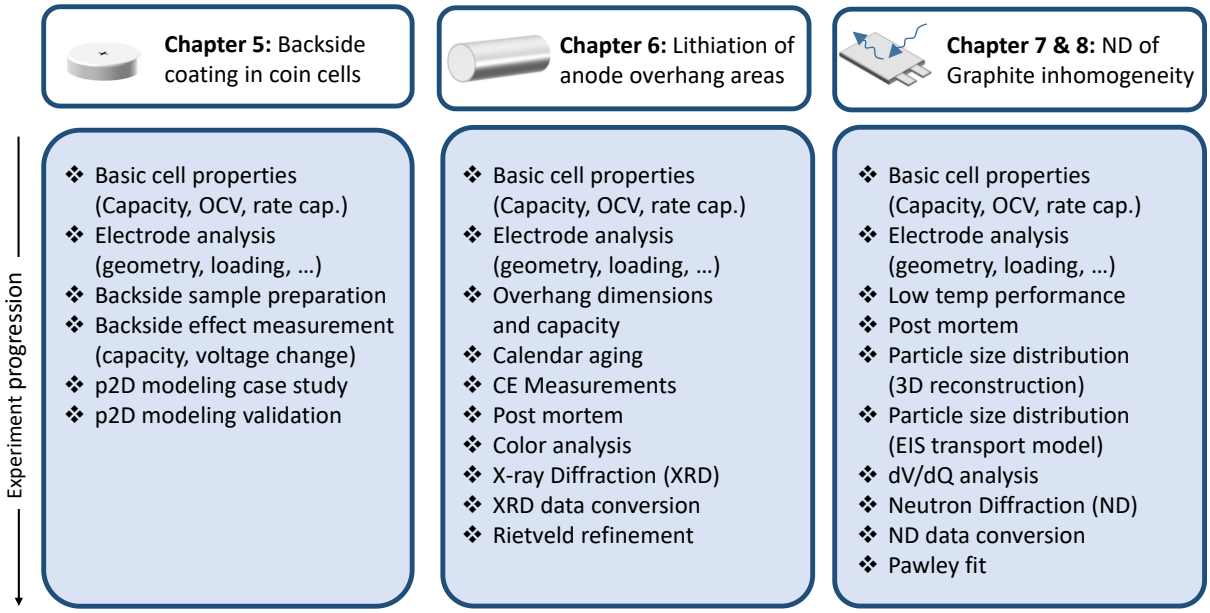

Figure 23 Overview of the experimental techniques applied in the backside coating, overhang lithiation, and in situ phase coexistence experiments.

4.1 Experiment fundamentals

The following section gives a brief overview of the type of cells tested, the test profiles, and the testing equipment used.

4.1.1 Lithium-ion cells

Two types of commercial cells were used for the experiments, cylindrical 18650 format cells, and small (< 10 Ah) pouch cells. For the overhang test the A123 APR18650m1a cell with LFP cathode and graphite anode is used. The ND relaxation experiment uses the small format pouch cell SLIP543048U by Skyrich Power, sold in Germany under the name of Superior Lipopower (SLIP). For the ND relaxation experiment with varied anode loading, several custom-made pouch cells with different loading but identical electrode composition (NCM(111)/ graphite), were purchased from CustomCells Itzehoe GmbH.

Similarly, for the backside lithiation experiment, small format cells with the active material pairing LFP/ graphite and a single electrode pair or two electrode pair were purchased together with single-coated and double-coated electrode material from CustomCells Itzehoe GmbH. Due to the variety of samples tested, details of the samples are discussed in the sections of the respective experiment.

4.1.2 Standard battery tests

All samples are optically inspected for damages and weighed upon delivery. After that the internal resistance, the capacity, and resting potential are measured. The cycling and resistance tests are conducted at controlled temperature of 25 ± 0.1 °C in climate chambers (Binder KT, Espec LU 123, and Voetsch VT 4021) under forced convection. The cell tester used is BaSyTec CTS 32 channel system.

A useful way to describe the charge and discharge rates of a battery is the C-Rate. 1C is defined as the current that galvanostatically discharges a battery in one hour from 100 % SoC to 0 % SoC. The reference capacity for this 1 hour discharge is the nominal capacity of the battery.

Capacity

The capacity is measured in a series of two charge and discharge cycles. The battery is charged constant current constant voltage (CCCV) with a constant current of 1C to the end of charge cut off voltage U_{max} that is held until the current drops to C/20. The battery is then discharged at 1C until the end of discharge cut off voltage U_{min} is reached. The discharged capacity of the second cycle is taken as the rated capacity C_{actual}, which may be lower than the $C_{initial}$ capacity of the cell, if the cell is aged. U_{max} and U_{min} depend on the active material pairing in the cell.

In the following, the SoC is defined with respect to the actual cell capacity C_{actual}:

$$SoC = \frac{Q_{\mathrm{stored}}}{C_{\mathrm{actual}}} \tag{23}$$

SoC_{actual} is the corresponding state of charge with reference to the current capacity, $SoC_{initial}$ with reference to the initial capacity $SoC_{\mathrm{initial}} = \frac{Q_{\mathrm{stored}}}{C_{\mathrm{initial}}}$.

Open circuit voltage

The open circuit voltage (OCV) as a function of the battery SoC is measured with the CC-OCV method: The cells are charged and discharged at a very low rate of either C/50 or C/100 with a constant current without CV phase. The cut off voltages are determined by the given cell chemistry. The low rate reduces the cell polarization. The accuracy of this method is limited by the SoC dependency of lithium-ion battery cell impedance which may cause higher cell polarization at low and high SoC [137].

However, this is considered to be a minor issue, given that the experiments do not specifically focus on fully charged or discharged cells and the DVA analysis results were deemed sufficient. As a consequence, the time-consuming method to derive the OCV from step wise incremental charge/ discharge processes was not applied.

Internal resistance

The internal resistance at 1 kHz AC frequency (R_{1kHz}) is tested to identify outliers among new samples and potential damage or deterioration due to aging or testing for samples undergoing testing. The impedance of lithium-ion batteries is SoC dependent. Thus, all samples were tested at 50 % SoC to maintain equal sample conditions. The tests are conducted with a HIOKI BT3562 battery tester.

4.1.3 Cell contacting

Different four-point measurement setups were used depending on the sample cell design (Figure 24). The cylindrical A12318650m1a cells were contacted with EES custom-made cell holders using gold plated contact needles (a). For laboratory tests, the pouch cells were contacted using custom-made boards with copper contacts (c). The copper bars and cell contacts were roughened up before measurement with wire wool to reduce contact resistance due to oxidation. For the sample chamber of the cryostat a more compact way to contact the cells was required. Here the pouch cells were contacted with 2 mm banana plugs soldered to a Hilumin (nickel plated steel) stripe of about 2 cm length and 5 mm width. The Hilumin stripe was welded to the cell contacts with a Sunstone pulse welder (CD DPM 2) (b). The stability of the contacts was supported with a shrinking hose and insulating tape. Standard cell holder (MPD BA2032) for the CR2032 format were used for the coin cell tests.

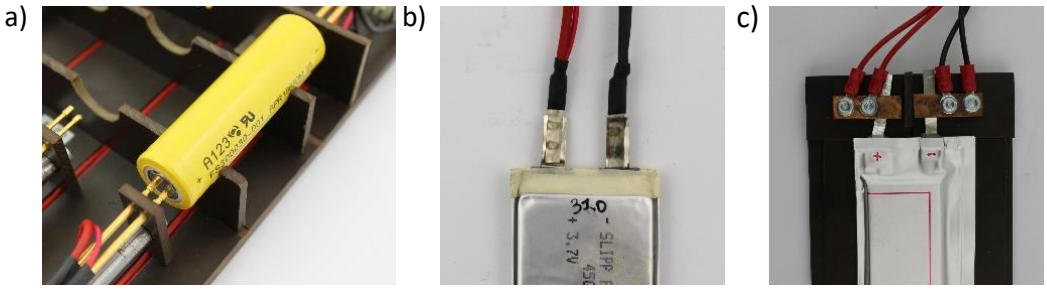

Figure 24 Four-point measurement setups for cylindrical cells a), pouch cells with insulating tape removed (welded) b), pouch cells (copper contacts) c).

As a security measure all cell tests with pouch and cylindrical cells were conducted with an automatic shutdown routine. The specific upper and lower limits for battery temperature, current, and voltage are defined in the respective BaSyTec test procedure and are deduced from the battery safety data sheet. The temperature was measured with a PT100 probe attached to the surface of the battery.

4.2 Coulometry

Coulometry measures the in- and outgoing charge through a battery. If these measurements are undertaken with a high degree of accuracy (high precision coulometry), this technique can be utilized to measure the effect of anode overhang areas on the cell capacity.

4.2.1 Coulombic efficiency measurements

The coulombic efficiency *CE* of a battery is defined as the ratio of charge in Q_c and charge out $Q_d$in a full cycle. The initial state and the final state of the battery need to be equal.

$$CE = \frac{Q_d}{Q_C} \tag{24}$$

For an ideal battery *CE* is 1. Parasitic effects such as lithium loss due to SEI growth or electrolyte oxidation cause a small charge loss during each cycle $CE < 1$. However, for a commercial cell that lasts several thousand cycles, these losses are small and roughly constant for constant cycling conditions with fixed temperature and rate [138].

CE measurements can show the effect of anode overhang areas in batteries acting as a sink or source for lithium. If lithium diffuses into an overhang area and is stored there, it is not available anymore for quick cycling which reduces the *CE* < 1. At certain conditions, this lithium may be released and can again contribute to the battery capacity. This increases the coulombic efficiency and can, until the overhang areas are depleted, increase the coulombic efficiency beyond unity *CE* > 1.

Coulombic efficiency measurements of a commercial cell with overhang areas include losses due to parasitic effects and overhang effects. However, these effects can be distinguished. For the investigated cell the overhang effects were much greater and diminish characteristically during cycling (section 6.3.2)

4.2.2 Coulombic efficiency setup

High precision measurements of *CE* require a high precision in current and voltage measurements as well as sufficient time resolution and stable temperature conditions. Table 3 lists the requirement for the measurement setup described by Smith et al. to achieve $\Delta CE_{err} \leq 0.01\ \%$ [16].

Table 3 Comparison of the precision criteria by Smith et al. [16] and a BaSyTec CTS setup as well as the BaSyTec CTS setup with external current measurement. ΔI is the percentage of current accuracy. ΔV is the voltage measurement precision. Δt is the measurement interval. ΔT is the temperature fluctuation.

Dahn C/10	Setup BaSyTec CTS	Setup BaSyTec I external
$\Delta I < 0.01\ \%$	$\Delta I = 1$ mA (precision 5A range)	24-bit range + 20 mΩ
$\Delta V < 0.0001$ V	$\Delta V = 0.001$ V (precision)	$\Delta V = 0.001$ V
$\Delta t < 3.6$ s	$\Delta t < 0.1$ s	$\Delta t < 0.1$ s
$\Delta T < 1$ K	$\Delta T < 0.5$ K	$\Delta T < 0.5$ K
$\Delta CE_{err} \leq 0.01\ \%$	$\Delta CE_{err} > 0.01\ \%$	$\Delta CE_{err} \leq 0.01\ \%$

Cycling was performed with a BaSyTec CTS battery test system. All tests were conducted at a controlled temperature of 25 ± 0.1 °C using a BINDER KT170 climate chamber. The BaSyTec CTS does not have sufficient current precision to fulfill the current criteria. For the C/5 cycling of the A123 samples (1100 mAh) a precision of 0.02 mA is needed. Thus, additional 20 mΩ shunts were placed in the current path between the battery test system and the battery cells. The voltage drop across each shunt were measured with an ultra-low noise, 24-bit sigma-delta analog-digital converter from Analog Devices (AD7193). This enabled the measurement of the currents flowing into and out of each battery cell with a higher resolution and precision than the battery test system. These current data were recorded synchronously by the battery test system. To minimize temperature influences on the measurements,

the analog-digital converter board and the shunts were also placed inside the climate chamber at 25 °C to improve the accuracy of CE measurements as recommended in literature [139]. The battery surface temperature was measured with an NTC temperature sensor attached to the battery. The observed change in surface temperature during cycling was < 0.5 °C. Figure 25 shows the setup with four cells measured in parallel.

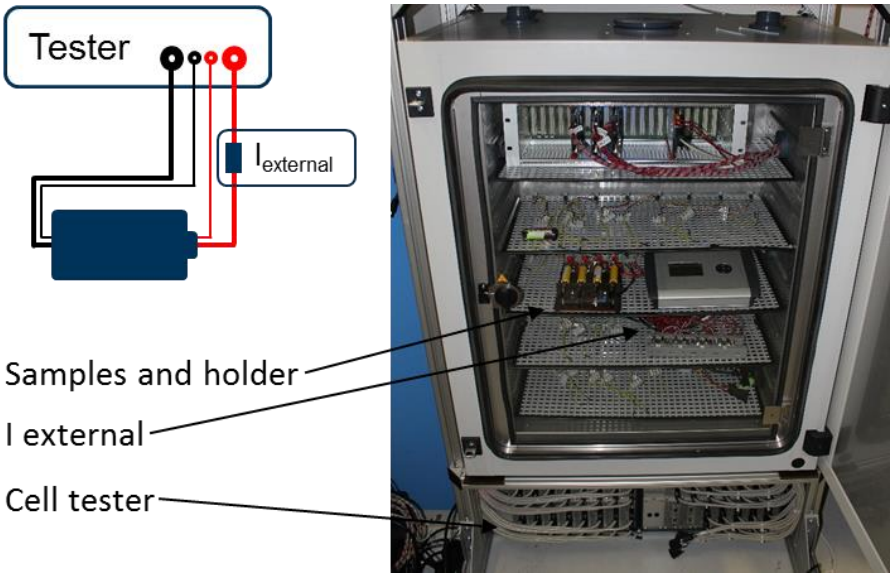

Figure 25 Setup for CE measurements with four A123 18650m1a cells.

4.3 Electrochemical impedance spectroscopy

The impedance of a lithium-ion battery is the result of a range of electrical and electrochemical processes in the battery that contribute to the internal resistances. Correspondingly, information about these processes can be extracted from the impedance data, which is the basis for modeling of the cell by means of electrical circuit models. In this work electrochemical impedance spectroscopy (EIS) is applied to analyze the tortuosity of electrodes and to measure the temperature dependence of internal resistances of full cells.

4.3.1 Fundamentals

In an EIS measurement a sinusoidal voltage $U = U_0 \sin(\omega t)$is applied to a lithium-ion battery and the characteristic current response $I = I_0 \sin(\omega t + \varphi)$ is recorded. ω is the angular frequency. U_0 and I_0 are the amplitudes and φ is the phase shift between the signals. The impedance is defined as the ratio between voltage and current. With the Euler formula it can be represented as a complex number

$$Z(i\omega) = \frac{U(i\omega)}{I(i\omega)} = |Z(i\omega)|e^{i\varphi}, \quad |Z(i\omega)| = \frac{U_0}{I_0}. \tag{25}$$

Impedance data is commonly depicted through plotting the imaginary part $-Im\{Z\}$ against the real part $Re\{Z\}$for several frequencies, so called *Nyquist* plot (See Figure 26) [140].

EIS measurements are called *galvanostatic* (GEIS), if a current excitation is applied and the voltage response is recorded, and are called *potentiostatic* (PEIS), if a voltage excitation is applied and the current response is recorded. Typically, measurements of full cells are performed galvanostatically, because the amount of charge added and removed from the battery is the same and it is ensured that the SoC of the battery does not drift during several measurements in a row. This is not a problem for the tortuosity analysis, since the electrodes do not intercalate lithium. For these measurements PEIS is used.

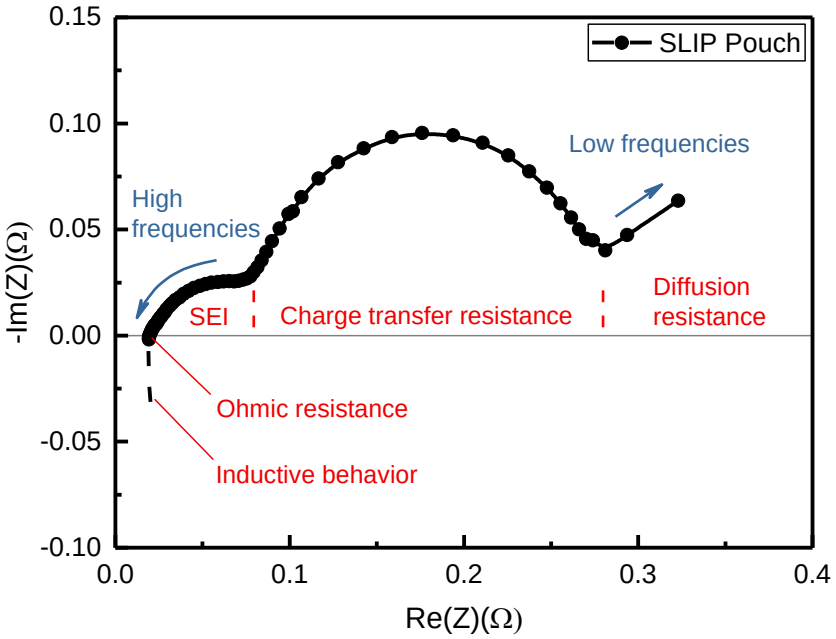

Figure 26 Impedance spectrum of SLIP Pouch cell. Characteristic sections marked red.

Figure 26 shows an impedance spectrum of a lithium-ion battery. The linear increase at low frequencies is commonly attributed to ionic diffusion in the electrolyte and modeled with a Warburg element [140]. The overlapping semi-circles at mid-frequencies are identified as due to the SEI layer and charge transfer processes [140]. They are modeled with RC-Elements. At the zero point of the curve the imaginary part is zero. At this frequency the cell behaves like an ohmic resistor.

To get reliable results from an EIS of a battery some constrains need to be considered in the setup of the measurement. At excitations with very low frequencies the state of the battery is altered during the signal because the battery is charged and discharged considerably within a period. With the SoC of the battery the battery voltage changes. The same problem occurs for high signal amplitudes. Because of this, a typical range of excitation frequencies for lithium-ion batteries is 10 mHz to 10^5 Hz [140]. The measurements for this thesis were constrained to this range. Similarly, the current during EIS was limited to max. 0.05C of the sample battery.

4.3.2 Tortuosity analysis (EIS)

The transmission line model (TLM) is an established model to analytically describe a porous electrode as a cylindrical pore for faradaic (ideally non-polarized) and non-faradaic (ideally polarized) processes [141][142]. It can be utilized to derive the electrode tortuosity from Nyquist plots of symmetric cells. Figure 27 (A) illustrates the contributing internal resistances of such a pore in a porous electrode.

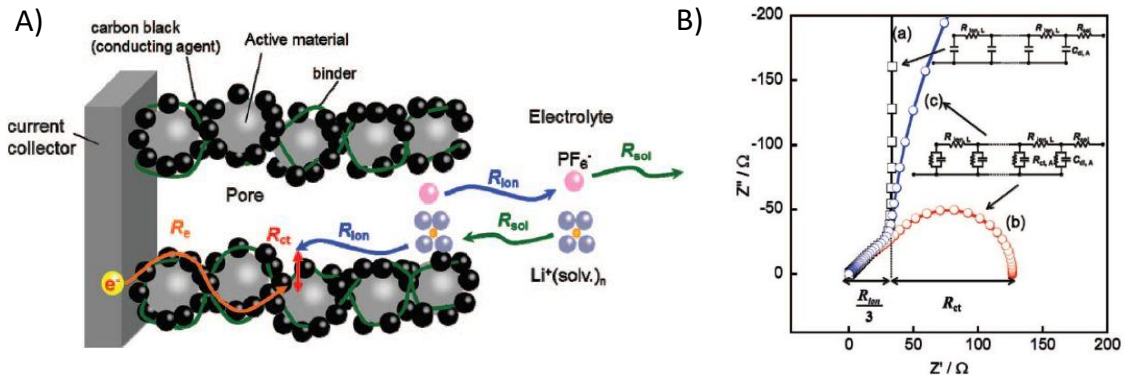

Figure 27 (A) Schematic of internal resistances at porous electrodes for lithium-ion batteries. (B) Simulated Nyquist plot for a cylindrical pore for a non-faradaic TLM model (a) and faradaic TLM models (b, c). Figures by Ogihara et al. Reprinted from [142] with permission form IOP Publishing, Ltd..

For a faradaic process, for example in a lithium-ion battery electrode, the impedance Z_ω can be calculated analytically to

$$Z_\omega = \sqrt{\frac{R_{ion}\,R_{ct}}{(1+i\omega R_{ct}C_{dl})2\pi r}}\coth\sqrt{\frac{R_{ion}\cdot(1+i\omega R_{ct}C_{dl})2\pi r}{R_{ct}}}\,L\ [142]. \tag{26}$$

The expression includes the length L and radius r of the pore, the charge transfer resistance R_{ct}, the ionic resistance R_{ion} in pores and the capacitance C_{dl}. Figure 27 B) shows the calculated impedance spectra for a non-faradaic process (a), and two examples of a faradaic process with different parameter sets (b, c).

Landesfeind et al. showed that for a lithium-ion battery electrode under absence of faradaic charge transfer reactions (so called *blocking condition*) and the assumption that electronic resistances are negligible compared to ionic resistances, the general impedance of the TLM model reduces to a simplified term Z_{red} with $R'_{ion} = \sum R_{ion}$ and $Q'_s = \sum Q_s$ summarized over the pores [41].

$$Z_{red} = \sqrt{\frac{R'_{ion}}{Q'_s(i\omega)^\gamma}}\coth\left(\sqrt{Q'_s(i\omega)^\gamma}\right). \tag{27}$$

To adjust for the non-ideal polarization conditions under blocking conditions, the RC-Elements are substituted with constant phase elements Q_s with the constant-phase exponent γ. With this the ionic resistance R_{ion} of an electrode can be extracted from an EIS measurement through linear extrapolation $\omega_{low} \to \infty$ of the low frequency regions, as for the ideal capacitor case [41] (See Figure 27 (B,a)).

$$Z_{El.}|_{\omega_{low}\to\infty} = \frac{R_{ion}}{3} + R_{HFR} \tag{28}$$

With the ionic resistance known, the MacMullin number N_M and tortuosity τ are calculated with the expressions (eq. (29, eq. (30) derived from the definition $N_M \overset{\text{def}}{=} \frac{\tau}{\varepsilon}$ and Ohm's law.

$$N_M = \frac{A \cdot \kappa}{2 \cdot h_{electrode}} \cdot R_{ion} \tag{29}$$

$$\tau = \frac{A \cdot \kappa}{2 \cdot h_{electrode}} \cdot R_{ion} \cdot \varepsilon_l \tag{30}$$

The measurements of the CR2032 symmetric cells were conducted with a Biologic VMP3 in a frequency range of 200 kHz to 100 mHz. The amplitude of the excitation signal was set to $U_0 = 10$ mV. Measurement data showed a slight dependency on sample age and environmental conditions, which is discussed with the experimental results in section 8.2.6.3. The sample construction is outlined in section 4.4.3.

4.3.3 Temperature dependence

Impedance spectra of lithium-ion batteries are strongly temperature dependent due to the temperature dependency of electrochemical processes and material properties [29]. Figure 28 shows the impedance spectra for a $LiNiO_2$ cathode at various temperatures. The strong increase in size of the second semi-circle indicates a sharp increase in charge transfer resistance. Thus, all measurements are performed at standard conditions (300 K, 1 bar) in a climate chamber unless otherwise specified.

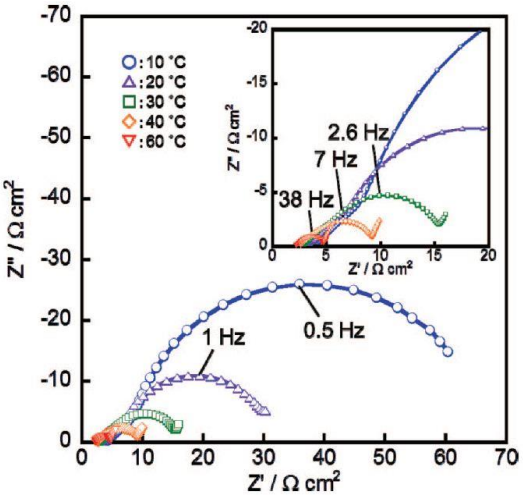

Figure 28 Temperature dependence of $LiNiO_2$-based positive electrodes in a symmetrical cell setup at 50 % SoC in 1M $LiPF_6$ EC/DMC/EMC (30/40/30) electrolyte. Figure reprinted from [142] with permission from IOP Publishing, Ltd..

For the Slip $LiCoO_2$/graphite pouch cell several measurements were conducted to investigate the low temperature performance (section 7.3.2). In this case instead of the Nyquist diagram the impedance is displayed for characteristic frequencies to illustrate the impact on the internal cell processes without modeling each spectrum with an electrical circuit.

4.4 Post mortem analysis

Some insights on commercial battery cells cannot be gained from conventional non-destructive battery tests. Cell disassembly and post mortem analysis in this theses were conducted to determine fundamental cell properties (layer thickness, loading, …), to investigate the active material composition by means of EDX measurements to perform color analysis of local anode lithiation, to extract electrodes for half-cell and full cell *dV/dQ* analysis, to conduct tortuosity analysis by means of SEM and EIS, to extract electrodes for local XRD measurements, and to optically inspect aging related defects (electrolyte dryout, lithium plating).

4.4.1 Cell disassembly and electrode preparation

For analysis of the capacity recovery effect several A123 APR18650M1A cylindrical cells were disassembled as shown in Figure 29.

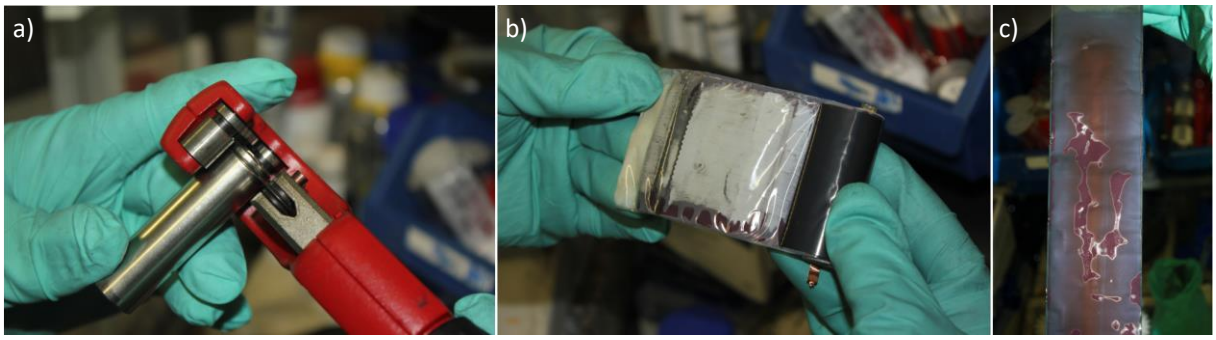

Figure 29 Removal of the insulating cover and cutting of the cell casing (a). Inspection of the jelly roll and separation of anode and cathode (b). Electrode washing with DMC (c).

For disassembly, the cells are transferred in a glovebox with O_2 and H_2O removal in argon atmosphere (MBRAUN; <1 ppm H_2O & <1 ppm O_2). The metal casing is cut open with a pipe cutter (a). Anode, cathode, and separator are extracted and separated (b). The time needed for the procedure up to this point is approximately 30 minutes. The electrodes are then washed with dimethyl carbonate (DMC) for 20 min to remove electrolyte remnants (c). The electrodes are dried at vacuum for 20 min up to 60 min. The electrodes are then cut and pictures for color analysis are taken. The samples selected for XRD are then packaged in PA/PP coated aluminum foil sealed at 50 mbar vacuum and 190 °C.

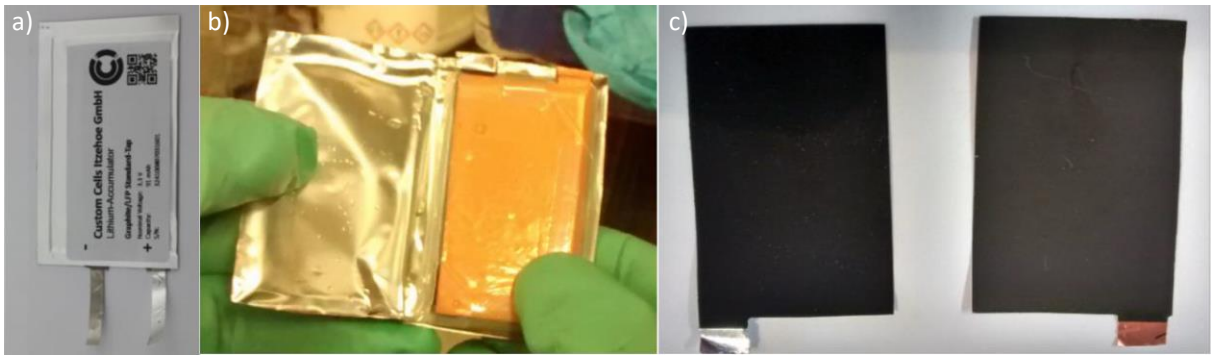

Figure 30 Pouch cell (a). Electrode stack (b). Cleaned and dried electrodes (c).

Pouch cells from SLIP and CustomCells were disassembled for additional information accompanying the neutron diffraction experiments as shown in Figure 30. The process is identical to the procedure applied to cylindrical cells with the exception that scissors are sufficient to open the cell. Instead of unrolling the jelly roll, the electrode stack needs to be cut open with a scalpel.

4.4.2 Half-cell profiles

Active material vs. Li/Li^+ coin half-cells are built in the standard format of CR2032 from Hohsen Corp. coin cell parts. For additional corrosion stability the parts are made out of SUS316L steel. Electrode disks of 14.00 mm to 15.00 mm are punched out from either electrodes extracted from cells or uncycled electrode material. As the counter electrode Rockwood lithium of < 0.2 mm thickness and > 99.9 % purity is used. For most cells VWR glass microfibers filter No. 691 were used as separator. The initial porosity of the separator is > 90 % but it is strongly compressed in the coin cell environment. Nonetheless excellent rate capability can be achieved.

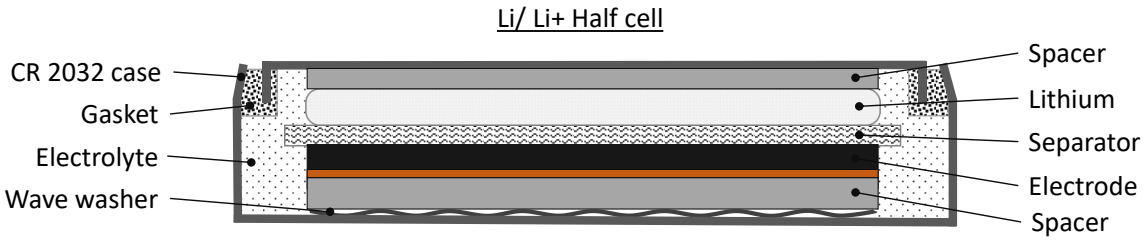

Figure 31 Schematic representation of the electrode vs. Li/ Li+ half-cell.

The half-cells undergo formation to build the protective SEI layer. The formation procedure is given in Table 4 and is based on the procedure given by the custom cells manufacturer for the stock graphite electrodes. For the initial test procedure, the cell capacity is approximated with the area $A_{cut} = \pi r^2$ of the cutout and the mass loading c_i given by the electrode manufacturer.

$$C_{N,HC} = \mathrm{c_i} \cdot \mathrm{A_{cut}} \tag{31}$$

For electrodes obtained through post mortem the capacity is approximated based on the total cell capacity $C_{N,HC} = \frac{\mathrm{A_{cut}}}{\mathrm{A_{total}}} \cdot C_{N,FC}$.

4.4.3 Symmetrical cells

Figure 32 shows the coin cell layout used for symmetrical cells. Instead of active material and lithium, two electrodes with identical active material are used. The electrodes are held in place with a wave washer and spacers. In contrast to the half-cell design the electrolyte does not contain a lithium salt such as $LiPF_6$ to prevent intercalation reactions to be visible in the EIS measurement. It contains the solvents EC and DMC in a (1:1) ratio and Tetrabutylammoniumperclorat ($TBAClO_4$). Initial cells were built with 2x glass fiber separator and electrolyte with an electrical conductivity κ_l of 0.322 mS/cm. After it was noticed that the glass fiber separator continues to be further compressed over time, thus altering the tortuosity calculations, it was substituted with two layers of Bruckner Evapore HDPE separator (10 µm, 39 % porosity). For these tests a second electrolyte mixture with a higher electrical conductivity κ_l of 1.711 mS/cm was used. Symmetrical cells are solely built for EIS measurements and cannot be reversibly charged or discharged. Consequently, there is no initial test and formation procedure.

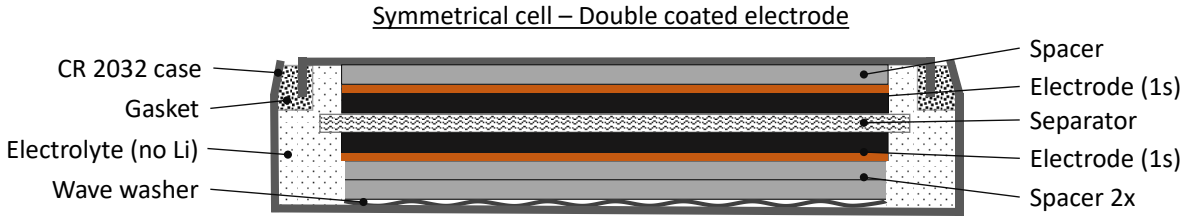

Figure 32 Schematic representation of the symmetrical cell design for tortuosity measurements.

Table 4 Initial test procedure for formation and stabilization of anodes adopted from CustomCells. Tests were performed in a controlled environment at 25 °C.

Step		Parameters	Termination
1 Formation	Cyc-1, CCCV-Charge	I = 0.1C, $U = U_{max}$	$I <$ 0.1C
2 Formation	Cyc-1, CCCV-Discharge	I =-0.1C, $U = U_{min}$	$I >$ -0.1C
3 Formation	Cyc-2, CCCV-Charge	I = 0.1C, $U = U_{max}$	$I <$ 0.1C
4 Formation	Cyc-2, CCCV-Discharge	I =-0.1C, $U = U_{min}$	$I >$ -0.1C
5 Stabilization	Cyc-1, CC-Charge	I = 0.2C	$U < U_{max}$
6 Stabilization	Cyc-1, CC-Discharge	I =-0.2C	$U > U_{min}$
7 Stabilization	Cyc-2, CC-Charge	I = 1C	$U < U_{max}$
8 Stabilization	Cyc-2, CC-Discharge	I =-1C	$U > U_{min}$

4.5 Electrode characteristics

There are a lot of advantages in using commercial cells for in situ or post mortem experiments, such as the low variation in cell quality compared to laboratory cells. However, a major disadvantage is that the full information on cell parameters is not available. The material safety datasheet (MSDS) of a commercial cell may offer some information on the electrode composition, but this information cannot always be trusted and is often not quantitative. Details of the cell design are typically not disclosed and geometrical information on the electrodes, jelly roll or cell stack is omitted. In the following the procedure to determine electrode geometries, loading, density and porosity for all experiments is outlined.

4.5.1 Geometry and weighing

After opening the cell and separating the electrodes as outlined in section 4.4.1, the geometric parameters are measured with a meter at a precision of ± 1 mm. The parameters are the anode area A_A, the anode overhang area A_O, the cathode area A_C, the overall length and width of the electrode and separator as well as the position of the tabs $x_{tab\,i}, y_{tab\,i}$. The height of the anode d_A, cathode A_C, current collector d_{CC-A}, d_{CC-C} and separator are measured with a Mitutoyo digital micrometer with a precision of ± 1 µm.

The weight of the components is measured with the analytical balance Sartorius Quintex with a readability of ± 0.1 mg. 14.00 mm diameter punch outs of anode cathode and separator are measured. For the weighing it is important that the electrodes are washed and dried to remove additional weight by electrolyte remains. The weight of the current collector m_{cc} is subtracted from the weight of the electrode punchout $m_{elec}$to gain the weight of the coating m_s.

4.5.2 Density, porosity, and loading

The electrode density $\rho_{elec,meas}$ is calculated from the coating weight and volume

$$\rho_{elec,meas} = \frac{m_s}{V_s} = \frac{m_{elec} - m_{cc}}{A_{cutout} \cdot h_{elec}}. \tag{32}$$

To calculate the solid material volume fraction ε_s

$$\varepsilon_s = \left(\frac{\rho_{elec,meas}}{\rho_{elec,solid}}\right) \tag{33}$$

we need to determine the density of the electrode with a porosity of zero $\rho_{elec,solid}$ wich is determined with equation (34).

$$\rho_{elec,solid} \cong \frac{1}{\frac{f_{AM}}{\rho_{AM}} + \frac{f_{Binder}}{\rho_{Binder}} + \frac{f_{C65}}{\rho_{C65}}}. \quad (34)$$

Typically, the mass fractions of active material f_{AM}, binder f_{Binder} and carbon black f_{C65} are not given by the manufacturer and thus is estimated based on experience with cell production and slurry composition. The calculation of $\rho_{elec,solid}$ focuses on the main components of the electrode. Additional contributions, such as added carbon nanotubes for increased electrical conductivity, are neglected. The bulk densities of electrode materials are listed in Table 5.

Mass and volume fractions obey the following consistency conditions.

$$\varepsilon_s = \varepsilon_{AM} + \varepsilon_{C65} + \varepsilon_{Binder} \quad (35)$$

$$f_{AM} + f_{Binder} + f_{C65} = 1 \quad (36)$$

With the active material mass fraction f_{AM} the mass loading can be calculated with eq. (37).

$$m_{load} = \frac{(m_{elec} - m_{cc}) \cdot f_{AM}}{A} \quad (37)$$

The porosity ε_l, the volume fraction of the electrode pores, is determined from eq.(38). Since it is assumed that all pores are filled with electrolyte, the porosity is equivalent to the volume fraction of the electrolyte and thus marked with index $l = liquid$.

$$\varepsilon_l = (1 - \varepsilon_s) = \left(1 - \frac{\rho_{elec,meas}}{\rho_{elec,calc}}\right) \quad (38)$$

Although this determination of mass loading and porosity may contain assumptions made about the binder and conductive additives, these values are typically good approximations, given that the mass fraction of active material is of the order of 95 % in commercial cells.

Table 5 Density of non-active material electrode components. *Powder property dependent. **Sigma Aldrich quota for PVDF (CAS 24937-79-9) and Carbon Black (CAS 1333-86-4) powder.

Component	Density (g/cm^3)	Source
Cu	8.92	[143]
Al	2.70	[143]
PVDF Binder	1.7*	**
C_{65}	1.7*	**

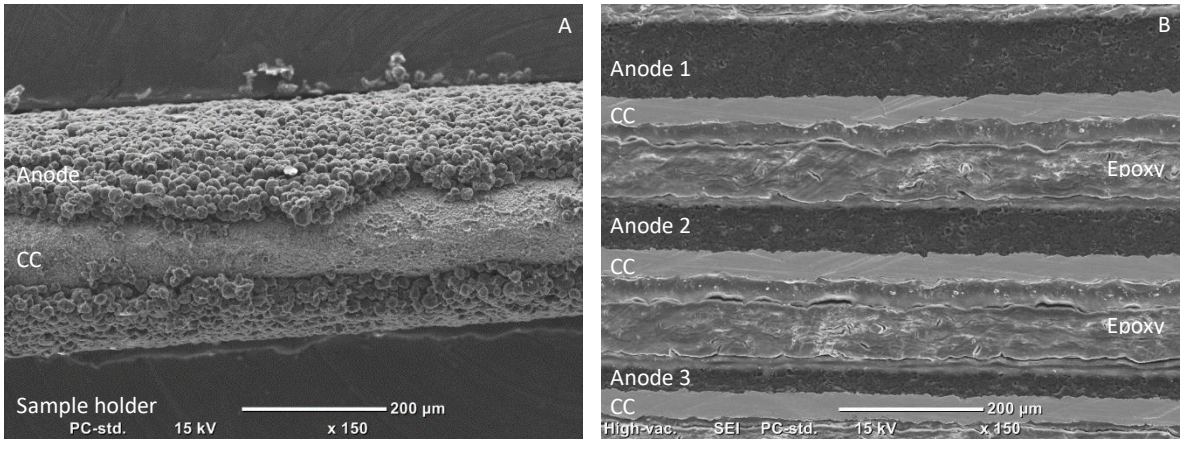

Figure 33 Cross-section image of a graphite anode (A). The electrode is bent 180° to partially exfoliate the active material layer. Cross-section image of three graphite anodes with varying layer thickness (B).

4.5.3 Scanning electron microscope imaging

Scanning Electron Microscope (SEM) images were taken to analyze the elemental composition, surface properties, particle radii distribution, and tortuosity of electrodes.

4.5.3.1 Setup and procedure

SEM images were taken with a JEOL JSM 6000 equipped with EDX at the laboratories of the Chair of Technical Electrochemistry of TU-Munich (Prof. Gasteiger). While the sample is at vacuum during the imaging process in the instrument, during the setup the samples are in contact with air. Thus, only delithiated anodes were used for imaging to prevent damage to the sample due to oxidation.

The electrodes, prepared as described in section 4.4.1, are cut to ≈2x2 mm^2 samples which are attached to the sample holder with conductive copper tape. The holder is placed inside the SEM and the sample chamber is vacuumed. Magnification, focusing, and acceleration voltage is adjusted until the image quality is sufficient. For most images an acceleration voltage of 10 kV was used.

4.5.3.2 Cross-section Images

Initially, a simple procedure was used to prepare samples for cross-section SEM. For that an electrode is bent 180° until parts of the active material exfoliate from the current collector (See Figure 33 A). While this procedure gives acceptable results, seldom an orthogonal viewpoint can be achieved in the images. Additionally, due to the frayed boundary it is only an approximated cross-section.

The following procedure was applied to prepare samples that improve upon these shortcomings. Several electrodes are arranged in a stack separated by wax paper and fixated with polyethylene brackets (Figure 34, 1). Epoxy Resin (Epo Thin 2, 20-3440-32) is mixed with epoxy hardener (Epo Thin 2, 20-3442-016) in a 2 to 1 ratio. The mixture is stirred (1000 rpm, 300 mbar) in a planetary mixer (Thinky ARV-310) for 2 minutes. The electrode stack is placed inside a sample holder and filled with epoxy glue until fully covered. The sample is placed inside a vacuum chamber to remove air trapped in the porous electrode (2). After hardening for 48 hours the epoxy covered electrode stack is removed from the holder.

To remove excess epoxy glue and to achieve a flat surface the sample is grinded in two steps and subsequently polished (Buehler Beta Grind Polisher). In the first grinding step a 6 µm diamond suspension (Buehler MetaDi) is sprayed onto a grit paper. After sufficient grinding the sample is cleaned and a different grit paper with 1 µm diamond suspension is used (3). The sample is then polished with Buehler MicroCloth. A finished sample is shown in (4). It is important that the electrodes are freed from epoxy on both sides of the sample to ground the current collectors during the SEM. This way the sample does not charge up during SEM and improved image quality can be achieved. Figure 33 B shows a cross-section image of three anodes. The anodes (Anode 1/2/3), the current collector (CC) and the epoxy soaked wax paper layers (epoxy) are marked in the image. Notably, a similar result cannot be achieved by cutting the electrodes with a scalpel, since the position of the graphite flakes will be moved or break out of the electrode. This is prevented with the epoxy covering.

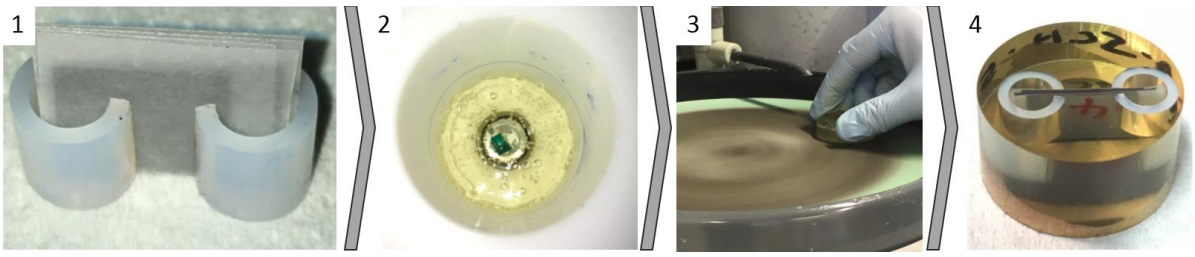

Figure 34 Preparation of SEM cross-section samples in four steps: (1) Electrode stack fixated with wax paper and polyethylene brackets. (2) Sample filled with epoxy under vacuum. (3) Removal of excess epoxy glue through grinding and polishing. (4) Finished sample.

4.5.4 Tortuosity analysis (SEM)

Two different techniques are applied to investigate electrode tortuosity in this work. The first method is to approximate the tortuosity from the top view and cross-section SEM images with the BruggemanEstimator Software tool developed by M. Ebner [42]. In the following the working principle of the software, the workflow to analyze a sample and the limitations of the method are presented.

Working principle

The method is based on the Differential Effective Medium (DEM) approximation introduced by Bruggeman in 1935. The porous medium is considered to consist of two materials, electrolyte with a diffusivity of D_1, and active material particles with diffusivity D_2 occupying a volume fraction ϕ_2. The effective diffusivity $D_{eff}(\phi_2)$ depends on the amount of active material in the electrode.

The change in diffusivity if some active material is added is proportional f to the loss in volume fraction of the electrolyte $\frac{\Delta\phi_2}{1-\phi_2}$.

$$D_{eff}(\phi_2 + \Delta\phi_2) - D_{eff} = f\frac{\Delta\phi_2}{1-\phi_2} \tag{39}$$

The effective diffusivity can then be calculated from the known initial state of solely electrolyte, $D_{eff}(\phi_2\{1\} = 0) = D_1$, by incrementally adding active material until the correct volume fraction is achieved in a process called *incremental homogenization* [144]. The proportionality factor for an anisotropic porous medium is described by a *proportionality tensor* $\boldsymbol{f}$**.** For arbitrarily shaped and oriented ellipsoids with a very small diffusion coefficient compared to the surrounding material $(D_2 \ll D_1)$, the tensor is given as:

$$\boldsymbol{f} = -\boldsymbol{D_{eff}}[\boldsymbol{I} - \boldsymbol{A}]^{-1} \tag{40}$$

With $\boldsymbol{I}$ being the identity matrix and $\boldsymbol{A}$ the depolarization tensor. The eigenvalues of $\boldsymbol{A}$ contain the information of particle dimensions and the eigenvectors v_A contain the particle orientation.

$$A_k = \frac{abc}{2}\int_0^\infty \frac{dt}{(t+k^2)\sqrt{(t+a^2)(t+b^2)(t+c^2)}} \tag{41}$$

For small changes in the volume fraction $\Delta\phi_2 \to 0$ equation (39) becomes the differential equation

$$\frac{\partial \boldsymbol{D_{eff}}(\phi_2)}{D_{eff}} = -[\boldsymbol{I} - \boldsymbol{A}]^{-1}\frac{\partial\phi_2}{1-\phi_2} \tag{42}$$

that can be solved by integration and compared to the Bruggeman coefficient definition

$$\frac{\boldsymbol{D_{eff}}}{D_1} = \varepsilon^{I+\alpha} = \varepsilon^{[I-A]^{-1}} \tag{43}$$

to find the following equation linking the Bruggeman coefficient tensor with the depolarization tensor:

$$\boldsymbol{I} + \alpha = [\boldsymbol{I} - \boldsymbol{A}]^{-1} \tag{44}$$

With this equation the effective diffusivity tensor can now be calculated from particle dimensions and orientation.

$$\frac{\boldsymbol{D_{eff}}(\phi_2)}{D_1} = \prod_{i=1}^{N}\left(\boldsymbol{I} + \frac{\mathrm{Ln}(\varepsilon)}{N}\left(\boldsymbol{I} + \alpha_{B'}^{B'}\{i\}\right)\right) \tag{45}$$

In this equation ε is the electrode porosity and $\alpha_{B'}^{B'}$the Bruggeman exponent tensor transformed from the particle to the electrode coordinate system. Furthermore, it can be shown that the Bruggeman exponent tensor is the arithmetic mean of the Bruggeman exponent tensor of the individual particles.

$$\alpha_{eff} = \frac{\mathrm{Ln}\left[\boldsymbol{D_{eff}}(\phi_2)/D_1\right]}{\mathrm{Ln}(\varepsilon)} - \boldsymbol{I} = \frac{1}{N}\sum_{i=1}^{N} \alpha_{B'}\{i\} = \langle \alpha_{B'} \rangle \quad (46)$$

For additional information on the particle weighting function as well as proof of equation (45) and (46) the reader is referred to M. Ebner appendix B, C and D [42].

Workflow

The BruggemanEstimator software tool uses the Mathematica (Wolfram software) environment. Figure 35 presents the four steps to calculate the anisotropic Bruggeman exponents as well as to export information on the particle radii distribution.

In the first step the user creates a virtual particle population with the desired resolution of ellipsoidal shapes. The program then pre-calculates the Bruggeman exponents for these shapes by solving equation (41). In the second step top view and cross view images are imported and active material particles are labeled by manually fitting the long and short axis of an ellipse. In the third step, the user measures the scale given SEM image (pixel) and manually gives the value of the scale in µm. This step is only necessary if the user wants to output the particle radii distribution. In the fourth step, the program calculates the Bruggeman exponents $\alpha_x, \alpha_y, \alpha_z$ and outputs information on shape distribution and particle axis ratio.

1

Create the virtual particle population and look up tables for the Bruggeman Calculation.

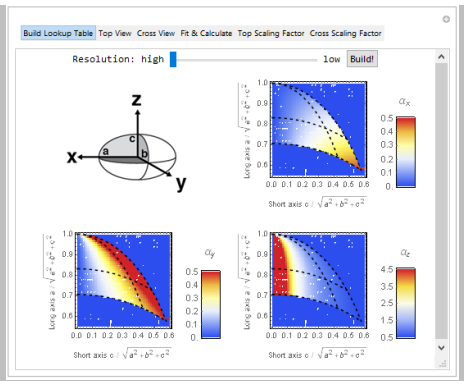

2

Upload of topview and cross-section SEM images. Manual fitting of particles with elliptical shapes.

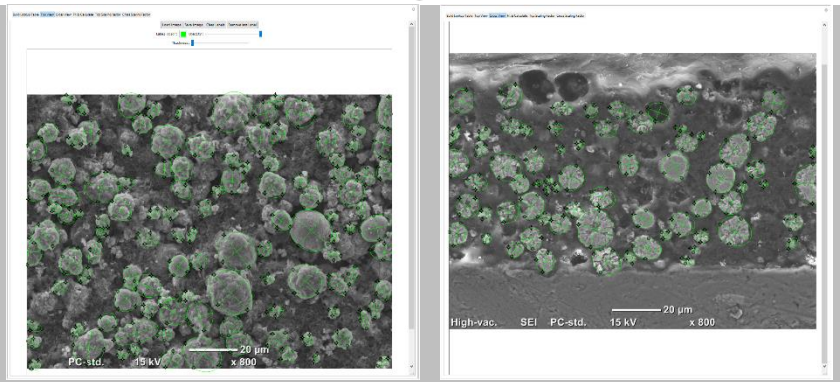

3

Set the scaling (µm/ pixel) for topview and cross-view images.

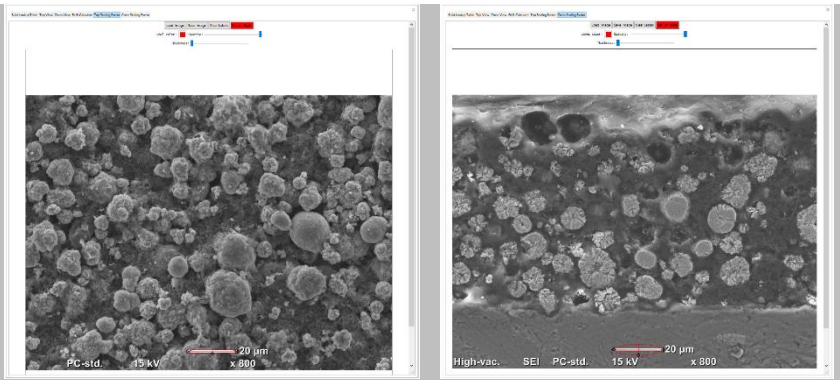

4

Readout of the particle distribution. Calculation of the Bruggeman coefficient α_x α_y α_z.

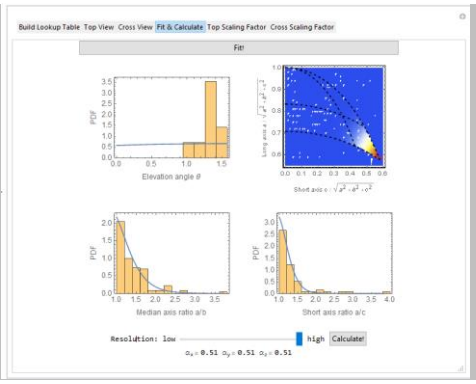

Figure 35 Workflow for particle radii and tortuosity estimation with the BruggemanEstimator tool.

Limitations

While the BruggemanEstimator tool provides a comparatively simple and accessible way to calculate electrode tortuosity, several limitations apply:

1. Inactive components such as polymer binder and carbon black are neglected and only the volume fraction of active material particles is considered. Thus, the volume fraction of blocking material is underestimated, especially for electrodes with large amounts of binder.
2. For the derivation of the Bruggeman Exponent tensor it is assumed that no correlation among particle volume, shape, and orientation exist. This can be the case if, for example, the milling process is different for large and small particles.
3. The three-dimensional shape distribution may not be accurately captured from the 2D SEM images. For example, if images were not taken perfectly orthogonal to the sample. Also, surfaces altered in the process of sample preparation (e.g. cross-section images from cut electrodes).
4. The SEM section investigated may not be representative for the electrode as a whole. For example, a clean section of an electrode that is otherwise heavily covered with electrolyte decomposition products.

Ebner et al. estimate an accuracy of ± 10 % compared to reference 3D tomography data [42].

4.5.5 Particle radii distribution

The Bruggeman Software tool was slightly extended to export the particle radii distribution not originally output by the software tool. With the scale of the SEM image the particle size information (ellipse axes) is converted from pixels to µm and additionally analysis is performed and output (See Figure 36).

This includes the total number of particles, the mean and median radii values, standard deviation and variance as well as quantile values. Histograms show the radii distribution, probability distribution and cumulative probability distribution. All values are given for the long axis (c-c') and short axis (a-b) of the elliptical particles as well as a combined data set (comb.). Additionally, the three best fitting distribution functions are calculated and compared.

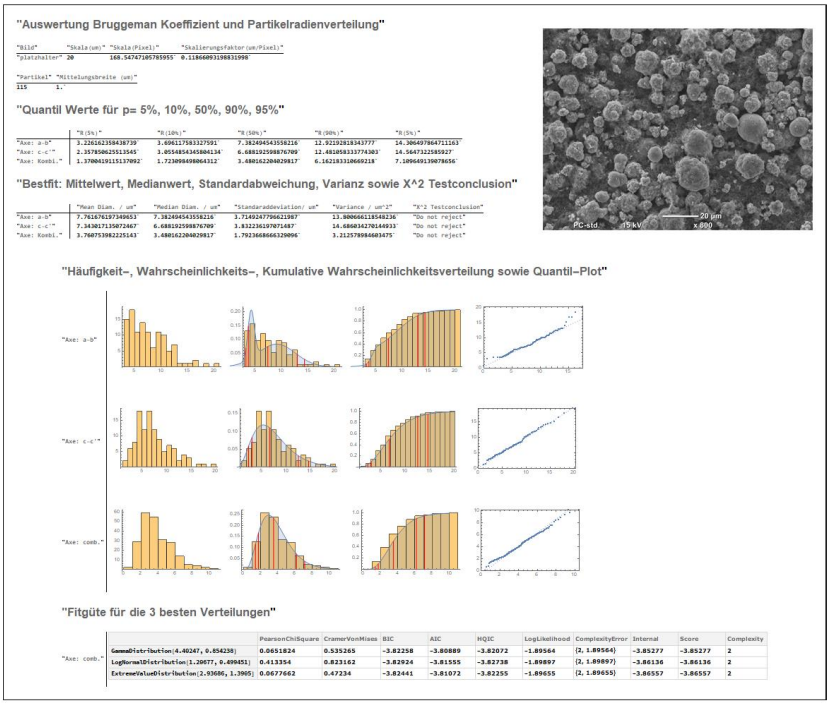

Figure 36 Exemplary results sheet of the particle radii distribution given for a cathode SEM image.

4.6 Color analysis

Graphite shows a well-known color change upon intercalation of lithium. This can be used to quickly approximate the local SoC for a large surface area of an electrode. In this work the effect is used to detect lithium transport to the graphite overhang areas. For that, anodes are extracted from cells post mortem and images of the color distribution are taken. The method is restricted to anodes since the cathode materials NMC (111) and LFP do not show a pronounced color change upon lithiation.

4.6.1 Phenomenological description

The spectrum of observable colors (a) and corresponding RGB values (b) are shown in Figure 37. Fully lithiated LiC_6 graphite is golden. With decreasing amount of LiC_6 in a LiC_6 / LiC_{12} mixture, the color changes from golden to golden-brown to reddish-brown. At lower lithiated states the color changes over blue-grey to metallic dark grey.

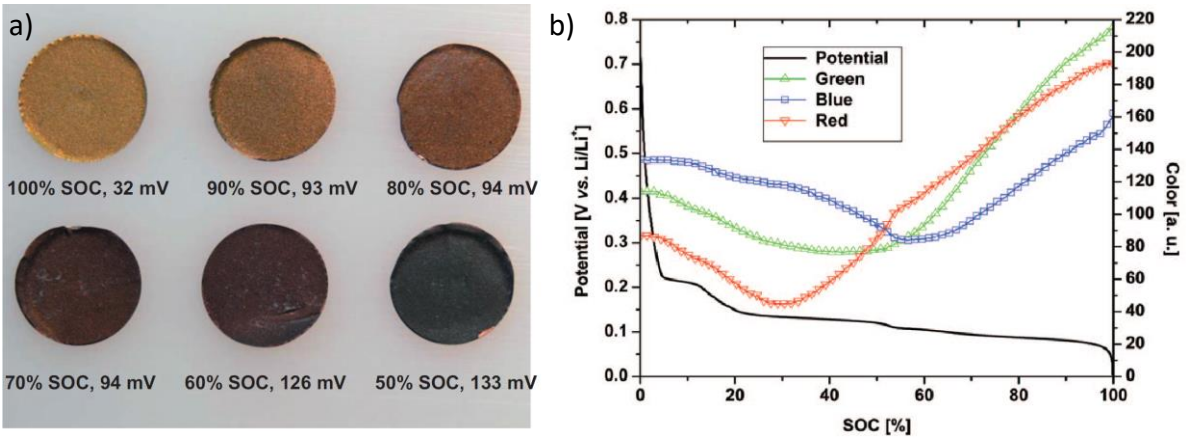

Figure 37 Anode cutouts at varying degrees of lithiation given with their approximate SoC and the voltage cutoff for the lithiation procedure (a). Half-cell potential V vs. Li/Li^+ and red, green and blue values of graphite SFG44 (90 %) and PVDF (10 %) measured in situ with a glass window cell during lithiation (b). Figure by Maire et al.. Reprinted from [52] with permission from IOP Publishing, Ltd..

Below 50 % SoC blue dominates the RGB values and the electrode appears black/ dark grey with differences in the SoC hardly visible to the naked eye. Since light in the optical spectrum does not penetrate deeply into the particle, colorimetry can only measure lithiation at the surface of particles. The lithiation of the bulk of the particle may differ to the surface state, for example due to limitations in the lithium transport from the edge of a particle to the center [133]. This is particularly problematic for in operando measurements.

4.6.2 Imaging setup

Images were taken of washed and dried electrodes with a SONY Alpha 7 II camera with a FE 55 mm F1.8 ZA objective at fixed sample, camera, and lighting position. Since most of the samples were lithiated the electrodes had to remain inside the glovebox while the photos were taken. The camera was positioned outside of the glovebox to allow for easier handling and to prevent damage to the camera from vacuum in the glovebox antechamber. The fluorescent lamp of the glovebox was used as light source. To reduce reflections ambient light was shielded partially with a dark cover. Figure 38 a) shows an unedited image of a non-lithiated graphite electrode overhang area. Each sample was photographed together with a reference card for white balancing.

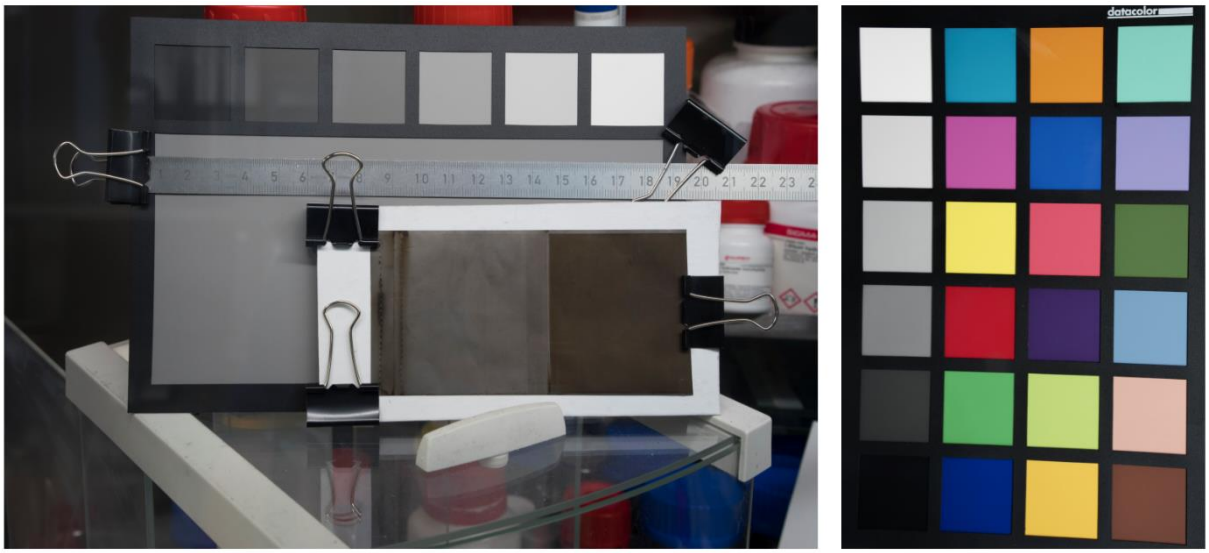

Figure 38 Uncut image of Sample with reference white card (left). Datacolor reference card used for color calibration (right).

4.6.3 Image processing

The unedited images taken with this setup suffer from a distorted color representation due to absorption of the glovebox glass window and the internal camera color calibration. To get an accurate representation of the electrode colors, the images are white balanced and color calibrated. In the first step, each image was white-balanced with the reference grey value (20 %). In the second step, a reference color profile was applied to each image.

Figure 38 b) shows the Datacolor SpyderCheckr 24 color reference card used to create the corrected color profile. The reference card was placed inside the glovebox and an image was taken. The color profile was then adjusted until the reference values given by the manufacturer were in alignment. Table 6 lists the changes to the original image. Notably, the green values are altered most in the color profile. This is expected, since glass more strongly absorbs in the green spectrum.

Image correction was conducted with Adobe Photoshop Lightroom v5.7.1. with Camera Raw 8.7.1 and SpyderCheckr v1.2.2. For better visibility of color gradients, brightness is slightly increased for the electrode images in the manuscript and the supplementary files.

Table 6 Color profile used to correct images taken with SONY Alpha 7 II camera. The values are given as percentage changes.

	Hue	Saturation	Luminance
Red	-10	+14	-7
Orange	-3	0	-6
Yellow	-5	8	-7
Green	-20	-16	-10
Aquamarine	-11	-15	-8
Blue	-12	+1	+9
Lila	-13	-8	-3
Magenta	-1	-4	-7

4.7 Differential voltage analysis

Differential Voltage Analysis (DVA) is a non-invasive and non-destructive technique to analyze lithium-ion batteries. It allows to make the individual contributions of anode and cathode to the cell behavior visible without the necessity to perform individual measurements in half-cell setups. It is a technique commonly applied to analyze aging effects of batteries such as loss of cyclable lithium, loss of active material or balancing changes [145][5]. However, in this work it is applied to prepare and analyze neutron diffraction measurements. In the following the fundamentals of the technique and the use cases are outlined.

4.7.1 Fundamentals

In a lithium-ion battery, anode and cathode are in series connection. In a simplified cell voltage model, following Bloom et al., the cell voltage V_{cell} is the difference between $V_{cathode}$ and V_{anode} [146–148].

$$V_{cell} = V_{cathode} - V_{anode} \tag{47}$$

If we differentiate this equation with respect to the cell charge, we find that the $\left(\frac{dV}{dQ}\right)_{cell}$ is linear combination of the individual contributions from anode and cathode.

$$\left(\frac{dV}{dQ}\right)_{cell} = \left(\frac{dV}{dQ}\right)_{cathode} - \left(\frac{dV}{dQ}\right)_{anode}. \tag{48}$$

The inverse $\left(\frac{dQ}{dV}\right)_{cell}$ is not a linear combination.

$$\left(\frac{dQ}{dV}\right)_{cell} = \frac{1}{(dV/dQ)_{cathode} - (dV/dQ)_{anode}} \tag{49}$$

When $\left(\frac{dV}{dQ}\right)_{cell}$ is plotted against the SoC or the degree of lithiation of a battery this is considered as DVA. If $\left(\frac{dQ}{dV}\right)_{cell}$ is plotted against the cell voltage, it is described as Incremental capacity Analysis (ICA). Figure 39 gives examples of the original cell voltage (a) compared to the DVA plot (b) and the ICA plot (c).

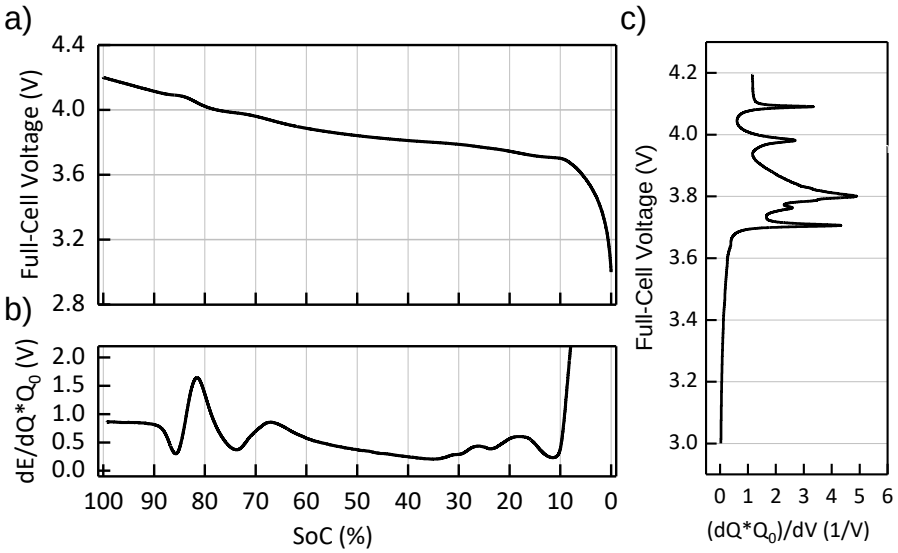

Figure 39 OCV profile of a lithium-ion battery. (a) Corresponding DVA spectrum (b) ICA spectrum (c)

Features in the DVA and ICA plots need to be interpreted differently. Maxima in the *dV/dQ* plot represent phase transitions while maxima in the *dQ/dV* profile represent phase equilibria [146]. For this work the DVA representation was chosen over the ICA representation due to the focus on phase transitions that better visualizes the change in lithiation for Li_xC_6 as well as the typically better peak separation for DVA.

4.7.2 Profile reconstruction

The first step in applying DVA is to measure the OCV of the full cell and the anode and cathode half-cell profiles. Depending on the test object, this may require post mortem of the cell to gain electrode material. From the electrode material half-cells vs. Li/Li^+ are built and the OCV is measured (section 4.1.2). Figure 40 shows the half-cell profiles of a graphite anode (a) and an NCM(111) cathode as used the custom-made pouch cells for ND experiments. The derivatives show the characteristic *dV/dQ* minima and maxima of the individual phase evolution of the electrode materials depending on the state of lithiation.

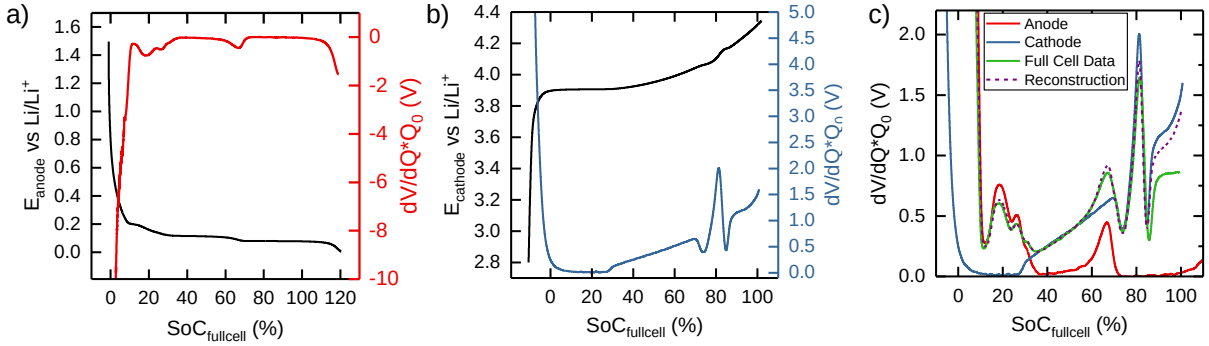

Figure 40 Voltage and differential voltage of graphite anode material (a) and NCM cathode material (b) as well as both in superposition (c).

To depict the *dV/dQ* profile against the normalized SoC of the cell, it is multiplied with the capacity of the cell Q_0.

$$\frac{dV}{dQ}Q_0 = \frac{dV}{dQ/Q_0} = \frac{dV}{dSoC} \tag{50}$$

The half-cells have a smaller capacity than the full cell. Additionally, anode and cathode half-cells are typically made with the same electrode area determined by the coin cell design. Due to this, the balancing of anode and cathode of the original cell is not maintained. As a result, the half-cell profiles cannot simply be added together to the full cell profile, but needs to be rescaled and shifted. This is done according to the following equation [149]

$$Q_0 \left.\frac{dV_{\mathrm{cell}}}{dQ}\right|_{\zeta} = \alpha_{\mathrm{p}} \cdot q_{0,\mathrm{p}} \left.\frac{dv_{\mathrm{p}}}{dq_{\mathrm{p}}}\right|_{\zeta+\delta_{\mathrm{p}}} + \alpha_{\mathrm{n}} \cdot q_{0,\mathrm{n}} \left.\frac{dv_{\mathrm{n}}}{dq_{\mathrm{n}}}\right|_{\zeta+\delta_{\mathrm{n}}}. \tag{51}$$

$\left.\frac{dV_{\mathrm{cell}}}{dQ}\right|_{\zeta}$ is the derivative of the full cell voltage for an arbitrary charge content of ζ. $q_{0,\mathrm{p}}$ and $q_{0,\mathrm{n}}$ are the capacities of the anode and cathode half-cells. The half-cell capacities are scaled with the scaling factors α_{p} and α_{n}. Additionally, the individual contributions of anode and cathode are shifted with an ampere hour offset δ_{p} and δ_{n} to align the electrodes horizontally.

The analysis was conducted with a MATLAB script developed at the EES by Peter Keil. To reduce noise in the signal amplified by the derivative, the DVA data are additionally smoothed with 5 pt next neighbor averaging. The finished DVA profile is then used to analyze the full cell OCV curve.

4.7.3 Application of DVA

DVA was applied in preparation and analysis of both ND experiments to determine the target SoC.

4.7.3.1 Target SoC

For the graphite relaxation experiment full cells are discharged to a specific target SoC. During the discharge and the subsequent relaxation neutron diffraction data is collected and the phase evolution of the graphite anode is analyzed. Knowledge of the target SoC is required to measure in the SoC range

where the ND is sensitive to SoC change. Due to the scarcity of measurement time at a neutron source, it is required to determine the target SoC not through a series of ND measurements at the instrument but in advance, which was done with DVA.

The target SoC has to fulfill the following criteria.

1. It is possible to discharge the cell to the target SoC at all temperatures investigated in the experiment. This is not prevented by, for example, capacity loss, and high overvoltages at low temperatures.
2. The target SoC has to be within the range of lithiation states where the Neutron diffraction is sensible to graphite state changes. This means that either the reflection peak position or intensity changes with the lithiation.
3. For the comparison of several cells, the same state of lithiation in the anode is achieved after discharge independent from cell balancing and capacity differences.
4. Lower target SoC are preferred to higher target SoC, since it assumed that the polarization of the anode increases with discharge rate and duration.

Figure 41 shows the *dV/dQ* profile of a pouch cell for ND measurement. The positions of the maxima are numbered and well aligned with the measurement maxima. The maximum at the center identifies the graphite phase change from the LiC_{12}/ LiC_6 mixture (> 0.5 Ah) and the LiC_{12}/ LiC_{12} (liquid) at this full cell SoC the anode is exactly 50 % lithiated at LiC_{12}. Further maxima can be attributed to distinct graphite states LiC_{18} (3) LiC_{24} (4) LIC_{36} (5) and LiC_{48} (6) based on the staging model of graphite [33]. From diffraction experiments in literature [33, 50] it is known that at low states of lithiation below LiC_{18} the graphite reflections shift in their 2θ angle and intensity. Thus, this SoC range is suitable for full cell discharge and relaxation investigation. The minimum at Q_0 = 190 mAh between (4) and (5) was chosen as target SoC because it is at the center of the sensitive SoC region. The remaining capacity corresponds to 24 % remaining SoC. With all tests this analysis is repeated and the target SoC of the comparison samples are adjusted to obtain identical degrees of lithiation in the anode. Subsequently, low temperature discharges are conducted with the cells to ensure that the chosen target SoCs are attainable at the discharge rate and temperature during the experiment.

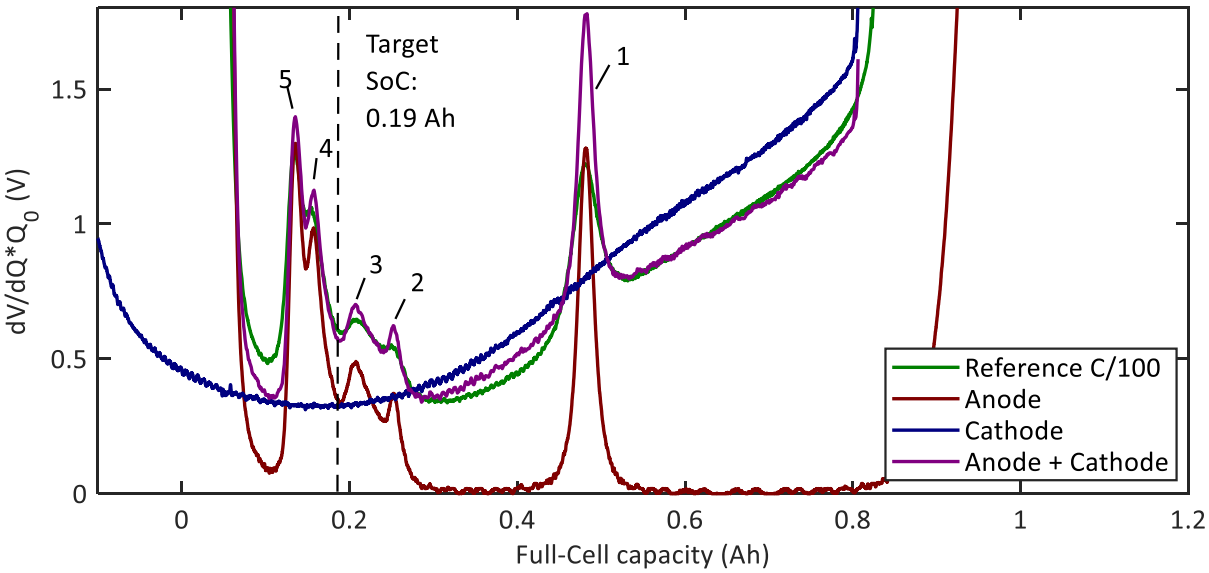

Figure 41 *dV/dQ* profile of a pouch cell for ND measurement. Maxima in the anode profiles are marked 1-5. The dashed line marks the target SoC.

4.7.3.2 Anode utilization

In addition to the determination of the target SoC, DVA can be applied as a plausibility check to the phase analysis of the ND measurements. The position of the graphite peak that separates the low and mid voltage plateaus is identified in the DVA of the full cell (See Figure 41, black line). This peak marks 50 % lithiation of the anode where all graphite is at the LiC_{12} state. The position of this maximum relative to 100 % SoC of the full cell is compared to the position of the maximum relative to the fully lithiated half-cell. This way the lithiation of the anode at 100 % full cell SOC is determined. This value is compared to the results of the ND phase analysis. Here the degree of lithiation is calculated from the integral intensity ratio of the LiC_{12}, LiC_6 reflections observed for a full cell at 100 % SoC.

4.8 Diffraction

Diffraction is a widely used method to analyze batteries. The diffraction techniques are categorized as *ex situ* and *in situ* or *in operando*, depending on the state of the battery sample during the measurements. Since X-rays are electromagnetic radiation and cannot penetrate multiple layers of metal, such as the current collectors in a battery, is applied to investigate the bulk active material or in laboratory made in situ cells with x-ray windows. The possibilities to investigate large format cells in situ are limited. This can be achieved with neutron diffraction. In this section it is outlined how XRD and ND are applied in the overhang and in situ experiments.

4.8.1 Fundamentals of diffraction

Active material such as graphite, LFP and NMC, in batteries are crystalline and thus can be analyzed using the existing toolset of crystallography. Subjected to X-rays, the incoming x-ray beam is scattered elastically at the atoms electrons which are arranged in an orderly fashion in the lattice planes of the crystal. While most X-rays cancel each other out due to destructive interference, in some directions, depending on the crystal structure, they interfere constructively, which is described by the Bragg equation [143].

$$n\lambda = 2\, d_{hkl}\, \sin\theta \tag{52}$$

Here λ is the wavelength of the incoming beam, d is the distance between crystal planes, θ is the incident angle and n is a positiv integer. From the resulting diffraction pattern, the materials structural characteristics such as atomic positions, lattice constants, crystal symmetries can be identified. Each diffraction peak can be related to a family of parallel, reflecting planes in the crystal lattice characterized by the Miller indices *h k l* that define the reciprocal of the axial intersects. The intensity I_i^{calc} of the diffraction peaks depends on a multitude of factors beyond the crystal structure, such as the instrument and beam properties which will be discussed in detail along with the profile analysis algorithms in section 4.9.

Application of diffraction to batteries

Active materials in batteries undergo structural changes during lithiation. If, for example, the lithiation of a lithium atom expands the unit cell of a crystal the change in axes length changes the scattering properties and thus the intensity profile I_i^{calc} of this material. Vice versa, the contraction during deintercalation causes a change in the intensity profile I_i^{calc}. In principle, by measuring the intensity profile of active materials with XRD or ND, the state of lithiation can be determined in situ or ex situ and correlated with other data of the battery, such as battery voltage levels or coulombic efficiency. However, how the intercalation or deintercalation of lithium changes the active material and whether the intensity changes can be measured depends on the specific active material. For graphite this is discussed in detail in chapter 3.

In principle, diffraction allows for time-resolved and spatially-resolved in situ measurements of the SoC in batteries. Whether this can be achieved in practice depends on the beam properties, sample composition and geometric properties.

Differences in Neutron and X-ray scattering

X-rays are scattered at the electron hull of atoms and the elastic scattering processes are described by Thomson scattering [143]. Due to the asymmetry of the electron density distribution in solids, the scattering cross section depends on the $\sigma_{coh,x}$ incident angle. It also depends on the incident wavelength. To prevent inelastic scattering, the chosen wavelength to investigate the sample needs to avoid material dependent absorption energy levels. The number of electrons for atoms increases monotonically with the atomic number Z. The scattering cross section can be approximated with $\sigma \sim \mathrm{Z}^2$. The atomic scattering factor for XRD decreases with the scattered angle θ and consequently the intensity of crystal reflections decreases with θ as well.

Neutrons are not charged and thus not scattered by the electronic hull but the atomic core. Since the core is approximately spherical and the scattering process angular independent, the atomic structure factor shows little intensity loss at high θ compared to XRD. It also does not increase monotonically with the number of electrons, but depends on the number of neutrons in the core as well which results in a large variation in scattering cross sections for small and large atoms. Table 7 shows a comparison of the coherent σ_{coh} scattering cross sections for XRD and ND for selected materials. For crystal structure analysis ND and XRD are complementary techniques. Which technique is suitable depends on the materials used and the observed 2θ range.

Sample limitations

X-rays cannot penetrate thick layers of metals and thus are blocked by the aluminum core of the pouch foil or the metal casing of cylindrical cells as well as the aluminum and copper current collectors in a battery. In situ operation is possible for custom cells with a built in X-ray window or with small single layers cells and high energy X-ray sources such as Molybdenum or synchrotron radiation. The post mortem measurements of single electrode layers enclosed in a pouch foil presented in chapter 6 were only possible due to the short wavelength Mo source.

For ND the sample size is limited by the amount of electrolyte in the cell. The organic solvents such as Ethylene carbonate (EC), Propylene carbonate (PC), Dimethyl carbonate (DMC) or Diethyl carbonate (DEC), contain large amounts of hydrogen which has a high incoherent scattering cross-section of $\sigma_{inc,n} = 80.26\ \mathrm{barn}$ (see Table 7). Incoherently scattered neutrons contribute to the background but not to the diffraction signal.

The state-of-the-art lithium-ion battery uses porous electrodes to increase the surface area of the active material and thus the rate capability. The electrode slurry is made from powdered active material, binder, and conductive additives. For XRD and ND, this means, that an in situ battery sample will always be powder crystal sample. The particles and the crystalline centers in the particles can be approximately described as randomly distributed.

Table 7 Comparison of coherent σ_{coh} and incoherent σ_{inc} scattering cross-sections for selected materials. For X-rays the scattering cross-section $\sigma_{\mathrm{coh,x}}$ is approximated with the proportionality $\sigma \sim \mathrm{Z}^2$. Data from NIST Centre for Neutron Research.

Element		H_1	Li_3	C_6	Al_{13}	Mn_{25}	Fe_{26}	Co_{27}	Ni_{28}	Cu_{29}
X-ray	$\sigma_{coh,x}$(barn)	1	9	36	169	625	676	729	784	841
Neutron	$\sigma_{coh,n}$(barn)	1.76	0.45	5.55	1.50	1.75	11.22	0.80	13.3	7.49
Neutron	$\sigma_{inc,n}$(barn)	80.26	0.92	0.00	0.01	0.4	0.4	0	5.2	0.55

For every Bragg reflection all possible orientations of the crystals are present in a powder sample which leads to the observation of diffraction rings around the beam center (Debye-Scherrer-Rings) at a flat plate detector, instead of discrete Laue spots [150] observed for single crystal diffraction. A minimum particle size and quantity is needed for reliable diffraction results. To avoid peak broadening due to crystal size effects [151] the crystallites need to have sufficient thickness to provide enough parallel planes for the Bragg reflection relative to the length of the wavelength of the beam. For the graphite measurements presented in this thesis, the crystal size effect is considered negligible, since the majority of the particles in the size distribution well exceed a diameter of 0.1 or 0.2 µm typically given as upper limit for the size effect [152].

Considering the statistical distribution of particle orientations, only a minority of the particles is correctly positioned to fulfill the Bragg condition at any given point of a measurement. Non-sufficient amounts of reflecting crystallites for some orientations result in spotty Debye-Scherrer-rings. This may cause wrong measurements of intensity ratios between reflections considering that the detectors such as the STRESS-SPEC detector measure only a fraction of the Debye-Scherrer-Rings. This effect alongside the high penetration capabilities of neutrons results in a minimum sample volume requirement for neutron diffraction. For a battery sample at the STRESS-SPEC instrument this is approximately 1 cm^3 of active material in the beam to achieve a sufficient signal to noise ratio at quick measurements, based on experience with past measurements. Given that the size of the aperture is limited, the samples thus need multiple electrodes to achieve a minimum thickness of about 2-3 mm.

4.8.2 Post mortem X-ray diffraction

All X-ray diffraction experiments were conducted at the Material Science Lab at the Mayer Leibnitz Zentrum (MLZ) in Garching with the technical support of A. Kriele. The series of measurements investigated lithiation gradients in overhang areas of graphite anodes.

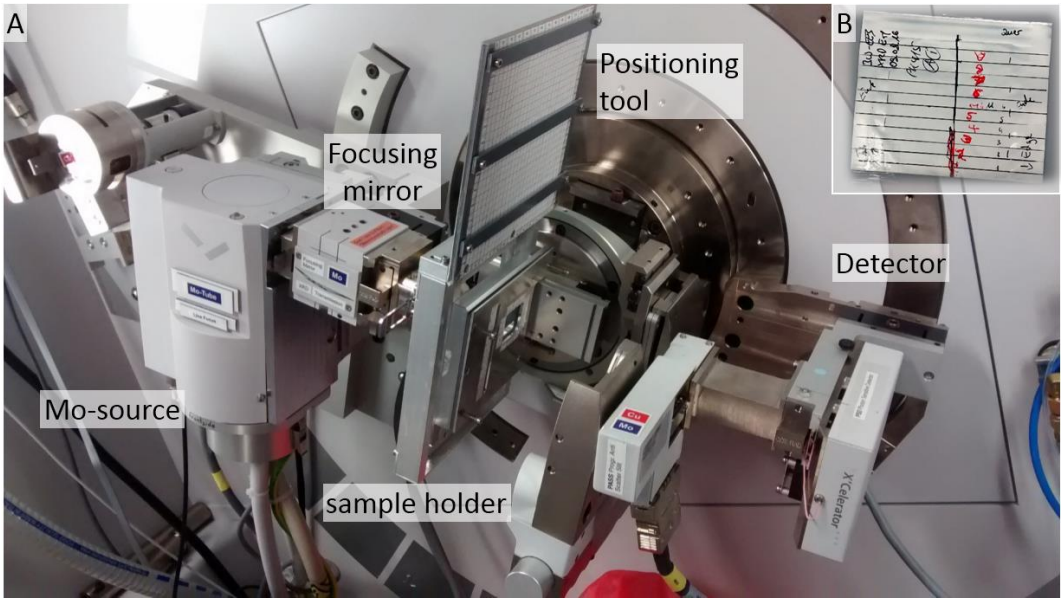

Figure 42 XRD setup with PANalytical Empyrean™ X-ray diffractometer, Molybdenum source, and electrode sample holder (A). Sealed electrode sample with measurement positions marked (B).

4.8.2.1 Experimental setup

Diffraction analysis was performed with the PANalytical Empyrean™ X-ray diffractometer shown in Figure 42 (A). Mo-$K_{\alpha 1}$ radiation was used with a wavelength of $\lambda = 0.70932$ Å at an acceleration voltage of 55 kV at a current of 40 mA. The sealed electrodes (Figure 42, B) were placed in the center of the goniometer circle (radius 240 mm) and were measured in transmission mode, which requires a high X-ray beam penetration depth realized by a focusing mirror. Hence an elliptic graded W/Si multilayer

mirror with an equatorial divergence of the beam of less than 0.055° was used to collimate the divergent beam from the X-ray tube to the secondary focus of the goniometer circle at the detector. Figure 43 shows the beam path in transmission geometry.

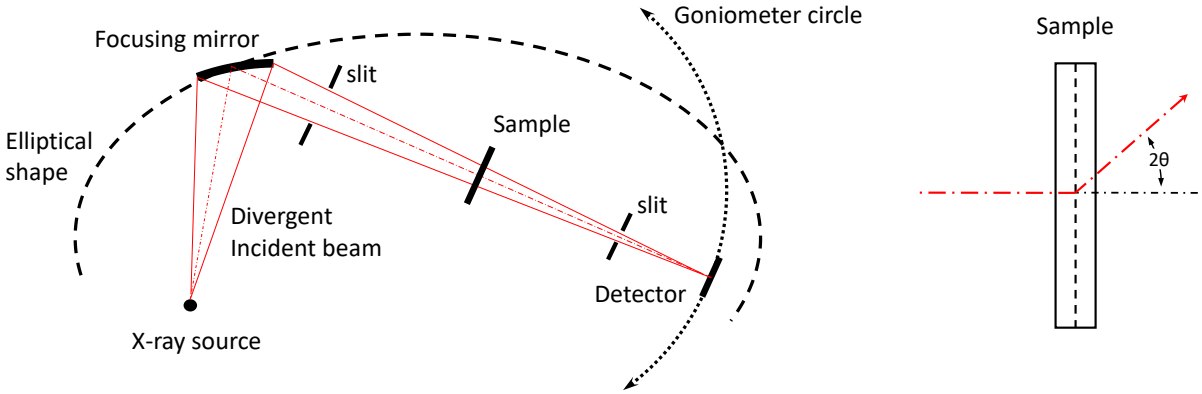

Figure 43 Transmission geometry used for XRD experiments with a flat sample.

A 1D real time multistrip X`Celerator™ detector with an efficiency of 30 % for Mo $K_{\alpha 1}$ radiation and a pixel resolution of 0.002° in 2θ was used to collect the data. The Mo-K_{β} radiation is suppressed to a level below 0.5 % by the focusing mirror. The axial divergence was reduced by inserting Soller slits with an opening of 0.02 rad at the incident and transmitted beam path. The beam cross-section at the sample was reduced to 10 mm x 0.38 mm using masks and a 1/4° Ta divergence slit. For standard measurements, 4-16 patterns were collected typically over a 2θ-range of 7-37° with a step size of 0.008° and a counting time per step of 36.8 s. Long term measurements used up to 170 patterns with a 2θ-range of 5-55°. The sealed electrodes were mounted on a sample holder and oriented perpendicular with respect to the incident beam during the measurement. The custom-built sample holder for small pouch bags is shown in Figure 44. The sample position was adjusted manually with a positional resolution of 0.5 mm (see positioning tool in Figure 42).

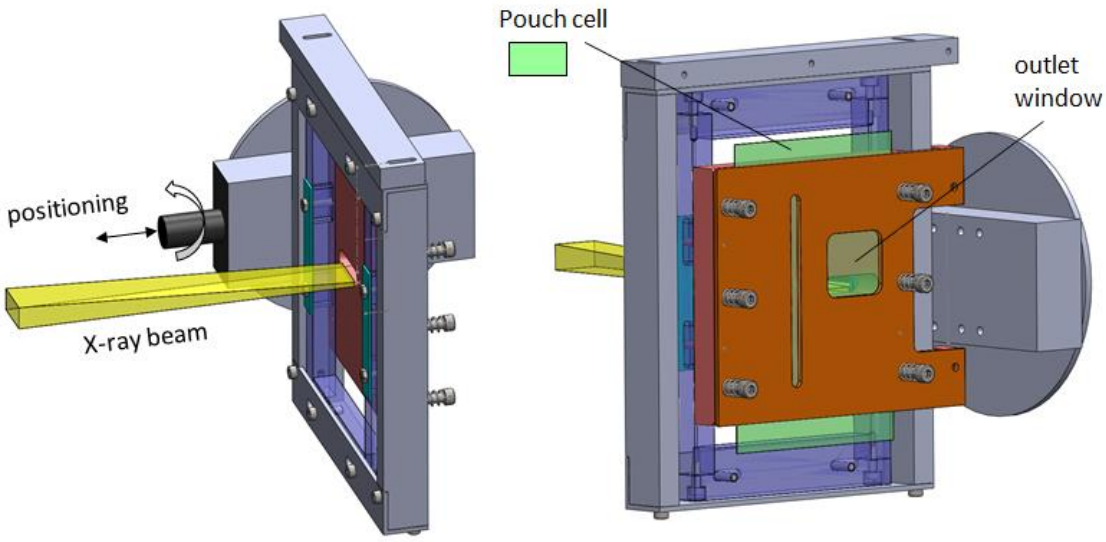

Figure 44 Mounting of Pouch cell at X-ray diffractometer designed by A. Kriele at the Material Science Laboratory FRMII. (Image provided by A. Kriele).

4.8.2.2 *Experimental limitations*

As shown in Figure 42 b), the XRD samples are electrodes sealed in pouch foil. There are several drawbacks to this method. Figure 45 shows the diffraction measurement of a lithiated graphite electrode with the contributions of the pouch foil (amorphous background), the current collector (Cu), and pouch foil (Al). The signal intensity of Cu and Al is much higher than that of the LiC_{12} reflection. The Li_xC_6 reflections at ≈20 °2θ are drowned out by the overlapping Cu and Al reflections and the weak ≈33.5 °2θ reflections need to be used for refinement. In addition, the sample holder does not allow to spin the electrode to minimize the effect of preferred orientation. Both problems could be solved by the mechanical removal of the active material and measurement of the powder prepared in a capillary.

Despite these problems sealed electrodes were used due to several advantages. Removal of the active material would destroy the electrode making repeated measurements at slightly different positions impossible. Also, a much higher spatial resolution in terms of measurement position on the electrode can be achieved with the 0.5 mm wide XRD beam compared to manual removal of an electrode section in a glovebox. Also, the sealed electrode samples can be prepared much quicker which reduced the already considerable measurement time necessary for the XRD experiments. The amorphous background of the pouch foil is tolerable because it does not overlap with the Li_xC_6 reflections. Samples measured with conventional PET foils to seal the electrode (without aluminum layer) showed quick degradation due to diffusion of oxygen through the foil. In contrast samples sealed with pouch foil showed excellent long-term stability. This was tested with a lithiated graphite photographed before the XRD measurements and after 2 months of storage outside of the glovebox in a sealed state. The sample showed identical color distribution before sealing and after 2 months of storage.

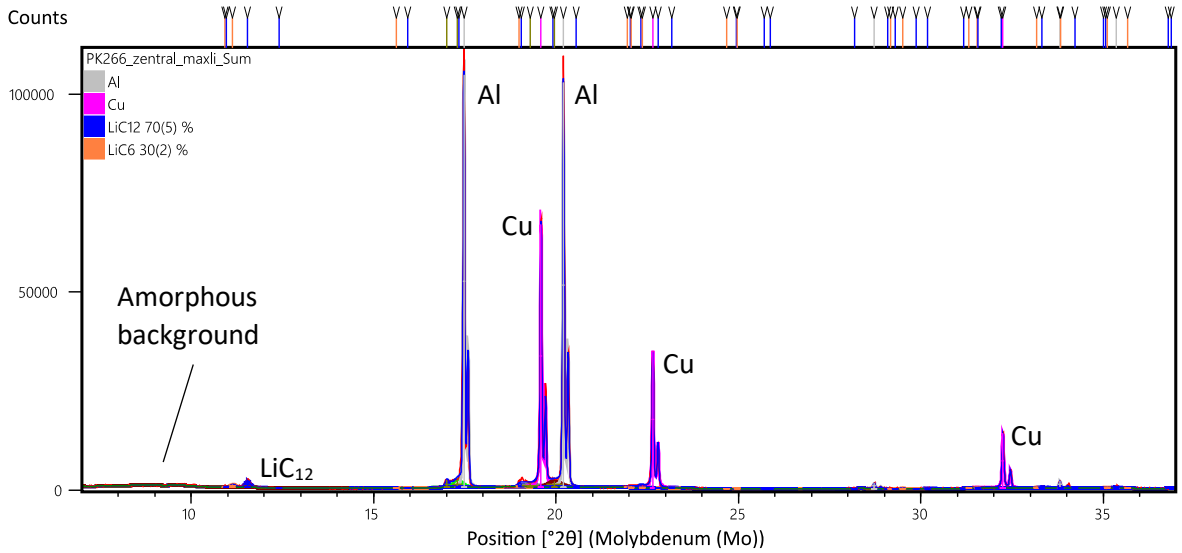

Figure 45 Diffraction measurement of a lithiated graphite electrode. Cu, Al and LiC_{12} reflection positions are marked to highlight the difference in signal intensity. The amorphous background is attributed to the polyethylene pouch foil coating.

4.8.3 In situ neutron diffraction

In situ neutron diffraction data were collected at the material science diffractometer STRESS-SPEC at the MLZ in Garching with the technical support of the instrument scientists Michael Hofmann and Weimin Gan. Identical setups were used for both ND diffraction experiments presented in chapter 7 and 8.

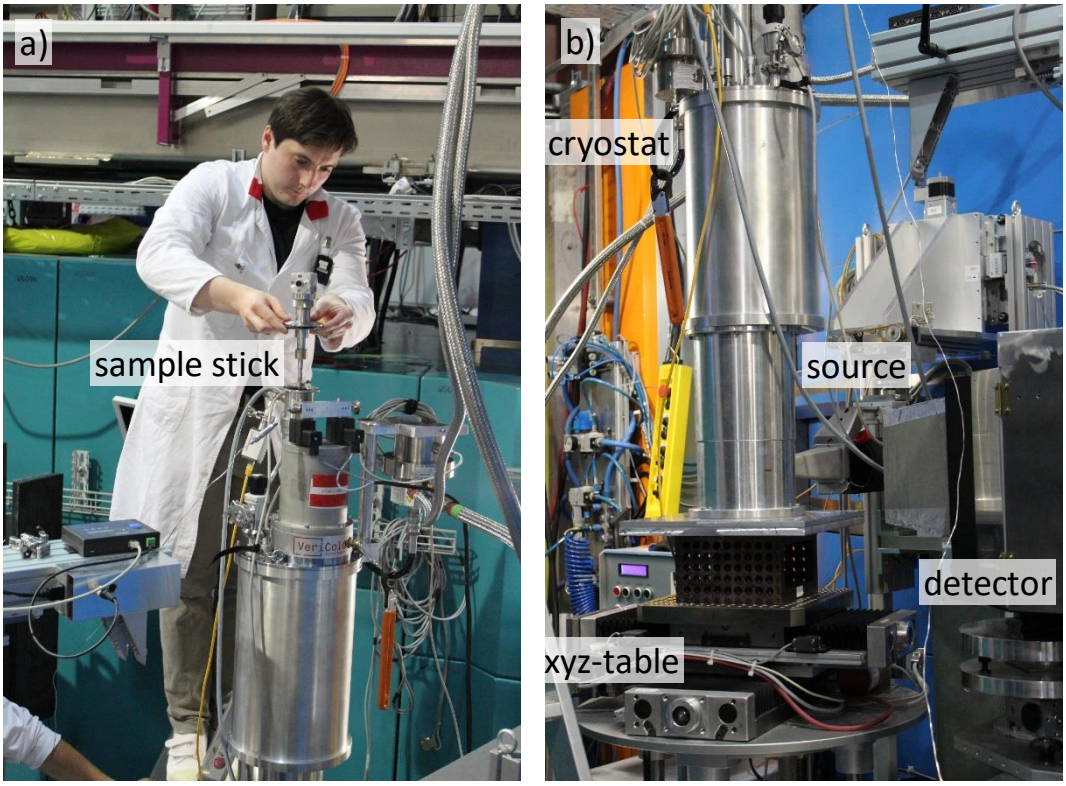

Figure 46 Insertion of the sample stick into the cryostat setup at the FRMII STRESS-SPEC Instrument (a). ND-setup with beam source, detector, XY-table. The exit point of the neutron beam is marked red (b).

4.8.3.1 Experimental setup

The thermal beam port of the neutron source at MLZ provides a flux of thermal neutrons of approx. $9 \cdot 10^9 \frac{\mathrm{n}}{\mathrm{cm^2\,s}}$ at the monochromator [153]. For the measurements a GE(311) monochromator was chosen. After the application of the monochromator the neutron flux is approx. $2.4 \cdot 10^7 \frac{\mathrm{n}}{\mathrm{cm^2\,s}}$ and the wavelength is ~ 2.1 Å. The scattering gauge volume $V_g \approx 0.5$ cm^3 is set by a 5 x 20 mm^2 entrance slit and a 5 mm radial collimator. The instrument uses a two-dimensional position sensitive He^3 detector (PSD) with a 25 x 25 cm^2 detector area with 256 x 256 pixels. The detector sample distance is 1035 mm. The samples are measured in transmission geometry. The batteries are placed onto a sample stick and inserted into a cryostat for temperature control. Helium is used as contact gas for thermal coupling. The cryostat is placed onto an XYZ-table that allows to position the sample with an accuracy of ±10 µm. The ND setup is shown in Figure 46. Cycling was performed with a BioLogic VSP potentiostat equipped with a 100 A booster unit. To prevent lithium-plating, all charging was performed at 300 K.

4.8.3.2 Wavelength calibration

Precise knowledge of the wavelength is required for a reliable Rietveld analysis of the diffraction data. The wavelength is determined with NIST SRM 640d Si standard powder to a precision of ±0.0003 Å at room temperature. Measurements of the Si reflections at 40°, 65°, 80°, and 100 °2θ are conducted and combined to a single 30° - 110° pattern. Since the structure of Silicon is exactly known, the wavelength and the sample displacement can be gained from the Rietveld refinement. Figure 47 shows the combined diffraction data and the refined profile for the Si-calibration of the relaxation experiment (chapter 7).

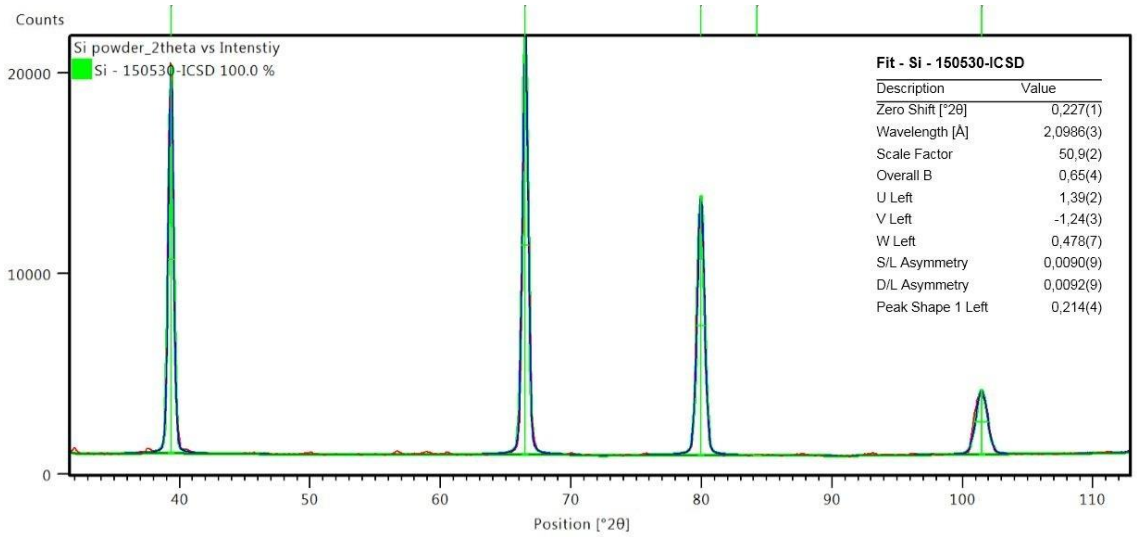

Figure 47 NIST SRM 640d Si standard powder diffraction data and refinement.

4.8.3.3 Sample positioning

The correct positioning of the sample is complicated by the fact that the sample on the sample stick is inside the cryostat and cannot be seen from the outside. The battery sample itself is fixated manually at the sample stick and the position may vary by approx. ± 2 mm in all directions. Additionally, the sample stick can be rotated inside the cryostat.

For the calibration the exact position of the cryostat is determined with the laser positioning tool at STRESS-SPEC. In the first step the sample is rotated until it is aligned in a 45° angle to the beam and the position is marked at the cryostat. For all further calibration steps, the sample position is changed through moving the cryostat setup with the xyz-table. The y axis is parallel to the sample and the x axis is orthogonal to the sample. Each axis is now scanned from -7 mm to +7 mm with respect to the initial position. The step size is 1 mm. For each step the intensity is recorded for 1 minute and the position with maximum intensity is chosen. The height (z) and y position are adjusted only once for the first sample and the position is kept. The x axis scan is repeated after each sample exchange before further measurements.

4.8.3.4 Resolution limitations

Since the experiments focus on lithiated graphite phases during discharge and relaxation, diffraction data is collected in a limited 2θ-range of $28° < 2\theta < 42°$. The limited fixed 2θ-range allows for fast continuous data collection in 3 min intervals with sufficient signal quality. For measurements showing slow graphite phase changes during relaxation, data were combined to 6-60 min intervals to improve signal to noise ratio. However, since doubling the measurement time increases the signal to noise ratio only by a factor of $\sqrt{2}$, improvements are limited.

4.9 Crystal structure analysis

The diffraction data is analyzed to retrieve the phase composition of the sample and to draw conclusions about the state of lithiation on the anode and the overall state of the battery. For that multiple analysis techniques are employed.

The large amount of diffraction data sets recorded provided a challenge for the data analysis. In the XRD experiment over 70 diffraction data sets and for the ND experiments approx. 1000 data sets were generated. The XRD data was fully analyzed with Rietveld refinement using the Highscore software package [154]. The limited 2θ range of the in situ ND data includes only a single reflection of the Li_xC_6 phases and thus cannot be analyzed with Rietveld analysis. Here a Pawley fit is applied.

For the large amount of ND data, a two-pronged strategy was used. The majority of the data was analyzed with a MATLAB script with automated background fitting and fit optimization. In some cases, a sufficient fit result was not achieved with the script, most often due to overlapping peaks or insufficiently fitted background. In these cases, the data was fitted manually with the Highscore software package. In the following the applied techniques are described.

4.9.1 Rietveld refinement

Rietveld refinement is a fitting method for diffraction patterns. It compares a theoretical profile generated from crystallographic data with the measured profile and minimizes the differences through variation of the model parameters. Highscore uses the proprietary BCPE (Bound Constraints Parameter Estimation) algorithm to minimize the residual function WSS in a general non-linear least square form.

$$WSS = \sum_i w_i \left| I_i^{exp} - I_i^{calc} \right|^2, w_i = \frac{1}{\sqrt{I_i^{exp}}} \tag{53}$$

Here I_i^{exp} is the experimental intensity profile and I_i^{calc} the calculated intensity profile.

4.9.1.1 Intensity function

The intensity I_i^{calc} at a given position θ_i is sum of the contribution of *k* reflection peaks and *j* phases and the background. The intensity is calculated with the equation

$$I_i^{calc} = S_F \sum_{j=1}^{Nphases} \frac{f_j}{V_j^2} \sum_{k=1}^{Npeaks} L_k \left| F_{k,j} \right|^2 S_j(2\theta_i - 2\theta_{k,j}) P_{k,j} A_j + b_i. \tag{54}$$

The comprised variables are; the phase scale factor S_F, the phase volume fraction f_j, the phase cell volume V_j, the Lorentz-Polarization factor L_k, the structure factor $F_{k,j}$, the profile shape function $S_j(2\theta_i - 2\theta_{k,j})$, the preferred orientation parameter $P_{k,j}$, the absorption factor A_j and the background function b_i. For the sake of brevity details on the parameters S_F, f_j, V_j, and L_k are omitted here but can be found in the Highscore support package.

The background b_i is approximated with a linear function in the MATLAB script. For the files analyzed with Highscore either a manually set background or the Highscore function *Determine Background by Search Peaks* was used.

4.9.1.2 Structure factor

The structure factor $\left|F_{k,j}\right|^2$ is the squared absolute value of the reflected waves from all atoms within the unit cell and calculated by

$$\left|F_{k,j}\right|^2 = m_k \left| \sum_{n=1}^{N} f_n e^{-B_n \frac{\sin^2\theta}{\lambda^2}} \left(e^{2\pi i (hx_n + ky_n + lz_n)} \right) \right|^2. \tag{55}$$

m_k is the multiplicity of the k^{th} reflection with the Miller indices *h, k, l*. f_n is the atomic scattering factor of the n^{th} atom with the coordinates x_n, y_n, z_n. B_n is the temperature factor. Highscore automatically choses whether atomic scattering for neutrons or X-rays f_n depending on the chosen diffraction technique.

4.9.1.3 Profile function

The Pseudo-Voigt profile function PV was used for XRD and ND data.

$$PV(2\theta_i - 2\theta_k) = I_n \left[\eta_k \left(\frac{1}{1 + \frac{2\theta_i - 2\theta_k}{\omega_k}} \right) + (1 - \eta_k) e^{-\ln 2 \left(\frac{2\theta_i - 2\theta_k}{\omega_k} \right)^2} \right] \quad (56)$$

The profile is a linear combination of a Lorentz function and a Gauss function and thus includes a combination of Gaussian (e.g. Doppler broadening) and Lorentzian (e.g. lifetime broadening) line broadening effects. Equal contributions are assumed and the mixing parameter η_k is set to 0.5 for neutrons. The angular dependence of the full width half maximum (FWHM) ω of the diffraction peaks is described by the Caglioti equation

$$\omega^2 = W + V \tan\theta + U \tan^2\theta \quad (57)$$

where *W, V* and *U* are the refined half width parameters. The Caglioti function was sufficient to achieve good fit quality for the ND data but in the case of the XRD data the Thomson-Cox-Hastings extension (TCH) was used.

$$\Gamma_G^2 = W + V \tan\theta + U \tan^2\theta + P/\cos^2\theta \quad (58)$$

$$\Gamma_L = X/\cos^2\theta + Y + \tan\theta + Z \quad (59)$$

In the TCH approach the Gaussian and Lorentzian contributions to the profile function have their own set of halfwidth parameters *W, V, U, P* and *X, Y, Z* that are refined independently.

FWHM constrains

In some cases, the degree of overlap between phases was too great to achieve a reasonable fit quality or even convergence of the Rietveld fit. This was the case for, for example, in situ measurements of Li_xC_6 during fast discharge. In these instances, the FWHM between different phases was constrained

$$\omega_k \equiv \omega_i. \quad (60)$$

The FWHM and corresponding TCH parameters *U*, *V*, *W* are still refined, but are the same for all phases. This simplification is based on the assumption that both phases are subject to the same experimental conditions, such as beam size, instrument geometry, detector, and sample positioning, and thus similar peak broadening is expected. Furthermore, it is assumed, that the profile parameters (size broadening, strain and preferred orientation) of two phases Li_xC_6 and Li_yC_6 for $|x - y| < 0.1$ will not radically differ in their crystallographic structure.

4.9.1.4 Preferred Orientation

Battery electrodes are not ideal samples for powder diffraction. The correction of intensity changes due to preferred orientation is crucial for the analysis of these samples. The graphite anode material investigated in XRD and ND exhibits plate-like crystallites. Graphite naturally forms flakes due to the strong covalent bond within the planar graphene layers but weak van der Waals bond in between layers in the z direction of the crystal. Naturally, in a powder of plate like particles the particles will tend to orientate in parallel to each other. In addition, the compression of the graphite electrode during the calendering step in the production will amplify this tendency. The challenge is increased by the framework condition, where neither the XRD nor the ND sample can be rotated during measurement.

W.A. Dollase provides an analytical expression to correct the diffraction intensities of samples with axially symmetric, flat-plate like crystallites for preferred orientation [155].

$$P_{k,j} = \frac{1}{m_k}\sum_{n=1}^{m_k}\left(P_{MD}^2\cos^2\alpha_n + \frac{\sin^2\alpha_n}{P_{MD}}\right)^{-\frac{3}{2}} \quad (61)$$

Here P_{MD} is a refinable factor (March Dollase factor) and α_n is the acute angle between the scattering vector and the normal to the crystallites. This expression was set as default correction mechanism.

However, many graphite XRD samples continued to show deviations in the integrated intensities and insufficient R-values after inclusion of the March Dollase correction. Fit quality greatly improved after multiple preferred orientations were considered. A texture with complex orientations is considered plausible given that the samples are non-ideal at the microscopic level (plate like crystallites) and the macroscopic level (particle shape, particle orientation in the electrode). In this case the observed intensity I_{obs}^{hkl} can be corrected with $\mathrm{I}_{\mathrm{ideal}}^{\mathrm{hkl}} = \mathrm{I}_{\mathrm{obs}}^{\mathrm{hkl}} \cdot \bar{W}(hkl,\alpha)^{-1}$ where $\bar{W}(hkl,\alpha)$ is the texture factor. According to Järvinen et al. the texture factor can be described by a series expansion with symmetrized spherical harmonics functions Y_{ij}

$$\bar{W}(hkl,\alpha) = \sum_{ij} C_{ij}Y_{ij}(\theta_{hkl},\varphi_{hkl})P_i(\cos\alpha) \quad (62)$$

C_{ij} are refineable parameters and P_i are Legendre polynomials. The functions need to fit the Laue class of the analyzed phase [156]. Table 8 lists the functions suitable for the 6/mmm group up to the 6th order chosen by the selection rules given by Järvinen.

Table 8 Series expansion functions for 6/mmm crystals [156].

$Y00$	1
$Y20$	$\frac{1}{2}(3\ \cos^2\theta - 1)$
$Y40$	$\frac{1}{8}(35\cos^4\theta - \ 30\cos^2\theta + 3)$
$Y60$	$0.625(231\cos^6\theta - \ 315\cos^4\theta + \ 105\cos^2\theta - 5)$

4.9.1.5 Fit quality

Despite great effort to achieve perfect agreement between the measurement data and the Rietveld refinement fit, discrepancies between the observed intensity values I_{ko} and calculated intensity values I_{kc} remain. As a measure of the discrepancy of the best fit model and the experimental data R-factors are given. For individual Bragg reflections the R-Bragg value R_B [157] is defined by

$$R_B = \frac{\sum|I_{ko} - I_{kc}|}{\sum I_{ko}} \cdot 100. \quad (63)$$

As a measure of the overall quality of the fit the weighted profile R-factor R_{wp} is given [157].

$$R_{wp} = \frac{\sum w_i\left|I_i^{exp} - I_i^{calc}\right|^2}{\sum w_i I_i^{exp}} \cdot 100 \quad (64)$$

As a rule of thumb R_{wp} values of < 15 were deemed sufficient for samples with a high degree of overlap between phases and a low signal-to-noise ratio. For individual reflections the target R_B value was 1 and up to 5 was deemed sufficient for low quality samples.

4.9.2 Pawley method

The neutron diffraction data collected over a limited 2θ-range is not sufficient for a Rietveld refinement of the crystal structure of Li_xC_6 since only a single reflection or few reflections are observed. In this case a Pawley fit is performed. The Pawley fit refines each peak independently and does not resolve the influence of preferred orientation, strain and size broadening on the intensity distribution. It does require knowledge of the space group of the phase as input. The peak positions are calculated from the unit cell and known symmetry. The reference data for all phases is given in Table B.1 to Table B.5 in the appendix. Identical to the Rietveld refinement procedure, the pseudo Voigt profile function (56) and Caglioti FWHM function (57) are used for fitting.

The Pawley fit gives the peak position, peak shape, intensity as well as unit cell parameters of the refined phases, but does not generally give a quantitative measure of how much of each phase is present. This information is crucial for the interpretation of the state of lithiation. However, in some cases the relative quantity of the phases can be extracted from the fitted intensities. In the case of the neutron diffraction data a series of measurements with identical experimental conditions was undertaken. We can thus compare the relative state of a phase with the state at earlier or later time steps. The Pawley-fit approach was also used for the XRD data, but only for the Al-phases to better handle the intensity mismatch due to preferred orientation and texture.

Structure factors of LiC_6 and LiC_{12}

The relative share of certain phases can be calculated manually from the intensities determined by the Pawley fit. For LiC_{12} and LiC_6 the crystal structure is known and the structure factor can be calculated. The structure factor for the observed 001 reflection of LiC_6 is

$$|F(hkl)| = |-6b_C + b_{Li}|. \tag{65}$$

The structure factor for the 002 reflection of LiC_{12} is

$$|F(hkl)| = |6b_C + b_{Li}|. \tag{66}$$

The factors b_{Li} and b_C are the neutron scattering length for lithium and carbon. Through comparison of the corrected Intensities $I/|F(hkl)|^2$ the amount of each phase in the material and the overall degree of lithiation are calculated.

5 Lithiation of anode backside coatings

Coin cells are a longstanding tool in battery research to investigate the performance of electrodes vs. Li/Li^+. They are not only used to research freshly produced material, but also to investigate material extracted from cells to support the full cell analysis. Technical challenges arise from the fact that these electrodes are fully double-sided coated and not specifically made for half-cell analysis. Research institutes which want to analyze electrode material from commercial cells need to consider the correct sample preparation. A possible assumption is that the backside due to being faced away from the Li/Li^+ will be inactive unless the cell is cycled extremely slowly (≈0.01C). Figure 48 shows the perceived limited surface area the backside coating has with the coin cell electrolyte at the electrode sides of the disk.

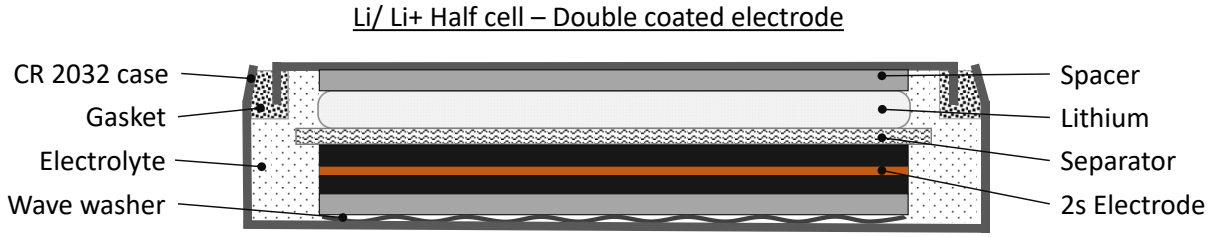

Figure 48 Schematic of a coin cell Cross-section with a double-coated anode vs. Li/Li+.

The backside experiment was used to investigate the influence of the backside coating on cell OCV, capacity, and voltage relaxation by means of experiment and p2D (pseudo 2-dimensional) modeling. It tests the assumption, that potential backside effects can be mitigated through measurements at high rates and investigates the technical implications for coin cell analysis of post mortem electrodes.

The student Korbinian Wachutka supported the backside coating experiment as part of a research internship and his master thesis *Untersuchung und Modellierung des Einflusses mehrseitig beschichteter Elektroden auf die Eigenschaften von Knopfzellen* [158]. Korbinian Wachutka conducted measurements and analyzed half-cell samples and material samples prepared by the author. The simulation model presented in section 5.3 was set up and parametrized by the student under guidance of the author. The parameter studies presented in section 5.5 were conducted by the student under guidance. Data previously presented in the students' work is referenced with *Data from* [158].

5.1 Challenges working with commercial cells

Potential problems associated with backside coated electrodes can be easily circumvented by using single-coated parts of the electrode if these exist in the commercial cell under test. This was seldom the case for cylindrical or prismatic commercial cell samples analyzed at the EES, but sometimes the case with pouch cells where the outermost electrode layer was not coated. It is not possible to manufacture single-coated copies of the double-coated electrode material from commercial cells since key information, such as precise weight-% of binder, carbon black and active material, is not made available by the manufacturer in the material safety datasheets of cells.

Backside Removal

The coating can be removed from a cell either by mechanical force or by dissolving of the electrode or a combination of both. Figure 49 shows the mechanical removal of one side of a two-sided LFP cathode. A drawback of this method is potential damage to current collector and to the remaining coated electrode side. Alternatively, electrodes from cells manufactured with water-based slurries can be

dissolved with water, and N-Methyl-2-Pyrrolidone (NMP) based slurries can be dissolved with NMP. This way active material is removed with less mechanical force. This procedure requires to shield the remaining electrode side from the solvent. While this method is suitable for non-lithiated electrode material, it is problematic for electrodes obtained post mortem, especially anodes. Anodes from commercial electrodes are lithiated. Water must not be brought inside the glovebox environment and the lithiated anode will react with air or water outside of the glovebox. Little information is available in literature about the effect of backside coating on cell performance or the preparation of electrodes from post mortem investigations. Guides for academic researchers to produce high quality coin cells are available [159] but they largely focus on manufacturing electrodes and do not focus on post mortem electrodes or cover these effects. Lee et al. report an influence of backside coated electrodes on the coulombic efficiency and discharge capacity [160]. Though for this experiment pouch cells were investigated and removal techniques were not discussed.

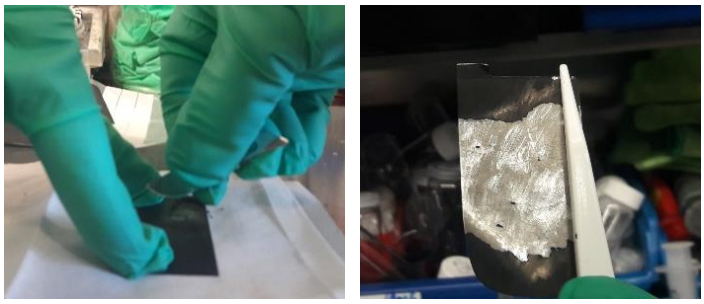

Figure 49 Mechanical removal of active material from double-coated LFP cathode (left). Electrode with removed backside and lightly damaged current collector (right). Glovebox work Jörn Wilhelm. Image taken by K. Wachutka reprinted from [158].

5.2 Experimental design

Single-coated and double-coated graphite and LFP electrodes as well as custom-made graphite-LFP pouch cells were purchased from CustomCells Itzehoe GmbH to assess the impact of backside coating on coin cell performance qualitatively and quantitatively. Graphite was chosen because it is the most common anode material in lithium-ion cells. LFP was chosen due its flat OCV characteristic. The Information on the electrode properties is summarized in Table 9.

Table 9 Electrode parameters for graphite and LFP material from CustomCells. * Data not provided.

Parameter		C6-1S	C6-2S	LFP-1S	LFP-2S
Mass loading	mAh/cm^2	2.2	2.2	2.0	2.0
Capacity C_N	mAh	3.4	6.8	3.1	6.2
Active material	%	96	96	-*	-*
Current Collector		Cu	Cu	Al	Al
Coating height	µm	80.1	70.1	113.2	114.8

Each pouch cell contains a single-coated and double-coated sheet for anode and cathode. The cells are charged to a target SoC and subsequently disassembled as outlined in section 4.4. This way the backside coating has a defined initial lithiation for the coin cell experiments. This is not possible for the coin cells made from double-coated anodes, because the backside is in an unknown state after formation. Consequently, single-coated and double-coated samples are made from non-formated sheets as well as from electrodes extracted from cells. For comparison, samples with double-coated electrodes where the backside is removed are made for each type as well. The samples with material extracted from post mortem are categorized by the SoC of the disassembled cell; 0 % S0C, 50 % SoC and 100 % SoC. All samples are listed with identifiers and number of samples in Table 10.

Table 10 Coin cell samples for backside coating tests.

Sample-ID	Description	Source	# Samples
1S-R-C6	One-sided coating Graphite	Raw material	6
1S-R-LFP	One-sided coating LFP	Raw material	6
1S-E-C6	One-sided coating Graphite	Extracted	6
1S-E-LFP	One-sided coating LFP	Extracted	5
2S-R-C6	Two-sided coating Graphite	Raw material	6
2S-R-LFP	Two-sided coating LFP	Raw material	6
1S-R-BR-C6	One-sided coating Graphite, backside removed	Raw material	6
1S-R-BR-LFP	One-sided coating LFP, backside removed	Raw material	6
1S-E-BR-C6	One-sided coating Graphite, backside removed	Extracted	6
1S-E-BR-LFP	One-sided coating Graphite, backside removed	Extracted	6
2S-E-0-C6	Two-sided coating Graphite, backside 0 % SoC	Extracted	4
2S-E-0-LFP	Two-sided coating LFP, backside 0 % SoC	Extracted	4
2S-E-50-C6	Two-sided coating Graphite, backside 50 % SoC	Extracted	6
2S-E-50-LFP	Two-sided coating LFP, backside 50 % SoC	Extracted	6
2S-E-100-C6	Two-sided coating Graphite, backside 100 % SoC	Extracted	3
2S-E-100-LFP	Two-sided coating LFP, backside 100 % SoC	Extracted	3

Table 11 BaSyTec Measurement procedures of OCV, rate capability, and relaxation tests. For the rate capability test only C/10 is shown. Data from [158].

STEP	C-RATE (CC)	VOLTAGE LIMIT (CV)	MONITORING / S	STOP-CONDITION
RELAXATION				
PAUSE			10	t > 0.5h
CHARGE	0.1		10	$U > U_{max}$
CHARGE		$U = U_{max}$	10	I < 0.05C; t > 24h
DISCHARGE	1		1	$U < U_{min}$
PAUSE			5	t > 2h
PAUSE			30	t > 63h
OCV				
PAUSE			10	t > 0.5h
DISCHARGE	0.02		30	$U < U_{min}$
CHARGE	0.02		10	$U > U_{max}$
DISCHARGE	0.02		10	$U < U_{min}$
CHARGE	0.5		5	t > 600 s
PAUSE			60	t > 600 s
RATE CAPABILITY				
PAUSE			10	t > 60s
DISCHARGE	1		10	$U < U_{min}$
DISCHARGE		$U = U_{min}$	10	I > -0.05C; t > 24h
PAUSE			10	t > 15 min
CYCLE-START				
CHARGE	0.1		10	$U > U_{max}$
CHARGE		$U = U_{max}$	10	I < 0.05C; t > 24h
DISCHARGE	0.1		10	$U < U_{min}$
DISCHARGE		$U = U_{min}$	10	I > -0.05C; t > 24h
CYCLE-END				Cycles > 2
PAUSE			10	

Not all measurements are performed with all the samples, because of sample defects (backside removal) or because the sample's lost it's well-defined backside lithiation state after the first measurement (double-coated). The test procedures encompass OCV and rate capability tests, as well as the time dependence of the voltage relaxation. OCV tests are performed with a moderately slow constant current charging and discharging rate of C/50. For all OCV tests the lithiation is measured first, followed by the delithiation step. The rate capability tests cover C/10, C/5, C/2, 1C, 2C. The delithiation step is performed with a CCCV procedure. The lithiation is performed with only a constant current charging procedure with exception of the slow rate C/10. For the relaxation measurements the voltage is recorded during 64 hours after a 1C charging or discharging step. Table 11 summarizes the measurement procedure.

5.3 Backside p2D modeling

A two-dimensional Newman type model is set up to simulate the backside lithiation effect. The model calculates the time dependent lithium concentration distribution and potential distribution in the cell. For that it solves the Poisson equation and diffusion equation in the three domains (anode, cathode, separator) and two phases (liquid, solid) of the cell. The interface reaction is described by the Butler Volmer equation (71). The Newman model has been discussed extensively in the literature and is thus not presented here to its full extent. For a more comprehensive description see [86].

In its classical form [97], with a one-dimensional representation of the electrode and separator domain, it disregards diffusion processes parallel to the current collector and is thus not applicable to describe lithiation and delithiation of the backside coating. Full 3D models of electrodes such as described in [161] are too computational extensive to scale from µm sized blocks to a full coin cell electrode of 1.5 cm^2. Other common Newman model extensions such as full cell models that combine multiple p2D models with a 3D current collector and thermal models similarly do not include lateral diffusion. The solution to this challenge is to extend the Newman model to two-dimensional anode, cathode, and separator domains. The computational complexity can be reduced by using the rotational symmetry of the electrode disc in the coin cell. Figure 50 shows the cross-section of the cell from center to the outer edge as implemented in the COMSOL model. The dimensions of the electrode, separator, and electrolyte reservoir are adopted from the CR2032 coin cell format. The Newman model does not include a thermal model, since the heating of the coin cell under load is negligible. The model parametrization, equations and parameter set are described in the appendix A.1 to A.3.

Due to the complexity of LFP simulation, which requires a more sophisticated approach to model the LFP phase transition that is beyond the scope of the intended proof of principle, the simulation was only performed for graphite anodes. To access whether the experimentally observed utilization of the backside electrode can be reproduced qualitatively, the rate dependent discharge is modeled for a graphite double-coated electrode.

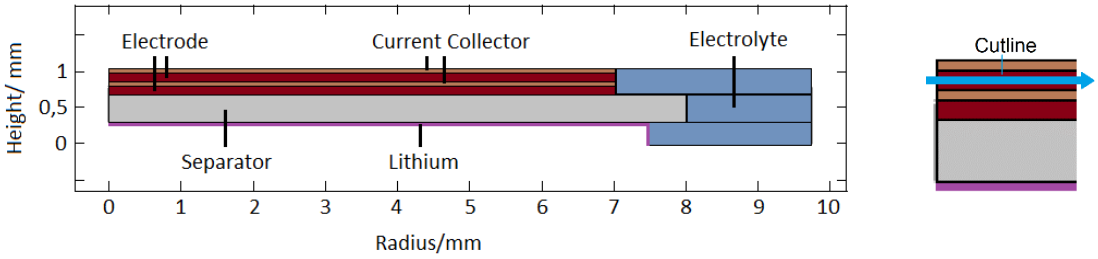

Figure 50 Coin cell domains as implemented in the COMSOL model. Zoom in with cutline for the export of the radii dependent concentration and potential distribution in the backside coating. Black lines in the electrolyte mark boundaries in the model but do not hinder the flow. Image reprinted from [158].

5.4 Experimental results

The backside coating broadly affects the coin cell performance for double-coated graphite as well as LFP electrodes. This includes the cell OCV, capacity, and relaxation processes. Mechanical removal of the backside can cause damage to the electrode but mitigates the unwanted backside effects.

5.4.1 Effect on OCV

Figure 51 shows OCV measurements for two double- and two single-coated samples. Table 12 shows the corresponding cell capacities and capacity changes. The measurement data reveals a greatly different cell capacity and open circuit voltage for single and double-coated samples which indicates a strong impact by the backside coating. The graphite samples exhibit the well-known voltage plateaus associated with two phase regimes. From 100 % to 50 % Lithiation the 80 mV plateau is associated with the LiC_{12} / LiC_6 regime, from 50 % to ≈30 % the 150 mV plateau is associated with the LiC_{12} / $LiC_{12\text{-liquid}}$ regime.

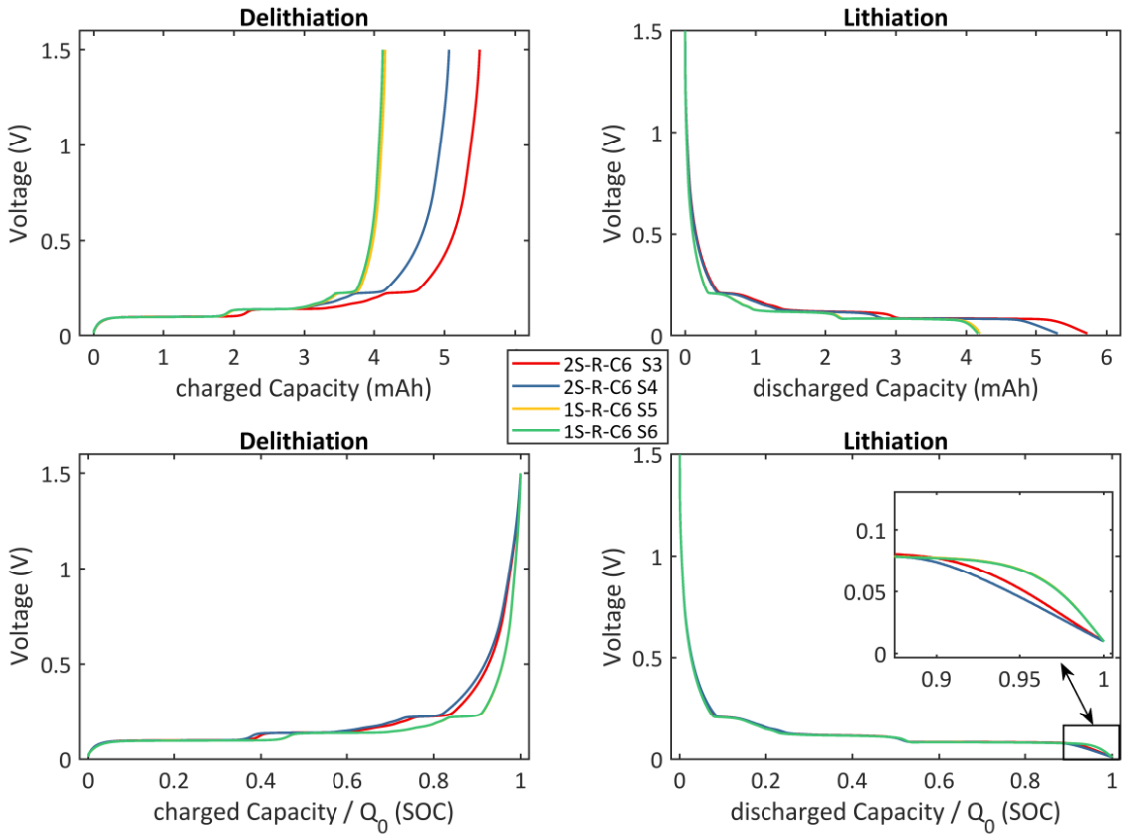

Figure 51 OCV vs. Li/Li^+ for double-coated (2S) and single-coated (1S) graphite samples for delithiation (left) and lithiation (right). In the upper graphs the cell voltage is depicted vs. the cell capacity, while in the lower graphs it is shown against the normalized capacity. Data from [158].

At lower lithiation states the voltage reaches a plateau at 220 mV before rising quickly to the end of measurement criterion of 1.5 V. In lithiation as well as delithiation the double-sided samples have an approximately 30 % larger capacity than the single-coated samples. The mass loading of back and frontside is identical and thus the 30 % capacity increase directly corresponds to a 30 % usage of the backside capacity. The samples do not show a difference in the height of the two-phase regime voltage plateaus in either delithiation or lithiation. Differences arise close to the fully delithiated state, where the double-coated sample shows a flatter voltage increase compared to the single-coated cells. This cannot be attributed only to the increase in cell capacity, since the differences remain for the normalized data. The differences are less visible for lithiation compared to delithiation. While the non-normalized plot shows a shift in the OCV due to different capacity, the normalized presentation shows

little difference except at the end of lithiation where the double-coated sample voltage falls off less quickly. This is due to the fact that at low lithiation high voltage gradients arise quickly for small lithiation differences between backside and frontside, while close to the fully lithiated state the voltage plateaus.

Similarly to the graphite anodes, the measurements of the LFP electrodes show a strong impact on capacity and open circuit voltage for double-coated samples. Figure 52 compares OCV measurements for two double and two single-coated samples. The corresponding capacity changes are listed in Table 12 along with the graphite results.

Table 12 Capacity of graphite and LFP single- and double-sided coin cell samples. Lithiation and delithiation at a rate of C/50. Data from [158].

		Single	Double	C_D/ C_S (%)
C_c (mAh)	Delithiation	4.14 ± 0.02	5.28 ± 0.22	128 ± 4
C_c (mAh)	Lithiation	4.12 ± 0.03	5.52 ± 0.21	132 ± 4
C_{LFP} (mAh)	Delithiation	3.64 ± 0.00	6.15 ± 0.10	169 ± 2
C_{LFP} (mAh)	lithiation	3.40 ± 0.01	5.38 ± 0.10	158 ± 2

The LFP electrodes shows a nearly perfectly flat OCV that falls and rises sharply close to maximum and minimum lithiation. This is attributed to an on/off – fully charged/ fully discharged – behavior of individual nm sized LFP particles which in combination with LFP single particle OCV function causes the overall flat characteristic [162]. The double-coated samples show a strong capacity increase in lithiation as well as delithiation compared to the single-coated electrodes. The $\sim 60\ \%$ increase is higher than the $\sim 30\ \%$ observed for the graphite electrodes. Similar to graphite, the capacity increase directly corresponds to a 60 % usage of the backside electrode.

The higher degree of backside utilization can be explained through the shape of the OCV and the greater electrode layer thickness. With the cell voltage independent from the degree of lithiation no differences in the utilization of backside and frontside arise due to potential gradients. The strongly utilized backside lowers the lithium concentration in the electrolyte encapsulated at the backside, but with a 114 µm layer thickness compared to 70 µm for graphite, the cross-section for electrolyte exchange between the backside and the reservoirs at the sides are 63 % larger which allows for a quicker exchange and thus lower overpotentials. At the close to fully lithiated or delithiated state where gradients can arise, the OCV is considerably less steep compared to single-coated samples. Similarly to graphite, this alters the shape of the OCV even for the normalized data. Compared to graphite the backside influence is generally greater and not limited to lithiation.

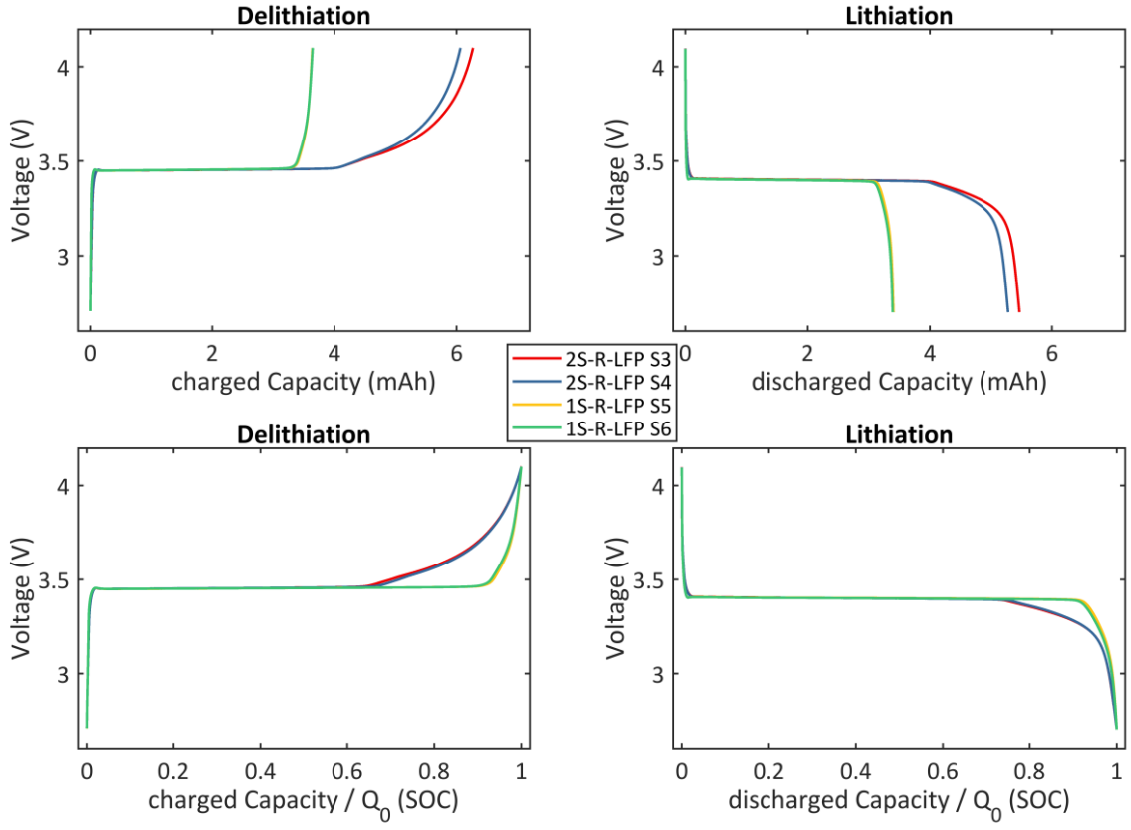

Figure 52 OCV vs. Li/Li$^+$ for double-coated (2S) and single-coated (1S) LFP samples for delithiation (left) and lithiation (right). In the upper graphs the cell voltage is depicted vs. the cell capacity, while in the lower graphs it is shown against the normalized capacity. Data from [158].

Backside SoC influence

The double-coated samples examined so far were made from Custom Cells electrode material and underwent the formation cycle described in section 5.2 before OCV measurements. Consequently, the backside coating was at an undefined SoC. Based on the observed capacity usage of 30 % the graphite backside remained mostly delithiated during the formation steps. In the following these results are compared to samples with a well-defined state of lithiation for the backside coating.

Figure 53 shows three samples with double-coated electrodes extracted from a pouch cell at 0 %, 50 % and 100 % full cell SoC, which corresponds to a fully delithiated, a half way lithiated, and a fully lithiated anode upon disassembly, with respect to the overall limitations in lithiation due to full cell balancing (degree of lithiation is never 100 % for anodes due to oversizing relative to cathode). Table 13 shows the coin cell capacities as well as the capacity increase with respect to the single-coated electrodes.

The samples show a capacity ranging from 4.6 mAh to 5.6 mAh in the lithiation and delithiation steps which is between 21 % and 41 % higher than the capacity of the reference single-coated electrodes. Similarly, all samples show the flattening of the OCV during the end of delithiation. Notably, the backside SoC causes an $\sim 50\ \mathrm{mV}$ offset for the 100 % SoC sample compared to 50 % and 0 % SoC sample. During delithiation this offset is positive. During lithiation the offset is negative. This is due to the charged center part of the electrode backside that influences the cell voltage, but is out of reach for quick lithium ion exchange because the exchange happens through the sides of the backside electrode.

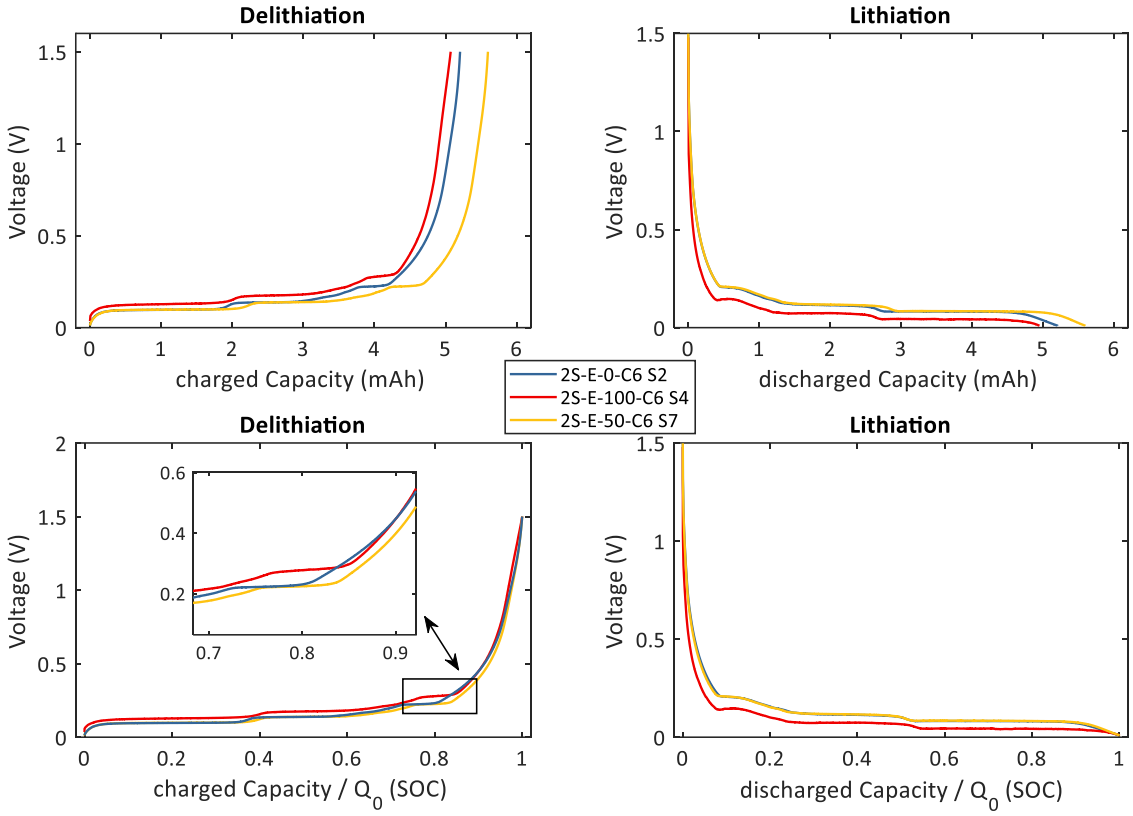

Figure 53 OCV vs. Li/Li^+ for double-coated graphite samples for delithiation (left) and lithiation (right). The electrodes were extracted from cells at a SoC of 0 %, 50 %, and 100 %. In the upper graphs the cell voltage is depicted vs. the cell capacity, while in the lower graphs it is shown against the normalized capacity. Data from [158].

The variation in cell capacity can be explained by the large spread of capacities observed for double-coated samples. An example is given with sample 2S-R-LFP S2 and 2S-R-LFP S4 in Figure 52. Figure 54 shows the OCV measurement of three double-coated LFP electrodes extracted at a full cell SoC of 0 %, 50 %, and 100 %. The corresponding degree of lithiation of the cathodes is fully lithiated, half way lithiated and fully delithiated, with respect to the full cell balancing. The capacity turnover in lithiation and delithiation for all samples ranges from 4.6 mAh and 5.3 mAh which is on average between 32 % and 47 % higher compared to the single electrode capacity. While the 50 % sample has the highest absolute capacity, all samples have nearly identical OCV curves in the normalized representation. This is due to the balancing of the full cell where also the 0 % full cell SoC sample can still be considerably lithiated to attain a similar OCV as for the 50 % and 100 % sample. This is not the case for the delithiation. Here, the 100 % SoC sample shows a sharper voltage increase than the 50 % and 0 % sample due to a fully depleted backside.

Table 13 Capacity of graphite and LFP double sided coin cell samples with 0 % SoC, 50 % SoC, and 100 % SoC backside lithiation. Data from [158].

		0 % SoC	50 % SoC	100 % SoC
C_c (mAh)	Delithiation	5.20	5.60	5.07
C_c (mAh)	Lithiation	5.21	5.60	4.95
%-Change		126	135	121
C_{LFP} (mAh)	Delithiation	4.90	5.31	4.60
C_{LFP} (mAh)	lithiation	4.65	5.02	4.69

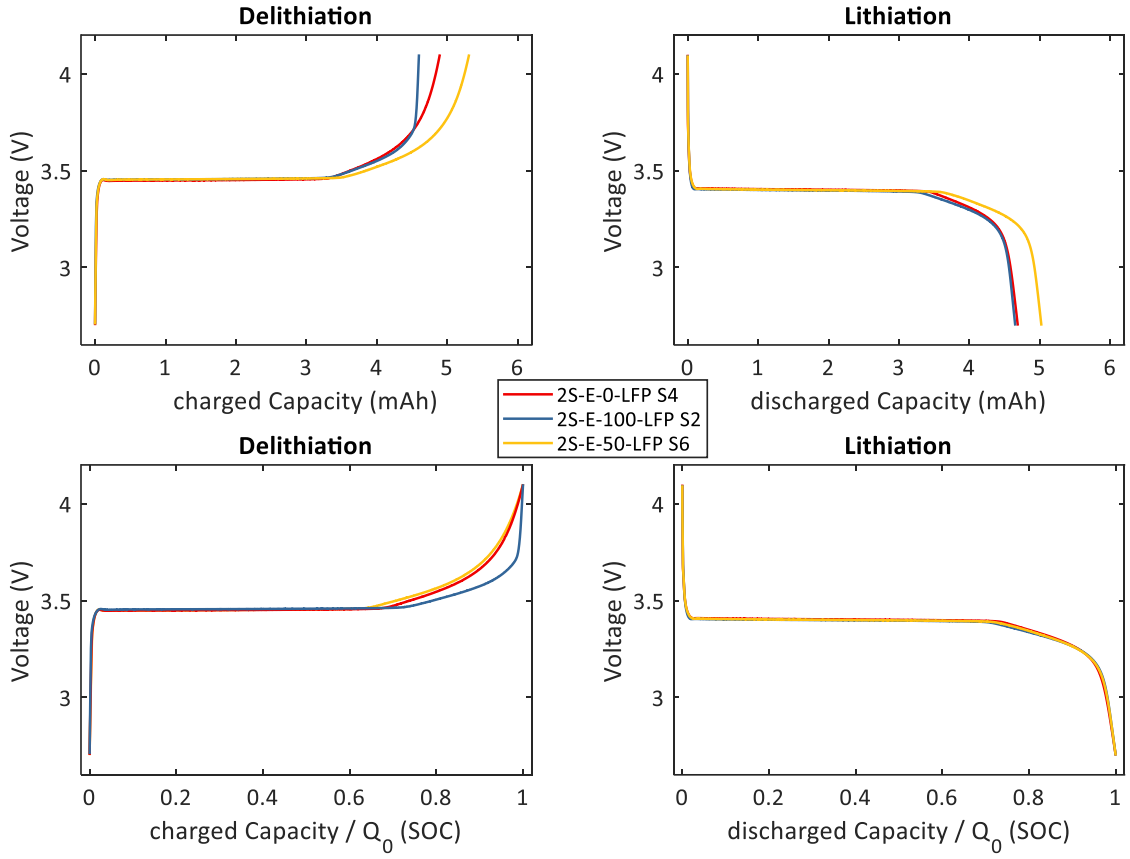

Figure 54 OCV vs. Li/Li$^+$ for double-coated LFP samples for delithiation (left) and lithiation (right). The electrodes were extracted from cells at a SoC of 0 %, 50 %, and 100 %. In the upper graphs the cell voltage is depicted vs. the cell capacity, while in the lower graphs it is shown against the normalized capacity. Data from [158].

The measurements do not show an overall offset of the OCV as observed for the 100 % SoC graphite sample. This is expected, given that the OCV of LFP is flat and thus largely independent from the initial degree of lithiation as adjusted through the full cell SoC. Additionally, as shown in Table 13, the part of the backside partaking in the charging and discharging procedures is larger than for graphite and thus will not remain at the initial state for several cycles.

Backside coating removal

The measurements presented so far showed a clear influence of the electrode backside onto the SoC dependent OCV. Can mechanical removal of the backside avoid the influence?

Of the initially six graphite samples for backside removal, three were destroyed in the process, most often due to tearing of the current collector. Also, three out of six LFP samples were destroyed in the process. For some samples, active material on the frontside was affected by the removal and partially rubbed off. Figure 55 shows a comparison of a graphite sample made from single-coated raw material (S1-R-C6), double-coated from raw material with backside removed (1S-R-BR) and extracted from a full cell with backside removed (1S-E-BR). The samples with removed backside show a capacity of 4.25 Ah which is slightly higher than the 4.14 Ah reference capacity of a single-coated electrode. A reason for this could be that the residual graphite was not fully removed. However, the capacity is expected to vary due to limited coin cell manufacturing precision. The normalized presentation shows nearly identical OCV curves with slight deviations at low states of lithiation (see inlet). While minimal, these differences could be explained by damage to the electrodes in the process of the backside removal that causes a local resistance increase or loss of active material.

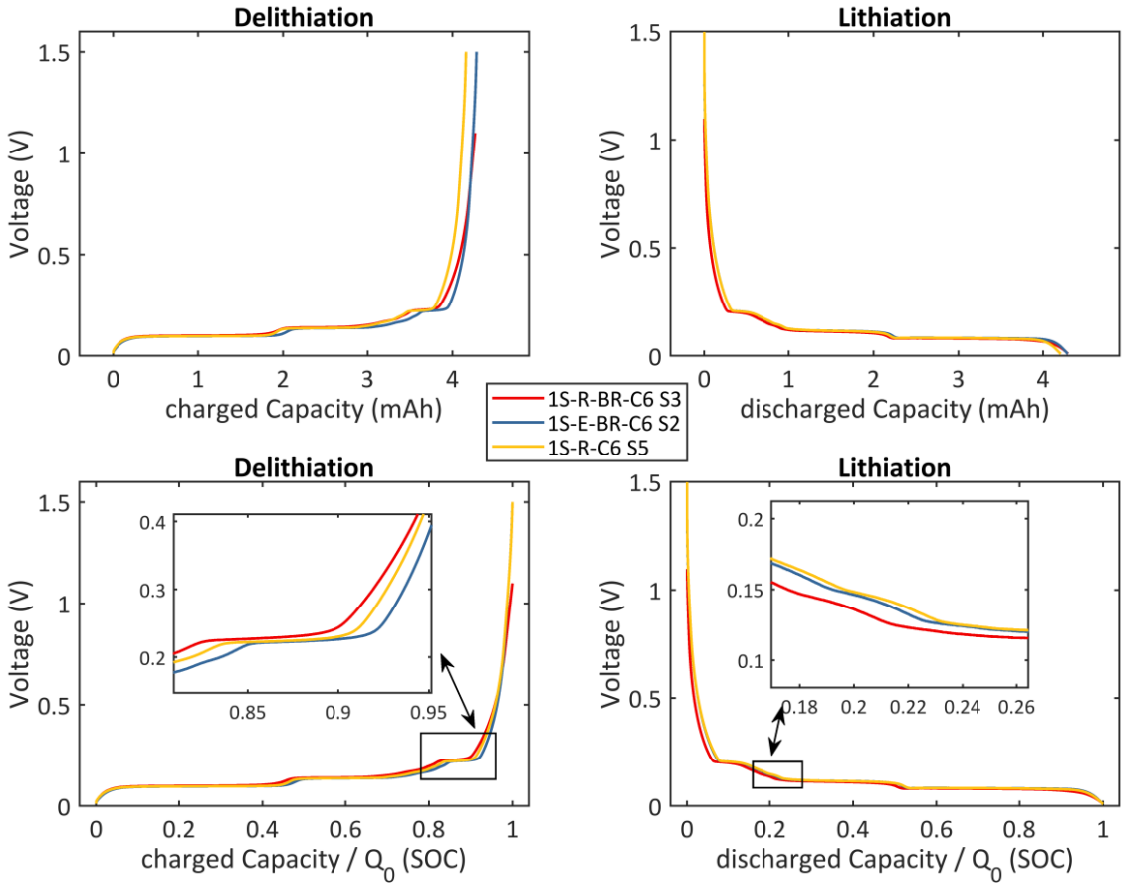

Figure 55 OCV vs. Li/Li$^+$ for single-coated graphite samples for delithiation (left) and lithiation (right). The electrodes are made from raw material (1S-R-C6), extracted from full cells (1S-E-BR), and from double-coated electrode material with backside removed (1S-R-BR). In the upper graphs the cell voltage is depicted vs. the cell capacity, while in the lower graphs it is shown against the normalized capacity. Data from [158].

Overall, the OCV curves of the samples are identical within the precision that could be achieved with the handmade coin cells in the laboratory. In conclusion, mechanical removal provides a workable solution to measure OCV from post mortem material unaltered from backside effects.

5.4.2 Effect on rated capacity

As the electrode backside participates in the lithiation and delithiation processes of the coin cell, it exchanges lithium with the electrolyte encapsulated in the porous backside electrode. For the Li$^+$ ions in this electrolyte segment the direct path to the metallic lithium reservoir is blocked by the current collector. Thus, Li$^+$ concentration gradients can only equalize by means of diffusion through the small electrode cross-section at the sides of the electrode (see the schematic in Figure 48). If these gradients remain, the increase in concentration overpotential prevents further lithiation or delithiation of the active material at the backside and thus overall limits the capacity contribution of the backside. OCV measurements at constant currents of C/50 or C/100 take 50 to 100 hours for a single lithiation or delithiation step. This provides a long-time span for this equalization process to occur and maximizes the contribution of the backside active material.

Making use of this limitation, can a reliable approximation of an OCV be measured with a double-coated electrode by using a higher constant current rate of C/10 instead of C/50 or C/100? Does a check up procedure at the common C-rate of 0.5 C or 1 C yield identical capacities for single and double-coated electrodes? To investigate this, the rate capability tests of single-coated and double-coated graphite and LFP samples in the C-Rate range of C/10 up to 2C (Figure 56) were conducted.

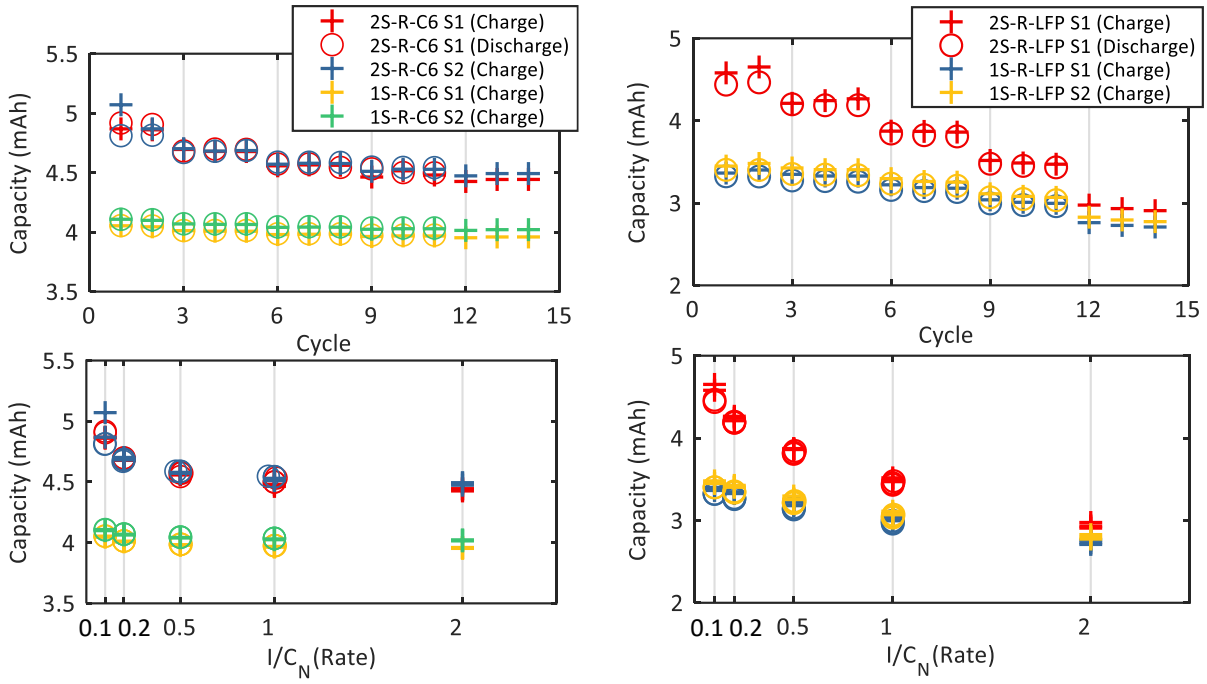

Figure 56 Rated capacity for single-coated and double-coated graphite (left) and LFP (right) samples from 0.1C up to 2C. The upper graph shows capacity vs. cycle number. The lower graph depicts capacity vs. C-rate. Data from [158].

Table 14 compares the capacity data averaged over all cycles per rate and samples. The single-coated graphite samples show a nearly constant capacity of 4.0 Ah from C/10 up 2C, which is expected given the generally good rate capability of graphite anodes. The double-coated samples show a consistently higher capacity for all rates. The capacity of the double-sided electrodes is 120 % of the capacity of the single electrode reference at C/10, but drops consistently with each rate increase. Yet, at 2C the backside still contributes 12 % extra capacity to the measurement. Similarly, the double sided LFP sample shows consistently higher capacities than the single sided reference samples. At C/10 the double-sided sample provides 34 % more capacity than the reference sample. This is higher than the backside contribution for the graphite sample and is consistent with the higher contribution seen in the OCV measurements. At higher rates the backside contribution falls off more rapidly than for graphite. This can be attributed to the higher electrical resistance due to backside coating. The electrical conductivity of carbon coated LFP electrode is of the order of 1 S/cm [163] compared to 1000 S/cm of a graphite electrode [29]. The increased overpotentials due to additional ohmic resistance limit the withdrawable capacity in the rate capability test.

Table 14 Rated capacity data for single and double-coated graphite and LFP samples. Data from [158].

	0.1C	0.2C	0.5C	1C	2C
$C_{\mathrm{C-1s}}$ (mAh)	4.08	4.04	4.01	4.00	3.99
$C_{\mathrm{C-2s}}$ (mAh)	4.89	4.67	4.57	4.52	4.46
$C_{\mathrm{C-2s}}/\ C_{\mathrm{C-1s}}$ (%)	120	116	114	113	112
$C_{\mathrm{LFP-1s}}$ (mAh)	3.39	3.34	3.21	3.03	2.76
$C_{\mathrm{LFP-1s}}$ (mAh)	4.53	4.22	3.85	3.47	2.94
$C_{\mathrm{LFP-2s}}/\ C_{\mathrm{LFP-1s}}$ (%)	134	126	119	115	106

In conclusion, the contribution of the backside electrode is not limited to slow C/50 or C/100 OCV measurements. A slight increase to C/20 or C/10 does not circumvent the capacity increase and corresponding change in OCV curve. At higher rates the backside contribution is reduced, but it is still noticeable with ≈15 % at 1C. As a result of this, the correct capacity of a coin cell made with a single-coated electrode cannot be approximated with a medium rate measurement of a coin cell made with a double-sided electrode.

5.4.3 Effect on voltage relaxation

The OCV of the electrode backside and frontside are different, if the SoC of the electrode sides differ. Therefore, it is expected that the backside will alter the cell voltage and voltage relaxation behavior. To clarify this, the relaxation process CC lithiation and delithiation was measured. Figure 57 shows the voltage relaxation of double (2S-R-C6) and single-coated (1S-R-C6) graphite cells after a 1C charging process (graphite delithiation) up to a 1.5 V cut off voltage. After an exponential decrease the cell voltage stabilizes after ≈20 hours. The three double-coated samples reach a resting potential of $212 \pm 2\ \mathrm{mV}$ while the single-coated samples rest at a higher voltage of $490 \pm 40\ \mathrm{mV}$. The single-coated samples show an 80 mV spread, however, this does not indicate a major difference in the degree of lithiation, considering the steep OCV for low states of lithiation. The voltage difference between double and single-coated samples is about 300 mV. If one was judging the cell capacity from a comparison with the OCV (Figure 55), one would conclude that the remaining graphite lithiation is about 5 % for the single-coated cells and 28 % for the double-coated cells. This shows that the half-cell electrode SoC would be significantly misjudged if the backside coating influence was disregarded. Also, the interpretation of 28 % extractable capacity is false, since the electrode frontside is fully discharged, which caused the cell to reach the cut of voltage. Since the electrolyte at the backside only connects to the reservoir of the whole cell only at the sides of the backside electrode, it is highly likely, that the SoC is inhomogeneous with a highly lithiated center region that cannot be fully delithiated even at a low rate of C/50 as described in section 5.4.1.

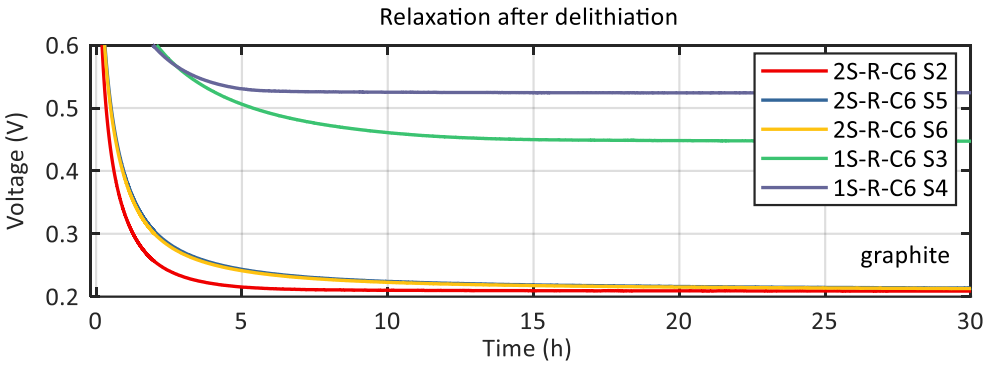

Figure 57 Voltage relaxation of graphite samples after CC delithiation at 1C with double (2S) and single-coated (N) electrodes. Data from [158].

Figure 58 shows the voltage relaxation of double (2S-R-LFP) and single-coated (1S-R-LFP) LFP cells after a 1C discharging process (LFP lithiation) down to a 3.0 V cut off voltage. At the end of discharge the half-cells regain some of their voltage as temporary overpotentials during discharge lapse. The cell voltage reaches a maximum at about 1 hour after discharge and then continuously declines slowly for all samples. The relaxation process is not completed at the end of the 30 hour measurement period. The double-coated cells show a 5 mV smaller maximum and a lower resting potential at the end of the measurement. Overall, the differences between double-coated and single-coated cells are small and less than 10 mV. The effect on the resting potential by the backside is limited by the flat OCV of LFP.

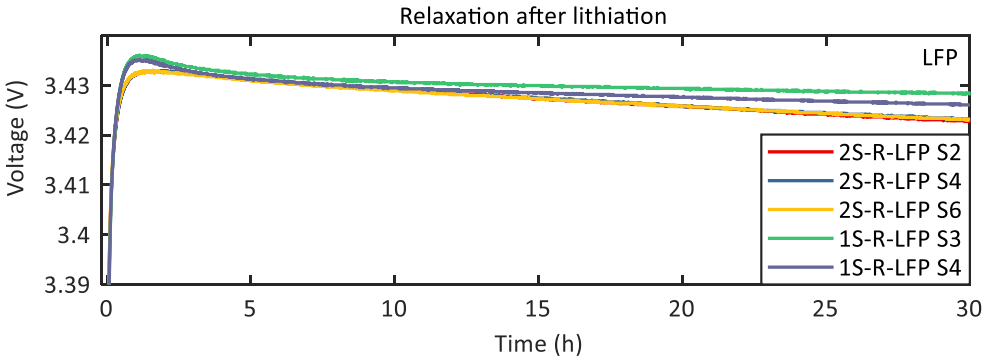

Figure 58 Voltage relaxation of LFP samples after CC delithiation with double- (2S-R-LFP) and single-coated (1S-R-LFP) electrodes. Data from [158].

Constant Current Constant Voltage

Figure 59 shows the voltage relaxation after 1C-CC delithiation of four graphite electrodes extracted at full cell SoC of 100 % and 50 % with 2 samples at each initial state. One of each sample is subjected to an additional constant voltage phase ($I < 0.1$C) to test whether the electrode backside can be depleted and an equal resting potential can be achieved. After 30 hours the 100 % SoC samples show a cell voltage of 320 ± 13 mV the 50 % SoC samples show 219 ± 6 mV. The samples with additional constant voltage discharge show a slightly higher voltage since they were further charged. Overall, the effect of the additional CV phase is marginal compared to the differences caused by the initial lithiation state of the backside. In conclusion, the constant voltage phase is not sufficient to equalize the lithiation of the electrode backsides.

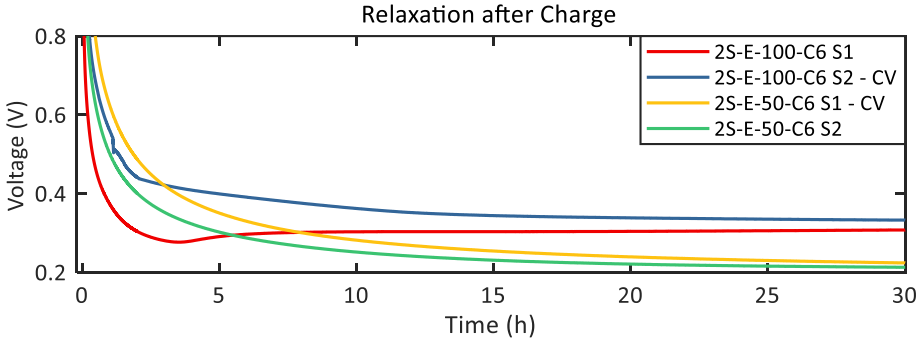

Figure 59 Voltage relaxation after CC delithiation for double-coated graphite samples at 50 % and 100 % backside SoC. The samples with additional constant voltage phase are marked with CV. Data from [158].

In contrast to the graphite samples, an additional constant voltage phase does influence the LFP resting potential more strongly than the state of lithiation of the electrode backside. Figure 60 shows the voltage relaxation after 1C-CC lithiation of four LFP electrodes extracted at full cell SoC of 100 % and 50 % with 2 samples for each initial state. One of each sample is subjected to an additional constant voltage phase ($I > -0.1$ C). The CC only samples overall show a quicker voltage relaxation and a higher resting potential than the CC-CV samples. After 1 hour the CV samples show a 60 mV lower cell voltage. After 30 hours the relaxation process is not concluded and the CC-CV samples remain at a 10 mV lower resting potential. While the 100 % and the 50 % CC samples show a slightly higher voltage than their 100 % and 50 % CC-CV counterpart, the effect of the backside SoC is much less than off the additional CV phase. This is observation is consistent with the flat OCV of LFP. Unless the backside electrode is close to be fully lithiated or delithiated a shift in the state of lithiation will not alter the cell potential.

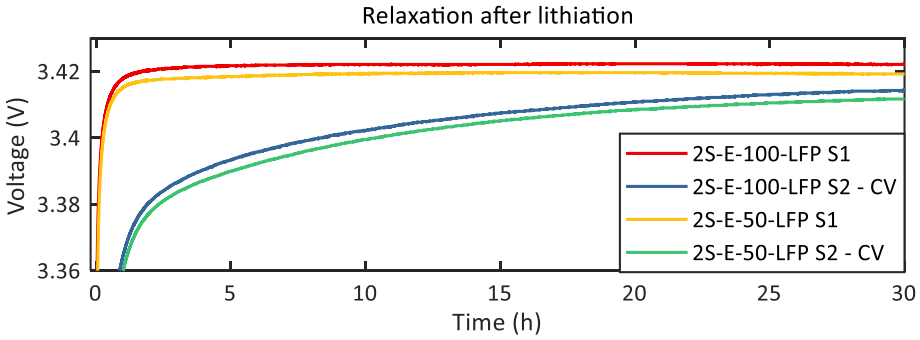

Figure 60 Voltage relaxation after CC delithiation for double-coated LFP samples with 50 % and 100 % backside SoC. The samples with additional constant voltage phase are marked with CV. Data from [158].

5.5 Modeling results

The 2D-p2D Newman model reproduces the effects on discharge voltage and cell capacity of the backside coating qualitatively.

5.5.1 OCV and rated capacity

Figure 61 shows the simulation of a C/50 discharge of a double-sided graphite electrode. The experimental data is also from a double-sided electrode. Both models, the classical Newman model and the 2D no backside model reproduce the OCV well because the overpotentials are negligible at very low C-rates and the equilibrium potential of the measurement is tabled in the model. The double-sided models do not reproduce the OCV equally well. The experimental data and simulation results do not match well, but the effect of a flatter voltage drop at full lithiation is observed for the 2S electrodes.

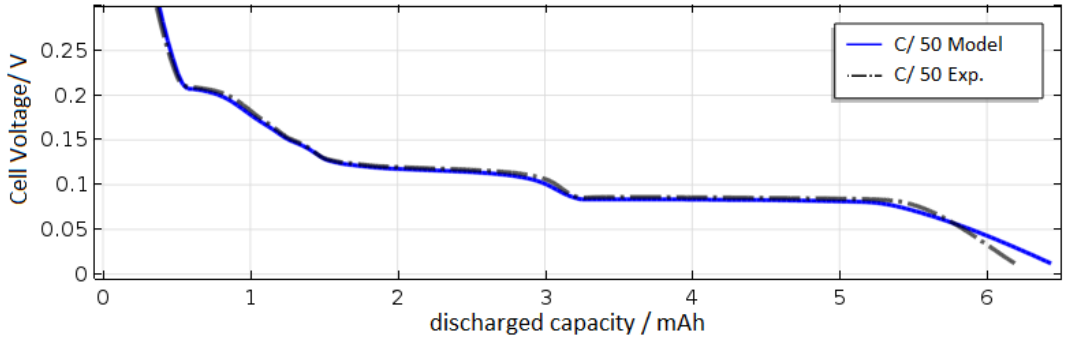

Figure 61 Graphite OCV vs. Li/Li$^+$ measured and modeled at C/50. The electrochemical model includes the backside electrode. Image reprinted from [158].

Figure 62 shows cell voltage vs. discharged capacity for discharge (lithiation) for C/5, C/2 and 1C for the modeling data as well as measurements with a double-sided sample. The experimental data shows a higher capacity loss and voltage drop at higher rates compared to the single sided electrode. The backside coating causes additional ohmic resistance. The 2S-model reproduces this effect and shows a higher capacity loss at higher rates.

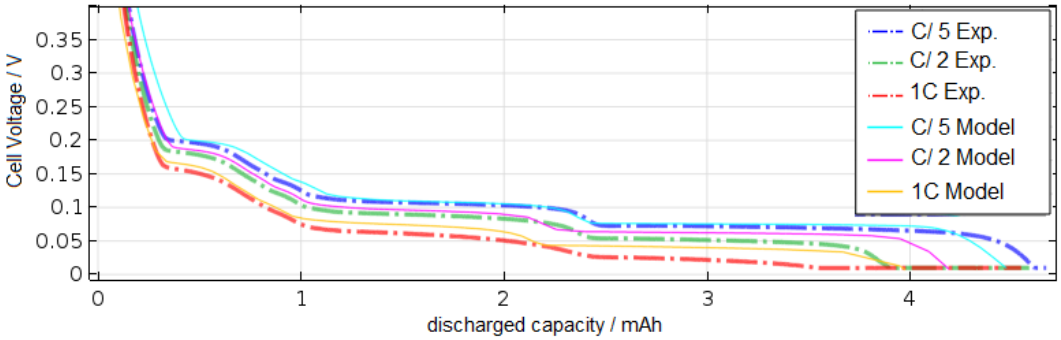

Figure 62 Graphite discharge voltage at C/5, C/2 and 1C measured and modeled with the electrochemical model including a backside electrode. Image reprinted from [158].

5.5.2 Lithium distribution

The experimental data shows that the active material at the backside of the electrode is utilized during lithiation and delithiation processes in the half-cells. From this the question arises whether the backside is homogeneously or inhomogeneously utilized, and how the resulting SoC distribution looks like.

To investigate this, the lithium concentration in the electrolyte, the lithium concentration in the active material and the capacity contribution of the backside are looked at in detail. Figure 63 shows the lithium concentration in the electrolyte for the cross-section view of the half-cell during a 1C discharge. Initially the cell is in a perfectly homogeneous state and the Li-concentration is 1 mol/liter in all segments. Shortly after begin of the half-cell discharge, the concentration in the frontside part of the electrode and the separator in close proximity drops to ca. 90 % of the initial concentration as lithium intercalates in the graphite. However, the electrolyte concentration drops more strongly in the backside electrode to ca. 50 - 85 %. At 70 minutes, shortly after end of discharge, the lithium concentration at the electrode frontside is only slightly lower at about 85 % of the initial concentration due to constant replenishing with the large electrolyte reservoirs in the separator and edge of the coin cell. The backside electrode drops to ca. 30 - 40 % of the initial concentration.

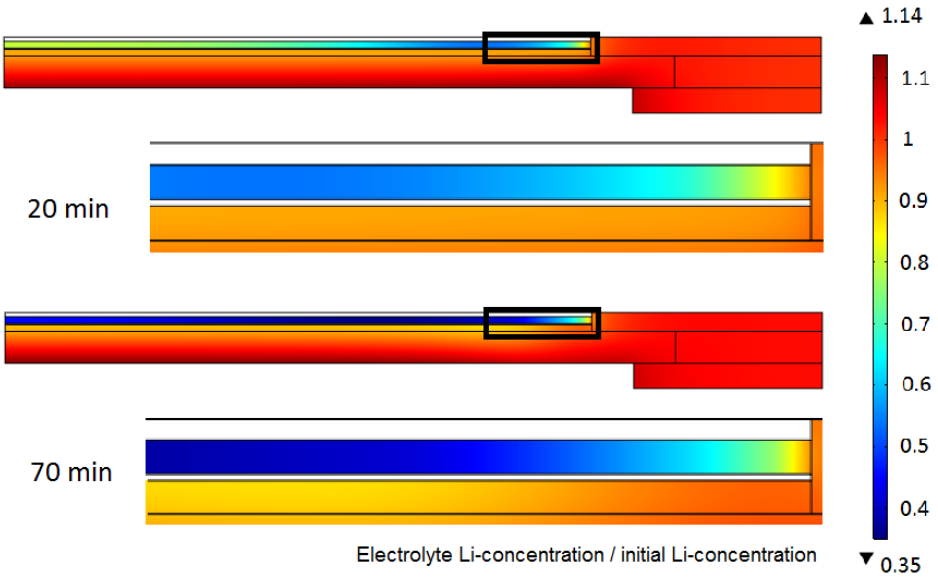

Figure 63 Cross-section view of the Lithium concentration in the electrolyte at two different points in time during a 1C discharge. The black frame marks the location of the close up where the backside coating is in contact to the electrolyte reservoir. Image reprinted from [158]. The schematic of the COMSOL model is shown in Figure 50.

At both time steps the model shows a concentration gradient inwards with higher lithium concentration close to the edges of the electrode that have contact with the electrolyte reservoir. Figure 64 shows the electrolyte concentration along the cutline at the middle position of the backside electrode from the center (0 µm) to the edge (7000 µm). At 1C the electrolyte concentration locally drops below 90 % more quickly than at C/5 discharge where the concentration remains above 9 % at all points. But only 130 minutes in the C/5 discharge the electrolyte concentration at the electrode center drops to 30 %, below the concentration levels seen after the full 1C discharge. The concentration levels at the edge close to the reservoir are higher than for the 1C discharge, because there is more time for diffusion to diminish the concentration gradient with the electrolyte reservoir. The concentration at the backside is lower for values for C/5 compared to 1C due to a higher capacity contribution of the backside.

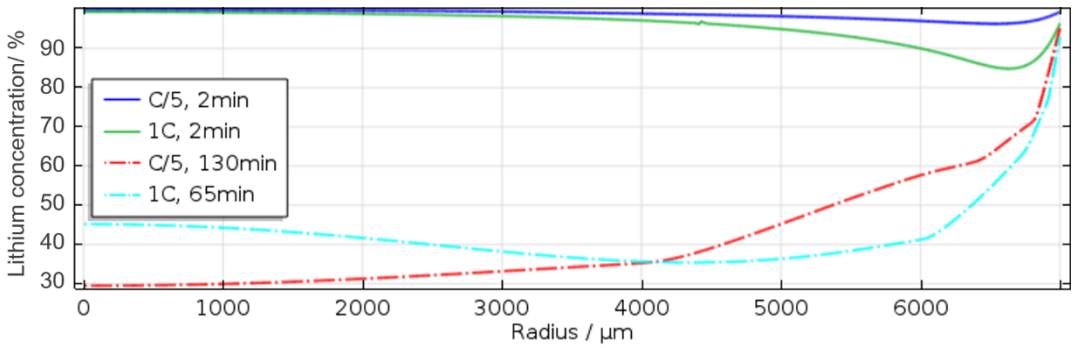

Figure 64 Lithium concentration in the electrolyte across the backside of a double-coated graphite electrode from the center (0 µm) to the outer electrode rim (7000 µm) during lithiation. Image reprinted from [158].

Figure 65 shows the average lithium concentration of the graphite particles from center to edge in the backside electrode. The end of discharge is shown for three discharge rates C/50, C/5, and 1C. At 1C the backside shows strong lithiation of up to 80 % at the outer region r ≈ 7000 µm. The degree of lithiation falls off sharply to about 6 % of lithiation at r ≈ 6000 µm. Towards the center the degree of lithiation falls off further to 3 %. At C/5 the lithium concentration is 6 % and thus twice as high as for the 1C discharge. The high degrees of lithiation seen at the outermost part fall of less sharply than for the 1C discharge causing larger parts of the backside electrode to be higher lithiated with for example 10 % of lithiation at 4200 µm radius compared to 3 % for 1C. At C/50 much higher degrees of lithiation are achieved in the center (23 %) and the outer parts (≈40 %).

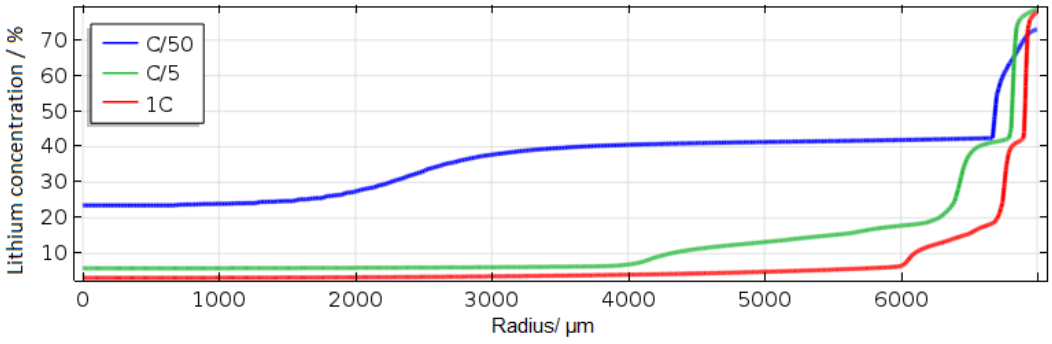

Figure 65 Lithium concentration across the backside of a double-coated graphite electrode from the center (0 µm) to the outer electrode rim (7000 µm). The graph depicts the end of discharge at C/50 (blue), C/5 (green) and 1C (red) discharge rate. Image reprinted from [158].

By comparing the local lithium concentration in the electrolyte active material, we find, that the lithium concentration drop in the electrolyte limits the intercalation into graphite in the backside electrode. The longer the discharge phase, the more lithium can diffuse into the backside electrolyte from the

large electrolyte reservoirs in the separator and side areas of the coin cell. The more lithium is present in the electrolyte the lower the concentration overpotentials and the higher the utilization of the backside electrode. Table 15 compares the experimentally determined backside utilization with the results of the 2D-p2D model. Experiment and model are in good agreement in the overall trend of increasing backside utilization with lower C-rate. While excellent agreement is achieved at 1C, the model overestimates backside utilization by 6 % for the C/5 measurement and by 13 % for the C/50 measurement. While an overall good simulation of the rated capacity was achieved with the best fit parameter set, some deviations in the discharged capacity remain that limit the overall precision achievable with this model. A possible explanation is an underestimation of the electrode tortuosity, as is a common problem in Newman model simulation, since the effect of inactive components (binder, carbon black) on electrode tortuosity is hard to determine experimentally [41, 42]. A higher than anticipated tortuosity could limit the diffusion process towards the center and thus reduce the degree of lithiation especially in long term measurements.

Table 15 Simulation and measurement of graphite backside electrode utilization. Comparison of the capacity of cells with backside electrodes (C_{2s}) and without backside electrode (C_{1s}) as well as the simulated capacity contribution of the backside (C_{back}). Data from [158].

	C/50	C/5	C/1
Experimental C_{2s}/ C_{1s} (%)	138	118	113
Simulation C_{back} used (%)	51	24	13

5.6 Post mortem

A double-coated graphite electrode vs. Li/ Li^+ half-cell was opened after a 1C charge (delithiation of the graphite). Figure 66 shows the frontside and backside of the electrode. While the frontside is homogeneously grey indicating a delithiated state, the backside shows a large reddish colored partially lithiated center region (white arrow ≈ 6 mm) and an approx. 0.5 mm broad transition area with a strong lithiation gradient and an approx. 0.5 mm delithiated grey area. The radially inward going lithiation gradient observed here is in good qualitative agreement with the backside electrode simulation.

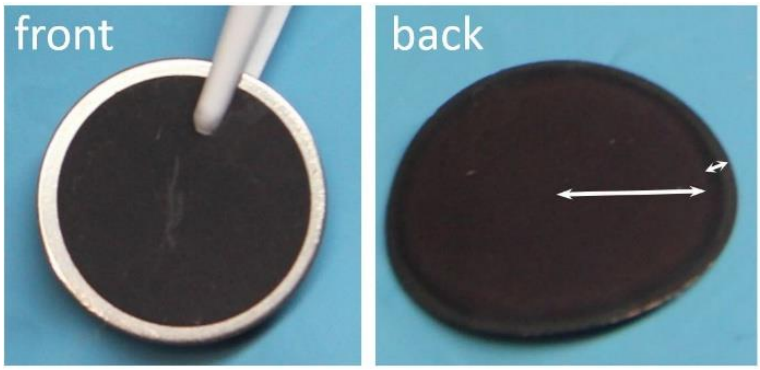

Figure 66 Front and backside of a double-coated graphite electrode after a 1C charge (delithiation). The frontside is homogeneously grey. Reddish center region of the backside (white arrow ≈ 6 mm). Lithiation gradient at the electrode rim (small arrow, ≈ 1 mm). In the image of the front, the electrode is pinched against a white glass fiber separator sheet. Glovebox operation Jörn Wilhelm. Image taken by K. Wachutka. Image reprinted from [158].

5.7 Summary and conclusion

The measurements show that the backside coating clearly affects the coin cell capacities as well as discharge voltage profiles. The effect is present in graphite electrodes as well as in LFP electrodes. Slow measurements to determine the equilibration potential for *dV/ dQ* or to determine the maximum capacity of the cell are most strongly influenced. The backside contributes up to 30 % additional capacity for graphite and up to 70 % for LFP. The different state of lithiation of the backside causes the OCV to flatten where the material shows strong lithiation dependent changes in the equilibrium potential, for example at low lithiation states of graphite. This effect cannot be removed by rescaling of the OCV measurement. The utilization of the backside is not limited to low rates such as C/50 or C/100. Rated capacity tests show consistently higher capacities for the double-coated electrodes with 12 % additional capacity for graphite and 6 % additional capacity for LFP even at 2C discharge. Relaxation experiments find that the time evolution of cell voltage during rest as well as the resting potential depend on the state of SoC of the backside coating. Efforts to mitigate this effect by applying an additional CV phase to fully deplete the backside before resting were unsuccessful.

The utilization of a graphite backside electrode was modeled qualitatively and, with limitations, quantitatively with a 2D-extension of a classical Newman model. While the front electrode is connected to large electrolyte reservoirs and changes its lithium concentration only moderately during lithiation, the lithium concentration of the electrolyte in the pores of the backside electrode changes drastically. A strong lithium concentration gradient builds towards the edges of the electrode where it is in contact to the electrolyte reservoir. Since the lithium concentration determines the local potential and thus whether intercalation is favorable, this gradient causes a mirrored gradient in the lithiation of the backside active material. The simulation shows that the backside is not utilized homogeneously but rather from the edge close to the electrolyte reservoir towards the center of the electrode. This lithiation gradient was observed in the post mortem investigation of a double-coated electrode.

The results show that it is not possible to determine correct capacities or precise OCVs with backside electrodes present, even at higher rates. The removal of the backside is necessary for precise measurements. Samples with mechanically removed backsides showed identical results with single sided electrodes. However, some loss of material due to damage in the process of removal needs to be considered. The difficulty of removal and likelihood of damage to the current collector depends on the adhesion of the electrode and thus on manufacturing details, such as slurry solvent, binder composition, and calendering parameters. They cannot be generalized from the CustomCells electrodes used for this experiment. Mechanical removal, in contrast to removal via use of solvents such as water, can be conducted in inert gas atmosphere in a glovebox, which is a great advantage for the work with post mortem electrodes that are partially lithiated.

Electrode areas without a cathode counterpart but connected to the electrolyte reservoir may take part in the lithiation and delithiation processes in the cell. This includes anode overhang areas in full cells which are investigated in the following section.

6 Lithiation of anode overhang areas

The previous chapter has shown that electrode sections without counterpart influence the capacity of laboratory cells made from electrodes harvested from commercial cells. In this chapter, the investigation is extended to overhang areas of commercial cylindrical cells. The graphite anode electrodes are analyzed with local X-ray diffraction, high precision coulometry, and post mortem color analysis to assess the impact on capacity measurements and SoH determination due to diffusion of lithium into and out of the overhang area during calendar aging of the cells.

Parts of this chapter have previously been published in the Journal of Power Sources under the title *Cycling capacity recovery effect: A coulombic efficiency and post mortem study* [138].

6.1 Overhang areas in literature

The diffusion into and out of electrode overhang areas was first noticed during high precision aging studies. Two types of studies form the basis for aging experiments: calendar aging experiments where batteries are stored at various conditions for several months or years [5–9], and cycling studies where batteries are repeatedly charged and discharged [10–12], often replicating real use scenarios [13]. These experiments rely on precise capacity measurements to correctly distinguish between irreversible effects, such as loss of cyclable lithium, and reversible effects, such as temperature dependent rate capability. New ultra-high precision coulombic efficiency experiments may reduce the need for costly long-term measurements through early detection of side reactions and better predictability of battery lifetime [14, 15]. The changes in CE due to degradation processes through parasitic reactions are very small. Thus, CE studies of these processes require precisely set currents, high precision voltage measurements as well as strictly controlled sample environments [16].

The high sensitivity of these measurements under controlled sample conditions led to the discovery of a surprising reversible capacity effect. Studies found *anomalous transient CEs* (Gyenes et al.) with $CE > 1$ in high precision cycling experiments after storage [17, 18]. This behavior was linked to anode *overhang*, acting as a lithium-ion source or sink depending on the preceding conditioning [18]. The term anode overhang describes areas of the anode active material that do not have a cathode counterpart. The lack of a counter electrode results from the negative electrode in a lithium-ion cell being built slightly larger than the positive electrode. This is a common design feature to assure 100 % cathode-anode overlap and to avoid lithium plating at the border area of the graphite anode [19]. The analysis of a 220 mAh wound pouch bag cells with 1 mm side overhangs showed a lithiation of the overhang regions after high SoC storage. Previous studies determined that the storage SoC affected the CE for up to 1000 h of subsequent cycling [18]. Reversible and SoC-depending capacity increase was also observed by Lewerenz et al., who performed calendar and cyclic aging experiments with 8 Ah cylindrical cells at elevated temperatures [20]. They also attributed the effect to anode overhang areas.

6.1.1 Objective of overhang investigation

To study the effects of large overhang areas in detail, cylindrical lithium-ion cells which feature wide overhang areas of 2-6 cm in addition to smaller side overhang areas of 1.5 mm were examined. These areas without cathode counterpart are located at the innermost and outermost winding of the jelly roll (Figure 67 b)). They are ionically connected to the lithium electrolyte reservoir. Given the slow lithium diffusion processes in batteries – can these areas be lithiated and do they influence CE and capacity measurements in commercial cells? To investigate this, CE and post mortem analyses of commercial cylindrical cells after long term storage at SoCs ranging from 0 % to 100 % were conducted.

The post mortem analysis consists of a qualitative assessment of the overhang area through observation of color changes complemented by ex situ XRD for quantitative local information.

6.2 Design of experiment

The commercial $LiFePO_4$|graphite battery cells used in the experiments are of the type APR18650M1A made by the manufacturer A123. The graphite anode of this cylindrical cell type battery exhibits large overhang regions and excellent electrode stability, which aids sample preparation after battery disassembly. Further battery properties are listed in Table 16.

Table 16 Battery properties. [138]

Manufacturer	A123	Active material	Graphite| $LiFePO_4$
Model	APR18650M1A	Max./ min. voltage	3.6 V/ 2.0 V
Nominal capacity	1.1 Ah	Max. cont. current	+4 A/ -30 A
Mass	39 g	Areal capacity	1.4 mAh cm^{-2}
Anode coated area	2 x 76.5 cm x 5.8 cm	Cathode coated area	2 x 71.4 cm x 5.5 cm

6.2.1 Electrode geometry

A schematic of the electrode geometry is shown in Figure 67. The anode width is 58 mm and cathode width is 55 mm. The anode overhang is thus 1.5 mm at each side if the electrodes are ideally positioned. The cathode is considerably shorter (71.4 cm) than the anode (76.5 cm). Both anode and the cathode, are fully double-sided coated. The excess in length of the anode leads to overhang areas at the outermost and innermost part of the jelly roll as depicted in Figure 67 a) and b). The two largest overhang areas consist of a 2.0 x 5.8 cm^2 inactive region at the inner end and 6 x 5.8 cm^2 at the outer end of the anode coil. These overhang areas represent 5.2 % of the total anode area. The slim overhang area 68.5 x 0.3 cm^2 corresponds to 4.6 %. Together they represent about 10 % of the total anode area. The length of the cathode covered area marked in Figure 67 for the front (73.5 cm) and back (69.5 cm) is different from each other and from the length of the cathode (71.4 cm). This is due to the spiral winding of the electrodes in the jelly roll. The anode and the cathode are each connected by a single tab, centered at the electrode in close proximity. The tab area is about 1 cm^2 and the opposing electrode at this position does not have an active material counterpart similar to the overhang regions.

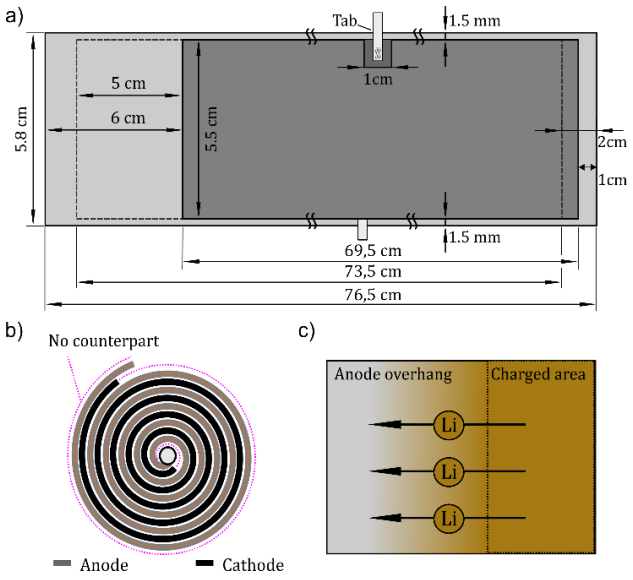

Figure 67 a) Schematic layout of the anode electrode area of sample cells with cathode counterpart (dark grey) and without cathode counterpart (light grey). The dashed lines show the cathode covered area on the flipside of the electrode. b) Schematic of a cylindrical cell's jelly roll consisting of anode, cathode, and separator (not shown). The overhang areas are highlighted (pink). c) Schematic of the lithium diffusion process from a charged area (golden) to an uncharged overhang area (grey). [138]

6.2.2 Calendar aging

As part of a calendar aging study [5], 16 batteries were stored at 40 °C for 20 months at different SoCs. The SoC range examined in the experiment covers 0 to 100 % SoC in 10 % steps with additional steps at 5 %, 45 %, 55 %, 65 %, and 95 % for higher resolution. The SoC is defined with respect to the actual cell capacity C_{actual} (section 4.1.2). To assess the SoH, the batteries underwent a periodic check up procedure to determine actual capacity, to perform DVA and to identify changes in the battery resistance. The check up procedure was carried out at 25 °C every 2-4 months with a higher frequency of tests at the beginning of the storage experiment. For a detailed description of the calendar aging setup and measurements, the reader is referred to [5]. Additionally, two batteries stored at 50 % SoC and 25 °C for 20 months were included to study lithiation into overhang areas at room temperature. An additional battery was investigated as reference for the balancing measurement of a fully charged graphite electrode. For this purpose, the battery was charged to 100 % SoC using a constant current CCCV procedure (3.6 V, 100 mA, $I < 0.01C$).

Table 17 Battery aging data. Capacity loss and resistance increase during 20 months storage at temperature $T_{storage}$. The capacity loss $\Delta C_{initial\text{-}last}$ is given as difference between the first check up $C_{initial}$ and last check up C_{last} after 16.3 month of storage. The battery resistance is measured at 1 kHz, a temperature of 25 °C and a SoC of 50 % during the check up procedure. R_{last}/ $R_{initial}$ describes the resistance increase between first and last check up. C_{actual} is the capacity the samples are stored at after the last check up. SoC_{actual} is the corresponding state of charge with reference to the current capacity, $SoC_{initial}$ with reference to the initial capacity (section 4.1.2). [138]

Sample	$C_{initial}$	C_{last}	$\Delta C_{inil\text{-}last}$	$R_{initial}$	R_{last}	R_{last}/ $R_{initial}$	$SoC_{initial}$	SoC_{actual}	C_{actual}	$T_{storage}$
Id	Ah	Ah	Ah	mΩ	mΩ		%	%	Ah	°C
S00	1.056	1.018	0.038	15.149	17.223	1.14	0	0	0.000	40
S05	1.065	1.002	0.063	15.387	16.973	1.10	5	5	0.050	40
S10	1.068	0.991	0.077	15.347	17.954	1.17	9	10	0.099	40
S20	1.061	0.972	0.089	15.471	18.229	1.18	18	20	0.194	40
S30	1.066	0.969	0.097	15.131	17.521	1.16	27	30	0.291	40
S40	1.073	0.963	0.110	15.210	17.521	1.15	36	40	0.385	40
S45	1.053	0.940	0.113	15.040	17.909	1.19	40	45	0.423	40
S50	1.067	0.961	0.106	15.235	18.216	1.20	45	50	0.480	40
S55	1.068	0.956	0.112	15.252	17.891	1.17	49	55	0.526	40
S60	1.059	0.949	0.110	14.823	17.477	1.18	54	60	0.569	40
S65	1.065	0.955	0.110	15.482	17.868	1.15	58	65	0.621	40
S70	1.055	0.940	0.115	15.242	18.150	1.19	62	70	0.658	40
S80	1.064	0.928	0.136	15.781	18.819	1.19	70	80	0.742	40
S90	1.056	0.907	0.149	15.238	17.853	1.17	77	90	0.816	40
S95	1.069	0.920	0.149	15.099	17.390	1.15	82	95	0.874	40
S100	1.059	0.920	0.139	15.306	18.336	1.20	87	100	0.920	40
S00-25	1.060	1.0505	0.009	15.108	15.579	1.03	0	0	0.000	25
S50-25	1.066	1.0223	0.043	14.995	15.606	1.04	50	50	0.511	25
CV100	1.061	-	-	15.231	-	-	-	-	-	-

All samples are listed in Table 17 with their corresponding identifiers. The identifier (Id) is composed of S for Storage, CV for constant voltage and a number for the storage SoC (SoC_{actual}). For batteries stored at 25 °C the temperature value 25 is added. Furthermore, Table 17 lists the state the samples are stored at after the last check up in absolute values C_{actual} and with reference to the initial capacity $SoC_{initial}$.

6.2.3 Test procedure

The SoC dependency of diffusion into large overhang areas was studied with three cells stored for 20 months at elevated temperature (40 °C) and high (95 %), medium (55 %), and low SoC (0 %). These samples S95, S55, and S00 were opened, the electrodes extracted, washed, and prepared for photography and XRD. Pictures were taken of the graphite color distribution at the thin side overhang regions as well as large overhang regions, cathode tab covered areas and active electrode area. X-ray diffraction measurements for sample S95 were performed at 20 positions along the electrode length up to the central tab location and 11 positions across the width of the electrode. An additional sample S50-25 was stored at 50 % SoC and room temperature (25 °C) to study diffusion into large overhang areas during long term storage at realistic storage conditions. As with S95, S55, and S00, the graphite color distribution was photographed and the graphite phase fraction measured in the largest overhang region. To see whether lithium diffusion out of and into the overhang area during storage affects the battery cycling, the samples S05, S10, S20, S40, S60, S80, S90 and S100 underwent high precision CE measurements. Constant current cycling was performed with 250 mA (~C/4) at 25 °C with 10 min resting periods between charging and discharging. The batteries were cycled between 2.5 V and 3.6 V.

After 30 cycles (~250 h), cycling is ended for samples S05, S60, S70, S90, and S100 after discharge. Sample S90 was disassembled within 2 hours. To further deplete the overhang lithium reservoir, the samples S05, S60, S70, and S100 were then stored at 0 % SoC and 50 °C for 50 hours. Every 10 h, the samples were discharged CCCV to 2.5 V (I = 100 mA, I < 0.01CA). After this procedure, the samples were disassembled, photographed and XRD measurements taken. CE measurements were continued up to 300 cycles (2000 h) for S10, S20, S40, and S80.

6.2.4 Post mortem

The cells were disassembled in a glovebox with O_2 and H_2O removal in argon atmosphere (MBRAUN: <1 ppm H_2O, <1 ppm O_2). The metal casing was cut open, anode, cathode and separator were extracted and separated. The electrodes were washed with dimethyl carbonate (DMC) for 20 minutes to remove electrolyte remnants. The electrodes were then dried at vacuum. Photos were taken before the electrodes were cut and packaged for XRD in PP/ PE coated aluminum foil and sealed at 50 mbar vacuum and 190 °C.

6.2.5 Coulombic efficiency setup

Cycling was performed with a BaSyTec CTS battery test system. All tests were conducted at a controlled temperature of 25 ± 0.1 °C using a BINDER KT170 climate chamber. For the coulombic efficiency measurements, additional shunts were placed in the current path between the battery test system and the battery cells (section 4.2.2). This enabled the measurement of the currents flowing into and out of each battery cell with a higher resolution and precision than the battery test system. These current data were recorded synchronously by the battery test system. To minimize temperature influences on the measurements, the analog-digital converter board and the shunts were also placed inside the climate chamber at 25 °C to improve the accuracy of CE measurements (section 4.2.2). The battery surface temperature was measured with an NTC temperature sensor attached to the battery. The observed change in surface temperature during cycling was < 0.5 °C.

6.2.6 Color setup

Images of washed and dried electrodes were taken with a SONY Alpha 7 II camera with a Sony FE 55 mm F1.8 ZA objective. The images were taken at a fixed sample, camera and lighting position. Photos are taken from outside the glovebox with the samples being inside the glovebox, at a lithiated state. The color representation is expected to be distorted due to absorption of the glovebox glass window and the internal camera color calibration. To get an accurate representation of the electrode colors, we performed white balancing and color calibration with each image using Datacolor SpyderCheckr 24

color reference cards placed inside the glovebox together with the samples. For better visibility of color gradients, brightness is slightly increased for the electrode images in this chapter and the full set of electrode images in the appendix (Figure B.1 to Figure B.12). Image correction was performed with Adobe Photoshop Lightroom v5.7.1, Adobe Camera Raw 8.7.1 and SpyderCheckr v1.2.2.

6.2.7 XRD setup

Diffraction analysis was conducted with setup and procedure as outlined in chapter 4.8.2 with Mo-$K_{\alpha1}$ radiation at λ = 0.70932 Å, 55 kV and 40 mA. The sealed electrodes were placed in the center of the goniometer circle (radius 240 mm) and were measured in transmission mode which requires a high X-ray beam intensity realized by a focusing mirror. Hence an elliptic graded W/Si multilayer mirror with an equatorial divergence of the beam less than 0.055° was used to collimate the divergent beam from the X-ray tube to the secondary focus of the goniometer circle at the detector. A 1D real time multistrip X`Celerator™ detector with an efficiency of 30 % for Mo Kα1 radiation and a pixel resolution of 0.002° in 2θ was used to collect the data. The Mo K_{β} radiation is suppressed to a level below 0.5 % by the focusing mirror.

The axial divergence was reduced by inserting Soller slits with an opening of 0.02 rad at the incident and transmitted beam path. The beam cross-section at the sample was reduced to 10 mm x 0.38 mm using masks and a 1/4° Ta divergence slit. For standard measurements, 4-16 patterns were collected typically over a 2θ-range of 7-37° with a step size of 0.008° and a counting time per step of 36.8 s. Long term measurements used up to 170 patterns with a 2θ-range of 5°-55°. The sealed electrodes were mounted on a sample holder and were kept perpendicular with respect to the incident beam during measurement. The sample position was adjusted manually with a positional resolution of 0.5 mm.

The refinements were carried out using the Highscore software package [154] with Thomson-Cox-Hastings (TCH) type [164] pseudo-Voigt profile functions either as Rietveld [165] or Pawley [166] fit, as implemented in the software. All refinements were carried out starting with the reference data sets for Al [167], Cu [168], Graphite [169], LiC_{12} [170] and LiC_6 [171] from the Inorganic Crystal Structure Database (ICSD) maintained by the FIZ Karlsruhe. The reference data sets as well as the fitting parameters, including standard uncertainties for all measurements, are tabled in the appendix (Table B.1 to Table B.5).

6.2.8 XRD analysis

The samples also contain lower lithiated structures than the crystallographically well established LiC_{12} phase. Given the limited resolution and angular range of our data and competing phase transition models, we adopt a simplified picture of lower lithiated phases (see discussion in Section 3.3.4). Lower lithiated phases are classified qualitatively according to the shift of the *c*-axis. Phases with shifted c-axes below 7.040 Å are considered as LiC_{18}. Phases with shifted c-axes below 6.900 Å are considered as $LiC_{\geq 24}$.

6.2.8.1 Pattern-shift due to coating position

Anode and cathode electrodes are coated on both sides of the current collector (CC). Each side is penetrated by the X-ray beam and contributes to the diffraction pattern. The relative displacement of the active material layers due to the current collector is ~15 µm. The total thickness of a double-coated electrode and thus the upper displacement limit for two graphite particles is ~90 µm (post mortem measurement of electrode). A simulation of the LiC_6, LiC_{12}, and graphite 002 reflections for two positions shifted by 100 µm in X-ray beam direction shows a resulting shift of 0.005 °2θ (Figure 68). The resulting shift is below the 0.008° step size of the diffractometer and thus negligible for a 100 µm displacement. However, it adds up to the peak-broadening of the reflection which is accounted for by the TCH-profile. The specimen displacement between different samples after sample exchange is corrected with the Cu reflection of the current collector.

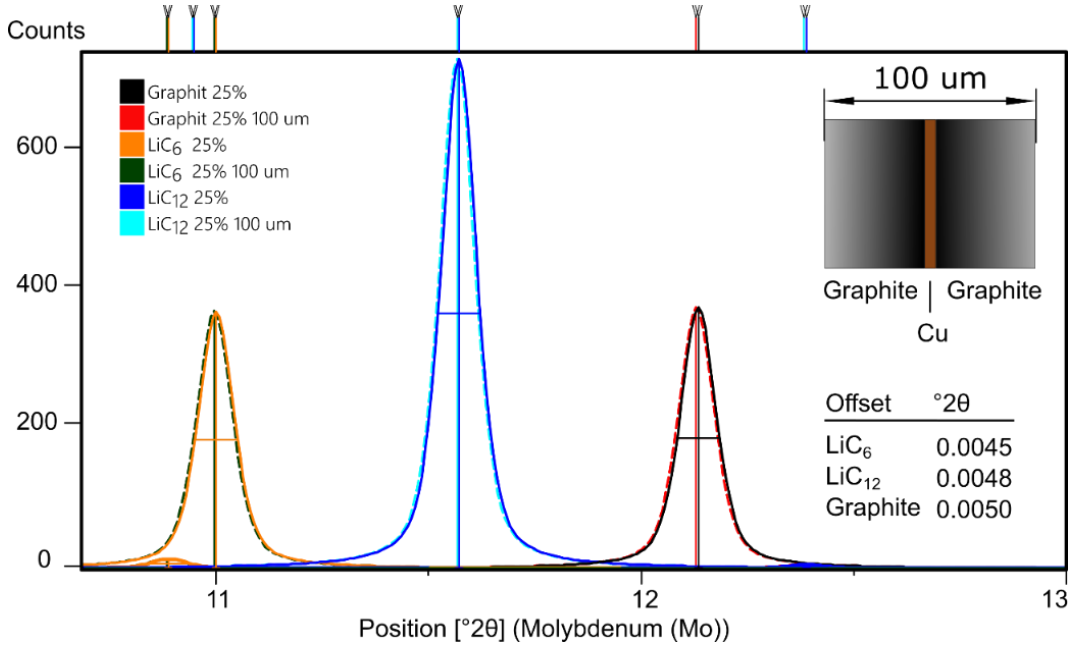

Figure 68 Simulated LiC_6, LiC_{12} and graphite reflections for two positions shifted by 100 µm in X-ray beam direction approximating the peak splitting due to different position in the beam for active material of front and backside coating. The resulting pattern shift of 0.005 °2θ is below the 0.008 °2θ step size of the diffractometer. For higher order reflections the shift increases. Reflections at 33°2θ are shifted by 0.013 °2θ. [138]

6.3 Results and discussion

This section presents the results of the overhang experiment. It begins with the non-reversible capacity losses during calendar aging, followed by the CE during subsequent cycling. In the post mortem analysis, the color distribution and lithiation of small and large overhang areas for calendar aged cells and cells with additional cycling are discussed. Finally, cells with lithiated overhang areas are subjected to a procedure to delithiate the overhang. The withdrawn capacity as well as the effect on the overhang are presented.

6.3.1 Calendar aging

To analyze the diffusion of lithium into the graphite electrode overhang regions, it has to be taken into account that due to calendar aging, the amount of usable lithium and thus achievable lithiation is reduced. Figure 69 a) shows the reconstruction of the full cell voltage of a new battery and the differential voltage spectrum from the half-cell data plotted versus full cell SoC b). At 100 % full cell SoC, the anode capacity is only utilized up to 80 %. The *dV/dQ* maximum at 70 % SoC marks the change from the LiC_{12} plateau and the LiC_{12}/ LiC_6 graphite voltage plateau. At the given battery balancing, a maximum lithiation of 57 % LiC_{12} and 43 % LiC_6 in the XRD is expected for a fully charged new battery. Figure 69 c) shows the capacity decrease during 16.3 months calendar aging at 40 °C. The capacity fade increases with storage SoC. At 0-30 % SoC, the losses are below 10 %, at 40-70 % the capacity loss is about 10 % and up to 14 % at 80-100 % SoC. The observed plateaus of capacity fade correspond to graphite stages [5]. Figure 69 d) shows the changes in the differential voltage spectrum for the battery with the highest capacity loss (S90) resulting from calendar aging at 40 °C. A comparison between the capacity and the R_{1kHz} resistance at initial measurements and after 16.3 months storage is given in Table 17. Battery resistances of all samples increased by less than 20 % R_{1kHz}. The homogeneous resistance increase indicates that there is no direct correlation between capacity fade and resistance increase. Electrode dry out was not observed as stored and new reference batteries showed visibly wet electrodes and separators during disassembly.

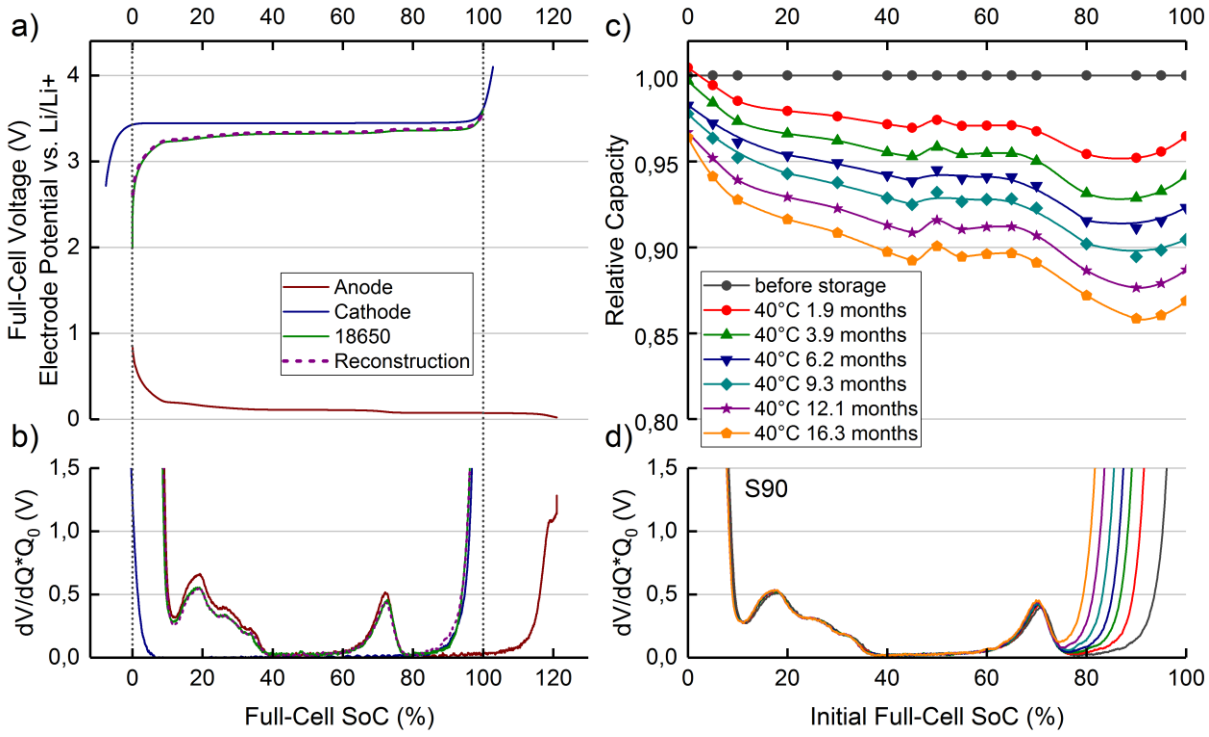

Figure 69 a), b) Full-cell voltage reconstruction from half-cell profiles. c) Capacity fade at 40 °C during calendar aging over storage SoC. d) Differential voltage profile for different stages in the aging process for the battery with the highest relative capacity losses (sample S90). [138]

6.3.2 Coulombic efficiency

When diffusion into or out of overhang areas changes the amount of lithium available for cycling, the coulombic efficiency is affected. To study this, the cells S05, S10, S20, S40, S60, S80, S90, and S100 were cycled and the battery capacity measured. High CE values very close to unity during long-term cycling of up to 1200 h confirm the excellent cycling stability of the examined LFP cells. Thus, no notable aging reactions have occurred which deteriorate the CE measurements.

Figure 70 demonstrates that there is a strong correlation between the storage SoC and the *CE* values: The batteries stored at high SoCs of 80 %, 90 %, and 100 % exhibit *CE* values greater than unity. This means that a slightly higher amount of charge is extracted during discharging than is inserted during charging. This can also be seen in Figure 71 a), where the charging and discharging capacities are shown for the first 30 cycles. The batteries stored at low SoC 5 %, 10 %, and 20 % with CE values lower than unity feature decreasing capacities throughout the cycling procedure. Figure 70 b) shows that initial *CE* values range from 0.994 to 0.996 for low SoC storage cells and increase successively towards 1. The batteries stored at medium SoCs of 40 % and 60 % consistently show *CE* values close to 1 and little capacity change during 250 cycles as seen for cell S40 in Figure 71 b).

These observations are consistent with the observations by Gyenes et al. [18] and can be explained by lithium diffusion into and out of the overhang areas. During long term storage at high SoC, lithium diffuses into the overhang area. During subsequent cycling, the overhang areas act as a lithium source and increases the amount of cyclable lithium. This effect results in a capacity increase of the battery and a $CE > 1$. After low SoC storage the reverse process occurs. When storing cells at low SoCs, the overhang areas remain largely non-lithiated. During subsequent cycling, the empty overhang areas act as lithium sinks and decrease the amount of cyclable lithium when the average SoC during cycling is higher than the SoC during storage. The corresponding difference in the anode potential drives lithium diffusion into the overhang areas and leads to $CE < 1$. After about 30 cycles the cycling procedure was interrupted for cells S10, S60, S90, and S100 when they were in a discharged state, as the cells were

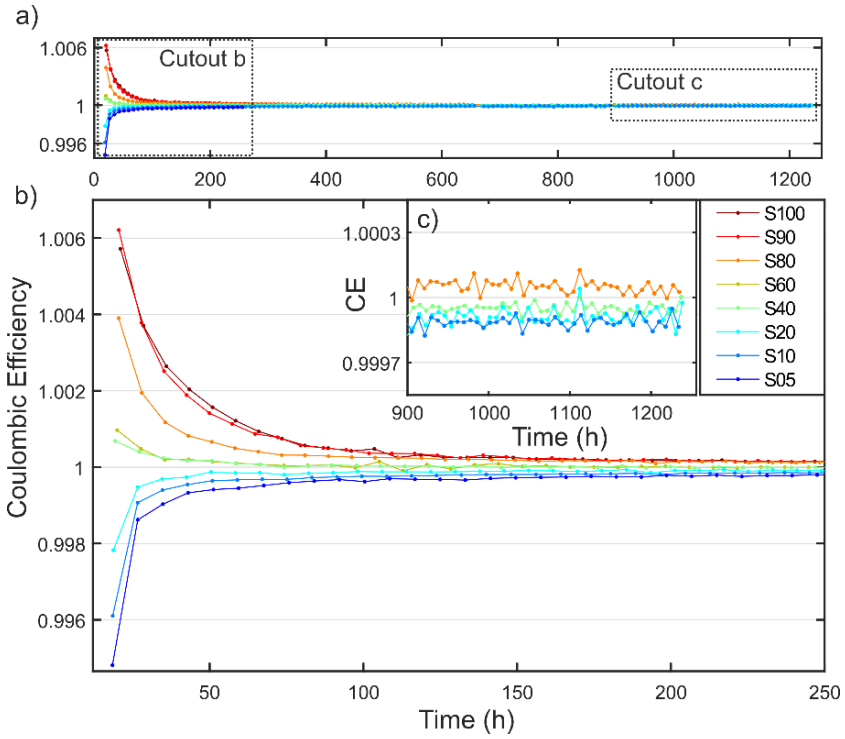

Figure 70 Coulombic efficiency during cycling after storage for 20 months at various SoC. The data up to 1200 h of cycling is shown in a). b) shows a close up of the initial 30 cycles. c) Cycling was continued for S05, S20, S40, and S80 for 1200 hours until all samples showed a narrow range of CE. [138]

disassembled for post mortem analysis. For the other four cells S05, S20, S40, and S80 cycling was continued for 1200 hours before disassembly. As shown in the inlet (Figure 70 c), after 1200 h of cycling battery S80 continues to show a *CE* > 1 and slightly than S05, S20 and S40. This was unexpected considering the results of Gyenes et al. [18] it was assumed, that the *CE* drops below 1 after approximately 800 h. As a consequence, the cycling procedure was restarted and continued up to 300 cycles (2000 h). The time the cells spent at low SoC during the interruption of the cycling procedure led to a certain acceleration of the overhang depletion of cell S80, as can be seen in Figure 71 b). Sample S80 shows a capacity increase of 2.0 % (22 mAh) after 250 cycles, 1.3 % (14 mAh) during the initial 30 cycles. Vice versa, Figure 71 b) shows a capacity decrease of cell S10 by 1.6 % (18 mAh) after 250 cycles, 0.5 % (5 mAh) after the initial 30 cycles. The capacity difference between S80 and S10 reduces from 6.9 % C_N measured directly after storage to 3.3 % C_N after 250 cycles, corresponding to 2000 h of cycling. Thus, the 40 mAh difference (3.6 % with respect to the nominal capacity) between these measurements is not caused by aging effects, but results from lithium outflow of overhang areas for cell S80 and lithium inflow into overhang areas for cell S05.

In many battery aging studies, the end of life is considered as a capacity fade of 20 % of the nominal capacity. Therefore, variations of 3 - 4 % in the capacity determination caused by the anode overhang areas can lead to substantial misinterpretations of battery aging processes and distorted battery life estimations. Applying this 20 % capacity fade limit, the end of life is reached at a remaining capacity of 880 mAh. The combined capacity difference of 40 mAh attributed to overhang area effects amounts to 18 % of the useable capacity range (220 mAh).

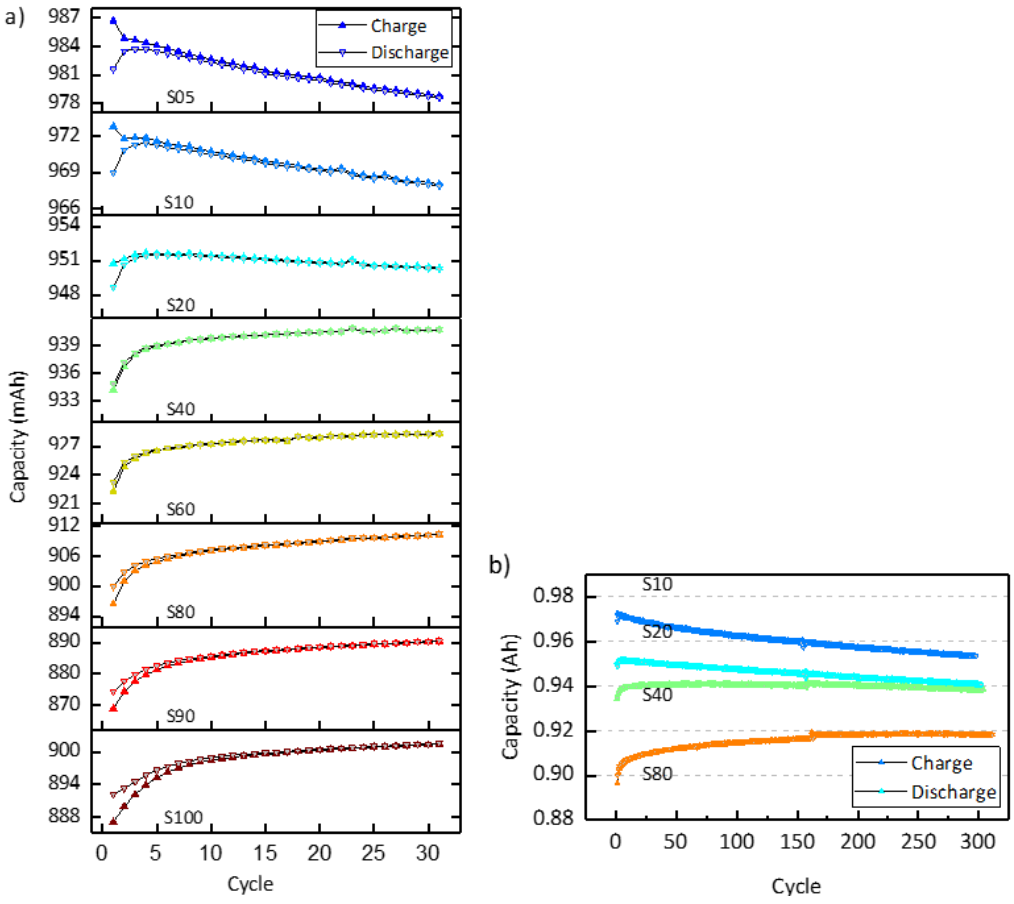

Figure 71 Charging and discharging capacity during the initial 30 cycles (250 h) after long term storage at different SoCs ranging from 5 % to 100 %. This demonstrates the capacity recovery for cells which exhibit CE values greater than 1. b) Extended cycling data of cells S10, S20, S40, and S80 comprising of up to 300 cycles (2400 h). Discontinuance and restart of the cycling procedure at cycle 160. [138]

6.3.3 Post mortem analysis

The *CE* observations can be consistently explained by lithium diffusion into the anode overhang areas. To obtain more detailed information about the spatial lithium distribution, post mortem analysis was conducted. The surface color distribution and XRD measurements are evaluated to determine local lithium concentrations.

6.3.3.1 Overhang lithiation after storage

After long-term storage at high SoC, considerable amounts of lithium can be found in the anode overhang regions. As the highest amounts of lithium are stored in the overhang areas for the cells which were stored at high SoC, the cell S95 was disassembled after 20 months of storage at 95 % SoC and 40 °C. This cell was not subject to subsequent charge-discharge cycling since this would have altered the lithium content in the overhang areas. Figure 72 shows the graphite color distribution (a) and graphite phase fraction along the length of the electrode (b) and across the width of the electrode (c) of this cell. The large overhang region at the left side, which represents the outer end of the jelly roll, is of purple color with a radial color gradient towards a light blue central part. The purple color of the overhang region indicates 50 % anode lithiation [52]. The brighter blue region indicates a lower lithiation of 30 - 50 %. In the cathode covered electrode area, color gradients are visible from purple over purple-brownish to golden. Golden areas indicate highly lithiated graphite with LiC_6 present [52]. The color distribution indicates a SoC gradient along the electrode length where the central areas show the highest lithiation. Close to the sides and edges, where overhang regions are located, the active anode shows purple color, and thus a lower SoC compared to golden, highly lithiated, central regions.

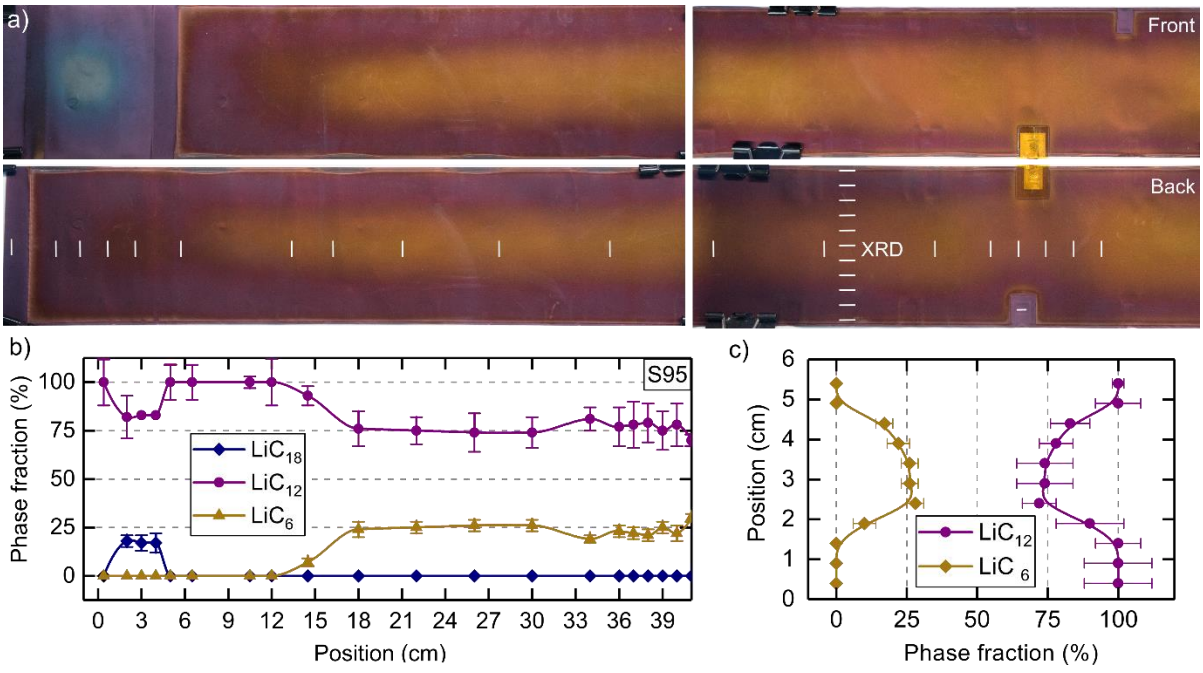

Figure 72 a) Anode of sample S95 stored at 95 % SoC including the overhang region up to the central tab. Varying degrees of graphite lithiation cause an inhomogeneous purple/ golden color distribution. b) Li_xC_6 phase fraction determined by Rietveld refinement from XRD measurements along the anode as marked in white on the backside image. c) Li_xC_6 phase fraction across the electrode width. [138]

In addition to the photographs of the electrode, XRD measurements were performed along the length and along the width of the electrode. The measurement positions are illustrated as white lines in the backside images of Figure 72 a). The lithiation gradients observed in the color distribution are also seen in the diffraction measurements. Figure 72 b) exhibits lithiation with LiC_{12} for the outermost 6 cm, the overhang area without cathode counterpart, and up to 6 cm into the active region. This is in agreement with the color distribution. At the center of the overhang area (2-4 cm) ~20 % LiC_{18} is observed. This

corresponds well to the lighter blue colored region at the center of the overhang region where a reduced lithiation is observed compared to purple colored graphite areas. From 12 cm towards the center of the electrode, LiC_6 is present in increasing and then stable amounts of 25 %. Along the width of the electrode (Figure 72 c)) a similar gradient is visible. While only LiC_{12} is present close to the sides, the amount of LiC_6 increases towards the center and plateaus at 25 %. The slight asymmetry in lithiation with regard to the center (2.9 cm width) is equally present in the color map and phase distribution as determined by XRD. The approximately 1 cm^2 large area of the anode with the cathode current collector tab as counterpart is recognizable in Figure 72 a) due to the imprint of the tab and light purple color. The color change and XRD measurement at the central position of this area shows a 100 % LiC_{12} lithiation (see appendix, Table B.13 for refinement data). Thus, the anode parts opposed to the cathode tab act as source and sink similar to anode overhang areas.

In summary, color distribution and XRD data show lithiation of overhang areas and strong gradients from electrode sides and edges towards the central areas. From the pattern of lithiation seen in Figure 72, we can draw conclusions on the transport process driving the lithiation of the overhang area. If the process was driven by diffusion through the active material, we would expect the lithiation of the large 6 cm overhang area coming solely from the adjacent active anode area on the right side. A phase boundary parallel to the active area boundary would have to emerge. Yet, the overhang is lithiated concentrically from all sides of the electrode, including side areas without direct contact to active anode area.

Thus, it is concluded that electrochemical processes effect the lithiation of the overhang areas: Lithium ions from the electrolyte intercalate into the overhang graphite material. Simultaneously, lithium from the active graphite area deintercalates. The resulting concentration gradient in the electrolyte equilibrates through liquid diffusion. The potential gradient between differently lithiated anode areas is the main driver for the overhang lithiation. High temperatures accelerate the lithiation of the overhang areas by reducing the charge transfer resistances at the electrode-electrolyte interface [32, 172] and increasing the diffusion coefficient of the electrolyte [25].

6.3.3.2 Overhang lithiation at different storage SoCs

To investigate the SoC dependency of large overhang area lithiation in more detail, post mortem investigation on two additional cells stored for 20 months at very low SoC (S00) and medium SoC (S55) was conducted. Figure 73 shows a comparison of the color distribution and graphite lithiation at the overhang area between cell S00, S55 and S95.

The overhang area of S00 is of light grey color and the cathode covered part is of grey-brown color. The XRD measurements show a majority of non-lithiated graphite in the overhang as well as at the edge of the active region. Additionally, 0-20 % of a slightly lithiated $LiC_{\geq 24}$ phase is observed. The c parameter of this phase is about 6.80 Å and strongly shifted towards the graphite *c*-axis parameter of 6.7220(1) Å [169] indicating minimal lithium content. The overhang area is not charged through lithium diffusion, as it is expected for low SoC storage. The remaining contribution of a minimal lithiated phase is consistent with our test procedure that discharges the battery to 2.0 V. Sample S55 shows a homogeneous grey blue color with a similarly brighter overhang region. XRD measurements show the overhang regions and active regions lithiated with predominantly LiC_{18} with fractions of higher lithiated LiC_{12} states.

To get a first impression of the temperature dependency of overhang lithiation, an additional cell S50-25 was stored at 50 % SoC and 25 °C. Compared to cell S55, this cell shows a similar grey-blue color and also predominantly LiC_{18} lithiated graphite in the overhang area. On average, the share of LiC_{12} is higher for S55 stored at 40 °C (0-46 %, avg. 19 %) than for S50-25 stored at 25 °C (0-29 %, avg. 11 %). Lithiation and the according color change, as shown in Figure 73 is equally present at the 2 cm

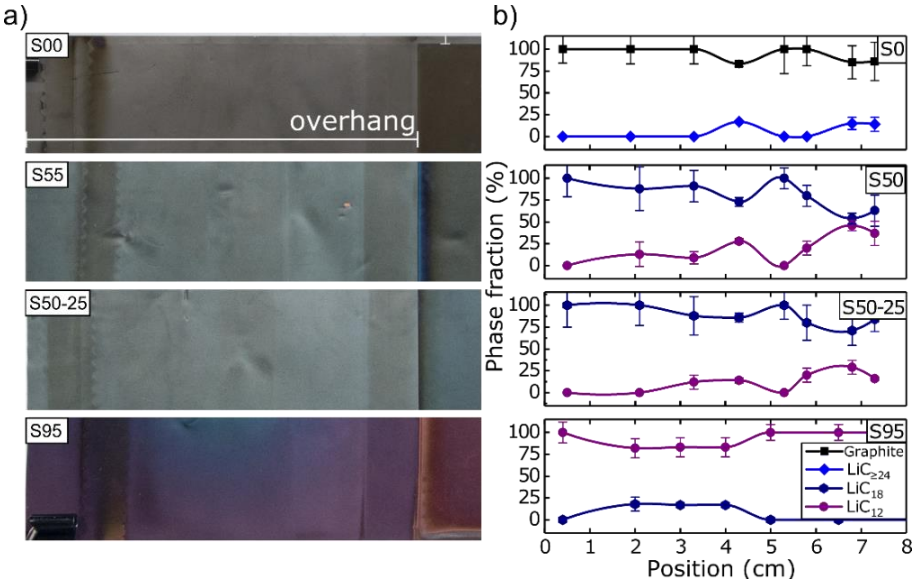

Figure 73 a) Anode overhang regions for batteries stored at 0 %, 50 % (25 °C), 55 %, and 95 % SoC along with b) measured Li_xC_6 phase fraction. The presented segments show the upper (S00), middle (S55, S55-25) and lower (S95) part of the overhang area. XRD measurement positions are as shown in Figure 72. The photographs and phase fractions demonstrate the dependency of the lithiation of the overhang areas on the storage SoC of the lithium-ion cell. [138]

overhang region at the inner part of the jelly roll (appendix Table B.1, Figure B.1 and Figure B.12). In conclusion, high storage SoC and elevated temperature are conducive to but not necessary for lithiation of large overhang regions. The common storage SoC of 50 % at room temperature is sufficient, given enough storage time, to obtain homogeneously lithiated large overhang areas.

The slight color difference between overhang region and active anode area is visible for all overhang regions, sides and edges, and all samples (see appendix: Figure B.1 to Figure B.12 for additional images). This is attributed to a thin passivation layer of the anode, commonly referred to as the SEI, which is the dominant aging mechanism of calendar aging in the absence of damaging processes such as mechanical strain and lithium plating during cycle aging [79, 173]. As shown in Figure 69 c), all cells show capacity loss as expected from passivation layers binding cyclable lithium. The batteries were stored at elevated temperatures which aids the evolution of passivation layers [80]. Klett et al observed an additional uneven deposition layer on top of the anode for deep cycled $LiFePO_4$|graphite batteries [174, 175]. The cycling of the calendar aging batteries was minimal and limited to the check up procedures. Therefore, a thick deposition layer as observed by Klett et al. is not thought to be the reason for the observed difference in color. Furthermore, scanning electrode microscope (SEM) images of the overhang area in comparison to active electrode parts (Figure 74) show a similar surface morphology with no indication of a thick covering layer in both areas.

In addition to the large overhang areas, we investigated the lithiation of the side overhang areas. They are thinner but considerably longer (0.15 cm x 70.2 cm) than the overhang regions at the electrode ends. With the shorter diffusion path, it is expected that the time needed to fill and deplete these areas is short compared to the overhang region at the end of the electrode. Figure 75 compares the side overhang region of a) S95 with b) S55, c) S00 and a fully charged reference sample d) CV100. Similarly to the large overhang regions, the sides are grey and delithiated for S00, partially lithiated and grey-blue for S55 and purple-red for S95. The side overhang regions take on the state of lithiation of the active region during storage. S00 shows a majority of graphite with a minor contribution of a slightly lithiated $LiC_{\geq 24}$ phase as seen for the large overhang area (Figure 73). S55 shows a mixture of LiC_{12} and LiC_{18} in with a lower contribution of ~20 % LiC_{12} in the side overhang compared to ~50 % in the active

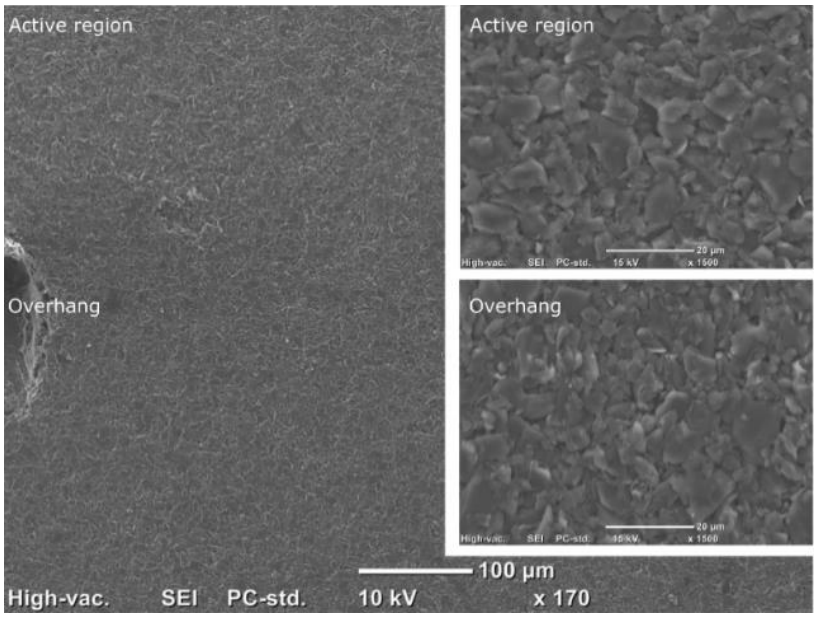

Figure 74 Scanning electrode microscope image (JEOL JSM 6000) of anode active region (cathode covered) and overhang area. The area shown is from the side overhang area of sample S00 stored at 0 % SoC and 40 °C for 20 months. A thick covering deposition layer is neither visible in the active nor in the overhang area. [138]

anode area at position 1 mm and 2 mm. For Cell S95 only LiC_{12} was found in the overhang as well as the active anode area. S00 shows a majority of graphite with a minor contribution of a slightly lithiated $LiC_{\geq 24}$ phase as seen for the large overhang area (Figure 73). S55 shows a mixture of LiC_{12} and LiC_{18} in with a lower contribution of ~20 % LiC_{12} in the side overhang compared to ~50 % in the active anode area at position 1 mm and 2 mm. For Cell S95 only LiC_{12} was found in the overhang as well as the active anode area.

To assess the accuracy of the phase identification of XRD, the graphite lithiation obtained through XRD for the fully charged reference cell CV100 are compared with the results of a *dV/dQ* analysis. The fully charged CV100 cell shows three sharply divided colored 1 mm wide areas, a light blue overhang, a golden highly lithiated area and a partial lithiated purple area in between.

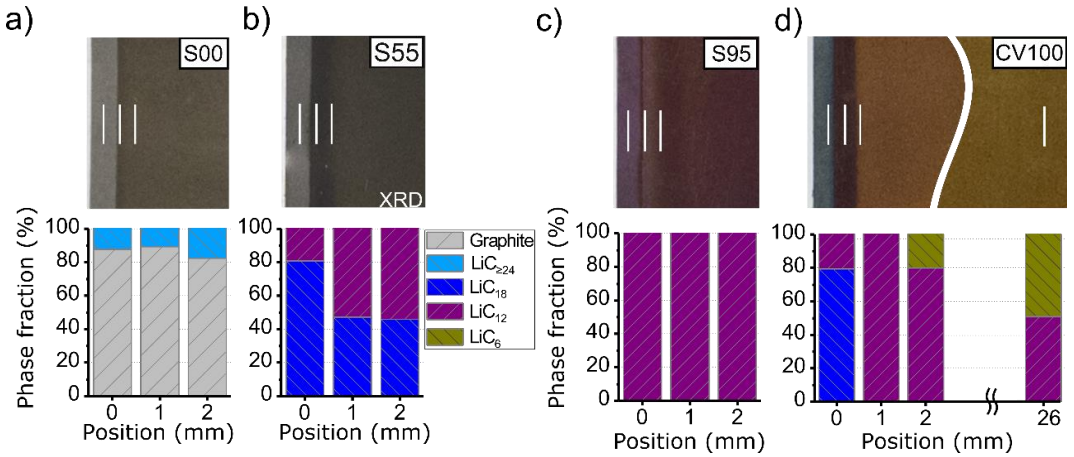

Figure 75 Close up image of the anode overhang region at the side (1.5 mm) of sample a) S00 b) S55 c) S95 and d) CV100 measured with XRD at three positions, each 1 mm apart. The reference for a fully charged non-aged and non-stored battery CV100 was measured additionally at the central electrode position 26 mm. For the corresponding backside images see appendix Figure B1-to B12. [138]

Consistent with this, XRD measurements show lower lithiated states LiC_{18} in the blue, LiC_{12} in the purple and LiC_{12}/ LiC_6 in the golden region. The LiC_6 fraction in the lithiated region close to the sides (2 mm) is with 20 % low compared to the 49 % measured at the center of the electrode (26 mm), indicating a reduction in lithium content at least partially due to the diffusion into the overhang. The observed 51 % LiC_{12} to 49 % LiC_6 ratio at the center is slightly higher than the 57 % LiC_{12}/ 43 % LiC_6 average ratio expected from *dV/dQ* analysis. This can be explained by the inhomogeneous SoC in the active anode area. With a LiC_6 gradient towards the central region, similar to cell S95, the higher than average lithiated areas at the center compensate for the lower than average lithiated areas at the sides. Thus, XRD and *dV/dQ* are in good agreement.

6.3.3.3 Depletion of overhang areas after CE cycling

To investigate qualitatively how quickly the overhang area can be delithiated, this section compares the overhang areas between samples after cycling and samples after cycling with additional CCCV discharges at low SoC. Cell S90 was opened directly after discharge after about 30 cycles for CE measurements without additional measures to deplete the overhang area. The cathode covered anode area is delithiated and is colored brown-grey (Figure 76 a)). The grey-blue colored overhang region indicates partial lithiation. This is confirmed by the XRD measurements of the central region which shows 60 % ± 25 % graphite and 40 % ± 15 % LiC_{18} (see Figure 76 a) for measurement position and appendix Table B.10 for detailed diffraction results). Within the margin of error, we see an even share of LiC_{18} and graphite. There are no lower lithiated phases $LiC_{\geq 24}$ in-between graphite and LiC_{18} present. At the measured position, the back area is not part of the overhang and therefore delithiated during discharge. Thus, the observed 60 % graphite are attributed to the back of the electrode.

Light grey colors at the sides and at the overhang in close proximity to the active region indicate delithiation. This is confirmed through XRD measurement of side overhang areas near the middle part of the electrode, which shows mainly graphite and a minor contribution of low lithiated phase $LiC_{\geq 24}$ of 11 % ± 5 % of a (*c*-axis = 6.854(7) Å) (see the inlet of Figure 76 b) and appendix Table B.17 for detailed diffraction results). When comparing the two cells S90 and S95 (Figure 73), which were both stored 20 months at a high SoC, the impact of cycling on the lithiation of the overhang areas becomes obvious. Whereas the cell without cycling exhibits a mixture of LiC_{12} and LiC_{18} phases, the cycled cell only exhibits LiC_{18} phases at the center. Thus, the lower average potential of the active anode area during cycling led to a lithium diffusion from the overhang area back to the active area, which explains the $CE > 1$ and the capacity increase in the cycling experiment.

6.3.3.4 Depletion of overhang areas after CE cycling and additional CCCV discharges

In completely discharged condition, the anode potential is highest (Figure 69 a) and the gradient between lithiated overhang areas and the active area is most pronounced. This leads to the fastest diffusion of lithium back to the active area [18]. In order to remove as much lithium as possible from the overhang areas, several cells were CCCV discharged repeatedly. The cells S100, S70, S60, and S05 were taken from the cycling procedure after ca. 30 cycles when they were completely discharged. Subsequently, they were exposed to five CCCV discharges with 10 h of relaxation in between. To accelerate diffusion, the storage and discharge procedure was carried out at 50 °C. After that, the cells were opened and post mortem studies were performed. The battery voltage during the five consecutive CCCV discharges with 10 h relaxation as well as the discharged capacity for each step for cell S100, S60 and S05 are shown in Figure 76 c). The cells show different voltage relaxation behavior, despite identical test procedures. Higher voltage levels are seen during relaxation for higher storage SoC batteries, due to remaining lithiated areas in the overhang region. The extracted capacity decreases monotonically with the number of discharge steps for all samples. The higher the previous storage SoC, the higher the extracted capacity. The extracted capacity decreases more sharply for the low SoC storage sample S05 (5 %) compared to sample S100.

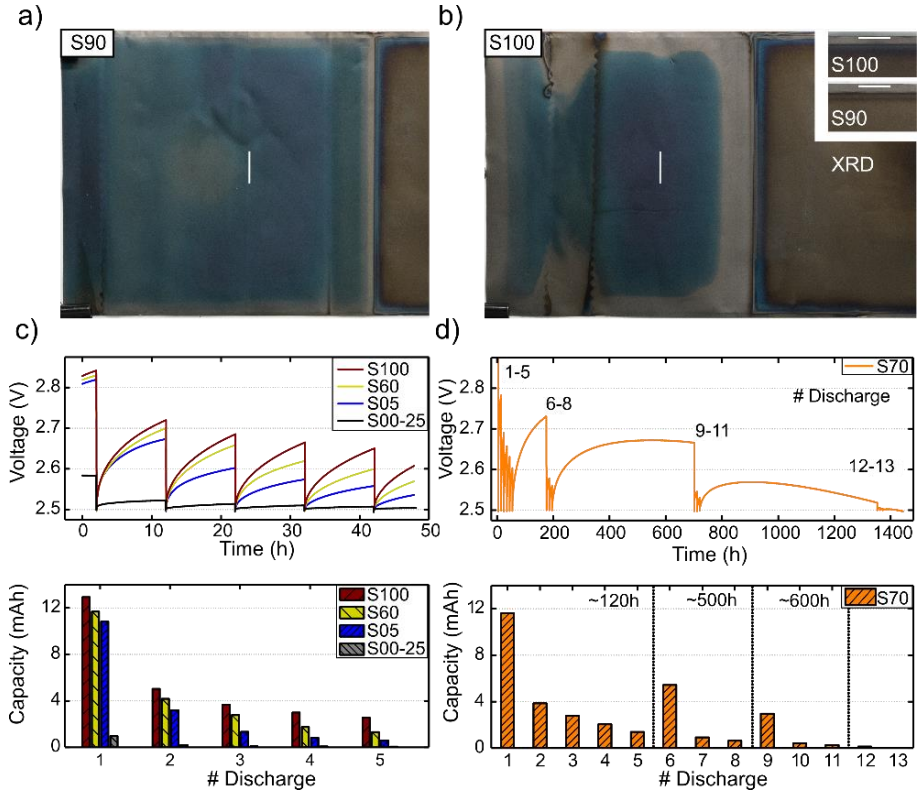

Figure 76 Anode overhang region for a) S90 and b) S100 after C/4 cycling for 250 h. The inlet shows side overhang regions. S100 additionally underwent five CCCV discharges and 50 h storage at 50 °C. White bars mark the XRD measurement positions. c) Battery voltage of S100, S60, S05, and S0-25 during CCCV discharge and subsequent 10 h relaxation. d) Sample S70 underwent 13 CCCV discharges with subsequent 10 h relaxation. More time was given for relaxation between discharge 5 and 6 (120 h), 8 and 9 (500 h) as well as 11 and 12 (600 h). [138]

For example, at the first discharge ~20 % more capacity was extracted for S100 compared to S05 (12.9 mAh compared to 10.8 mAh). At the fifth discharge, four times the capacity was extracted from S100 (2.6 mAh compared to 0.6 mAh). The effect of the discharge procedure onto the large overhang area is depicted in Figure 76 b) for the high storage SoC cell S100. As for sample S90, the overhang region shows a blue LiC_{18} lithiated graphite area as confirmed with an XRD measurement of the center area (Figure 76 b)). Similar to S90 the side overhang areas are delithiated. They are of light grey color and XRD measurements show a majority of graphite and a minor contribution of low lithiated phase $LiC_{\geq 24}$ of 15 % ± 8 % (*c*-axis = 6.839(7) Å). The grey areas observed for S100 after the five CCCV discharges are wider than for S90 (1 cm compared to ~1.5 mm). As the grey areas represent a lower degree of lithiation than the blue areas, it is confirmed that the subsequent discharges and the prolonged storage at low SoC have made lithium diffuse out of the overhang area back to the active area where it became available for discharging again.

Together these results confirm that the increase in capacity and $CE > 1$ during cycling of high SoC storage cells is caused by lithium influx from the overhang areas. They also show a difference in accessibility of large and small overhang regions. During *CE* cycling the small overhang regions are largely depleted during each discharge of each cycle at our chosen rate (C/4). This is in agreement with Lewerenz et al., who observed a 2-3 % higher capacity for C/4 discharges compared to 1C for a cylindrical LFP|graphite battery and attributed this to the “near part” of the anode overhang [115]. Thus, the withdrawable capacity stems from the larger 2-6 cm wide electrode-edge overhang regions. The rather large amount of capacity extracted from S05 during the first discharge seems to contradict this interpretation (Figure 76 c)), as one would expect a lower capacity for largely empty overhang areas. The discrepancy can be explained by the following:

First, the higher temperature during the depletion procedure at 50 °C compared to 25 °C during CE cycling frees additional capacity in the active anode area. Secondly, as suggested by Gyenes et al. [18], the overhang areas asymptotically approach the medium SoC of the cycling procedure, which is 50 % for full range cycling applied in the CE measurements.

To verify the second assumption, a cell stored at 0 %, S00-25, without prior cycling, was also exposed to the described depletion procedure. For this cell, it was expected that almost no lithium is stored in the overhang areas. Thus, no charge extraction and voltage recovery should occur for this cell. As can be seen in Figure 76 c), only a very minor amount of charge could be discharged for this cell and the voltage recovery is also small. The assumption is further supported by post mortem investigation of sample S80, S40, S20 and S10 after the *CE* measurements. All four samples show slightly grey-blue colored, partially lithiated large overhang areas (see appendix Figure B4, B6, B7, B8, B9).

As there was still a considerable voltage recovery after five CCCV discharges, another cell, S70 underwent an extension of the procedure for the three cells discussed above, with longer storage and more discharges. Figure 76 d) shows that there is a voltage recovery observable for almost 1000 h. Moreover, the amount of extractable charge increases with longer rest periods at 0 % SoC. In total, about 32.5 mAh could be extracted during the 13 subsequent CCCV discharge steps. This amount of charge represents 3.0 % C_N and can be considered as the full amount of charge stored in the large overhang area of the anode for this cell.

6.4 Summary and conclusion

Anode overhang ensures 100 % overlap of the electrodes and is thus a common feature in lithium-ion battery cell design. To study overhang lithiation, 16 batteries stored at 40 °C and 0 % to 100 % SoC were analyzed with a broad range of methods as part of a preceding calendar aging study.

The overhang areas and thus their lithium storage capability can be considerable and compared to full battery capacity. The 18650 $LiFePO_4$|graphite battery examined in this study has overhang areas of 10 % of the total anode area. The share of overhang area is approximately evenly split between 2 cm to 6 cm wide sections at the outermost and innermost part of the jelly roll and 1.5 mm thin stripes at the top and bottom of the electrode extending over the full anode length. By color assessment and X-ray diffraction measurements, it was shown that thin overhang stretches as well as large overhang areas can be lithiated during long-term storage. Overhang areas after storage at high SoC, show LiC_{12} lithiation and a graphite color change to purple-red. After storage or operation at medium SoC, mainly LiC_{18} lithiation and a graphite color change to grey-blue is observed. Little difference in overhang lithiation is seen between medium storage SoC batteries stored for 20 months at 40 °C and 25 °C. As expected, no increased lithiation of overhang areas was found at low SoC storage. In conclusion, high storage SoC and elevated temperature are conducive to, but room temperature and medium SoC are sufficient for lithiation of large overhang regions.

A distinct difference in perceived brightness between anode overhang and active area independent of lithiation was consistently present for all calendar aged cells. The effect is attributed to differences in graphite passivation layers, the origin of which is not fully understood. Despite this, good agreement is shown between the qualitative observations through color and quantitative measurements of the graphite phase fractions with XRD. Thus, the results support the validity of graphite color changes as qualitative measure of overhang lithiation as applied in this and previous work about anode overhang areas.

The lithiated overhang areas strongly affect capacity and *CE* measurements. For high SoC storage batteries, $CE > 1$ and successively increasing capacity is observed for more than 1200 h of cycling (50 days) as lithium diffuses out of the overhang area. This timescale is longer than previously

reported. Vice versa, empty overhang regions after storage at low SoC lithiate during cycling causing $CE < 1$ and a disproportionately decreasing capacity. Consequently, the storage history must be considered in the analysis of high precision CE measurements if excess anode area is present.

Furthermore, the tests show that SoH assessment for calendar aged batteries can be flawed if batteries are compared with tests conducted directly after long term storage at varying SoC. A 6.9 % C_N capacity difference between a low and high storage SoC battery decreased down to 3.3 % C_N after cycling. The long-term effects are predominantly attributed to large overhang areas and not the few millimeters thin side areas, as discharged batteries show grey colored depleted side areas after a few cycles compared to blue colored LiC_{18} lithiated large overhang areas. To reduce the reversible capacity effect and the resulting storage history dependence, the cell design of a cylindrical cell needs to avoid the large overhang areas at the outermost or innermost part of the jelly roll, for example by not coating these areas.

7 In situ investigation of inhomogeneous anode lithiation

The previous chapter has demonstrated the power of the diffraction method to analyze lithiation inhomogeneity in anodes in order to gain quantitative SoC maps of electrodes. However, the lithiation and delithiation of large overhang areas is a slow process and the resulting distribution is stable enough throughout the post mortem process to isolate electrodes through extraction.

This is not the case for inhomogeneity within the anode layer or graphite particles caused by transport limitations during discharge. It is especially problematic if the transport limitations are induced by low temperatures and the post mortem material extraction causes the cell to heat up and accelerate the relaxation process. By utilizing neutrons for scattering, diffraction can be used in situ for large samples, such as commercial batteries, without compromising the structural integrity and temperature of the sample. To investigate the graphite polarization and the timescale of graphite relaxation processes, the experimental proposal *Phase coexistence in Lithium-ion cells during high current discharge* was submitted to the MLZ under the number 10604. On April 4th the proposal was accepted and four days of measurement time at the instrument STRESS-SPEC were granted. Approximately one day was allocated for calibration and setup. The experiment was planned and conducted with Dr. Veronika Zinth. Technical support was provided by the instrument scientists Dr. Michael Hofmann, Dr. Weimin Gan and Dr. Stefan Seidlmayer.

Parts of this chapter have previously been published in the Journal of the Electrochemical Society under the title *In Situ Neutron Diffraction Study of Lithiation Gradients in Graphite Anodes during Discharge and Relaxation [176].*

7.1 Experiment outline

The discharge and relaxation process of a commercial pouch cell is monitored with time-resolved in situ neutron diffraction. The discharge rate and sample temperature are varied to assess the impact on the graphite phase polarization. For the interpretation of the observed effects, several additional cell properties such as low temperature performance, temperature homogeneity during operation, temperature dependent impedance, and anode electrode and particle properties are discussed. The anode phase coexistence is explained with a lithium distribution model. Temperature dependent graphite solid diffusion is calculated based on the presented distribution model and the diffraction data.

7.2 Experimental design

In the following the sample cell and core test procedures are introduced. In addition, the section outlines how the target SoC for the relaxation experiment is determined and how the structural analysis is limited by experimental resolution and the state of graphite lithiation models.

7.2.1 Sample cell

A commercial lithium-ion battery (C_1 = 540 mAh at 300 K, 3.7 V) with a graphite anode and $LiCoO_2$ cathode was studied in the experiments. The electrolyte contains $LiPF_6$, EC, and DMC. The battery is designed for high power use and allows 1C continuous charging and 12C continuous discharging in a temperature window of 0 °C to 60 °C. The specified storage temperature window is given as -10 °C to 45 °C. The battery dimensions are 5.0 cm x 3.1 cm x 0.54 cm (length x width x height) with 18 anode and 17 cathode sheets. The battery properties are summarized in Table 18.

7.2.2 Cycling procedure

A BaSyTec GSM cell tester was used for determination of temperature dependent capacity and rated capacity. The rated capacity was determined for CC discharging at 0.1C, 0.2C, 0.5C, 1C, 2C, 3C and 5C (3.0 V, 300 K, CCCV charging (I_{CC} up to 1C, I_{CV} < 0.1C, 4.2 V)). Temperature dependent capacity was determined with CCCV (*I* <0.1C, 4.2 V, 300 K) charging and CCCV (*I* <0.1C, 3.0 V) discharging at 40 °C, 25 °C, 10 °C, 0 °C, -5 °C, -10 °C, -15 °C and -20 °C. Temperature dependent impedance was determined with a sample that was discharged ΔQ = 420 mAh from 100 % SoC to a target SoC of 22 %. At this SoC AC impedance was measured with constant potential with a Biologic VMP3 in the frequency range of 10 mHz to 10 kHz. All tests were performed in a Binder KT170 climate chamber.

Table 18 Battery properties. [176]

Layout	High power pouch
Active material	Graphite | $LiCoO_2$
Capacity	540 mAh (C_1 @ 25 °C)
Max./ min./ avg.	4.2 V/ 3.0 V / 3.7 V
Max. cont. current	+1C/ -12C
Dimensions	5.0 cm x 3.1 cm x 0.54
Electrode sheets (a/c)	18/ 17
Areal capacity	1.4 mAh cm^{-2}

During the neutron diffraction measurements, cycling was performed with a BioLogic VSP potentiostat equipped with a 100 A booster unit. Prior to each discharge and relaxation experiment, the battery was charged to 100 % SoC using a constant current constant voltage (CCCV) procedure (4.2 V, 1C, *I* < 0.05C). To prevent lithium-plating, all charging was performed at 300 K. For the diffraction experiment, the battery was placed onto a sample stick (Figure 77) and inserted into a cryostat. Helium was used as contact gas for thermal coupling.

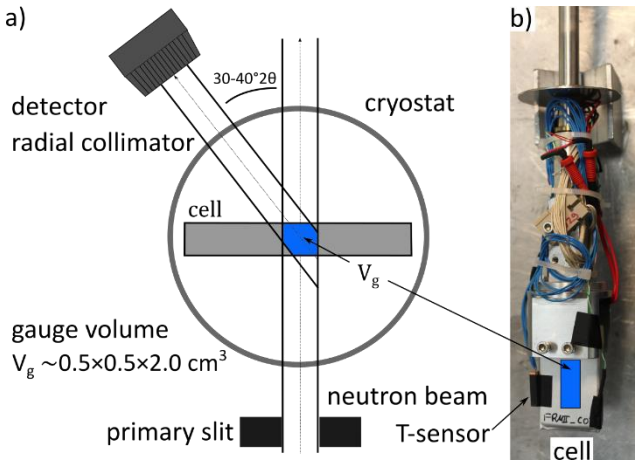

Figure 77 (a) Schematic of Stress Spec instrument with neutron beam trajectory. (b) Battery mounted on the sample holder of the cryostat. The area penetrated by the neutron beam is marked blue. [176]

7.2.3 Neutron diffraction setup

In situ neutron diffraction data were collected at the material science diffractometer STRESS-SPEC at Heinz Maier-Leibnitz Zentrum [153, 177]. The neutron wavelength was determined with NIST SRM 640d Si standard powder to λ = 2.0964(2) Å at room temperature. The Si diffraction data and refinement is shown in Figure C.1 in the appendix. The scattering gauge volume $V_g \approx 0.5$ cm^3 was set

by a 5 x 20 mm^2 entrance slit and a 5 mm radial collimator in front of the detector (Figure 77). Since the experiment focuses on lithiated graphite phases during discharge, diffraction data was collected in a limited 2θ range of 28° < 2θ < 42°. The limited fixed 2θ range allows for fast continuous data collection in 3 min intervals with sufficient signal quality. For measurements showing slow graphite phase changes during relaxation, data were combined to 6-30 min intervals to improve signal to noise ratio. The raw data correction and reduction were carried out with StressTextureCalculator [178]. Pawley analysis of the integral intensity of $Li_{1-x}C_6$ reflections was performed using Highscore [154] and MATLAB to fit the data. Integral intensities were determined using pseudo Voigt profiles. The MATLAB fit routine and Voigt profile implementation are given in detail in the appendix C1 and C2. For strongly overlapping peaks the FWHM (full width at half maximum) was constrained between reflections.

7.2.4 ND test procedure

Multiple scenarios were monitored to study the impact of discharge rate and battery temperature on the homogeneity of the graphite anode during discharge and relaxation. From a fully charged state, discharge at a rate of 0.9C (1.25 mA/cm^2) was performed for controlled temperatures of -10 °C, 0 °C and 25 °C. At 0 °C, additional higher rate discharges at 1.8C (2.5 mA/cm^2), 3.5C (5.0 mA/cm^2) and 5.3C (7.5 mA/cm^2) were conducted. For the sub-ambient temperature discharge experiments, the battery was cooled down to the target temperature for a cooling period of 45 minutes. In order to achieve the same state of lithiation in the graphite anode independent from temperature-induced polarization or a reduced capacity due to limited rate capability, an Ah-based discharge limit was used instead of a voltage cut-off. The battery was discharged to a target SoC of 22 % which corresponds to a fixed discharged amount of ΔQ = 420 mAh. The subsequent relaxation was monitored for up to 6 hours.

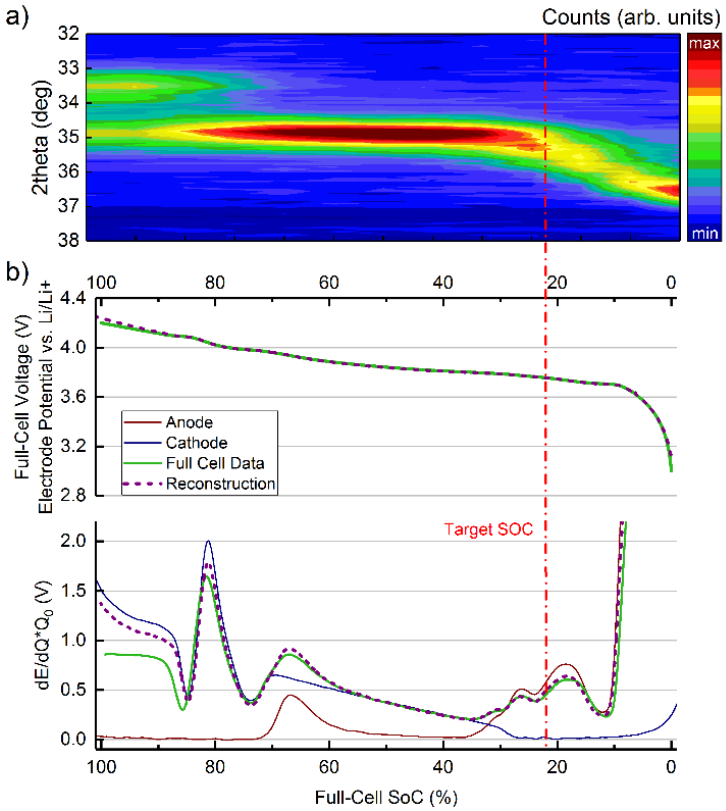

Figure 78 (a) Diffraction pattern of graphite reflection during discharging from 100 % to 0 % SoC at 0.8C. (b) $LiCoO_2$ and Graphite half-cell profiles from extracted electrodes along with the *dV/dQ* profile. The target SoC is marked as a dashed line in red. [176]

7.2.5 Target SoC determination

The particular target SoC of 22 % was chosen as a result of the following examination. As the full cell is discharged, the carbon in the anode is delithiated and undergoes a well-known structural change from LiC_6 over LiC_{12} and several lower lithiated phases $Li_{1-x}C_6$ to graphite. Figure 78 shows the two-phase regime of LiC_6 (0 0 1 reflection, 33.28 °2θ) and LiC_{12} (0 0 2 reflection, 34.66 °2θ) at 100 % - 70 % SoC. As the intensity of LiC_6 decreases, the intensity of LiC_{12} increases until only a single reflection is observed (70 % - 40 % SoC). At about 40 % SoC, the LiC_{12} reflection broadens and a continuous peak shift to higher 2θ values is observed. At 0 % SoC (3.0 V cut off voltage) the reflection at 36.28 °2θ is attributed to graphite. The corresponding *c*-axis (*d* = 6.729 Å) is in agreement with Dolotko et al. (d = 6.722 Å) [179] but higher than what is observed by Trucano et al. (*d* = 6.711 Å) [180], which indicates some residual lithiation in the measurement.

Figure 78 shows the full cell OCV (C/100) and OCV reconstruction as well as differential voltage profiles of anode and cathode half-cell data (graphite vs. Li/ Li^+, $LiCoO_2$ vs. Li/ Li^+). Good agreement between half-cell reconstruction and full cell OCV was achieved through scaling and shifting of the individual contributions of anode and cathode half-cell data. In agreement with the diffraction data, E(x) reconstruction shows the graphite voltage plateaus during phase transition regimes at 100-70 % SoC (80 mV) and 60-40 % (110 mV) full cell SoC. The *dV/dQ* data shows changes in slope and additional maxima at 25 % SoC (155 mV) and 20 % SoC (200 mV) where the ND data shows a shift to lower 2θ angle values towards graphite.

If a temperature or rate induced inhomogeneity in the electrode matrix or graphite particles is present during discharge, a fraction of the active material will deviate from the average state of lithiation of the electrode. With the target SoC set at 22 % SoC, the diffraction measurement is sensitive to phase coexistence as more delithiated states are shifted towards higher 2θ values. Graphite phases not yet affected by the discharge remain at 34.66° 2θ (LiC_{12}). In contrast, inhomogeneity at 70-40 % full cell SoC cannot be tracked as graphite does not show a change in intensity and angular position. A drawback of this approach is that, while the intensity and the existence of additional phases can be tracked, the degree of lithiation of each phase at low degree of lithiation cannot be directly determined as it is done for the LiC_6 / LiC_{12} fraction, since the description for intermediate states between LiC_{12} and graphite is subject of debate.

7.2.6 Structural analysis limitations

As outlined in section 3.3.4 the uncertainty regarding the transition mechanism limits the amount of information gained by phase analysis. According to the stage formation model, the transition from LiC_{12} to graphite is described by a periodic array of unoccupied layer gaps at low concentrations of intercalated lithium-ions [33, 34, 132]. While the staging model is well accepted for LiC_6 (Stage I) and LiC_{12} (Stage II), varying accounts of higher order stages (s > II) are given. Some recent diffraction experiments find a continuous change in *d*-spacing at lower lithiated states (x < 0.33) [46, 181]. Since only medium resolution diffraction data of a limited angular range were collected, the data basis is not sufficient to comment on the details of the phase transition. The analysis aims at providing a qualitative picture of the temperature and rate dependent phase inhomogeneity during discharge and the timescale until homogeneity is achieved. In accordance with Dolotko et al. [46] and our previous investigations of charging [22, 49] and discharging [56] processes, this work refers to lower lithiated phases as $Li_{1-x}C_{18}$ and $Li_{1-x}C_{54}$ to indicate a certain level of lithiation but without discussing structural features.

7.3 Performance tests

The performance of a battery is rate and temperature dependent. This section discusses the impact of discharge rate and temperature on the capacity and impedance of the sample cell used in this study.

7.3.1 Capacity rate dependence

At room temperature and CCCV discharge with 1C ($I < 0.1C$), the battery capacity is 540 mAh. The battery maintains most of its capacity at high rates with 530 mAh at 5C (Figure 79).

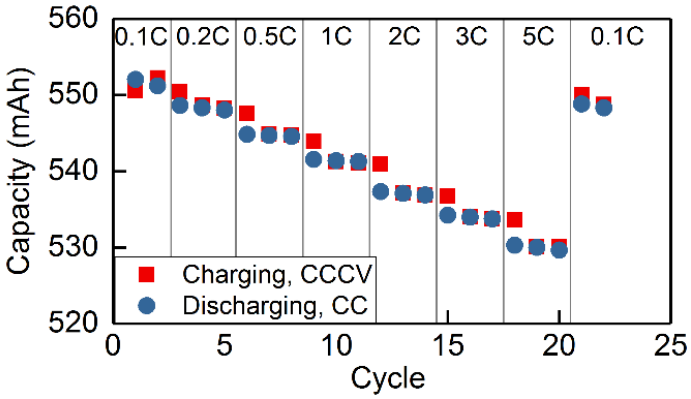

Figure 79 Rated capacity of the battery measured at 300 K with CCCV ($I < 0.1C$) charging and CC discharging. Charge and discharge rate are the same for 0.1C to 1C. For 2C, 3C and 5C the charge rate is 1C. [176]

7.3.2 Low temperature performance

When lowering temperature to -5 °C the available capacity decreases only slightly, but an increasingly larger share of capacity is discharged through the CV phase. At -15 °C more capacity is discharged in the CV phase (273 mAh) than in the CC phase (233 mAh).

The decrease in capacity at low temperatures is accompanied by an increase in cell impedance. Figure 80 shows the real part of the cell impedance for 0.01 Hz to 10 kHz. The corresponding Nyquist plots are shown in Figure 81. From 40 °C to -10 °C, the impedance increases moderately for high frequencies and more strongly at mid to low frequencies. The EIS mid to low frequency arcs are commonly attributed to the Li^+ diffusion across the SEI and to charge transfer process at the electrode/electrolyte interface. The full cell EIS contains anode and cathode contributions. The full cell impedance at low temperatures is predominantly attributed to the anode, based on $LiCoO_2$/ graphite three-electrode experiments that observed higher activation energy and higher charge transfer resistance for the anode below 25 °C [182]. The extended constant voltage phase and increase in charge transfer resistance show a limitation of charge transfer kinetics at the graphite surface in addition to the observation of multiple coexistent graphite phases at low temperatures. Rather abruptly, at -20 °C, very little capacity can be discharged in the CV phase and cell impedance overall increases sharply. This is attributed to electrolyte freezing. EC/ DMC/ $LiPF_6$ electrolyte has a well-known, poor low temperature performance due to the high melting points of EC (36 °C) and DMC (0.5 °C) [183]. Smart et al. observe a similar sharp drop to 15 % remaining dischargeable capacity at -20 °C for LP30 (1.0M $LiPF_6$ in EC:DMC (3:7)) [91]. Senyshyn et al. see reflections emerging below -15 °C in a diffraction measurement of LP 30 indicating an additional long range ordered phase not present at higher temperatures [89]. Thus, it is concluded, that electrolyte freezing did not occur during the diffraction experiment, since no electrolyte features were observed in the ND data and the cell temperature (-10 °C) was kept above the threshold of sharp overall impedance increase at -15 °C (Figure 80 b).

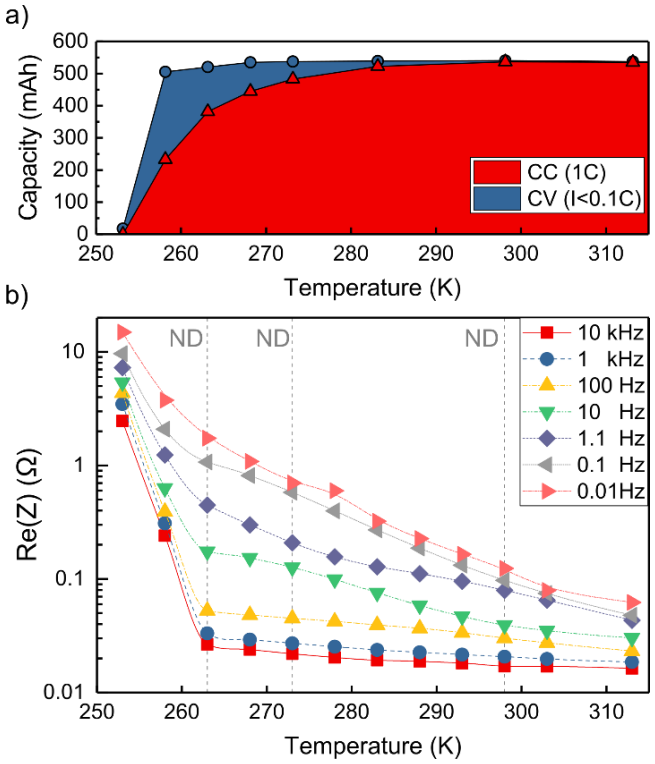

Figure 80 Battery capacity with CCCV (1C, $I < 0.1C$, 3.0 V) discharge at various temperatures (a). Charging was performed with a CCCV protocol at (1C, $I < 0.1C$, 4.2 V) charging at 25 °C. Real part of cell impedance measured at 22 % SoC for various frequencies (b). The dashed lines mark the battery temperature states during the diffraction experiment. [176]

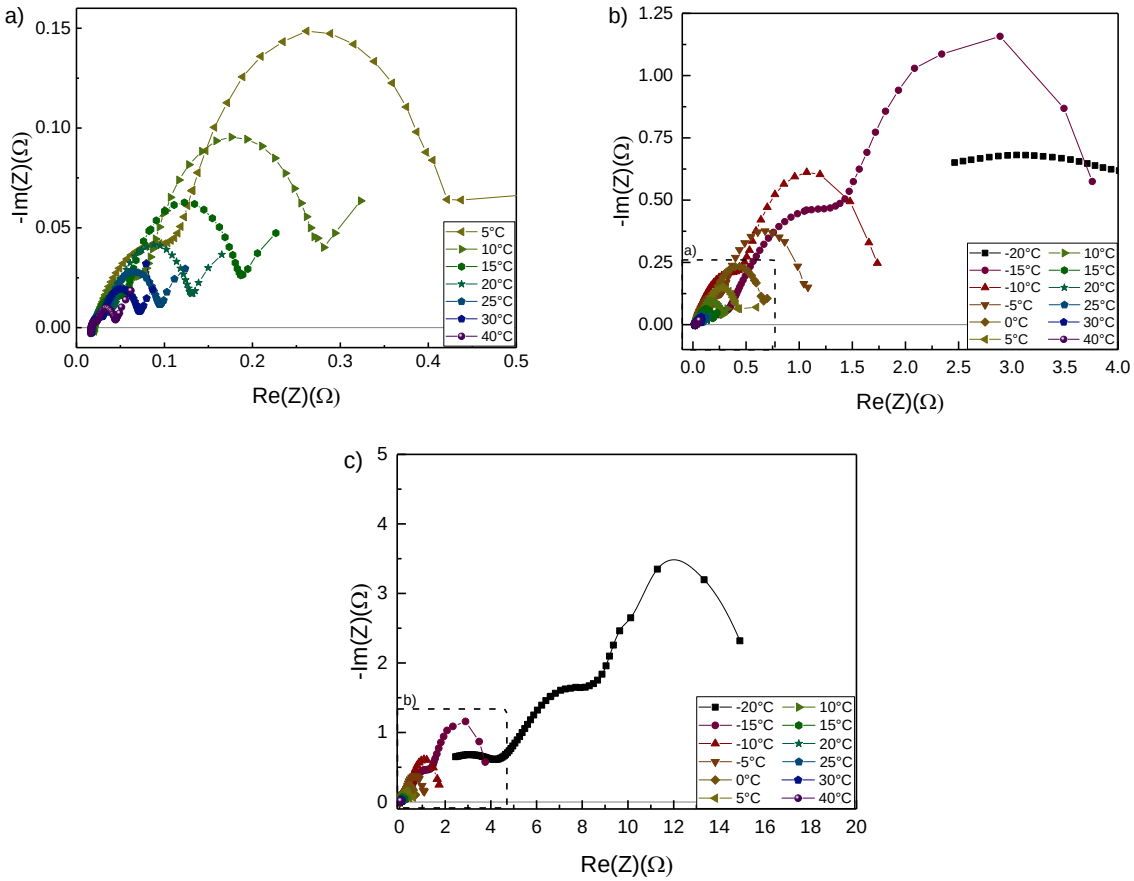

Figure 81 Nyquist plots of the temperature dependent impedance spectrum of the sample cell (a, b, c). All measurements were performed at a SoC of 22 %. [176]

7.4 Discharge and relaxation: Temperature variation

To study the impact of cell temperature on graphite phase inhomogeneity during discharge and relaxation, a fully charged cell was discharged (ΔQ = 420 mAh) to the target SoC at a moderate C-rate of 0.9C and varying temperature; 25 °C, 0 °C and -10 °C. At 0 °C cell temperature additional discharges at higher rate of 1.8C, 3.5C, and 5.3C were performed.

7.4.1 Cell potential and temperature profiles

The cell voltage during discharge and relaxation at varying temperature is presented in Figure 82 a). The average voltage during the partial discharge is 3.84 V at 25 °C but drops considerably by ~200 mV (0 °C) and ~400 mV (-10 °C) at lower temperature. Consequently, the cell voltage at the end of discharge differs for 25 °C (3.65 V), 0°C (3.36 V) and -10 °C (3.01 V). The discharge ends and relaxation begins at 0.88hours. Relaxation was monitored for ~2 hours at 25 °C and 6 hours at -10 °C where the highest degree of inhomogeneity was expected. The voltage relaxation is slower at lower temperatures. Voltage differences of 50 – 100 mV remain between -10 °C and 25 °C for ~1 hour during the rest period.

The cell voltage during discharge and relaxation at higher rates is presented in Figure 82 b). With a higher rate, the polarization increases and the average discharge voltage decreases to 3.55 V (1.8C), 3.41 V (3.5C) and 3.36 V (5.3C). A minimum and a subsequent maximum in the cell voltage is observed for the rates 3.5C and 5.3C shortly after the beginning of discharge. This is due to an improvement of transport properties and a resulting reduction in overpotentials as the battery heats up. The cell voltage at the end of discharge is 3.25 V for 1.8C and 3.22 V for 3.5C and 5.3C, higher than for 0.9C at -10 °C. With the last recorded voltage 3.737 V at 0 °C taken as reference, voltage relaxation is quickest at 5.3C (0.51 h) but only slightly slower at 3.5C (0.66 h) and 1.8C (0.72 h). In all cases, relaxation is faster than for the reference slow discharge (1.40 h).

The cell temperature change is presented in Figure 82 c) and d). During discharge, the sample heats up, reaches maximum temperature at the end of discharge and cools down during the relaxation period. With respect to the final resting temperature, the cell temperature increases by 1.8 °C (T_{rest} = 25 °C), 3.8 °C (T_{rest} = -0.2 °C) and 6.5°C (T_{rest} = -11.8 °C) for the varying temperature discharges (Figure 82 c) and by 9 °C (1.8C), 16 °C (3.5C) and 21 °C (5.3C) for the higher rate discharge. The cell heats up strongly at higher rates due to the absence of forced convection cooling inside the cryostat chamber. During relaxation, the cell cools down and T-T_{rest} decreases below 0.5 °C within 0.6 h (-10 °C), 0.4 h (0 °C) and 0.17 h (25 °C). Despite the significant temperature increase at higher rates, the time needed to cool down below 0.5 °C is similar for all cells; 0.52 h (1.8C), 0.63 h (3.5C), and 0.71 h (5.3C).

During relaxation at 0 °C, the voltage shows a qualitatively different behavior compared to 25 °C with a *dV/ dt* plateau at 1.2 to 2 hours after discharge (Figure 82 a) inlet). The periods of constant voltage increase can be explained through graphite multi-phase formation. Due to transport limitations, a fraction of the graphite remains at LiC_{12} while some of the graphite is delithiated to lower lithiated stages LiC_{18} and $Li_{1-x}C_{54}$. As the anode potential vs. Li/Li^+ is constant at 150 mV at stage II/IIL, it increases strongly at lower lithiated phases (Figure 78 b). During relaxation, the cell establishes thermodynamic equilibrium and the anode relaxes into single or two $Li_{1-x}C_y$ phases close to the mean lithium content of the discharge target SoC. The lithiation of *overshooting* (Bauer et al.) [184] graphite phases causing a voltage drop in the half-cell potential is visible as maximum or plateau in the full cell *dV/ dt* plot. The observations are consistent with Bauer et al. who find such behavior at low (0 < SoC < 0.25) and medium SoC (0.3 < SoC < 0.6) in the voltage and dilation relaxation after charging. They find that intercalation of plated lithium and temperature gradients can cause a similar and overlapping effects on the battery voltage during relaxation.

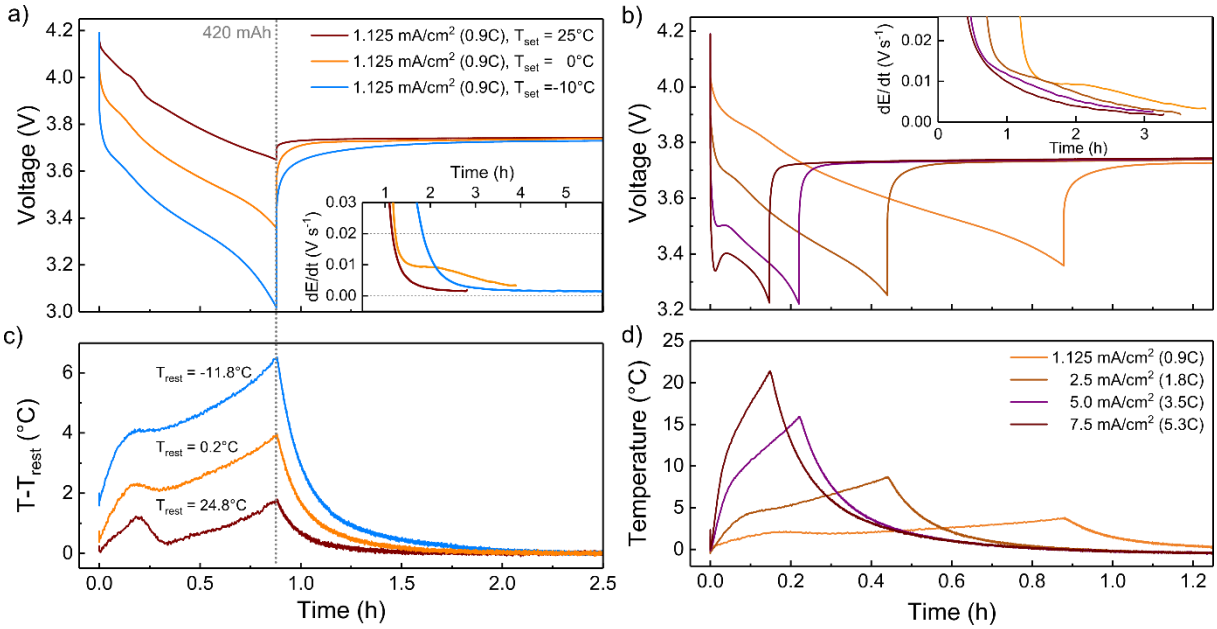

Figure 82(a) Cell voltage during discharge (0.9C, 1.25 mA/cm^2, ΔQ = 420 mAh) and relaxation at 25 °C, 0 °C and -10 °C. (b) Cell voltage during discharge and relaxation at 0 °C for various discharge rates (0.9C, 1.8C, 3.5C, 5.3C; ΔQ = 420 mAh). The inlets show the derivative *dV/dt* during relaxation. The gray dotted line marks the end of discharge. The temperature change during discharge and relaxation with respect to the final resting temperature (T_{rest}) is shown in (c) and (d). [176]

Lithium plating is excluded as a cause for the voltage relaxation features in the presented experiment, since the relaxation is measured after discharge and the samples were charged at a moderate rate at 25 °C where no plating is expected for a high power battery [49]. It can also be excluded that the voltage response is caused by the temperature change of the battery, considering that the shoulder in the *dV/dt* plateau is observed for up to 2.5 hours at 0 °C and the temperature gradients for only 0.4 hours (T-T_{rest}< 0.5 °C). In agreement with Bauer et al., the effect is not observed at higher temperatures (25 °C). In contrast to Bauer et al., the multi-phase voltage feature diminishes with higher rate (1.8C, 3.5C) and is not present at 5.3C. This can be explained by the temperature increase of up to 20 °C at higher rates compensating a potential increase in polarization due to higher currents.

7.4.2 ND contour plots, reflection intensities, and *d*-spacing

The in situ neutron diffraction data of the $Li_{1-x}C_6$ reflections during discharge and relaxation at 25 °C (a, d) 0 °C (b, e) and -10 °C (c, f) are shown in Figure 83. For comparison, selected points in time are marked in the contour plot and the reflection intensity is shown in the subplots a, b, c. The time evolution of the integral intensity (a) and *d*-spacing (b) of the graphite phases present during relaxation is presented in Figure 84. While at the beginning of discharge all three measurements show equal LiC_6/ LiC_{12} balance and a subsequent decrease in LiC_6 intensity with a corresponding intensity increase of LiC_{12}, pronounced differences arise at the later stages of discharge and relaxation that support the multi-phase interpretation of the voltage relaxation feature.

At 25 °C, a slightly broadened reflection with some remaining LiC_{12} (34.9°) and a second, lower lithiated phase (35.5°) shifted to higher angle is observed at the end of discharge. The integral intensity of the LiC_{12} is about 1400 a.u. at the end of discharge and decreases quickly during relaxation while the intensity of the second phase increases. The *d*-spacing of the lower lithiated phase increases continuously from 3.455 Å to 3.471 Å while the LiC_{12} reflection intensity reduces. In agreement with previous work [22, 56] this phase is identified as $Li_{1-x}C_{18}$. After 30 minutes, little change is seen in the ND data (Figure 83 a, d) and the profile can be fitted well with only a single $Li_{1-x}C_{18}$ phase.

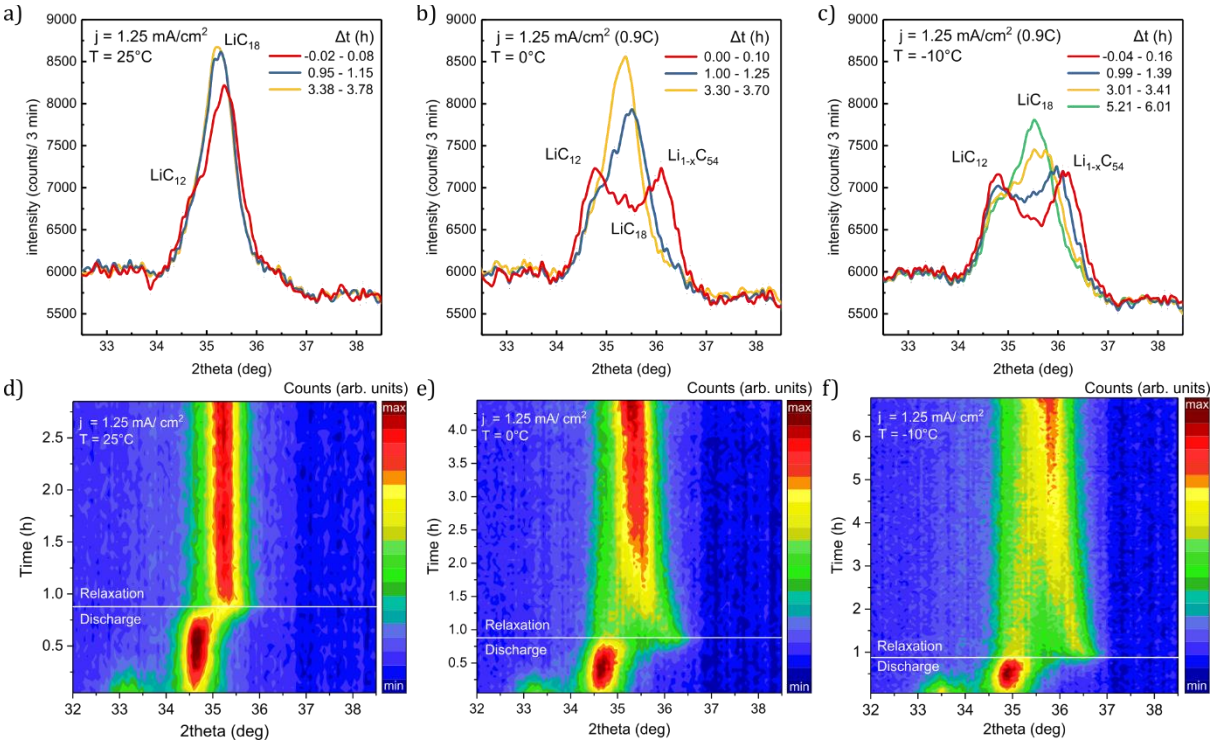

Figure 83 Diffraction data collected during discharge (0.9C, ΔQ = 420 mAh) and subsequent relaxation at temperatures 25 °C (a, d), 0 °C (b, e) and -10 °C (c, f). The top row (a-c) shows the $Li_{1-x}C_6$ reflections at the end of discharge (~0 h, red) and later during discharge (~1 h: blue, ~3 h: yellow, ~6 h: green). The bottom row (d-f) shows the corresponding surface plot of all patterns. Each pattern is collected over 3 minutes. (High intensity: red, low intensity: blue). [176]

In comparison to 25 °C, the anode shows greater polarization after discharge at 0 °C (Figure 83 b, e; Figure 84 a, b). Two distinct phases, LiC_{12} (34.9°) and a lower lithiated phase (36.2°) are observed with about equal integral intensity (~3800 a.u). With a *d*-spacing of 3.402 Å, this phase is identified as $Li_{1-x}C_{54}$ in agreement with previous work [22, 56]. Similar to what is observed at 25 °C, the reflection intensity and thus the amount of LiC_{12} decreases during relaxation while the $Li_{1-x}C_{54}$ phase is lithiated for both experiments at 0 °C and -10 °C. Consequently, the reflection intensity increases and the graphite phase is shifted to higher *d*-spacing values. Compared to 25 °C, this process is much slower at 0 °C. One hour after the end of discharge LiC_{12} still maintains 30 % of the combined reflection intensity. After 1.8 hours the intensity change and $Li_{1-x}C_{54}$ reflection shift slow down markedly. The anode maintains a degree of polarization until the end of measurement at 3.7 hours. The lower lithiated phase, initially identified as $Li_{1-x}C_{54}$, reverts back to $Li_{1-x}C_{18}$ (d = 3.453 Å) towards the end of the measurement. The slightly lower *d*-spacing, compared to the final state of LiC_{12} at 25 °C (d = 3.471 Å), is explained by some lithium remaining in the LiC_{12} state.

At -10 °C the diffraction data show an even greater polarization and a slower relaxation process than for 25 °C and 0 °C. Similar to the situation at 0 °C, two phases with about equal integral intensity, LiC_{12} (4000 a.u.) and $Li_{1-x}C_{54}$ (3450 a.u.) are observed at the end of discharge at -10 °C. $Li_{1-x}C_{54}$ is shifted to d = 3.387 Å, which indicates a slightly lower degree of lithiation compared to the corresponding graphite intercalation phase (d = 3.402 Å) at 0 °C. Over several hours, phase separation is clearly visible during relaxation (Figure 83). After 5.8 h relaxation, LiC_{12} (d = 3.510 Å) remains with 28 % of the combined integral intensity. The final *d*-spacing of the $Li_{1-x}C_{54}$ reflection (d = 3.435 Å) is lower than observed at 0 °C (d = 3.453 Å) which can be attributed to the temperature effect. The broadening of the anode reflection due to multiple phases present causes a lower observed maximum intensity for the last measured reflection data at -10 °C (7750 counts/ 3min), 0 °C (8450 counts/ 3min) and 25 °C (8650 counts/ 3min).

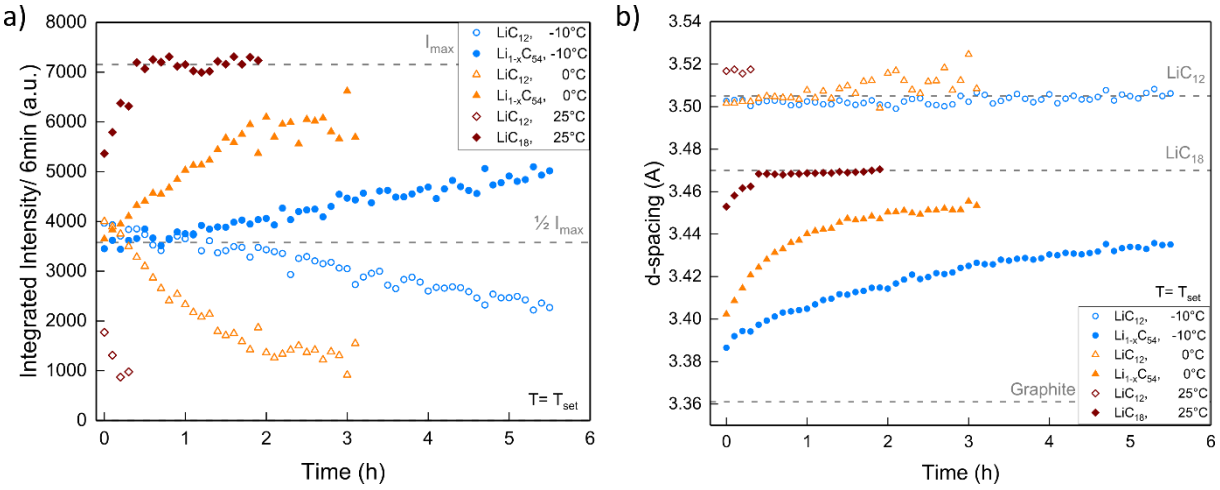

Figure 84 Integral reflection intensities (a) and corresponding *d*-spacing (b) of LiC_{12} and lower lithiated phases $Li_{1-x}C_6$ during relaxation after discharge at 25 °C, 0 °C, and -10 °C. Intensity and *d*-spacing reference values are marked with a gray dashed line as a guide for the eye. [176]

Notably, the *d*-spacing of LiC_{12} differs at the beginning of the relaxation process between measurements at 25 °C (3.517 Å) and at lower temperatures, 0 °C and -10 °C (3.502 Å) (Figure 84 b). The difference of 0.015 Å can be partially explained by thermal contraction. With a thermal expansion coefficient of $\alpha_c = 6.5 \times 10^{-5}$ Å K^{-1} for lithiated graphite [185], the temperature change from 25 °C to -10 °C corresponds to a shift of -0.008 Å (3.517 Å → 3.509 Å). The remaining difference of 0.007 Å is within the combined *d*-spacing uncertainty of 0.004 Å for both phases.

In summary, the multiphase interpretation of the voltage relaxation feature is in good agreement with the phase coexistence observed in the anode during discharge and relaxation. At 25 °C neither voltage nor diffraction measurements show lasting phase coexistence. At 0 °C the intensity change slows and $Li_{1-x}C_{54}$ reflection shift decreases for up to 1.8 hours after end of discharge (2.6 hours after start of discharge), which is the same time that the end of the *dV/dt* plateau is observed.

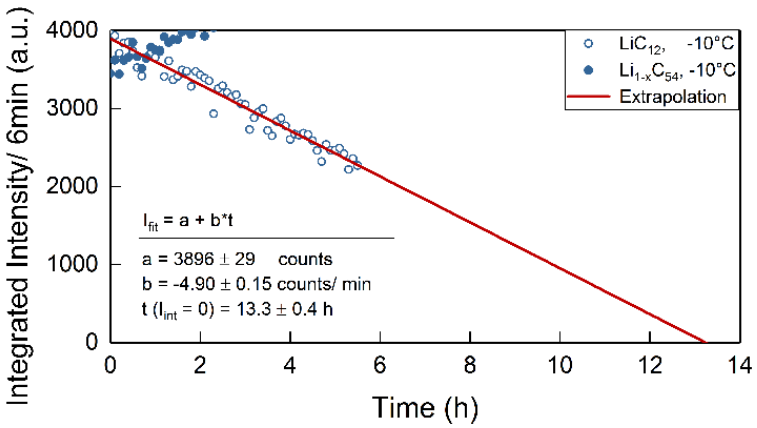

Figure 85 Linear extrapolation of the slowly decreasing integrated intensity share of LiC_{12} during relaxation after discharge at *T* = -10 °C. [176]

7.5 Interpretation of graphite phase coexistence

The observed graphite phase evolution and voltage relaxation can be explained well with phase separation due to transport limitations at low temperatures. This section discusses whether the phase separation can be localized and transport limitations on cell, layer, or particle level based on the sample and electrode design can be differentiated. Figure 86 shows potential contributions to graphite inhomogeneity observed in neutron diffraction experiments.

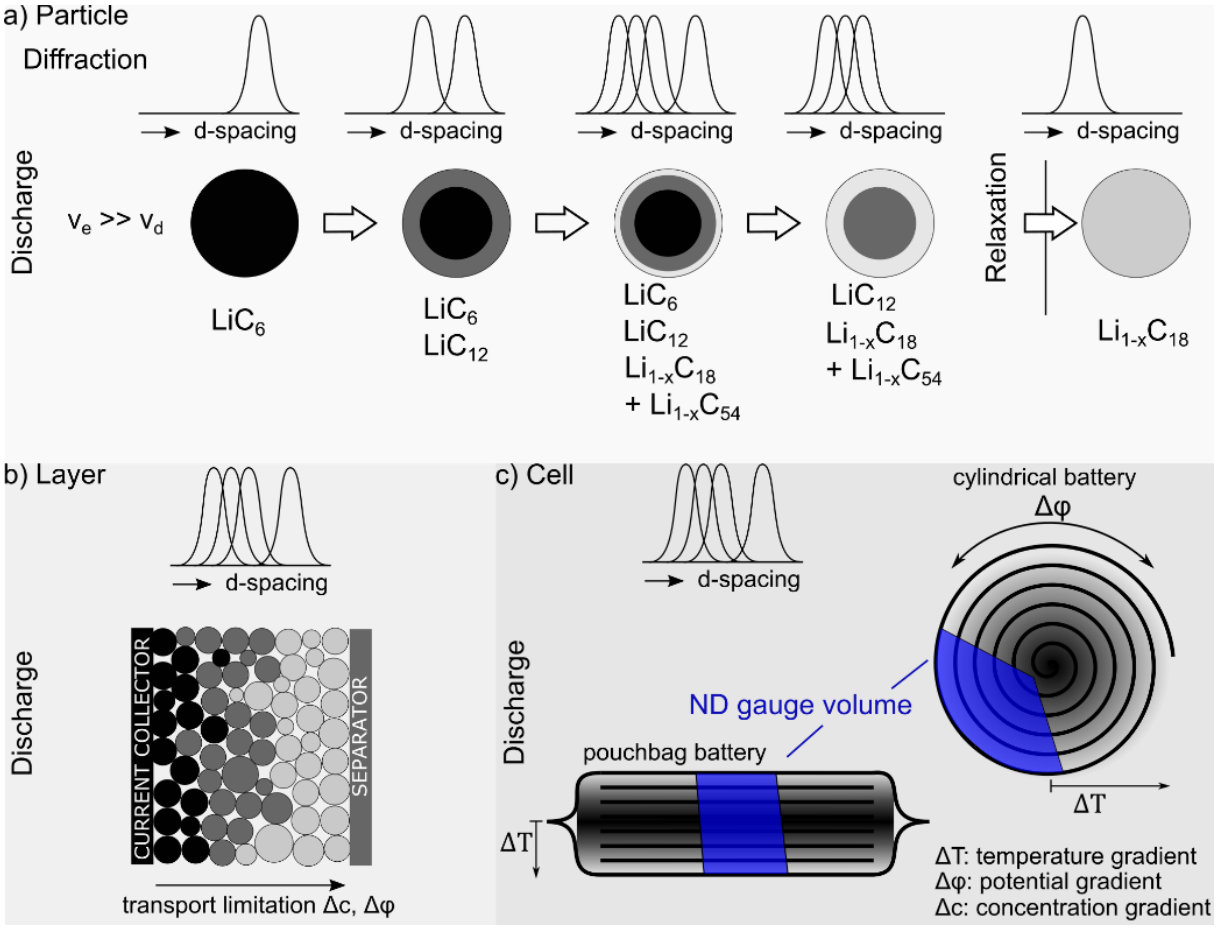

Figure 86 Possible causes for graphite inhomogeneity observed in neutron diffraction experiments at particle, layer, and cell level. a) *Particle:* Model of lithium distribution in a simple spherical particle and expected diffraction patterns if the rate of lithium extraction (v_e) is higher than the diffusion within the particle (v_d). Partially reprinted from Zinth et al. [56] with permission from Elsevier. See Zinth et al. for the opposite case $v_e << v_d$. b) *Layer:* Different degrees of lithiation between particles due to particle properties (size distribution) and transport limitations. c) *Cell:* Macroscopic SoC inhomogeneity in the cell due to temperature gradients (core – surface) or potential gradients (current collector). [176]

7.5.1 Potential gradients

With the neutrons fully penetrating the cell, data were commonly collected from a large scattering gauge volume (Figure 86). Simulations and experiments show that potential gradients due to the ohmic resistance of the current collector can cause local SoC inhomogeneity [64, 110]. This is pronounced for high-energy cylindrical cells with a single or few tabs and current collectors of ~1 meter length (18650). [58, 64] Thus, the gauge volume of an in situ ND measurement of a cylindrical cell typically comprises electrode layers with varying distance to the tab. If a potential gradient induced local SoC difference is present, multiple simultaneously present graphite states will be observed. Similarly, temperature gradients within a cell with a typically convection cooled surface and hotter core can cause local SoC differences due to higher overpotentials and slower kinetic transport processes at lower temperatures [25, 29]. Both effects are present in cylindrical and pouch bag batteries, but the contribution to the neutron diffraction pattern is significantly smaller for the chosen small format pouch cell. In our previous relaxation experiment with a cylindrical cell, the gauge volume averaged over 15 layers corresponding to ~50 cm tab distance (single tab) [22]. For the sample cell, the gauge volume averages over 20 layers but the variation in tab distance is < 2 cm. Despite the 1/25 reduction in tab distance, pronounced graphite phase coexistence at low temperatures as reported by Zinth et al. [22] is still observed. This supports the assertion that the measured lithiation gradients are not caused by local SoC gradients due to current collector induced potential drops.

7.5.2 Temperature homogeneity

Sufficient thermal homogeneity can be assumed in in all test scenarios. The maximum distance between center and surface is 0.27 cm for the sample cell compared to 0.9 cm for an 18650-cell configuration. Assuming identical electrode properties and thus similar heat transfer properties orthogonal to the electrode layers, the heat transfer resistance from surface to center is about three times lower for the pouch cell reducing the temperature gradient in high rate test scenarios. The surface-center temperature gradient can be approximated with the Biot number *B* [88].

$$B = \frac{h \frac{t_{\mathrm{Batt}}}{2}}{k} \tag{67}$$

With a total thickness t_{Batt} of 5.4 mm and assuming a convective heat transfer coefficient h = 5 $\mathrm{Wm^{-2}K^{-1}}$ (no ventilation in cryostat) at the cell surface and a thermal conductivity $k_{\perp}$ = 1 $\mathrm{Wm^{-1}K^{-1}}$ and $k_{\parallel}$ = 33.9 $\mathrm{Wm^{-1}K^{-1}}$ [87], the Biot number amounts to $B_{\perp} < 0.02$ in orthogonal direction and $B_{\parallel} < 0.003$ in the in-plane direction. It follows that the temperature at the core of the battery, and thus in the observed volume in the center, deviates by less than 2 % from the measured surface temperature [186]. The temperature deviation is thus less than 0.5 °C in the test scenario with the strongest heating (I = 7.5 $\mathrm{mA/cm^2}$, ΔT = 21 °C). From this follows that for all test scenarios the temperature variations in the gauge volume are too small to cause the observed graphite phase differences, given the small influence of less than 1 °C temperature change on electrolyte conductivity and diffusivity [25].

7.5.3 Particles and electrode morphology and transport

The graphite phase coexistence can be explained well with particle and electrode transport limitations (Figure 86), which can be shown by analyzing the electrode properties. Figure 87 shows top view (a) and cross view (b) SEM images of the anode. The particle size (c) and shape (d) is determined by matching 110 particles with an elliptical shape. The visual impression of spherical particles is confirmed by the ratio of long axis *c* and short axis *a* which is $c/a < 1.2$ for the majority of particles (d). Idealizing the particles as spherically shaped, the diameter distribution can be plotted and fitted well with normal distributions (c). The average diameter is d_{50} = 16.4 µm (d_{10} = 10.5 µm, d_{90} = 22.4 µm).

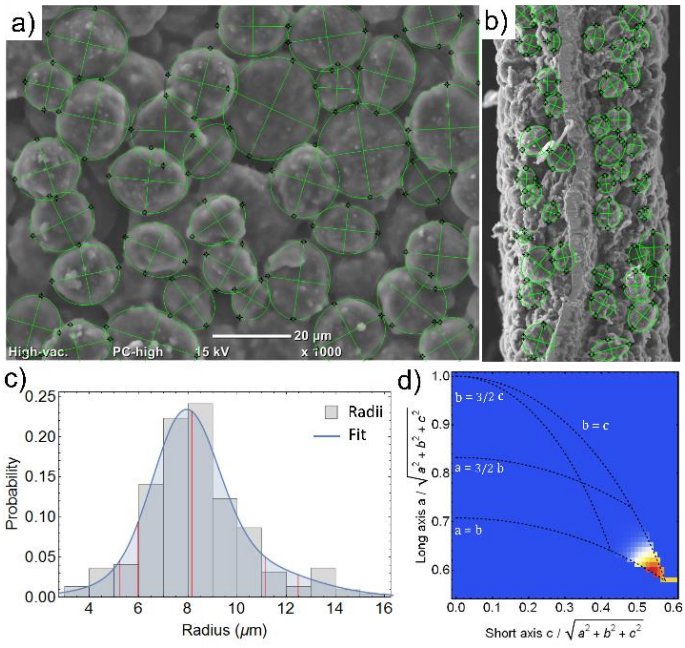

Figure 87 Top view (a) and cross view (b) SEM images of the anode. (c) Visually extracted graphite particle diameter distribution histogram and distribution fit. Red lines mark d_{95}, d_{90}, d_{50}, d_{10}, and d_5 quantile values. Particle shape distribution showing the short axis a plotted against the long axis c (d). Red pixels in the color map mark the most common axis ratio. [176]

7.5.4 Solid diffusion limitations

The observed phase coexistence can be explained by lithiation gradients within particles due to slow lithium diffusion. Figure 86 shows an idealized graphite particle upon delithiation with the speed of delithiation exceeding the rate of transport within the particle. In a process described by Heß et al. as shrinking annuli model, [133] the outer volume of the particle is delithiated causing layers with graphite at different stages of lithiation. Since the neutron wavelength is small enough to resolve these areas, each layer contributes to the diffraction pattern. At the end of discharge, a set of differently lithiated graphite layers remains, depending on the target SoC. During relaxation, lithium diffuses into less lithiated regions until thermodynamic equilibrium is achieved. In the example given in Figure 86, graphite LiC_{12}, $Li_{1-x}C_{18}$ and $Li_{1-x}C_{54}$ equalize until only $Li_{1-x}C_{18}$ is present and the corresponding diffraction pattern, initially showing the corresponding three reflections, shows only the remaining $LiC_{1-x}C_{18}$ reflection. Whether the final state of relaxation is a single stage (e.g. LiC_{12}) or a phase transition regime with two simultaneously present stages (e.g. LiC_{12} – $Li_{1-x}C_{18}$) depends on the average lithiation after discharge.

As shown in Figure 86, solid diffusion limitations of lithium in graphite can in principle describe the observed diffraction patterns. To test this assumption, the observed relaxation time is compared with the relaxation time expected from the solid diffusion process for the given particle size. The diffusion time τ for a given path can be approximated with $\tau = x^2/(4\,D_e)$ with D_e being the solid diffusion constant in Fick's law [29]. Given the symmetrical shape of the particle, the radius of a large particle $d_{90}/2$ = 11.2 µm is used as the diffusion length x. The estimated diffusion coefficients are $D_{e25} = 1.7 \cdot 10^{-10}\ \mathrm{cm^2\ s^{-1}}$ at room temperature and $D_{e0} = 2.8 \cdot 10^{-11}\mathrm{cm^2\ s^{-1}}$ at 0 °C. For -10 °C at the end of measurement time the diffusion coefficient is $D_{e-10} = 1.5 \cdot 10^{-11}\mathrm{cm^2 s^{-1}}$ and $D_{e-10E} = 0.7 \cdot 10^{-11}\ \mathrm{cm^2 s^{-1}}$ for the extrapolated time of equilibrium. The results are summarized in Table 19. For a proper assessment of these values, one has to consider that graphite is a complex material with a range of different morphological configurations [36, 37] and a varying degree of crystallinity, as well as temperature dependent [27, 28], anisotropic [39, 136], and stage dependent diffusion parameters [38, 39].

Table 19 Estimated effective graphite solid diffusion constants. [176] *Experiment end **Extrapolated

Temperature (°C)	Relaxation time (h)	Effective diffusion constant (10^{-11} $cm^2\ s^{-1}$)
25	0.5	17
0	3.1	2.8
-10	5.8*	1.5
-10	13.3**	0.7

Graphite bulk diffusion is three to four orders of magnitude faster than the observed relaxation times and thus cannot explain the phase coexistence. Based on Persson et al. who measured an in-plane diffusivity of highly ordered pyrolytic graphite (HOPG) of $4.4 \times 10^{-6}\ \mathrm{cm^2 s^{-1}}$ in an experiment and $10^{-7} - 10^{-8}\ \mathrm{cm^2 s^{-1}}$ based on first principle simulations of stage I and II graphite [39], we calculate the relaxation time for a polarized HOPG particle of equivalent size (d_{90}) to 0.07 s. Additionally, at 22 % SoC in our experiment, the graphite is at a low degree of lithiation where the lithium ions are expected to have even increased mobility (liquid like stages defined as L) compared to stage I and II graphite (dense stages). Levi et al. and Umeda et al. found one order of magnitude higher diffusivity for liquid like stages compared to dense stages [95, 135]. With the shrinking annuli description as depicted in Figure 86, phase boundaries between segments with different degree of lithiation are present within a particle. Consequently, the solid diffusion coefficients calculated from the particle size and relaxation time are only effective values averaging over these layers. Additionally to the stage dependence of diffusion speed, limitations through diffusion at phase boundaries have to be taken into account.

Persson et al. find much slower lithium-ion transport along grain boundaries ($\sim 10^{-11}$ cm^2 s^{-1}), which is slightly lower than what we approximated at room temperature but higher than what is observed at -10 °C. Overall, this is in better agreement with our data which suggests the limiting factor is the transport between crystallite boundaries rather than bulk transport. This is also consistent with earlier investigations of the graphite diffusion mechanism with galvanostatic intermittent titration technique (GITT) [187], potentiostatic intermittent titration technique (PITT) [188], and other electrochemical methods [27] that find diffusion constants $\sim 10^{-9} - 10^{-11}$ cm^2 s^{-1} for non-highly ordered graphite. The slowdown in relaxation with the temperature drop from 25 °C to -10 °C corresponds roughly to a reduction of the effective diffusion constant by one order of magnitude. This is in good agreement with Kulova et al. [28] who reports a similar slowdown from $1.9 \cdot 10^{-10}$ cm^2 s^{-1} (23°C) to $1.2 \cdot 10^{-11}$ cm^2 s^{-1} ($-15\ °C$) and Zhang et al. who reports a drop from $\sim 10^{-9}$ cm^2 s^{-1} to $\sim 10^{-10}$ cm^2 s^{-1} [27]. The diffusion coefficient D_{e-10E} estimated for -10 °C is in agreement to the results of our previous work [22] with a high energy cylindrical cell after charging.

7.5.5 Layer transport limitations

The gauge volume of 0.5 cm^3 collects the signal of a large number of particles and thus covers the whole size distribution and particles at various positions in the electrode layer. The state of lithiation of a particle may deviate from the average lithiation of the electrode due to numerous causes such as particle size, transport limitations, and electrical isolation. Smaller particles have a surface to volume ratio more favorable for fast lithiation since the ratio decreases with 3/*r* for spherical particles. Some particles may be less connected in the layer due to resistance differences from less contact area in the conductive network [77]. Lithium concentration gradients may arise in the layer due to electrolyte transport limitations [100, 103], especially in highly tortuous electrodes [41], causing graphite lithiation gradients through the layer with, i.e. greater delithiation close to the separator during discharge (Figure 86). All these effects lead to multiple, simultaneously observed graphite phases in the diffraction pattern. Despite these additional effects, the observed timescale of lithiation processes and effective diffusion constants agree with a core-shell mechanism as outlined by Hess et al. [133] and Seidlmayer et al., who observed gradual particle lithiation in small angle scattering experiments of anodes during discharge at a moderate rate [189].

7.6 Discharge and relaxation: Discharge rate variation

The neutron diffraction data of the graphite reflections (32° to 38° 2θ) during discharge and relaxation at 0 °C under variation of discharge rate is shown in Figure 88. The fully charged cell is discharged at 1.8C (a,d), 3.5C (b,e) and 5.3C (c,f) while diffraction data were continuously recorded over 3 min intervals. The time evolution of the integral intensity (a) and *d*-spacing (b) during relaxation is shown in Figure 89. Despite a rate increase by a factor of two to six, the anode shows a lower degree of polarization and faster relaxation compared to 0.9C measurements at 0 °C and -10 °C. Polarization of the anode with some remaining LiC_{12} and at least one additional phase with lower degree of lithiation ($Li_{1-x}C_{54}$) is observed for all rates. At 1.8C, the phases are well separated with more LiC_{12} integral intensity (3800 a.u.) than $Li_{1-x}C_{54}$ (3200 a.u.). In comparison, the contribution of the lower lithiated phase has an approximately equal share in intensity at 1.8C. Similar to the low-rate discharge at 0 °C the *d*-spacing of the $Li_{1-x}C_{54}$ phase shifts to 3.406 Å (at 1.8C), 3.412 Å (at 3.5C), and 3.406 Å (at 5.3C) respectively. At one hour after discharge, relaxation is well advanced for all higher rates. The remaining LiC_{12} contribution of approximately 25 % is seen in the asymmetry of the reflection in Figure 88 (blue). The $Li_{1-x}C_{54}$ phase after 5.3C discharge is lithiated slightly faster during relaxation than at lower rates, which causes an earlier shift to higher *d*-spacing values (Figure 89) and a less broadened reflection with a higher maximum intensity (8000 counts/ 3 min) compared to (7800 counts/ 3 min) at 1.8C and 0.9C. In summary, the cell shows a similar degree of polarization and slightly faster relaxation process at higher rates compared to the slow discharge at 0 °C.

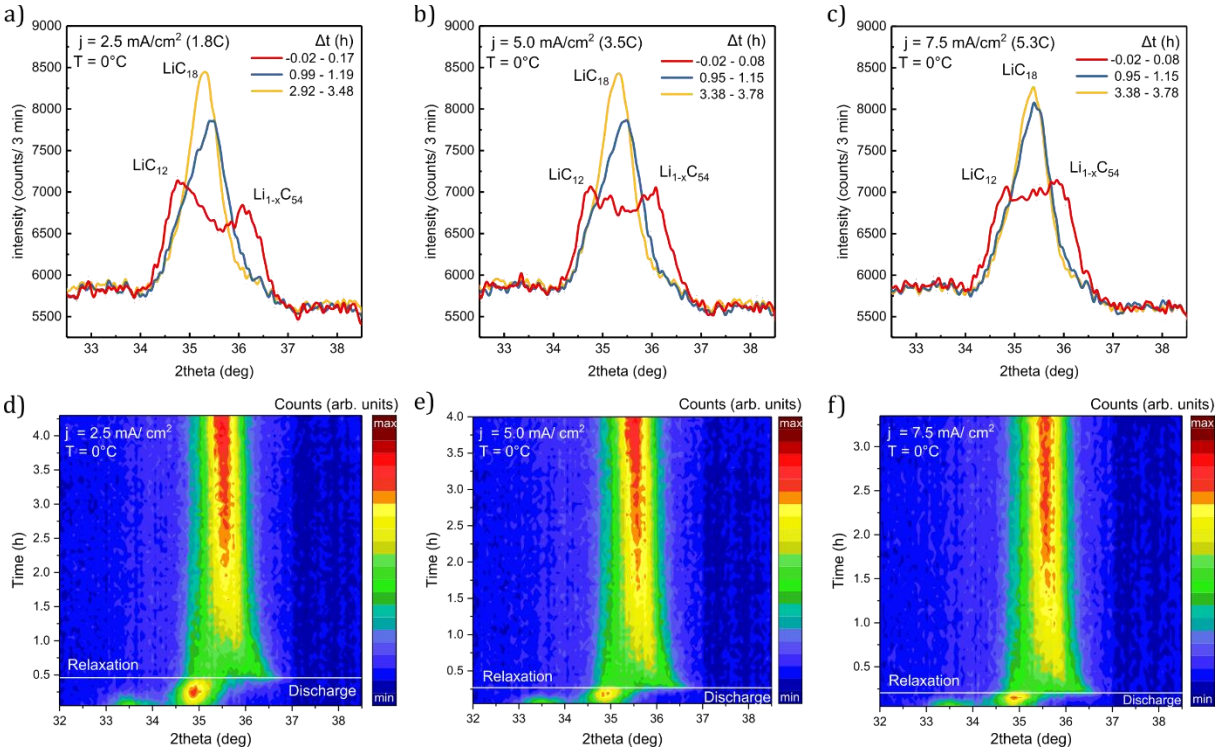

Figure 88 Diffraction data collected during discharge at 0 °C (ΔQ = 420 mAh) and subsequent relaxation at discharge rates of 1.8C (a, d), 3.5C (b, e) and 5.3C (c, f). The top row shows the $Li_{1-x}C_6$ reflections at the end of discharge (~0 h: red) and during relaxation (~1h: blue; ~3h: yellow). The bottom row shows the corresponding surface plot of all diffraction patterns. Each pattern is collected over 3 minutes. (High intensity: red, low intensity: blue). [176]

This can be explained by the increased heating of the cell at higher rates that causes temperature increases of 9 °C (1.8C) to 21 °C (5.3C) compared to only 4 °C at 0.9C. The self-heating of the cell reduces charge transfer resistances (Figure 80) and increases diffusion rates in solid and liquid phases [25, 28] and thus compensates the effect of higher rate. After one hour, when the cell has the same temperature for all discharge scenarios, intensity change and $Li_{1-x}C_{54}$ reflection shift continue at similar speed. In addition to the effect of cell heating, the lack of polarization increase at higher rates is consistent with the high power layout of the sample in contrast to our previous results with a high energy cylindrical cell where we observe a more pronounced inhomogeneity at higher rates [56]. The anode layer thickness of 51 ± 2 µm corresponds to the sum of three average particle diameters. With the close to spherical particle shape the electrode has a low tortuosity of $\tau_z = 1.6$ and a McMullin Number of $N_M = 4$, as determined from SEM 2D reconstruction, finding a Bruggeman exponent of $\alpha_z = 0.51$. This is close to the often used Bruggeman approximation $\alpha = 0.5$ for ideal spheres [190]. While limitations of the 2D reconstruction compared to 3D tomography [42] and other methods [41] have to be considered, tortuosity and McMullin Numbers are low compared to flake graphite [41]. The conclusion is, that the neutron diffraction data do not show a contribution of additional layer inhomogeneity at higher rates since a qualitative change in polarization or relaxation time is not observed. The low temperature and medium rate discharge scenario is most critical in terms of anode polarization since self-heating improves transport parameters and reduces polarization as well as relaxation time at higher rates. It is less clear to which extent particles differ in lithiation due to differences in size and surface area. Phase inhomogeneity and equalization between particles, if present, would be visible in the anode diffraction data in similar manner as solid diffusion limitations.

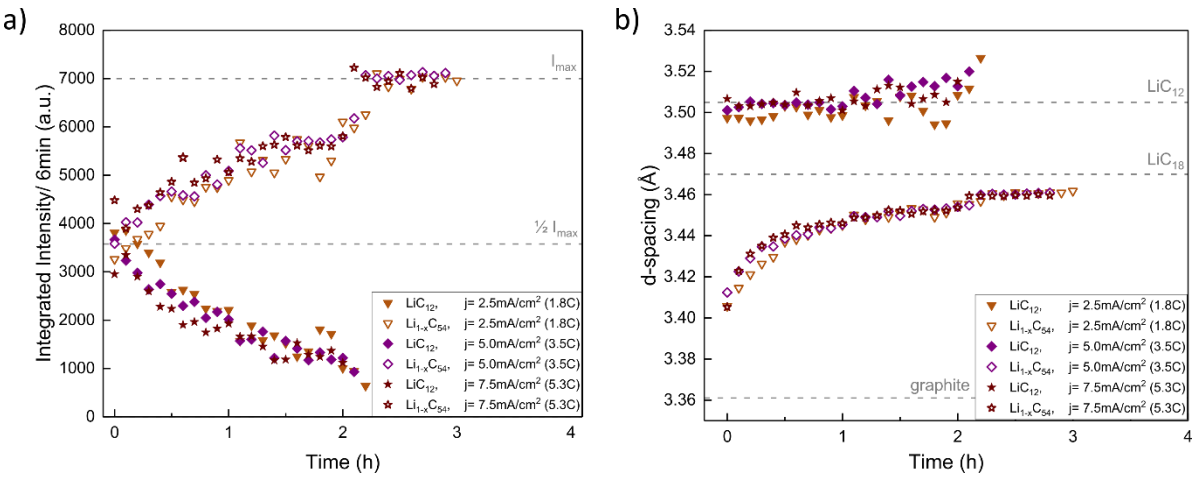

Figure 89 Integral reflection intensities a) and corresponding *d*-spacing b) of LiC_{12} and lower lithiated phases $Li_{1-x}C_{18}$ and $Li_{1-x}C_{54}$ during relaxation after discharge at 0 °C and 1.8C, 3.5C and 5.3C. Intensity and *d*-spacing reference values are marked with a gray dashed line as a guide for the eye. [176]

Equalization between particles through lithium exchange with the electrolyte slows considerably at low temperatures due to lower lithium diffusivity in the electrolyte and higher charge transfer resistance at the electrolyte particle interface. With graphite particle radii ranging from 4 µm to 16 µm (Figure 87) in the sample cell, a contribution to the observed phase coexistence cannot be excluded.

7.7 Conclusion

A combination of neutron diffraction, electrochemical cycling, and impedance measurements was applied to study the performance of a high power $LiCoO_2$/graphite pouch bag battery in the temperature range of -20 °C to 40 °C. The battery shows decreasing capacity and increasing charge transfer resistances as well as greater polarization during discharge with decreasing temperature.

In situ diffraction data of the anode during discharge and subsequent relaxation show an inhomogeneous lithiation of graphite with multiple coexistent phases. After discharge, the graphite phases equalize towards a single phase or two phases close to mean lithium content. Phase changes during relaxation are not only observed in diffraction but can also be seen directly in the full cell voltage response during relaxation. While barely polarized at room temperature, the graphite lithiation is strongly inhomogeneous after discharge at -10 °C with relaxation processes lasting longer than 6 hours. A rate of less than 1C is sufficient to cause strong polarization at 0 °C. Higher rates up to 5C do not increase polarization but rather decrease the relaxation time due to considerable self-heating of the battery during charge. The experiments show that in absence of active cooling the low-rate low-temperature use case is most prone for high anode polarization. Expanding on previous work with high energy cylindrical cells, we are able to exclude SoC inhomogeneity in the gauge volume due to internal temperature gradients as origin for the observed lithiation gradients, by sample choice of a small format pouch cell. Similarly, SoC gradients due to potential drops along the current collector were strongly reduced. The observed effects can best be explained with slow lithium diffusion in the solid phase. Through analysis of the relaxation times, an effective solid diffusion constant of $1.7 \cdot 10^{-10}\ \mathrm{cm^2\ s^{-1}}$ at room temperature and $0.7 \cdot 10^{-11}\ \mathrm{cm^2\ s^{-1}}$ at -10 °C could be derived for low lithiated graphite phases. This is attributed to slow lithium transport limited by grain boundaries between different phase domains or crystallites within the particles rather than in-plane transport. The experiment demonstrates that in situ neutron diffraction during discharge and equilibration processes provides lower and upper limits on graphite phase inhomogeneity. This approach can be applied to investigate the effectiveness of novel methods of electrode optimization, such as electrode structuring, in a complete cell system.

8 In situ investigation of anode layer inhomogeneity

The results of the relaxation experiment have shown that it is feasible to investigate fast discharge and relaxation experiments with small pouch cells by means of in situ neutron diffraction. To expand on the insights gained into graphite polarization and the timescale of graphite relaxation processes an additional experimental proposal was submitted to the MLZ. On 11.09.2015 the proposal *Effect of anode coating thickness on low temperature relaxation in lithium-ion batteries* was submitted for the instrument STRESS-SPEC under the Proposal no. 11535. Four days of measurement time were granted from November 7th to 10th 2016. Approximately one day was allocated for calibration and setup. The experiment was planned and conducted with Dr. Stefan Seidlmayer. Technical support was given by the instrument scientists Dr. Michael Hofmann, Dr. Weimin Gan, and Dr. Joana Rebelo-Kornmeier.

The student Maximilian Drexl supported the preparation for the ND experiment as a part of his master thesis: *Relaxationsverhalten von Konzentrationsgradienten in Lithium-Ionen-Zellen im Tieftemperaturbereich*. His contribution includes measurement and analysis of the custom-built sample cells, half-cell and symmetrical cell samples and post mortem material samples prepared by the author. Furthermore, the student analyzed particle radii distributions utilizing a script provided by the author. Data previously presented in the students' work is referenced with *Data from* [191].

After a brief outline of the experiment, the sample cell properties and the anode material characteristics are presented. The neutron diffraction data of discharge and relaxation is analyzed and the observed anode phase inhomogeneity is discussed in terms of transport limitations.

8.1 Experiment outline

The goal of the experiment, as outlined in the proposal, was to investigate the effect of anode layer thickness on the extent to which multiple LiC_{12} phases coexist during discharge and the speed at which these phases equalize to a single phase during relaxation. A specialized manufacturer produced custom-built NCM/graphite lithium-ion pouch bag cells with three different anode layer thicknesses with otherwise identical battery properties. The batteries are discharged from 100 % SoC to ca. 20 % SoC. Discharge and subsequent relaxation the batteries were continuously monitored in a 30°-40° 2-theta range in ≈5 min intervals and the graphite phase evolution observed. The originally proposed discharge rates of 0.1C and battery temperatures of -10 °C were adjusted during the experiment as the optimal recording times, the timescale of relaxation and phase splitting were better understood.

8.2 Sample cell characterization

For the neutron diffraction experiment 18 samples were manufactured by the small-scale manufacturer CustomCells Itzehoe GmbH. In addition to the cells anode and cathode electrode sheets were provided for material characterization purposes.

Figure 90 Neutron diffraction sample cells, High Energy (HE), Balanced (BA) and High Power (HP). The red square marks the area where the cell is free from adhesive tape. Image reprinted from [191].

8.2.1 Sample requirements

In order to avoid additional background as much as possible, it was requested that the samples do not have adhesive labels that are potentially picked up in the diffraction data. Additionally, excess separator, i.e. wrapped around the electrode stack for improved stability, should also be avoided. The manufacturer marked the area, where the beam can pass unaffected (See Figure 90). In order to rely on the cryostat experimental environment used in the previous relaxation experiment, the maximum cell width was limited to 5 cm.

Furthermore, it was requested that the cell stack is finished with single-coated layers at each side to avoid a backside overhang area that does not participate in the cycling process, but would be picked up in the diffraction signal. In commercial pouch bags this cannot be taken for granted, since use of double-coated outer layers may waste active material, but avoids problems with electrode curling due to one sided surface tension.

In coordination with the STRESS SPEC instrument scientists, the amount of active material necessary for a good signal and the maximum sample width due to incoherent scattering were approximated. The scattering length is highly material dependent and is especially high for hydrogen, which is mainly found in the battery electrolyte in Table 7. However, as the amount of electrolyte in the beam was unknown for the commercial cells in previous experiments, but is proportional to cell capacity and thus width. The width was taken as reference point. Based on previous experience, the minimal sample width of 3 mm and a maximum width of 1 cm were set for sufficient signal to noise ratio. The target width was set to 6 mm for all cells.

Table 20 Information on sample cells given by the manufacturer CustomCells GmbH. *The number of double-coated electrodes for BA cells was given as 13, but post mortem analysis found only 11 layers.

Cell type		High Energy	Balanced	High Power
Id	*Symbol (Units)*	*HE*	*BA*	*HP*
Electrode length	l_{elec} (cm)	5.6	5.6	5.6
Electrode width	w_{elec} (cm)	3.1	3.1	3.1
Anode active material		C_6	C_6	C_6
Anode active material fraction	$m_{\%,\mathrm{AM}}$ (%)	96	96	96
Anode areal capacity	c_{a} (mAh cm^{-2})	3.8	2.2	1.1
Cathode active material		NCM(111)	NCM(111)	NCM(111)
Cathode active material fraction	$m_{\%,\mathrm{AM}}$ (%)	86	86	86
Areal capacity cathode	c_{c} (mAh cm^{-2})	3.5	2.0	1.0
Single-coated layers	N_{S}	1	1	1
Double-coated layers	N_{D}	8	11* (13)	20
Nominal voltage	U_{N} (V)	3.6	3.6	3.6
Max. cut off voltage	U_{max} (V)	4.2	4.2	4.2
Min. cut off voltage	U_{min} (V)	3.0	3.0	3.0
Nominal capacity	C_{N} (mAh)	1033	799	712
Electrolyte		EC/DMC 2% VC	EC/DMC 2% VC	EC/DMC 2% VC
Lithium salt		$LiPF_6$	$LiPF_6$	$LiPF_6$
CC anode material		Cu	Cu	Cu
CC anode height	$h_{CC,a}$ (µm)	18	18	18
CC cathode material		Al	Al	Al
CC cathode height	$h_{CC,c}$ (µm)	20	20	20

8.2.2 Cell datasheets

The three types of sample cells; high energy (HE), balanced (BA) and high power (HP), are shown in Figure 90. All cells share the same basic design. The anode consists of graphite and the cathode of NCM-111. The nominal voltage is 3.6 V. The charge and discharge cut off voltages are 4.2 V and 3.0 V. The electrolyte is EC/ DMC with the salt $LiPF_6$ and the additive 2 % VC. The electrode width and length 3.1 cm x 5.6 cm is equal for all cells. The cells differ in the areal capacity and number of layers. The HE cell has 8 layers of each electrode with 3.5 mAh/ cm^2 areal capacity for NCM and 3.8 mAh/ cm^2 for the anode. The BA cell has 11 layers of each electrode with 2.0 mAh/ cm^2 NCM and 2.2 mAh/ cm^2 for graphite. The HP cell has 20 layers with 1.0 mAh/ cm^2 NCM and 1.1 mAh/ cm^2 for graphite. The anode/ cathode loading ratio is 110 %. This balancing is equal for all cell types. The number of layers increases with decreasing areal capacity to achieve a similar cell height and capacity. All cells have an additional single anode layer at the end of the stack to avoid an overhang layer. The layer number of the BA cell was stated to be 13 by the manufacturer but only 11 layers were found in post mortem analysis.

Notably, while the manufacturer gave detailed information on several aspects of the cell, some requested information was not provided and some properties were not included as requested. The manufacturer gave information on the anode (96 %) and cathode (86 %) active material fraction but did not disclose the type of binder and other additives. And while natural flake graphite was requested, subsequent SEM analysis found potato shaped particles which indicate artificial graphite (see section 3.1). The graphite powder manufacturer or product number were not disclosed. Table 20 summarizes the sample cell properties as given by the manufacturer.

8.2.3 Geometric properties

The geometric parameters of the sample cells are listed in Table 21. Figure 91 illustrates the nomenclature. The parameters were measured manually with a caliper with a reading accuracy of $\mathrm{err} = \pm 0.5\ \mathrm{mm}$. The cell height is approximately 5 mm and in line with the target height. Of all sample cells the balanced cell with 4.4 mm is the thinnest. This is likely due to the missing two electrode layers with respect to the initial 13 layers described by the manufacturer.

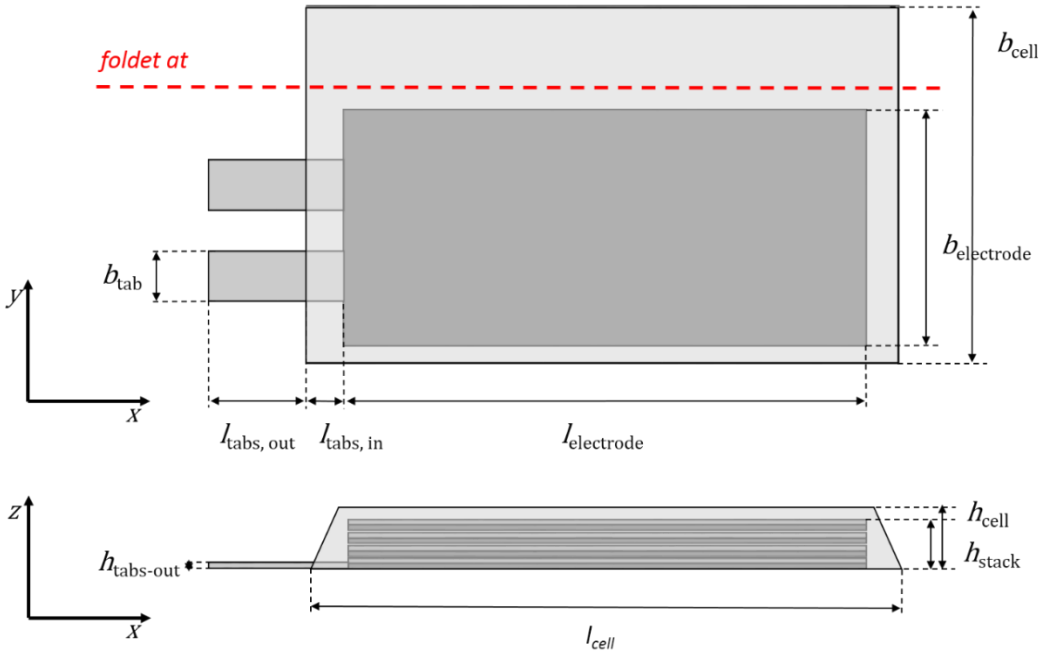

Figure 91 Sample cell schematic with dimensions.

There is notably more excess pouch foil compared to commercial batteries of similar size. However, fitting the cell into the 5 mm diameter cryostat chamber with a cell width of 5.3 mm was not a problem since the excess foil could be folded without damaging the cell.

Table 21 Cell dimensions. $\mathrm{err} = \pm 0.5\ \mathrm{mm}$. Data from [191].

Cell type			High Energy	Balanced	High Power
Id	*Symbol*	*Units*	*HE*	*BA*	*HP*
Cell length	l_{cell}	cm	8.7	8.7	8.7
Cell width	w_{cell}	cm	5.3	5.3	5.3
Cell height	h_{cell}	mm	5.3	4.9	5.2
Electrode stack height	h_{stack}	mm	4.9	4.4	4.7
Tab length (outside)	$l_{\mathrm{tab,out}}$	cm	2.7	2.7	2.7
Tab length (inside)	$l_{\mathrm{tab,in}}$	cm	1.2	1.2	1.2
Tab width	w_{tab}	mm	0.8	0.8	0.8
Tab height	h_{tab}	mm	0.1	0.1	0.1

8.2.4 Capacity, weight, and resistance

In the initial characterization the cells were tested for outliers in weight, internal resistance, and capacity. Figure 92 shows the R_i internal resistance and weight. The average weight of the cells is between 22 g and 25 g. The balanced cell is the lightest due to the missing layers. The internal resistance increases with areal capacity. Measured at 50 % SoC, the average resistance R_{1kHz}, increases from about $15\ \mathrm{m\Omega}$ for HP cells to $22\ \mathrm{m\Omega}$ for HE cells. Several outliers; BA-4, HP-2 and HP-4 (see Figure 92), were excluded from the average. These cells not only showed a sharp increase in internal resistance after the check up cycle, but failed soon after and were used for post mortem. The internal resistance of Ba-5 was not measured because the cell was internally short circuited to 0 V before the initial measurements.

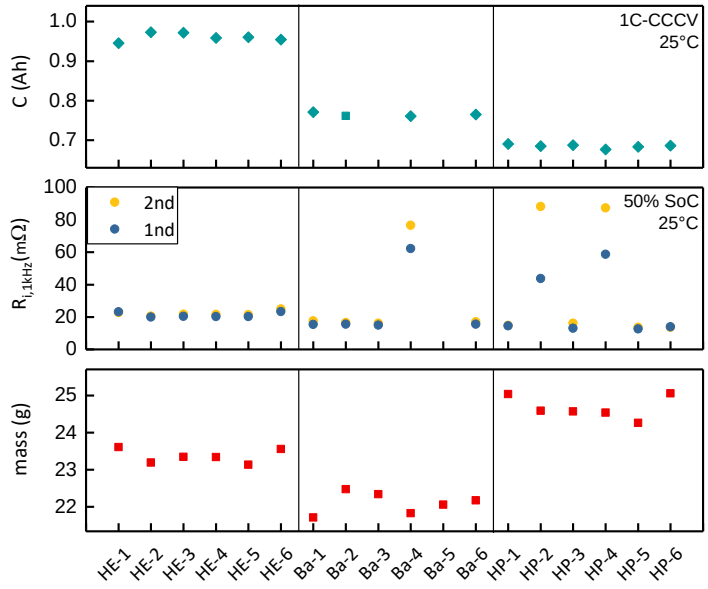

Figure 92 Cell weight and internal resistance (1 kHz) before (1st) and after the check up routine. Data from [191].

Table 22 lists the average values and standard deviation for cell capacity, 1kHz resistance, and mass. For all cell types the measured capacities are smaller than the capacity calculated from the areal capacity and electrode area given by the manufacturer. The deviation is higher for the HE cells (7 %) compared to the BA and HP cells (4 %).

Table 22 Cell capacities, resistances, and mass as determined with initial tests. Data from [191].

Cell		HE	BA	HP
$C_{\mathrm{N,calc}}$	mAh	1033	799	712
$C_{\mathrm{N,calc}}$	mAh	963 ± 10	765 ± 4	682 ± 4
Deviation	%	6.8	4.3	4.2
R_{1kHz}	mΩ	22.2 ± 0.7	16.9 ± 0.5	14.5 ± 1.0
m	g	23.4 ± 0.2	22.1 ± 0.3	24.7 ± 0.3

8.2.5 Material characterization

For further characterization of the cells and electrode material and to verify the manufacturer information the geometric properties of the electrode were measured and electrode segments weighed. The material parameters for the calculations are taken from literature and listed in Table 5

In LFP electrode material by CustomCells Itzahoe GmbH a significant loading gradient was noticed during the preparation of the Chapter 5 experiments. CustomCells confirmed in personal correspondence by phone that electrode samples may show deviating loading close to the edges of the doctor blade and that as a result only the electrode center pieces are cut out for electrode stacks. Therefore, the spatial homogeneity of the electrode height was checked before further tests. While a variation in electrode height up to 6 % was observed, the variation was random and no systematic gradient was observed. However, to avoid potential problems due to coating artifacts at the electrode sides, only electrode material 1-2 cm away from the edges was used for further measurements.

Table 23 Dimensions of cell materials. Averaged over approx. 30 local measurements per sample. Data from [191]. *no CC. **7.5mm disk no CC

Cell type			HE		BA		HP	
Description	Symbol	Units	Anode	Cathode	Anode	Cathode	Anode	Cathode
Electrode height*	h_i	µm	102±2	155±3	63.3±0.7	93±1	28±1	54±1
Electrode mass**	m_i	mg	16.7±0.4	49.3±0.3	9.2±0.2	27.5±0.3	2.7±0.2	13.9±0.3
Current Collector height	h_{cc}	µm	18±1	19.9±0.4	18±1	19.9±0.4	18±1	19.9±0.4
Pouch foil height	h_{foil}	µm	116±4					
Separator height	h_{sep}	µm	24.6±0.5					
Separator area	A_{sep}	cm^2	150					

Table 23 lists the material dimensions. The electrode height is lowest for the high-power cell with 28 µm for the anode and 54 µm for the cathode. The height is approximately double for the BA cells and triple for the HE cells. The measured height for the current collector and separator matches the manufacturer datasheet.

While the active material content is provided by the manufacturer, the exact amount of binder material and conductive additives is unknown. To approximate the porosity assumptions must be made regarding these components fulfilling the following boundary condition

$$m_{\%,\mathrm{AM}} + m_{\%,\mathrm{Bi}} + m_{\%,\mathrm{C65}} = 100\ \%. \tag{68}$$

Thus, for the following, the mass fraction of binder $m_{\%,\mathrm{Bi}}$ is defined as 2 % for the graphite anode and 5 % for NCM(111) cathode. The mass fraction for carbon black $m_{\%,65}$ is 2 % for the anode, 9 % for the cathode. In total binder and carbon black adds up to 5 % for the anode and 14 % the cathode in line with the manufacturer datasheet. With equation (68) the volume fractions are calculated (Table 24).

Table 24 Volume fraction of electrode materials for HE, BA, and HP cells. Data from [191].

Cell	HE		BA		HP	
Material	LiC_6	NMC	LiC_6	NMC	LiC_6	NMC
ε_s	0.56	0.47	0.58	0.44	0.47	0.4
ε_l	0.44	0.53	0.42	0.56	0.53	0.6
ε_{AM}	0.53	0.34	0.55	0.32	0.45	0.29
ε_{Bi}	0.01	0.05	0.02	0.05	0.01	0.04
ε_{C65}	0.01	0.08	0.01	0.08	0.01	0.07

With the porosity values the degree of utilization of the active material relative to the maximum possible amount of intercalated lithium can be calculated (Table 25).

Table 25 Active material volume V_{AM}, theoretical $Z_{v,th}$ and used $Z_{v,use}$ molar material amount as well as the utilization of the active material Δy are listed. Data from [191].

Cell	Material	$V_{\mathrm{AM}}(\mathrm{cm}^3)$	$Z_{v,th}\left(\frac{\mathrm{mol}}{\mathrm{cm}^3}\right)$	$\mathrm{Z}_{\mathrm{v,use}}\left(\frac{\mathrm{mol}}{\mathrm{cm}^3}\right)$	$\Delta y\ (\%)$
HE	LiC_6	$9.30 \cdot 10^{-3}$	28352	23470	82.78
	NMC	$7.74 \cdot 10^{-3}$	49017	25973	52.99
BA	LiC_6	$6.12 \cdot 10^{-3}$	28352	23610	83.28
	NMC	$4.23 \cdot 10^{-3}$	49017	27179	55.45
HP	LiC_6	$2.70 \cdot 10^{-3}$	28352	23396	82.52
	NMC	$2.13 \cdot 10^{-3}$	49017	27007	55.1

8.2.6 Particles and tortuosity

Particle radii and electrode tortuosity determine the effective transport parameters of the solid and liquid phase of the electrode.

The particle radii distribution of the graphite and NCM electrodes is approximated by the analysis of top view SEM images (section 4.5.5). Likewise, the tortuosity is approximated using top view and cross view SEM images and the tool BruggemanEstimator following the approach by Ebner et al. (section 4.5.4) In addition, the tortuosity is measured by means of EIS of symmetrical cells with the method of Landesfeind et al. (section 4.3.2). The consistency of the resulting parameters gained is evaluated.

8.2.6.1 Particles SEM

With the BruggemanEstimator tool the shape of the particles in the SEM images are marked with an ellipsis and the length of the minor and major axis is stored in a table. To improve the quality of the sample statistics, five SEM images were evaluated for each combination of battery type (HE, BA; HP) and electrode type (graphite, NCM). The total number of particles evaluated is listed in Table 26.

Table 26 Number of particles analyzed in SEM images. Data from [191].

	HE		BA		HP	
	C_6	NCM	C_6	NCM	C_6	NCM
# particles top view	821	1204	765	874	817	1129
# particles cross view	761	837	575	628	284	475

800 to 1200 particles were evaluated for the top view images and 280 to 760 particles in the cross view images. The number of particles evaluated for the cross-view SEM images decreases with the loading, due to the decreasing electrode with.

Figure 93 shows the top view and cross view SEM images of the graphite anodes of the HE, BA and HP cells. Figure 94 shows the particle radii distribution determined from the top view images. The corresponding cathode images and histograms are given in the appendix Figure C.3 .

The visual impression of the SEM images is that the graphite and NCM electrodes for different loadings, HE, BA, and HP are very similar. This is consistent with the manufacturer information, that the same active material and slurry compositions were used. The higher non-active material fraction of 14 % for NCM electrodes is visible as a netlike mass between particles mostly absent from the graphite electrodes with 96 % active material fraction.

Two systematic errors affect the measurement of the particle size. First, small particles are difficult to distinguish from non-active materials due to the limited resolution of the 800x magnification SEM images. Secondly, the fragmentation of the particles in the cross-view images due to grinding process and the low contrast to the surrounding epoxy glue makes it more difficult to correctly identify the particle boundaries. Naturally, the NCM secondary particles consist of primary particles, but also graphite shows an internal flake structure and not a fully solid body (Figure 93).

The best fit particle radii distributions shown in Figure 94 are not symmetrical. The fitting Mathematica routine in most cases fitted a mixture distribution of two standard deviations. The asymmetry is more pronounced for the cross-section images than for the top view images. This is unexpected, given, that identical distributions are expected. Whether this is due to favored orientation of the potato-shaped particles or the described systematic errors cannot be distinguished. Due to this, only top view images are considered for the particle radii distribution.

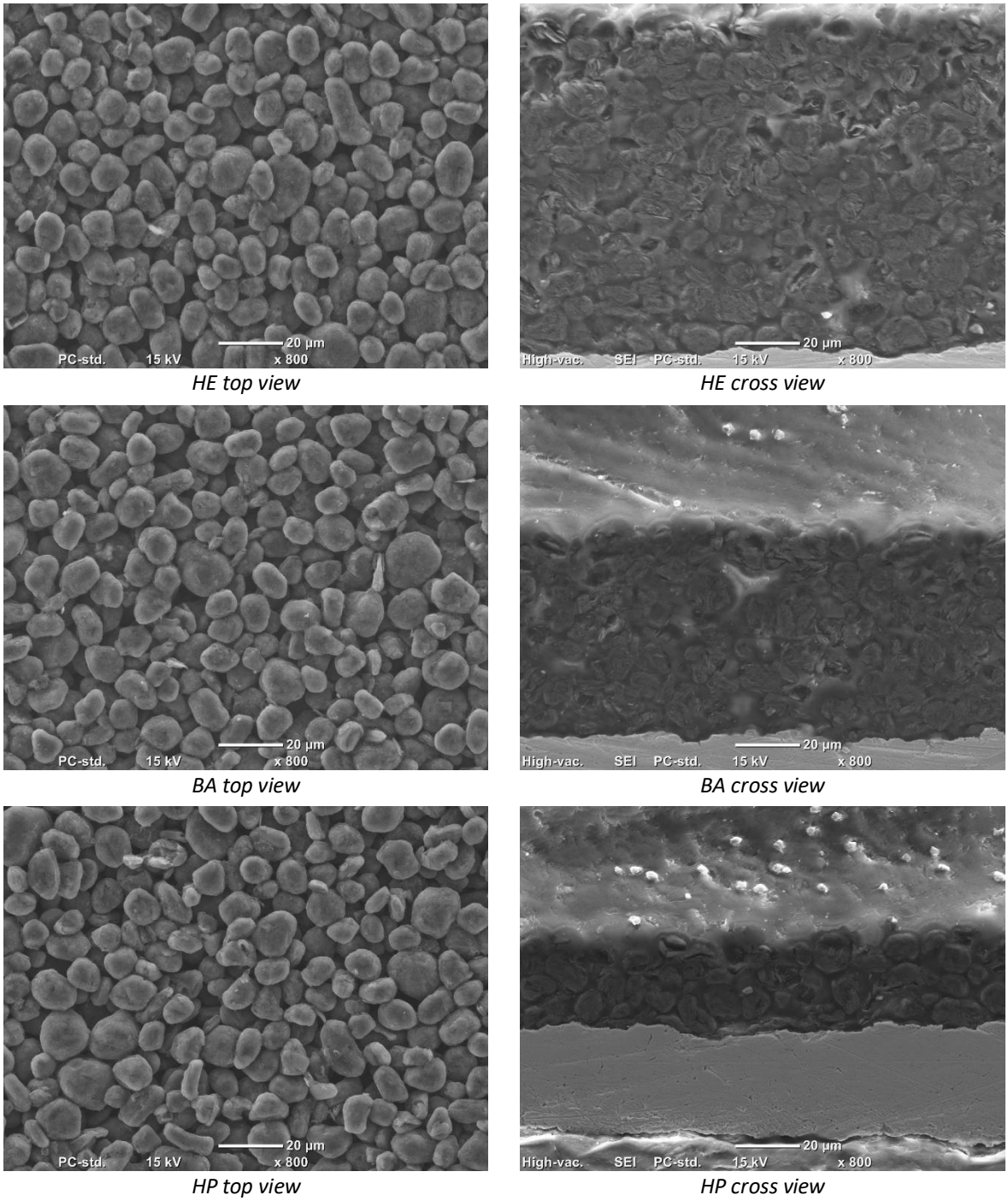

HE top view *HE cross view*

BA top view *BA cross view*

HP top view *HP cross view*

Figure 93 Top view and cross view SEM images of graphite electrodes for the HE, BA and HP samples with 800x magnification. Images taken by J. Wilhelm. Image reprinted from [191].

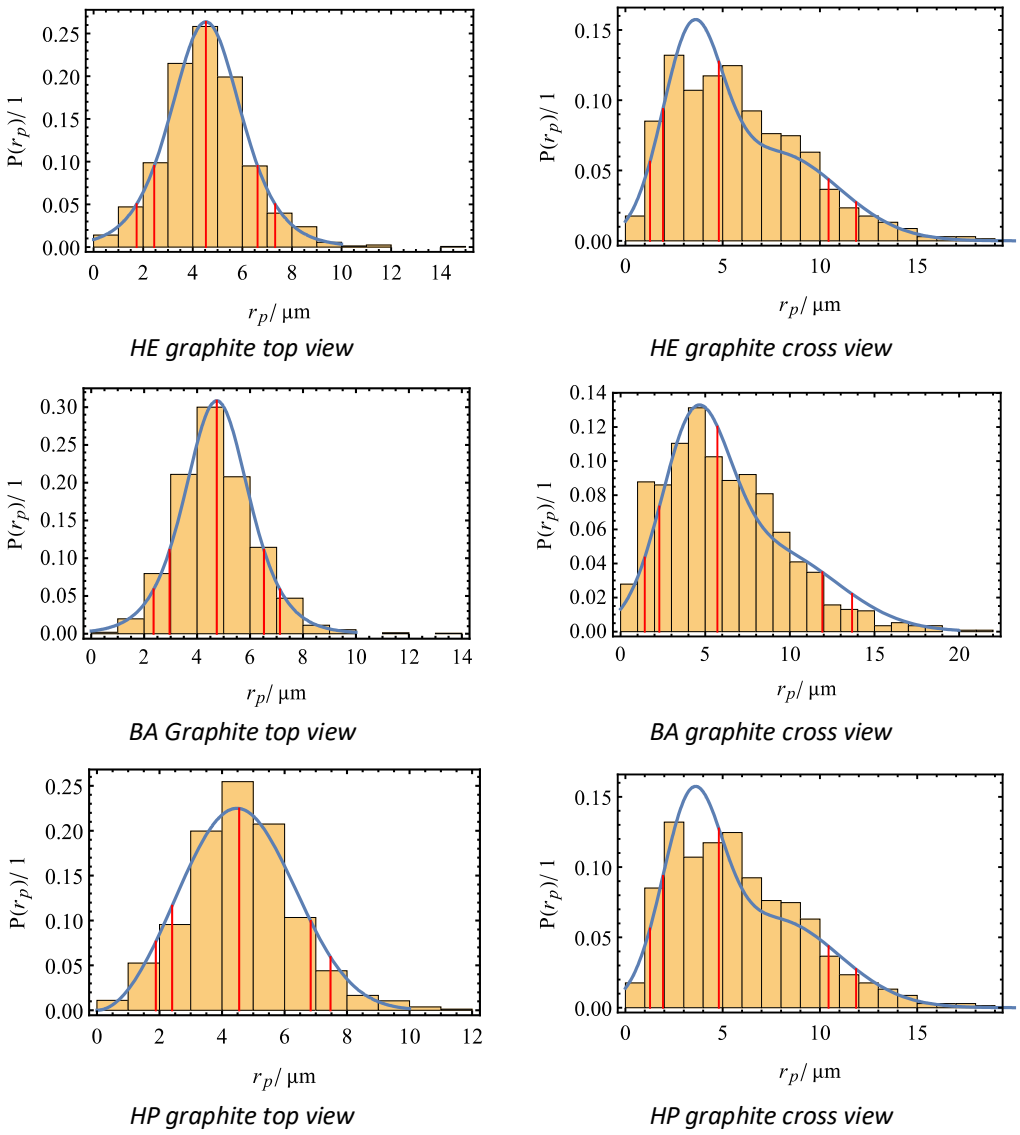

Figure 94 Probability distribution for particle radii for top- and cross-section SEM images of the graphite anode of the HE, BA and HP batteries. The blue line marks the best fit distribution. The red lines mark the percentile values where 5 %, 10 %, 50 %, 90 % and 95 % of the particle population have a smaller radius than the marked value. Data and image reprinted from [191].

Table 27 shows the median radius of the graphite and NCM particles as well as the 10 % and 90 % percentile values of the top view images. The median radius differs only slightly for the graphite anodes which supports the information of the manufacturer, that identical graphite material was used. The particle radii are used in the diffusion analysis in section 8.3.3.4 and 8.3.4.5.

Table 27 Percentile values for the radii distributions of graphite and NCM (secondary) particles. Data from [191].

	HE		BA		HP	
	r_p (µm)		r_p (µm)		r_p (µm)	
	C_6	NCM	C_6	NCM	C_6	NCM
Q (5 %)	1.9	0.7	2.6	1.0	1.8	0.8
Q (10 %)	2.5	1.0	3.0	1.3	2.6	1.0
Q (50 %)	4.6	2.4	4.7	2.4	4.7	2.3
Q (90 %)	6.6	4.9	6.4	5.7	6.8	5.4
Q (95 %)	7.3	5.8	7.1	6.7	7.5	6.8

8.2.6.2 Tortuosity SEM

With the BruggemanEstimator tool the Bruggeman exponent α is estimated from the top view and cross view images. Table 28 shows the Bruggeman-exponent α_z in z direction orthogonal to the current collector. With equation (46) and the liquid phase volume fraction ϵ_l, as measured from weighing the electrodes (section 8.2.4), the tortuosity τ is calculated. The Bruggeman exponent of the anode is within the range of 0.6 to 0.7 for all cell types. This is close to, but slightly higher than the value of 0.5 for ideal spheres. Given that the optical impression is, that graphite particles are of a largely spherical potato like shape, this is not unexpected. Correspondingly, the tortuosities of 1.3 to 1.8 for the graphite anodes are low.

Table 28 Bruggeman-exponent α_z and tortuosity τ calculated with BrugemannEstimator based on SEM images and the liquid phase volume fraction ϵ_l**.** Data from [191].

	HE		BA		HP	
	C_6	NCM	C_6	NCM	C_6	NCM
τ	1.6	1.8	1.58	1.4	1.3	1.3
α_z	0.6	0.53	0.66	0.55	0.69	0.57
ϵ_l	0.44	0.54	0.42	0.58	0.53	0.62

8.2.6.3 Tortuosity EIS

In addition to the SEM-image based approach by Ebner et al., the EIS based method by Landesfeind et al. was applied to measure the tortuosity. Potentiostatic EIS measurements were performed with symmetrical cells as outlined in section 4.3.2. The potential amplitude of the sinus perturbation was set to 10 mV with a frequency range of 100 mHz to 200 kHz and 6 measurement points per decade.

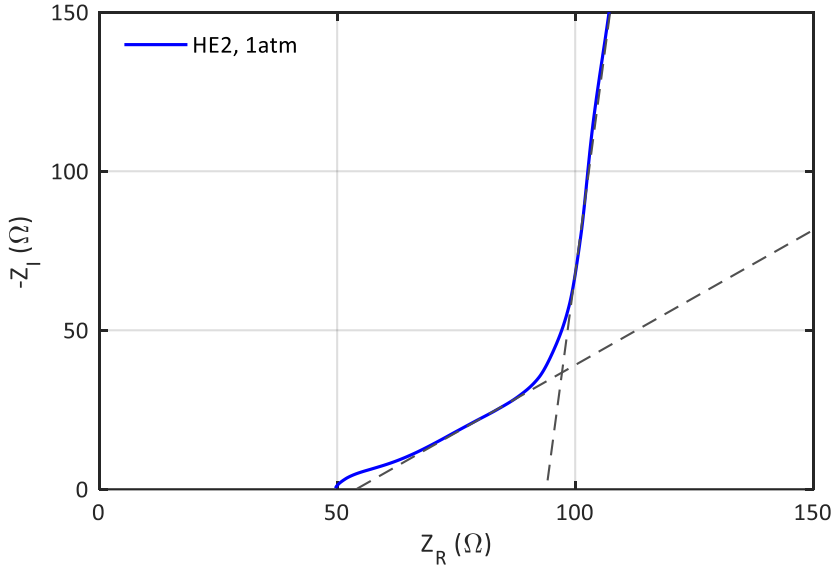

Figure 95 Nyquist plot of graphite type 1 symmetrical cell PEIS data. The dashed grey line highlights the linear segments of the data. Data from [191].

Figure 95 shows the Nyquist plot of the PEIS measurement of the HE graphite electrodes. Notably, the high frequency segments differs from the linear theoretical prediction. The deviation is caused by non-ideal internal resistances of the sample, such as the interface resistance of current collector and graphite as well as the interface resistance between cell casing and current collector, due to accumulation of excess electrolyte. This occurs in several measurements (appendix Figure C.5 and Figure C.6). In a personal conversation with Landesfeind the author was made aware, that the compressibility of the glass fiber separator may introduce a time dependent systematic error as the separator is slowly compressed over time and the impedance of the cell altered.

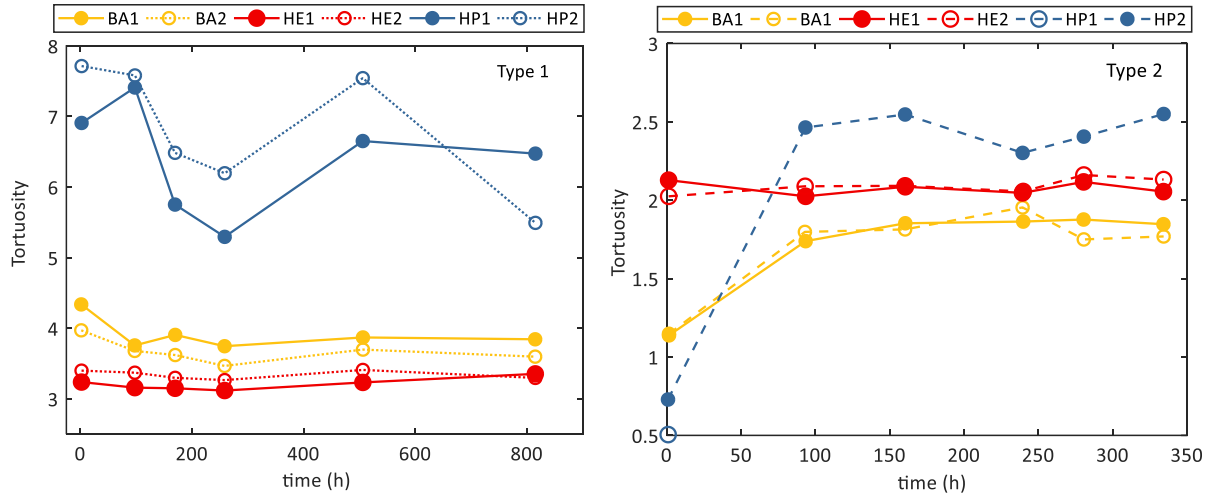

***(a)** Type 1 (glass fiber separator)* ***(b)** Type 2 (ceramic separator)*

Figure 96 Tortuosity change with time. Two samples, S1 and S2, for each loading HE, BA and HP. (a) shows results of type 1 half-cells. (b) shows the results of type 2 half-cells. Data from [191].

To evaluate potential systematic errors half-cells with glass fiber separator (type 1) and ceramic separator (type 2) were built. The impedance spectra were measured repeatedly for both types over a period of one month. In addition, the PEIS measurements were conducted while the sample cells were screwed in a vice. The sample was screwed in more tightly to increase the pressure qualitatively four times. During this test the casing was notably deformed.

Figure 96 shows the time dependency of the measured tortuosity for sample type 1 (a) and sample type 2 (b). The HE and BA cells show consistent tortuosity values varying by less than 0.5 over the course of 800 hours. While the tortuosity of the HP samples does show greater variation, it does not appear to depend on the resting time of the sample. While the PEIS data shows a shift of the impedance spectra towards greater ohmic resistances, the tortuosity does not show a systematic dependence on the sample age, since the slope of the high frequency and low frequency branch is not altered. Similarly, the tortuosity values measured with type 2 samples are mostly independent from sample age, with one exception. The BA samples S1 and S2 as well as the HP sample S2 show a strong increase in tortuosity between the first measurement data shortly after the manufacturing and the second measurement several days later. An explanation for this could be insufficient wetting of the Bruckner separator, which would explain why this is not observed for type 1 cells. However, sample HE-S1 and HE-S2 do not show this effect.

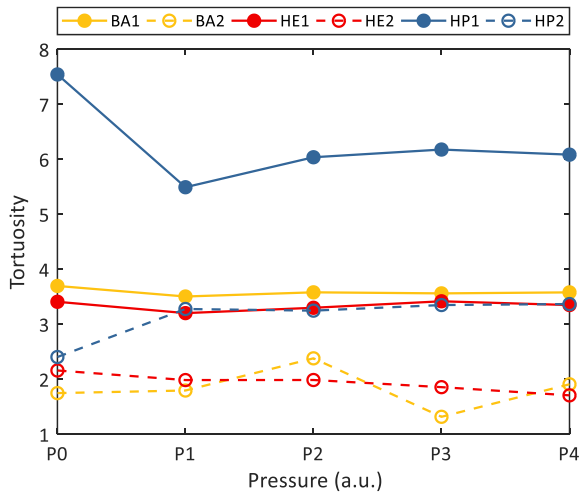

Figure 97 Tortuosity change with increasing pressure applied to the symmetrical test cell through a vice. P0 is ambient pressure. P4 > P3 > P2 >P1 > P0. Data from [191]. Types are marked with 1, 2.

Figure 97 shows the tortuosity change of type 1 and type 2 samples while being screwed in the vice. Despite sufficient pressure to deform the cell casing and to compress the glass fiber separator, no systematic change in the tortuosity is observed for both types. The PEIS data shows (Figure C.5 to Figure C.6), that increasing pressure does shift the impedance spectra to lower ohmic resistances, but the slope of the high frequency and low frequency branch is not altered and thus the tortuosity remains largely unchanged.

The time dependent measurements show consistency between the two samples of one type for all materials. However, the tortuosity values determined for the same electrode material differs between type 1 and type 2 samples. The Nyquist plots show overall higher impedance for type 1 cells compared to type 2 cells. This is expected, given the greater width of the glass fiber separator. Consequently, the $R_{ion}/3$ values determined for type 1, 30 to 70 Ohm are greater than the 3 to 15 Ohm observed for type 2. Notably, there are more artifacts and sample failures for the type 2 cells, presumably due to greater fragility of the 10 µm separator compared to glass fiber.

Table 29 Comparison of the tortuosity measured with PEIS and calculated through 3D reconstruction. The corresponding Bruggeman exponent α, the McMullin number N_M and porosity ε_l are given. For the PEIS measurements the tortuosity values are calculated with the t = 260 h of sample life data. Each value is the average of two samples of the same type, with the exception of the values marked with* where one sample failed. Data from [191].

Method	Material	N_M	τ	α	ε_l
PEIS Type 1	C6-HE	13.2	5.8	2.1	0.44
(Landesfeind et al.)[41]	C6-Ba	8.6	3.6	1.5	0.42
$\kappa = 0.32\ \mathrm{mS\ cm^{-1}}$	C6-HP	6.0	3.2	1.8	0.53
	NMC-HE	5.4	2.9	1.7	0.54
	NMC-Ba	4.5	2.6	1.8	0.58
	NMC-HP	7.1	4.4	3.1	0.62
PEIS Type 2	C6-HE	5.2	2.3	1.0	0.44
(Landesfeind et al.)[41]	C6-Ba	4.5	1.9	0.7	0.42
$\kappa = 1.71\ \mathrm{mS\ cm^{-1}}$	C6-HP	4.0*	2.1*	1.2*	0.53
	NMC-HE	4.1	2.2	1.3	0.54
	NMC-Ba	3.8	2.2	1.4	0.58
	NMC-HP	32.3*	20*	6.3*	0.62
BruggemanEstimator	C6-HE	3.7	1.6	0.6	0.44
(Ebner et al.)[42]	C6-Ba	4.2	1.8	0.66	0.42
	C6-HP	2.9	1.5	0.69	0.53
	NMC-HE	2.6	1.4	0.53	0.54
	NMC-Ba	2.3	1.3	0.55	0.58
	NMC-HP	2.1	1.3	0.57	0.62

Table 29 lists the tortuosity, McMullin Number, Bruggeman Exponent and porosity for type 1 and 2 PEIS samples as well as the results of the 3D reconstruction. The tortuosity values of the PEIS method are greater than the BruggemanEstimator results for all graphite and NCM loadings. Type 1 cells show similar tortuosities for NCM and graphite anodes within the range of 1.9 to 2.3, slightly higher than the tortuosity range 1.3 to 1.8 observed for BruggemanEstimator. Type 2 cells show higher tortuosity values ranging from 2.6 to 5.8 with on average greater tortuosity for the graphite electrodes. The disparity between the PEIS measurements and 3D reconstruction is well known in literature [41, 42]. The difference is frequently attributed to the fact that tortuosity calculation in 3D reconstruction neglects the contribution of non-active materials such as binder. The tortuosity error is estimated to ± 0.4 based on the fluctuation with sample age.

Overall, the measurements suggest a slight increase in tortuosity with higher loading for graphite and NCM cell. However, this is not a clear trend given the variations over sample age and outliers such as HP-3 (Table 29). The measurements confirm the low tortuosity of the electrodes compared to literature values of flake graphite supporting the 3D reconstruction results.

8.2.7 Thermal characterization

With the geometrical data and the material densities and weight the mass fraction of all cell components with exception of the electrolyte can be calculated. Since the electrolyte is the only component not known, its share is given through the difference between full cell weight and the cumulative weight of the components.

$$m_{elec} = m_{cell} - \left(\sum_i m_{component,i} \right) \tag{69}$$

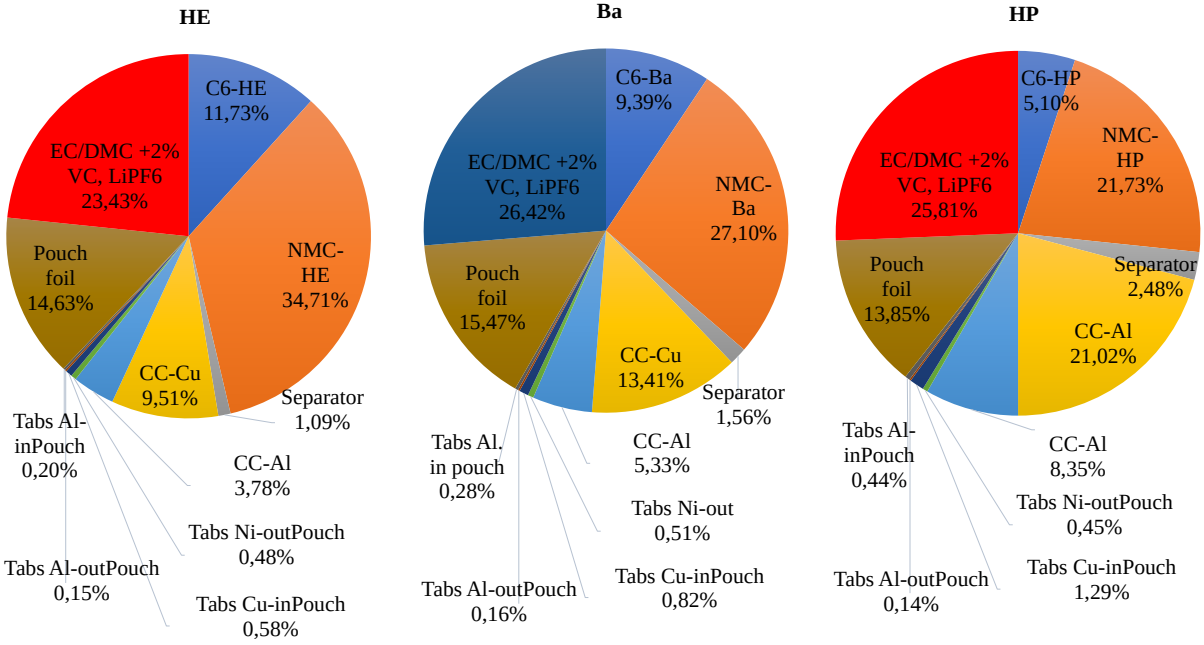

Figure 98 Weight fractions of HE, BA and HP cells. Data from [191].

Figure 98 shows the mass fractions for all components of HE, BA, and HP cells. The share of the active material decreases from 11.7 % (C6) and 34.7 % (NCM) for the HE cells to 5.1 % and 21.7 % for the HP cells. Correspondingly, the mass fraction of Cu and Al increases with more layers and thinner coating but constant CC thickness. The weight fraction of the electrolyte is between 23 % and 26 %. For comparison, the electrolyte mass fraction for 5 Ah pouch cells produced in the ExZellTUM research project is 18 % for NCM/graphite and 23 % for HE-NCM/Graphite cells. While this is a higher value than one would assume for a commercial lithium-ion battery, this is expected given the excess volume available for the sealed pouch casing (see Figure 90) and the fact that the cell was presumably filled with electrolyte manually. In this case, a fairly large safety margin of electrolyte is typically used, because the time until sealing and the amount of evaporated electrolyte is not known exactly. The high amount of electrolyte reduces the signal to noise ratio for the neutron diffraction measurements. The specific heat capacity, the characteristic lengths, the thermal conductivity, and the Biot number are calculated for each direction x y z by means of equation (21) and listed in Table 30. The heat capacity is lowest for the balanced cell due the two missing layers. For all cells and directions, the Biot numbers are below 0.1 and thus the temperature inhomogeneity in the cell is below 2 %.

Table 30 Thermal properties of the HE, BA and HP sample cells. Data from [191].

	Length mm			Thermal conductivity $Wm^{-1}K^{-1}$			Biot number			Spec. heat capacity $Jkg^{-1}K^{-1}$
	$L_{\parallel,x}$	$L_{\parallel,y}$	$L_{\perp,z}$	$\lambda_{\parallel,x}$	$\lambda_{\parallel,y}$	$\lambda_{\perp,z}$	$B_{\parallel,x}$	$B_{\parallel,y}$	$B_{\perp,z}$	C_{th}
HE	2.7	1.55	2.57	21.85	21.85	1.11	0.0064	0.0035	0.012	16.33
BA	2.7	1.55	2.32	31.68	31.68	1.03	0.0044	0.0024	0.013	13.39
HP	2.7	1.55	2.6	48.55	48.55	0.93	0.0029	0.0016	0.014	13.54

8.2.8 Cycle life

As a measure of overall cell quality, a brief cycling test was performed with a single cell of each loading type HE, BA and HP. The cells were CC-CC cycled at 0.5C from 3.0 V to 4.2 V for 200 cycles. Figure 99 shows the SOH of the cells normalized with the cell capacity calculated from the loading. After 200 cycles the SoH of all samples was greater than the 80 % EOL criteria. More than 90 % of the initial capacity remains for the HP and HE sample and more than 85 % for the BA sample. The EOL of the cells can be approximated through linear extrapolation of the aging data. A qualitative estimate for the samples EOL is 700 cycles for the HE cell, 800 cycles for the HP cell and about 350 cycles for the balanced cell, which shows the fastest aging.

The cycle life of the custom-made cells is lower than the 1000+ low-rate full cycles that can be achieved with commercial NCM graphite cells. However, the change in SOH of less than 1 % within 5 cycles needed for the neutron diffraction measurements is sufficiently small during most of the cell's life, with the exception of the rather sharp capacity drop during the initial cycles. The cells for the diffraction experiment underwent capacity determination and function tests prior to the experiment.

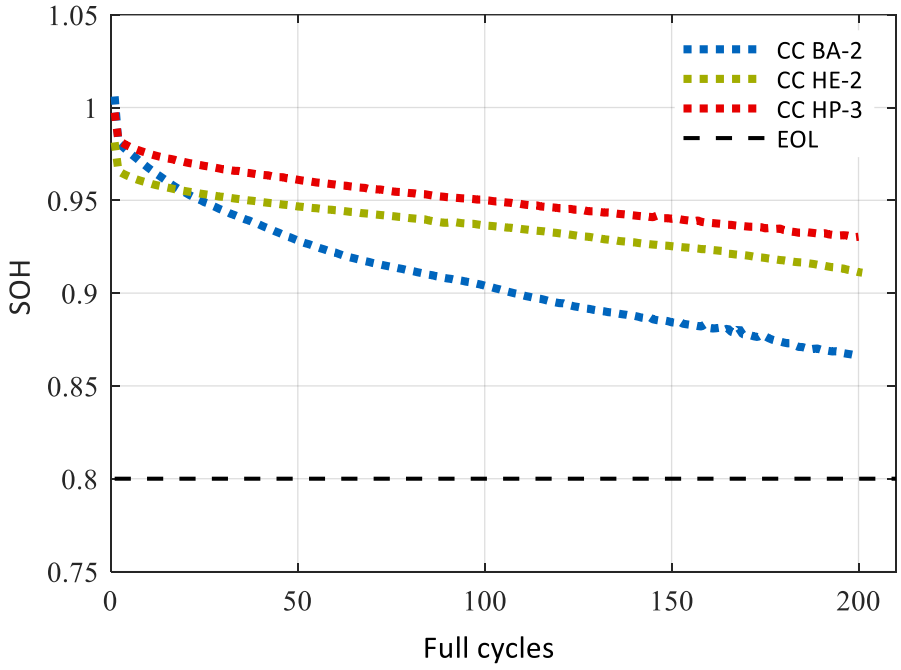

Figure 99 State of Health during CC cycling for custom cells HE, BA, and HP samples. Data from [191].

8.3 Diffraction experiment

This chapter discusses the results of the diffraction experiment on influence of electrode loading on relaxation times. To increase relaxation times and to ease the ND-time-resolution-requirements the relaxation tests were conducted at -5 °C and -20 °C.

In the following the preliminary tests for the preparation of the experiment as well as the data processing steps are outlined. The offsets between HE, BA and HP samples in the diffraction data is corrected and the intensity is scaled with the active material content. Then the reflection intensity and *d*-spacing are analyzed and the phases are identified. The time scale of the relaxation process is investigated and diffusion time scales are discussed.

8.3.1 Preliminary tests

The preliminary tests include the determination of the ideal discharge target SoC and the characterization of the neutron beam properties. Furthermore, it was tested whether the chosen target SOC can be reached for all loadings at low temperatures.

8.3.1.1 Target SoC Determination

The target SoC is chosen according to two goals. The first goal is to visualize the phase separation during and after discharge strongly. This is done by discharging the cell to a low SoC where the lower lithiated phases $Li_{1-x}C_6$ undergo a continuous change in *d*-spacing and 2-theta reflection position from LiC_{12} to graphite, as described in section 3.3 and 7.2.5. The second goal is to achieve comparable results for the cells with different loading through assuring the same final state of anode lithiation after discharge. To achieve this, the target SoC is chosen set not by a fixed DOD relative to full cell capacity but with a fixed lithiation of the anode electrode identified through *dV/dQ* analysis.

Figure 100 shows the full cell discharge OCV profile recorded at C/100 continuous discharge as well as the half-cell profiles of graphite anode and NCM cathode plotted against mAh and relative charge for all loadings HE, BA and HP. The normalized plots show very good agreement between different loadings with near identical OCV features. In addition to SEM and material data, this further confirms the manufacturer information that identical active materials were used. Figure 101 shows *dV/dQ* comparison for all loadings HE (a) BA (b) and HP (c). The combined profile of graphite and NCM half-cells (red line) reproduces the Full Cell C/100 reference profile (green line) well. The maxima in the *dV/dQ* profiles are numbered 1 to 5. The not numbered maxima on the right corresponds to the full cell charge cut off voltage and on the left to the full cell discharge cut off voltage. The maximum 1 corresponds to the change between the phase I/ II 90 mV plateau and the phase II/ IIL 130 mV plateau. The minimum between maxima 3 and 4 was chosen as target SoC for all loadings due to its center position in the lithiation range where graphite shows a phase shift (Figure 101). Within the view of the staging model this position marks the center of the phase 3L / phase 4L plateau [133]. In terms of graphite lithiation this marks the lithiation range between LiC_{18} and LiC_{24}, in the following labeled as $Li_{1-x}C_{18}$. Table 31 summarizes the target SoCs and the corresponding discharge capacity for all loadings. The target SoCs differ by 2 % which is in agreement with the manufacturer information, that the cells are equally balanced with a factor of 1.1.

Table 31 *dV/dQ* Analysis. Target SoC and discharge capacity $Q_{discharge}$. Data from [191].

Cell		HE	BA	HP
C_N	mAh	1033	799	712
Target SoC	%	23.6	23.8	22.9
Target DoD	%	76.4	76.2	77.1
Q_{remain}	mAh	244	190	163
$Q_{discharge}$	mAh	798	608	549

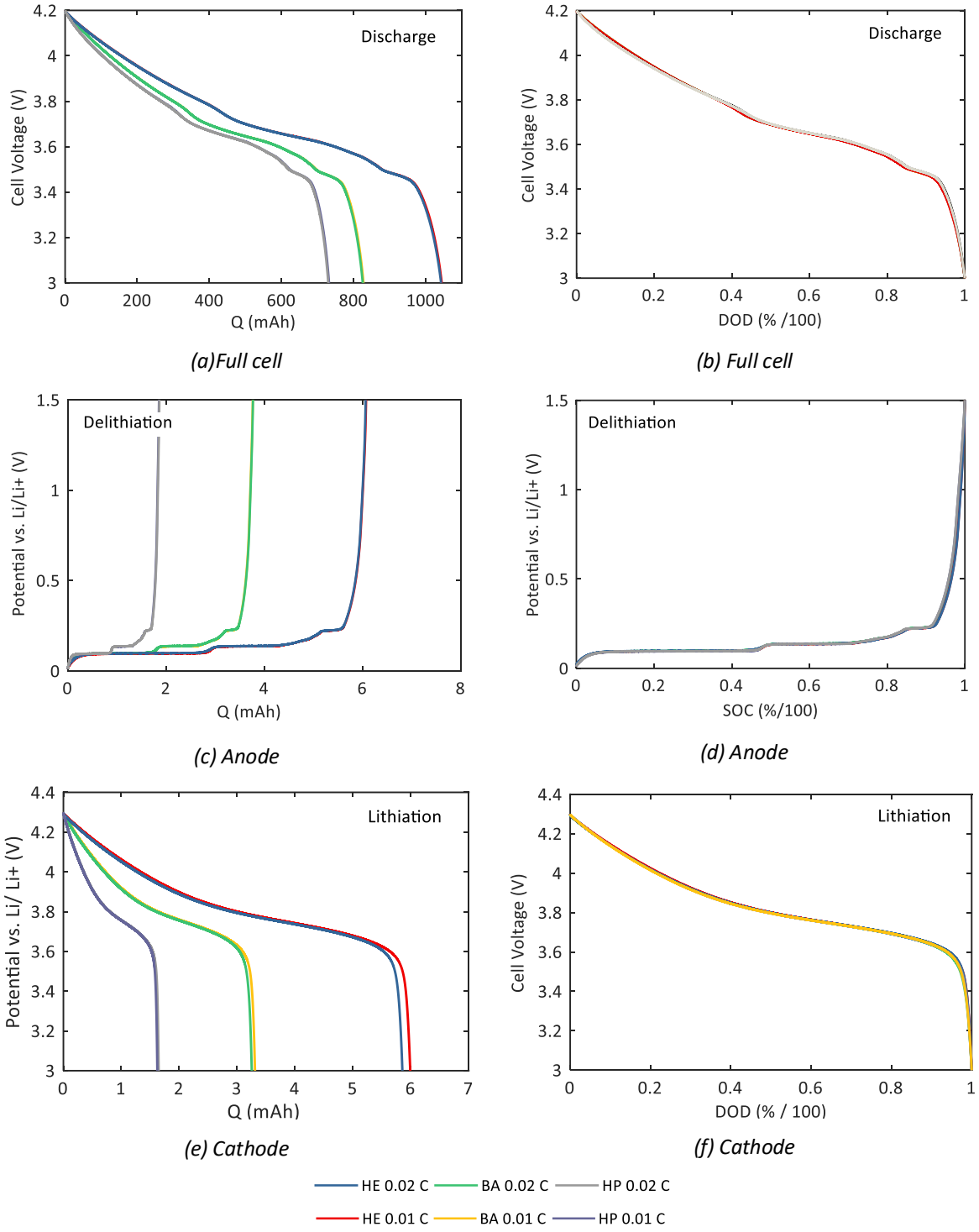

Figure 100 OCV profiles at C/100 and C/50 for HE, BA and HP full cells, graphite and NCM Li/Li$^+$ half-cells. Data from [191].

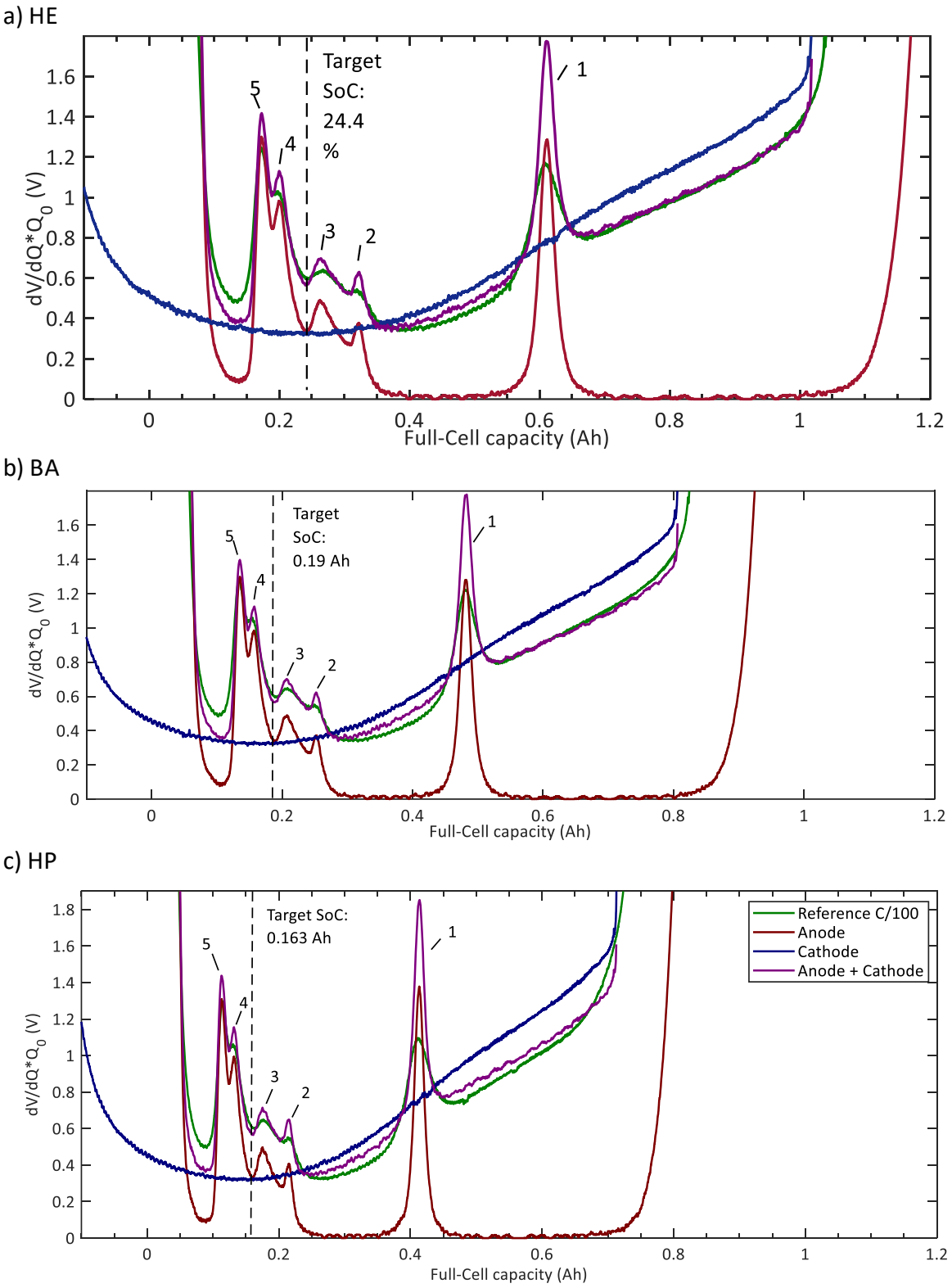

Figure 101 Differential Voltage profiles for (a) HE, (b) BA and (c) HP cells. Reconstruction of a C/100 reference profile with half-cell profiles. The dashed lines mark a minimum chosen as reference point for the discharge target SoC. Data from [191].

8.3.1.2 Low temperature Capacity

The HE, BA and HP batteries were discharged at 0 °C to test whether the target DoD for comparison can be achieved while the capacity is diminished at low temperatures. Due to the strict safety requirements in the reactor hall, deep discharge below 2 V and potential battery damage needed to be avoided. Figure 102 shows the discharge voltage and battery temperature at 0 °C forced convection conditions in a climate chamber. The batteries were discharged at 1C to the Ah target as defined in section 8.3.1.1 and remained above the 3 V lower voltage limit. The temperature increased by less than 2 °C for all batteries with the highest increase for the HE battery. The Ah difference between the target DoD and the capacity achieved at 3 V cut off voltage and forced convection was 19 mAh (HE), 55 mAh (BA), 49 mAh (HP). Since the cooling at natural convection in the cryostat is less efficient than cooling at forced convection, the Ah buffer was deemed sufficient.

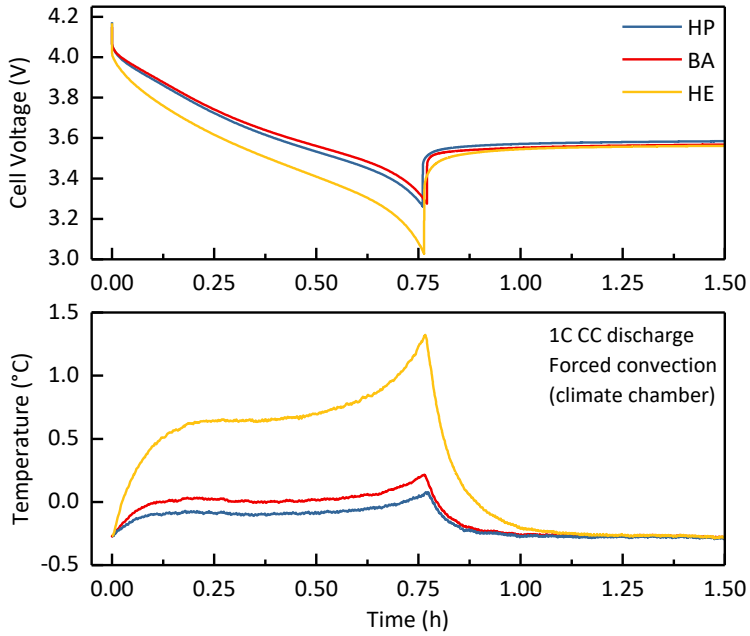

Figure 102 HE, BA and HP cell voltage and surface temperature during discharge at 1C-CC to target DoD at 0 °C forced convection conditions.

8.3.1.3 Beam characterization and data recording

As outlined in section 4.8.3.2 the wavelength of the neutron beam was characterized using NIST SRM 640d SI standard powder. The wavelength was determined to 2.10326(8) Å. The Si diffraction data and Rietveld refinement are shown in Figure C.2. In consistency with the previous ND experiment (section 7.2.3), a 5 x 20 mm^2 entrance slit, and a 5 mm radial collimator in front of the detector were used. The scattering gauge volume thus is 0.5 cm^3. The diffraction data is collected over 6 min per image at a fixed 2θ range of 28° < 2θ < 42°. Data sets were combined to increase signal to noise ratio wherever possible without loss of features during slow phase changes.

8.3.2 Diffraction data offset and scaling

Figure 103 a) shows the HE, BA and HP cells at their initial state of 100 % SoC cooled down to the target temperature for the discharge experiment. While the background for equal cell loadings, HE and HP samples at -5 °C and -20 °C, is nearly identical, the background differs between loadings. The background is angular dependent and decreases with 2θ angle due to quadratic sample shape that causes entry position dependent non-equal path length for neutrons through the sample compared to cylindrical shape. The average counts of the background over the 28° to 42° range are determined with Highscore and listed in Table 32. Compared to the HE samples, the background is about 1000 counts higher for the BA sample, and 1400 counts higher for the HP samples. This is expected, since the HE

cells have the lowest number of layers (8) compared to BA (11) and HP (20) and thus less aluminum and copper current collectors as well as electrolyte filled separator layers in the beam path. Figure 103 b) shows good agreement between the backgrounds after subtraction of the offset difference. While the background offset is minimal, notably, the maximum reflection intensity of LiC_6 and LiC_{12} is lowest for HP cells, medium for BA and highest for HE cells. While the SoC of the batteries and the degree of lithiation of the anode is approximately equal for all cells, the amount of active material in the gauge volume is not. This was expected, since the cell height criteria for the manufacturer were set to achieve a tolerable background for all loadings and not equal active material mass in the gauge volume.

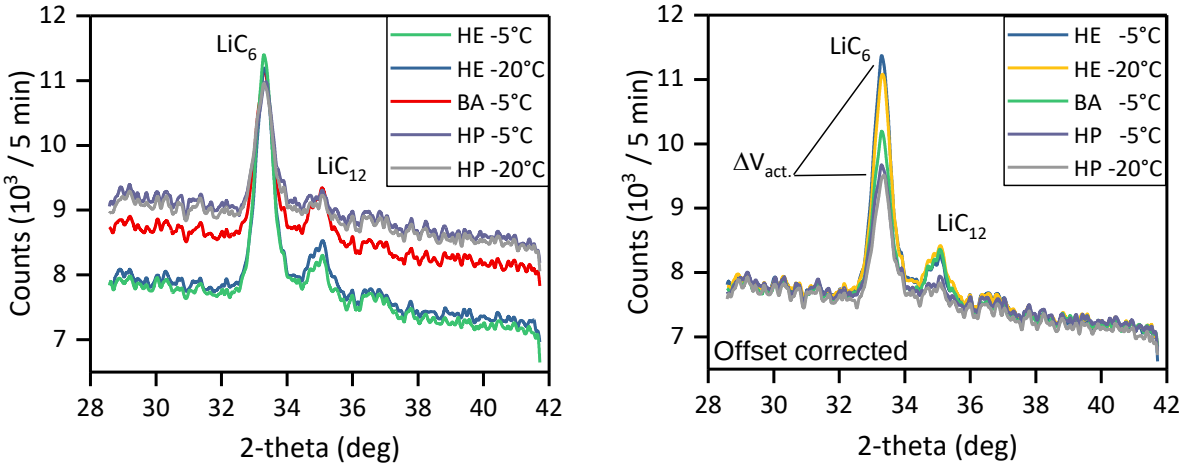

Figure 103 Sample cells at initial 100 % SoC state without (a) and with offset correction (b).

For comparison of the time dependent intensity changes, scaling factors are calculated to correct the reflection intensities for the differences in active material mass between cell types HE, BA, and HP. Scaling factors calculated with different approaches are listed in Table 32. $S_{\mathrm{load-CC}}$ is the scaling factor calculated based on the differences in mAh cm^{-2} as given by the manufacturer datasheet. S_{elec} is a scaling factor based on the electrode volume differences in the gauge volume $V_{\mathrm{elec-gauge}}$. $S_{\mathrm{elec}-\epsilon_s}$ is a scaling factor that corrects S_{elec} for the different solid material volume fractions ϵ_s. For comparison the scaling factor for ideal rescaling solely based on setting equal integrated intensities S_{I} is listed.

Table 32 Background counts and scaling factors $S_{\mathrm{load-CC}}$, S_{elec}, $S_{\mathrm{elec}-\epsilon_s}$, and S_{I}.

Cell	HE	BA	HP
Background avg. (counts)	7549 (-20 °C) 7708 (-5 °C)	8494 (-5 °C)	8795 (-5 °C) 8960 (-20 °C)
$V_{\mathrm{elec-gauge}}$ (cm^3)	0.082	0.069	0.056
ϵ_s	0.56	0.58	0.47
$S_{\mathrm{load-CC}}$	1	1.26	1.38
S_{elec}	1	1.18	1.46
$S_{\mathrm{elec}-\epsilon_s}$	1	1.14	1.76
S_{I}	1	1.37	1.72 (-5 °C) 1.79 (-20 °C)

All scaling factors scale the reflection intensity relative to the HE reference-sample. Figure 104 compares the maximum intensity of the LiC_6 peak as shown in Figure 103 (b) for the original data and scaled with the three different scaling factors for all loadings. All scaling factors improve upon the intensity difference in the original data. Figure 104 shows, that the inclusion of ϵ_s strongly improves the HP scaling.

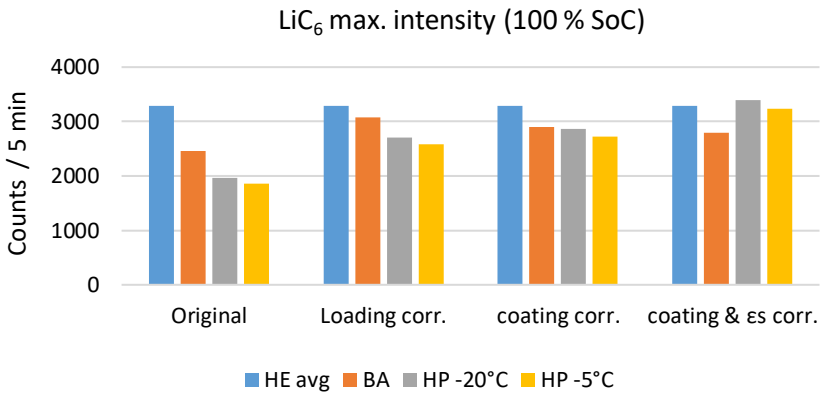

Figure 104 Rescaling of LiC_6 max. Intensity through loading, coating, and coating with porosity correction.

In the following analysis of the diffraction data, the line plots show original data and the fitted maximum intensities and integral intensities are scaled with $S_{\mathrm{elec}-\epsilon_s}$ for easier comparison of the time dependent behavior between different loadings.

8.3.3 Discharge and relaxation: HE-BA-HP -5 °C

The HE, BA and; HP samples are discharged to their target SOC at -5 °C set temperature. The voltage, temperature, and diffraction data are given.

8.3.3.1 Voltage and temperature profile

The cells are charged (CCCV, 1C, I < 0.05C) to their initial state of 100 % SoC outside of the cryostat environment at 25 °C to prevent lithium plating. The cells are then cooled down to the target temperature of -5 °C inside the cryostat for 45 min. Figure 105 shows the cell voltage and temperature after the cooling process. After an initial pause of 10 minutes the cells are discharged with constant current at 1C to the target SoC. The higher the cell loading (HE > BA > HP), the higher is the initial voltage drop at beginning of discharge (190 mV > 160 mV > 130 mV), the lower is the average voltage during discharge (3.41 V < 3.55 V < 3.59 V) and the lower is the end of discharge voltage (2.63 V < 2.75 V < 2.95 V). With higher loading the internal resistances increase and the rate capability decreases. Correspondingly, the temperature increase is highest for the HE cell (3.1 °C) compared to BA (1.9 °C) and HP (1.6 °C) measured between the maximum temperature and the resting temperature at t = 3 h. The resting temperature varies between cells by 0.5 °C and is at ≈ -3 °C slightly higher than the target of -5 °C. Setting of precise cell temperature was difficult due to different locations of the cell temperature sensor and the temperature control sensor which caused a short delay and offset.

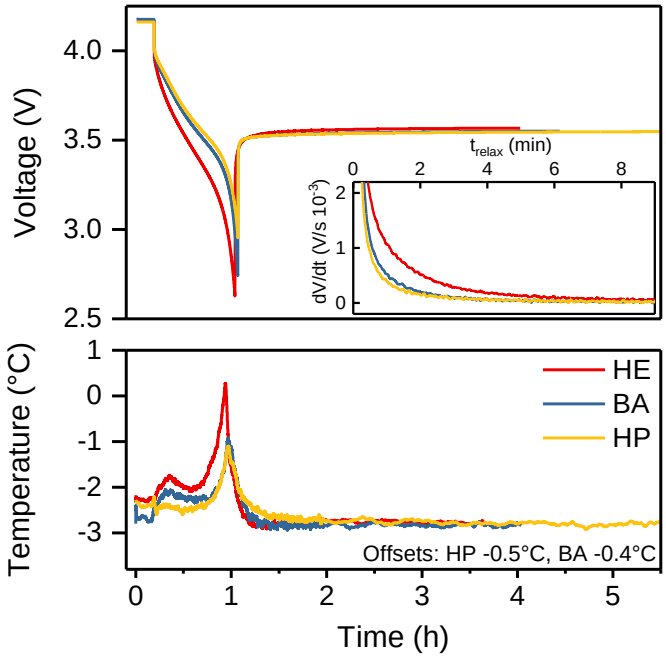

Figure 105 Cell voltage and temperature during 1C CC discharge and relaxation at T ≈ -3 °C for HE, BA and HP cells. A temperature offset was added to the BA (-0.5 °C) and HP (-0.4 °C) to equalize the resting temperature and to highlight the difference in the temperature increase during discharge. The inlet shows the derivative *dV/dt* during relaxation.

After reaching the target SoC the relaxation is monitored for several hours. The inlay in Figure 105 shows the differential voltage plot of the relaxation process. The voltage relaxation is faster for the HP cells compared to BA and HE. While small differences between the relaxation slopes persist for approx. 1 hour, within 8 minutes the difference in *dV/dt* decreases below $0.2 \cdot 10^{-3}$ V/s. This is considerably faster than what was observed in the previous experiment (section 7.5.4). Also, a *dV/dt* plateau as observed in the previous ND diffraction experiment (section 7.4.1) is not observed. Since these plateaus are caused by *overshooting graphite phases* (Bauer et al.) [184], this is an indication of little phase splitting.

8.3.3.2 Neutron diffraction: Initial state and discharge

The in situ neutron diffraction data of the $Li_{1-x}C_6$ reflections during discharge and relaxation for the HE (a,d), BA (b,e), and HP(c,f) cells are shown in Figure 106. The contour plots (d,e,f) show the time evolution of the reflection intensity over the 32° to 39° 2θ range from beginning of discharge to end of relaxation. The beginning of the relaxation period is marked. In addition the line plots (a,b,c) show the reflection Intensity at distinct moments in time, such as the beginning of relaxation ($\Delta t = 0$). Figure 107 shows the time evolution of the integral intensity (a) and the *d*-spacing (b) of the graphite phases during discharge. The integral intensity shown is scaled as discussed in (section 8.3.2) to offset differences in the active material content.

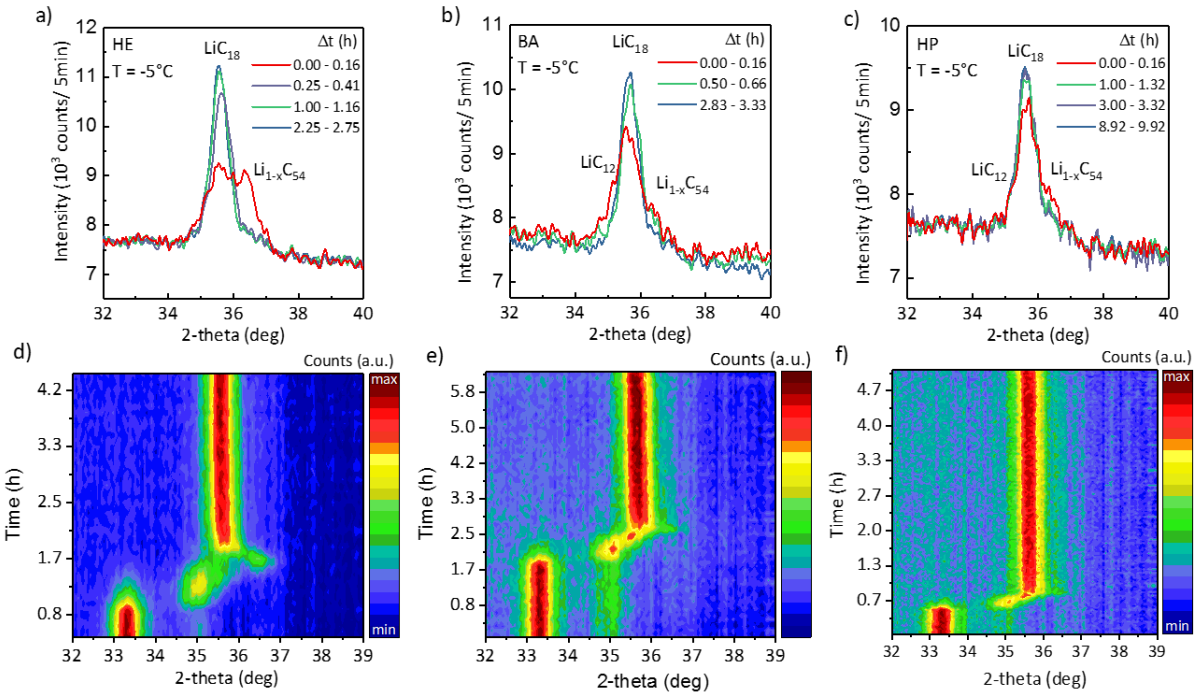

Figure 106 Diffraction data collected for HE (a,d), BA (b,e) and HP (c,f) cells during discharge at 1C and subsequent relaxation at -5 °C. The top row (a-c) shows the $Li_{1-x}C_6$ reflections at the end of discharge (~0h, red) and up to several hours after discharge (green, purple, blue). Each pattern is collected over 5 minutes with high intensity: red, low intensity: blue.

At the initial state before discharge the cells are at 100 % SoC. Table 33 shows the integrated intensity ratio, the LiC_{12} and LiC_6 phase fraction and *d*-spacing as well as degree of lithiation for the HE, BA and HP cells at the initial state. The *d*-spacing of LiC_{12} (3.501 Å) and LiC_6 (3.669 Å) is in good agreement with literature [171]. The anode lithiation is not equal for all cells, but varies between 0.85(1) and 0.91(2). This is consistent with the findings in *dV/dQ* analysis that target SoC needs to be lower for the HP cell than for the BA cell than for the HE cell. However, the difference there is ≈ 1 % and therefore not as large as the 6 % ± 3 % difference observed here.

During discharge the integrated intensity (Figure 107 b) of LiC_6 decreases and LiC_{12} increases as the anode is delithiated. During this the fitted *d*-spacing is consistent. At the end of discharge the LiC_6 intensity is gone and the phase is not visible anymore in the contour and line plots (Figure 106 a-f). The intensity of LiC_{12} increases until end of discharge where it plateaus (HP, BA) or drops (HE). The *d*-spacing is constant during pause and beginning of discharge and slightly shifts to lower values at end of discharge (Figure 107 a). The HE sample is the only sample that shows clear phase splitting with the emergence of a low lithiated phase $Li_{1-x}C_{54}$ with *d*-spacing close to but higher than graphite (Figure 107 a) and comparatively high intensity (≈ 1500). For the BA and HP sample the LiC_{12} phase shifts continuously from 3.50 Å to 3.45 Å (LiC_{18}).

Table 33 The Integrated intensity ratio I_{int}, integrated intensity corrected with structure factor $I_{int}/|F(hkl)|^2$, LiC_{12} and LiC_6 *d*-spacing and phase fraction as well as degree of lithiation for the HE, BA and HP cells measured during pause before discharge (Figure 104 b) are shown.

Sample	SoC	LiC_{12} I_{int}	LiC_{12} *d*	LiC_6 I_{int}	LiC_6 *d*	LiC_{12} $I_{int}/\|6b_C+b_{Li}\|$	I_{int} $LiC_6/\|-6b_C+b_{Li}\|$	LiC_{12}	LiC_6	Lithiation
	%	Cts*2θ	Å	Cts*2θ	Å	Cts*2θ	Cts*2θ	%	%	Li_xC_6
HE -5°C	100	4550(267)	3.501	20539(213)	3.669	3.2(2)	11.7(1)	21(1)	79(1)	0.89(1)
BA -5°C	100	11744(313)	3.498	33472(323)	3.670	8.1(2)	19.2(2)	30(1)	70(1)	0.85(1)
HP -5°C	100	2883(247)	3.502	15472(258)	3.669	2.0(2)	8.9(1)	18(2)	82(2)	0.91(2)
HE -20°C	100	5399(276)	3.499	19004(218)	3.668	3.7(2)	10.9(1)	26(1)	74(1)	0.87(2)
HP -20°C	100	2262(216)	3.503	10808(223)	3.666	1.6(2)	7.8(1)	20(2)	80(2)	0.90(3)

The difference in phase splitting between the HE, BA and HP samples is also visible in the contour and line plots. The contour plot of the HE sample (Figure 106) shows a clear phase split and maximum for a lower lithiated phase at 1.7 h and 36.5°2θ, while BA and HP show some intensity at higher °2θ values, the most intensity is shifting from ≈ 35°2θ (LiC_{12}) to ≈36°2θ (LiC_{18}). The line plots (Figure 106 a-c) show equal intensity of the $Li_{1-x}C_{54}$ phase and the LiC_{18} phase of about 9000 counts for the HE sample but much less intensity of the $Li_{1-x}C_{54}$ phase for the BA and HP sample at Δt = 0 beginning of relaxation.

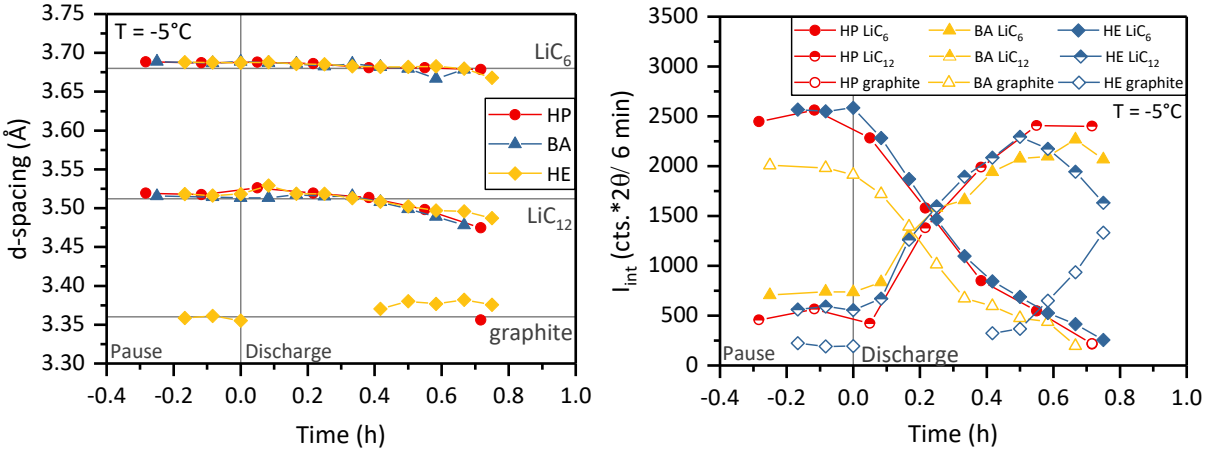

Figure 107 *d*-spacing (a) and integral reflection intensity (b) of all anode reflections during discharge at 1C and -5 °C for the HE, BA and HP cells. The starting point t = 0 h is set to the beginning of the discharge. The diffraction data includes a preliminary pause before discharge. The integral reflection intensity is scaled with the corresponding gauge volume correction factors (Table 32).

There are three further things to note in the data presented here. First, the lower anode starting lithiation of the BA sample is visible during delithiation since the scaled starting intensity of LiC_6 is lower (2000) and the LiC_{12} intensity is higher (500) than for the BA and HP sample (Figure 107 b). Second, there appears to be a residual amount of graphite in all battery types that is non-lithiated independently of the SoC of the battery. This phase with very small intensity is not consistently fitted due to its low signal to noise ratio, but appears to be present at high SoC (Figure 107) as well as after relaxation and heating (Figure 108). The origin of this phase is not clear. A possible explanation is contact loss of particles or separator background. Third, the line and contour plots show a higher degree of detail of the phase mixture than the results of the Pawley fit analysis. For example, the line plot of the BA cell at the beginning of relaxation shows asymmetric peak shape with an additional LiC_{12} shoulder that is not fitted independently from the LiC_{18} center reflection. This is because the signal quality is not sufficient for fitting three overlapping phases. As a result, the low lithiation phase fitted averages over several slightly different degrees of lithiation. This can also be seen in the increase of reflection FWHM that is further discussed in (section 8.3.5.2).

8.3.3.3 Neutron diffraction: Relaxation

Figure 108 shows the time evolution of the integral intensity (a) and the *d*-spacing (b) of the graphite phases during relaxation. Sample HE, BA and HP each show a dominant higher lithiated phase and a fading lower lithiated phase. The *d*-spacing of the higher lithiated phase is very close to the literature value of LiC_{18}, with a small offset for the HE sample. The low lithiated phase shows on average a slightly higher *d*-spacing than graphite. The LiC_{18} phase shows a minor drop and increase in shift to higher *d*-spacing values within the first 1.5 h of relaxation. For the low lithiated phase the high noise prevents closer analysis. The degree of phase separation at beginning of relaxation is higher for the HE sample, than for the BA sample than for the HP sample. During relaxation the intensity of LiC_{18} increases and the intensity of $Li_{1-x}C_{54}$ decreases. This process is very quick and the phase intensity is stable at t = 1.5 hours. However, the data shows a high intensity fluctuation for all samples complicating the analysis.

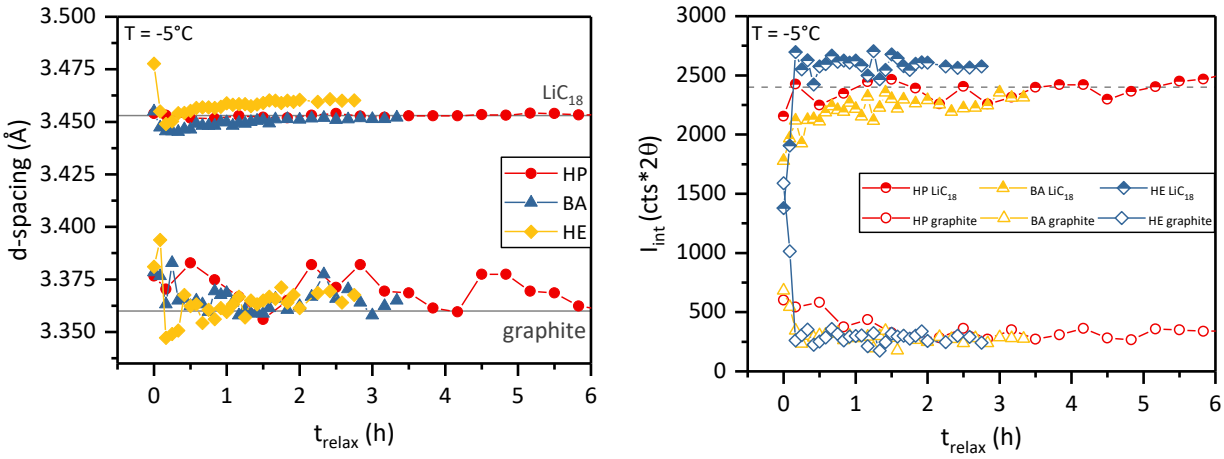

Figure 108 *d*-spacing (a) and integral reflection intensity (b) of all anode reflections during relaxatior after 1C discharge at -5 °C for the HE, BA and HP cells. t_{relax} equal zero marks the end of discharge and beginning of the relaxation. The integral reflection intensity is scaled with the corresponding gauge volume correction factors (Table 32). Graphite and low lithiated phases $Li_{1-x}C_{54}$ are lumped together. The *d*-spacing fluctuations are too high for a separate analysis.

Figure 109 shows the maximum intensity of the fitted reflections instead of the integrated intensity as seen in Figure 108 and previously used in chapter 7. Here, the time evolution of the intensity is much clearer, since the max. Intensity does not include the peak broadening due to overlapping phases. At approx. t = 1.5 h the relaxation process is over and the low and high lithiated phases maintain their intensity for all loadings. The relaxation process of the HE sample appears to be slightly faster than for the HE and BA sample despite the greater initial phase separation. A potential explanation for this is, that the temperature increase during discharge is higher for this sample and that the resting temperature of the BA and HP samples were 0.5 °C lower. This indicates that the temperature influence on relaxation is much greater than the electrode width.

In comparison to the previous experiment, where intensity changes were observed at 0 °C for longer than 6 hours of relaxation (section 7.5.4), the relaxation here is much faster independent of the electrode loading.

8.3.3.4 Transport and diffusion analysis

In the first ND experiment the model concept was introduced, that differently lithiated segments of particles are distinguishable in the ND data and that the time constant of the equalization between the segmented phases can be used to analyze the graphite solid diffusion constant (section 7.5.4). Following this concept, the ND of the HE, BA, and HP measurements at -5 °C are analyzed in the same way.

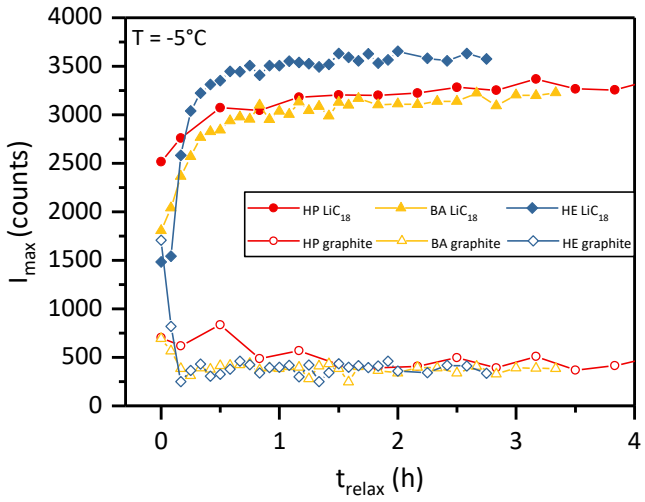

Figure 109 Reflection intensity maximum of all anode reflections during relaxation after 1C discharge at -5 °C for the HE, BA and HP cells. t_{relax} equal zero marks the end of discharge and beginning of the relaxation. The reflection intensity is scaled with the gauge volume correction factors (Table 32).

From the observed relaxation time and the particle size distribution the solid diffusion constant for solid diffusion processes is calculated. The diffusion time τ for a given path is approximated with $\tau = x^2/(4\,D_e)$ with D_e being the solid diffusion constant in Fick's law [29]. The SEM images show, that the particle shape is symmetrical (Figure 93) and that all cells share the same shape and radii distribution properties. The radius of a large particle $d_{90}/2$ is used as the diffusion length x. Large particles contribute more to the total volume of active material than small particles and are thus more visible in the ND data. The d_{90} is chosen for comparison with the first experiment, where this was also used as reference size.

With the relaxation time approximated from the maximum intensity change (Figure 109) to 1.75 hours for the samples HE, BA, HP, the diffusion coefficients at low lithiated graphite states of HE and BA are calculated to $D_{\mathrm{HE,BA-5}} = 1.7 \cdot 10^{-11}\ \mathrm{cm^2\ s^{-1}}$ and to $D_{\mathrm{HP}} = 1.8 \cdot 10^{-11}\mathrm{cm^2\ s^{-1}}$ for the HP cell. The results are summarized in Table 34. The diffusion coefficients are very similar, and assuming a large read-out error of ±0.5 h for the end of relaxation the values are indistinguishable within the measurement error of $D_{\pm} = 0.5 \cdot 10^{-11}\mathrm{cm^2\ s^{-1}}$.

Table 34 Estimated effective graphite solid diffusion constants at T ≈ -3 °C.

Sample	$d_{90}/2$ (µm)	Relaxation time (h)	Effective diffusion constant (10^{-11} $cm^2\ s^{-1}$)
HE -5°C	6.6	1.75	1.7
BA -5°C	6.5	1.75	1.7
HP -5°C	6.8	1.75*	1.8

8.3.4 Discharge and relaxation: HE-HP -20 °C

The relaxation times observed at -5 °C were surprisingly short and the phase splitting was suppressed. With the remaining measurement time at the neutron source, the experiment was repeated at very low temperatures for the samples with the greatest electrode width difference. The HE and HP samples were discharged to target SOC at -20 °C set temperature and the cell voltage, temperature and diffraction data were recorded.

8.3.4.1 Voltage and temperature Profile

As with previous samples the cells are charged (CCCV, 1C, I_{CV} < 0.05C) to their initial state of 100 % SoC outside of the cryostat environment at 25 °C to prevent lithium plating. The cells are then cooled down to the target temperature of -20 °C inside the cryostat for 45 min. Figure 110 shows the cell voltage and temperature after the cooling process. After an initial pause of 10 minutes the cells are then discharged with 0.25C at constant current to 34 % SoC. The lower rate and higher target SoC were chosen, since this allowed both cells to remain in the safety voltage window of the cell (U > 2 V).

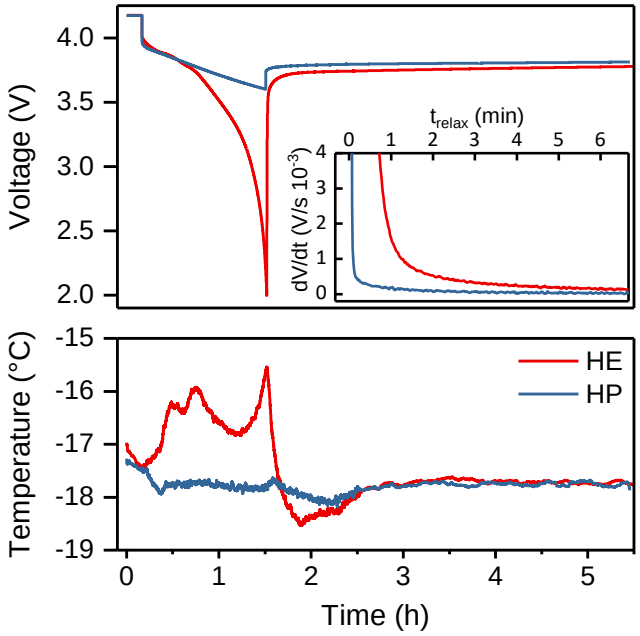

Figure 110 Cell voltage and temperature during 0.25C CC discharge and relaxation at T ≈ -18 °C for the HE and HP cell. The inlet shows the derivative *dV/dt* during relaxation.

The initial voltage drop at beginning of discharge is similar for the HE cell and the HP cell (160 mV and 200 mV). During discharge the voltage of the HE cell drops fast until 2 V is reached. In comparison to that the HP cell does not show a strong voltage drop. The average voltage during discharge is thus much lower for the HE cell (3.53 V < 3.76 V) than for HP. The temperature increase is greater for the HE cell (2.3 °C) than for the HP cell which barely heats up (0.2 °C). Both cells have a resting temperature of -17.8 °C.

After reaching the target SoC the relaxation is monitored for several hours. The inlay in Figure 110 shows the differential voltage plot of the relaxation process. The voltage relaxation is faster for the HP than the HE cell. While small differences between the relaxation slopes persist for approx. 1 hour, within 6 minutes the difference in *dV/dt* decreases below $0.5 \cdot 10^{-3}\,\mathrm{V/s}$. As for the -5 °C measurement, the *dV/dt* plateau is not observed.

8.3.4.2 Neutron Diffraction: Initial state and discharge

The in situ neutron diffraction data of the $Li_{1-x}C_6$ reflections during discharge and relaxation for the HE (a,b), and HP(c,d) cells are shown in Figure 111. The contour plots (c,d) show the time evolution of the reflection intensity over the 32° to 39° 2θ range from beginning of discharge to end of relaxation. The beginning of the relaxation period is marked. In addition, the line plots (a,b) show the reflection intensity at the beginning of relaxation ($\Delta t = 0$) and selected times later. Figure 112 shows the time evolution of the integral intensity (a) and the *d*-spacing (b) of the graphite phases during discharge. The integral intensity shown is scaled as discussed in (section 8.3.2) to offset differences in the active material content.

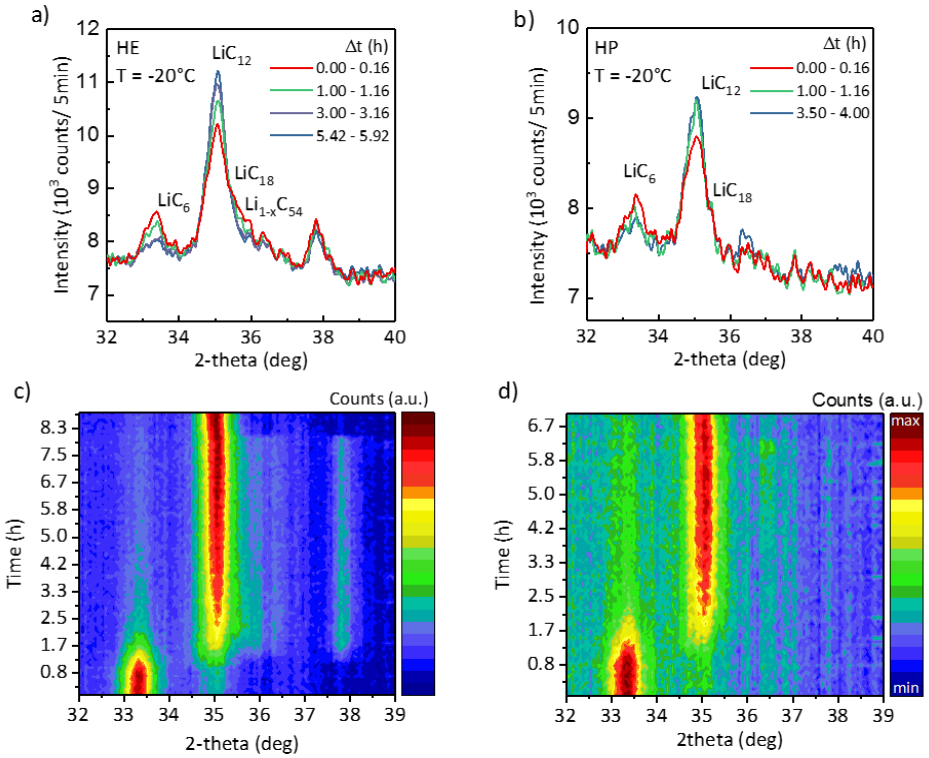

Figure 111 Diffraction data collected for the HE (a,c) and HP (b,d) cell during discharge (0.25C) and subsequent relaxation at -20 °C. The top row shows the $Li_{1-x}C_6$ reflections at the end of discharge (~0 h, red) and up to several hours after discharge (green, purple, blue). Each pattern is collected over 5 minutes. The contour plots show high intensity in red and low intensity in blue.

At the initial state before discharge the cells are at 100 % SoC. Table 33 shows the integrated intensity ratio, the LiC_{12} and LiC_6 phase fraction and d-spacing as well as degree of lithiation for the HE and HP cell at the initial state. The *d*-spacing of LiC_{12} (3.501 Å) and LiC_6 (3.669 Å) is in good agreement with the -5 °C data and literature [169, 171]. Within the measurement precision the anode lithiation of HE (0.87(2)) and HP (0.90(3)) are in agreement. As a result of this the scaled intensities match better than for the -5 °C cells (Figure 107).

During discharge the integrated intensity (Figure 112 b) of LiC_6 decreases and LiC_{12} increases as the anode is delithiated. During this period the fitted *d*-spacing is consistent. Since the target SoC is higher and the phase separation is stronger than for the -5 °C, the LiC_6 phase does not fully disappear during discharge. The phase maintains an integrated intensity of ≈ 800 counts for both cells and is still visible in the contour and line plots. The intensity of LiC_{12} increases until end of discharge up to ≈2000 counts for both cells. The *d*-spacing of LiC_6 and LiC_{12} is constant and maintains very good agreement with literature values [171] during pause and discharge (Figure 112 a,b).

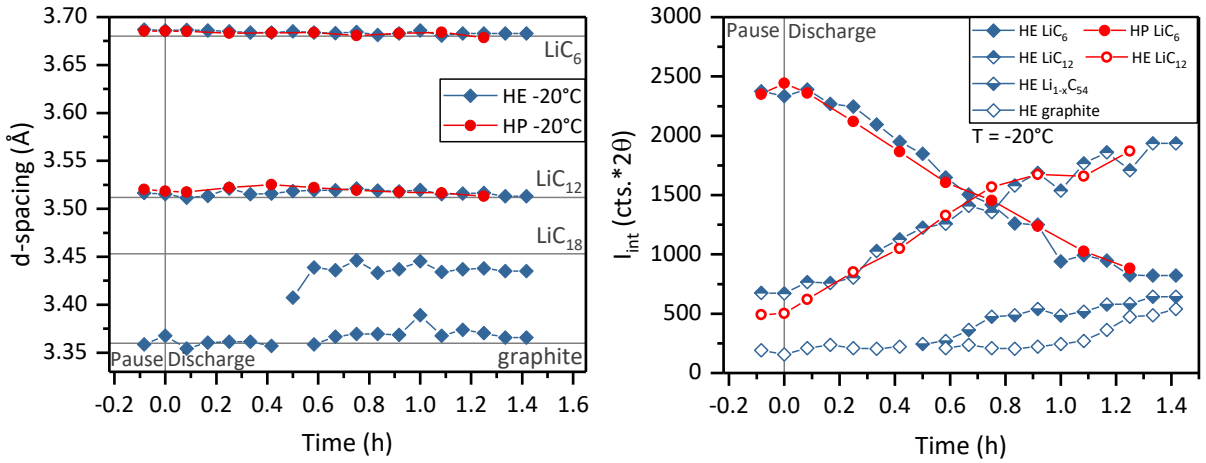

Figure 112 *d*-spacing (a) and integral reflection intensity (b) of all anode reflections during discharge at 0.25C and -20 °C for the HE and HP cells. Time equal zero is the beginning of the discharge. The diffraction data includes a preliminary pause before discharge. The integral reflection intensity is scaled with the corresponding gauge volume correction factors (Table 32).

The HE sample shows a clear phase splitting with the emergence of a low lithiated phase $Li_{1-x}C_{18}$ with *d*-spacing close to, but slightly lower than LiC_{18} (Figure 112 a). In addition, a fourth phase of very low lithiation and a *d*-spacing slightly greater than graphite increases in intensity at the end of the discharge (*t* = 1.2-1.4 h). Together, these low lithiated phases have a 1/3 of the total intensity. The phase splitting is also visible in the line and contour plots. The LiC_{12} reflection is strongly asymmetric and broadened towards higher °2θ values (35.5° to 36.5°) (Figure 111 a). Line and contour plots of the HE sample also show a strong feature at 37.8 °2θ. At more than °1 shifted from the non-lithiated graphite reflection, this feature cannot be linked to lithiated or non lithiated graphite within the measurement precision of the instrument. Instead, it is caused by electrolyte freezing which is discussed in section 8.3.4.4.

The HP sample does not show the feature at 37.8 °2θ (Figure 111 b). Also, the phase splitting is much less pronounced than for the HE sample. The 35 °2θ feature does show some asymmetry and broadening, but was best fitted with only a single LiC_{12} phase. With this detail lost in the fitting procedure, the *d*-spacing and integrated intensity figures only show the decreasing LiC_6 and increasing LiC_{12} phase (Figure 112 a,b). The residual amount of graphite that is consistently fitted for the HE sample independently of the SoC is not fitted for the HP sample. While it is assumed to be present, because lower signal to noise ratio it is less visible and thus not fitted.

8.3.4.3 Neutron diffraction: Relaxation at -20 °C

Figure 113 shows the time evolution of the integral intensity and the *d*-spacing of the $Li_{1-x}C_6$ phases during relaxation. Both samples show a LiC_{12} phase with increasing intensity, while the LiC_6 and lower lithiated phases lose intensity. The *d*-spacing of LiC_6 and LiC_{12} is constant and maintains very good agreement with literature. The $Li_{1-x}C_{18}$ and $Li_{1-x}C_{54}$ lower lithiated phases of the HE sample also maintain their *d*-spacing. After two hours of relaxation the HP sample shows the emergence of a new low lithiated phase $Li_{1-x}C_{54}$ close to graphite with slowly increasing intensity up to ≈500 counts at t_{relax} = 4 h.

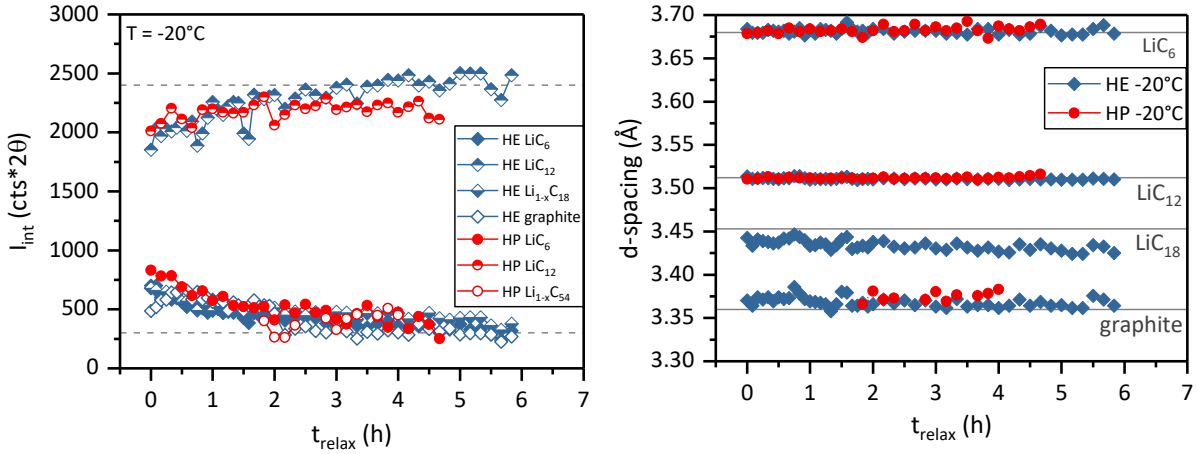

Figure 113 Integral reflection intensity and *d*-spacing of all anode reflections during relaxation after 0.25C discharge at -20 °C for the HE and HP cell. t_{relax} equal zero marks the end of discharge and beginning of the relaxation. The integral reflection intensity is scaled with the corresponding gauge volume correction factors (Table 32).

Figure 114 shows the maximum intensity of the fitted reflections instead of the integrated intensity as seen in Figure 113. The integrated intensity of the LiC_{12} reflection appears to be stable at ≈2400 counts and 3 hours of relaxation time. The maximum intensity continues to change until ≈4.5 hours of relaxation. The FWHM of the reflection decreases as the balance of the in the Pawley fit not fully resolved LiC_{12} LiC_{18} phase mixture changes. Similarly, at 4.5 hours the intensity of the HE phases are maintained and possible continuing changes are indistinguishable from the noise.

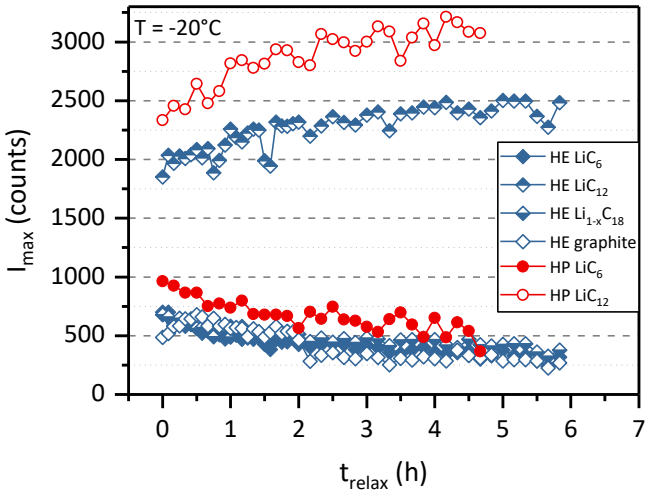

Figure 114 Reflection intensity maximum of all anode reflections during relaxation after 1C discharge at -5 °C for the HE and HP cells. t_{relax} equal zero marks the end of discharge and beginning of the relaxation. The reflection intensity is scaled with the gauge volume correction factors (Table 32).

In comparison to the previous experiment, where intensity changes were observed at -10 °C for longer than 6 hours of relaxation (section 7.5.4), the relaxation here is much faster independent of the electrode loading despite lower temperature of -18 °C.

8.3.4.4 Electrolyte freezing

To test whether the unidentified reflection at 37.8° in Figure 115 can be attributed to electrolyte freezing, a sample of the electrolyte used in the custom-made cells, LP 30 (EC:DMC 1:1, 1M $LiPF_6$), was cooled down and continuously measured with XRD. Figure 116 shows the diffraction pattern recorded with a wavelength of 0.7093187 Å (Mo-Kα_1). The angular range 28° to 42° covered in the ND experiment corresponds to approximately 9 to 14 °2θ for the Molybdenum Kα_1 wavelength. The position of the reflection in the ND measurement 37.8 °2θ corresponds to 12.5 °2θ for the XRD. Figure 115 shows, that initially the electrolyte does not show reflections, but during cooldown to -29 °C during XRD the crystallinity of the freezing electrolyte causes multiple close reflections around the 12.5°2θ position. This supports, that the reflection observed in the ND measurements is indeed caused by freezing electrolyte.

The XRD data also shows a reflection at 12 °2θ, which corresponds to 36.5° in the ND data. This reflection overlaps with the low lithiated $Li_{1-x}C_{54}$ and graphite reflections. While the XRD data suggests only 1/10 of the intensity compared to the 37.8 °2θ reflection, this may be different for neutrons, or different preferred orientations of freezing electrolyte. Since the structure of the frozen electrolyte could not be resolved with Rietveld refinement, whether this reflection is visible in ND is unclear. The sharp drop in the intensity of the low lithiated phases from relaxation end to heating (Figure 115 a) may therefore be due to accelerated relaxation or due to melting of the electrolyte.

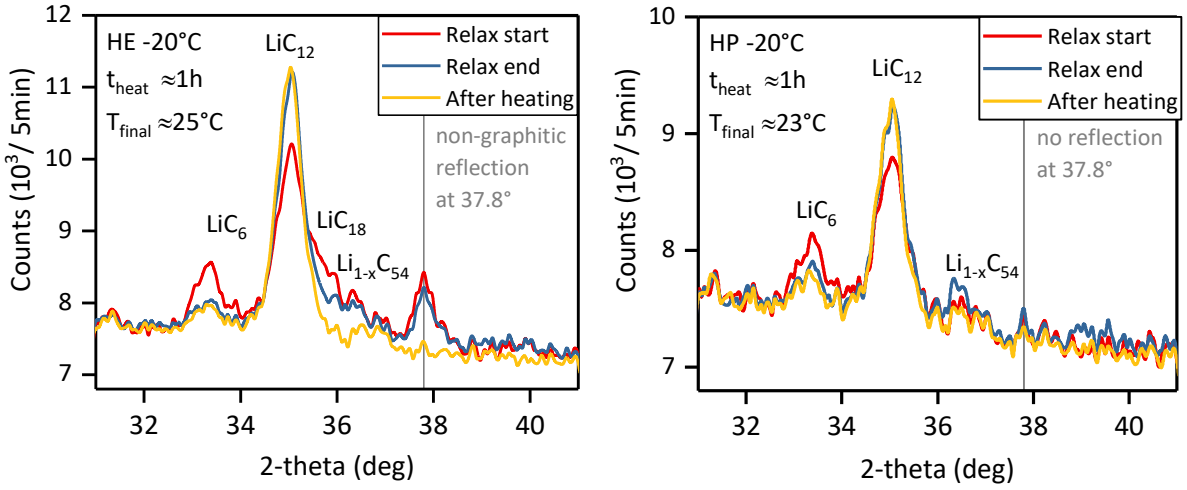

Figure 115 HE and HP sample after -20 °C discharge, relaxation and heating to room temperature. The HE cell shows a reflection at 37.8 °2θ that is not caused by lithiated graphite and disappears after heating the sample. The HP cell does not show this reflection.

In the XRD measurement, the intensity of the reflection increases strongly at -22 °C. This is four degrees Celsius lower than the -18 °C reached in the ND experiment. Taking into account the absolute temperature error of both sensors (±2 °C) and the longer relaxation times in the ND measurements the difference could be explained. However, this does not explain, why the 37.8°2θ reflection is not present at the HP sample. It can be speculated that this is a result of the lower electrode width of the HP sample, about a 1/3 compared to the HE sample. Diffusivity and conductivity of LP30 is concentration dependent [25]. Physicochemical simulations show [192] that significant concentration gradients can build up within the electrode. The differences in geometry could also influence the heat transfer of the heat generated in the battery.

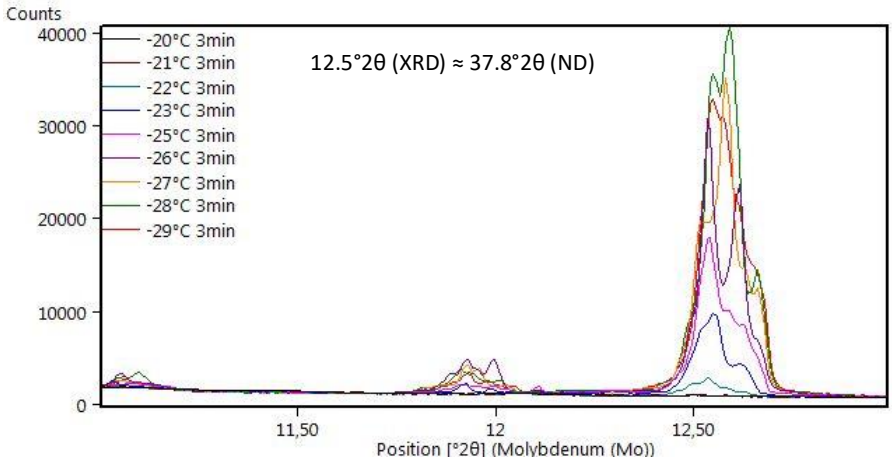

Figure 116 X-ray diffraction measurement of LP30 (EC: DMC, 1:1, 1M $LiPF_6$) during cooldown from -20°C to -29 °C.

Since tortuosity is similar for HP and HE (section 8.2.6.2) one might expect higher concentration gradients in the thicker electrodes, presumably causing local freezing. However, as this observation was made at the end of the series of experiments, the additional experiments and detailed electrolyte analysis necessary to verify these speculations were beyond the scope of this work.

8.3.4.5 Transport and diffusion analysis

The relaxation time scale of the HE and HP cells is analyzed following the lithiated shell model presented in section 7.5 and the diffusion calculations in section 7.5.4. Since the cells are built identically as the -5 °C samples, the particle shape and radii distribution properties are equal. From Figure 114 the period of time till end of relaxation is approximated to 4 hours for both samples.

With this the diffusion coefficients at low lithiated graphite phases are calculated to $D_{\mathrm{HE}-20} = 7.6 \cdot 10^{-12}\ \mathrm{cm^2\ s^{-1}}$ for the HE cell and to $D_{\mathrm{HP}-20} = 8.0 \cdot 10^{-12}\mathrm{cm^2\ s^{-1}}$ for the HP cell. With an estimated read-out error of ±0.5 h for the end of relaxation the values are indistinguishable within the measurement error of $D_{\pm} = 1.0 \cdot 10^{-12}\mathrm{cm^2\ s^{-1}}$. The results are summarized in Table 35.

Table 35 Estimated effective graphite solid diffusion constants at T ≈-18 °C.

Sample	$d_{90}/2$ (µm)	Relaxation time (h)	Effective diffusion constant (10^{-11} $cm^2\ s^{-1}$)
HE -20°C	6.6	4.0(5)	0.8(1)
HP -20°C	6.8	4.0(5)	0.8(1)

8.3.5 ND fit-quality assessment

In the following the R_{WP} value, the fit parameter FWHM and the time dependence of the background intensity are discussed to asses overall fit quality.

8.3.5.1 R-factors

Figure 117 shows the R_{WP} values of the Pawley fits for all HE, BA and HP measurements at -20 °C to 0 °C. The depicted data covers the whole duration of the measurements including pause, discharge, and relaxation. For all measurements, the R_{WP} values are between 0.75 and 1.75. This was deemed acceptable, since fast data acquisition was necessary to resolve the time dependent discharge and relaxation processes.

Some R_{WP} variations are noticeable in Figure 117. The first data point shows high fitting quality and low R_{WP} values due to the long pause with ≈ 8x recording time increasing the signal to noise ratio. An example for this is the first data point of HE -20 °C and BA -5 °C. Similarly, for last data points where files were combined to double the measurement time the R_{WP} values is lower. An example for this are the last four data points of HE -5 °C (t ≈ 4 h). With the exception of these effects R_{WP} is uncorrelated to the state of operation of the cell; pause, discharge, or relaxation and the fit quality is consistent.

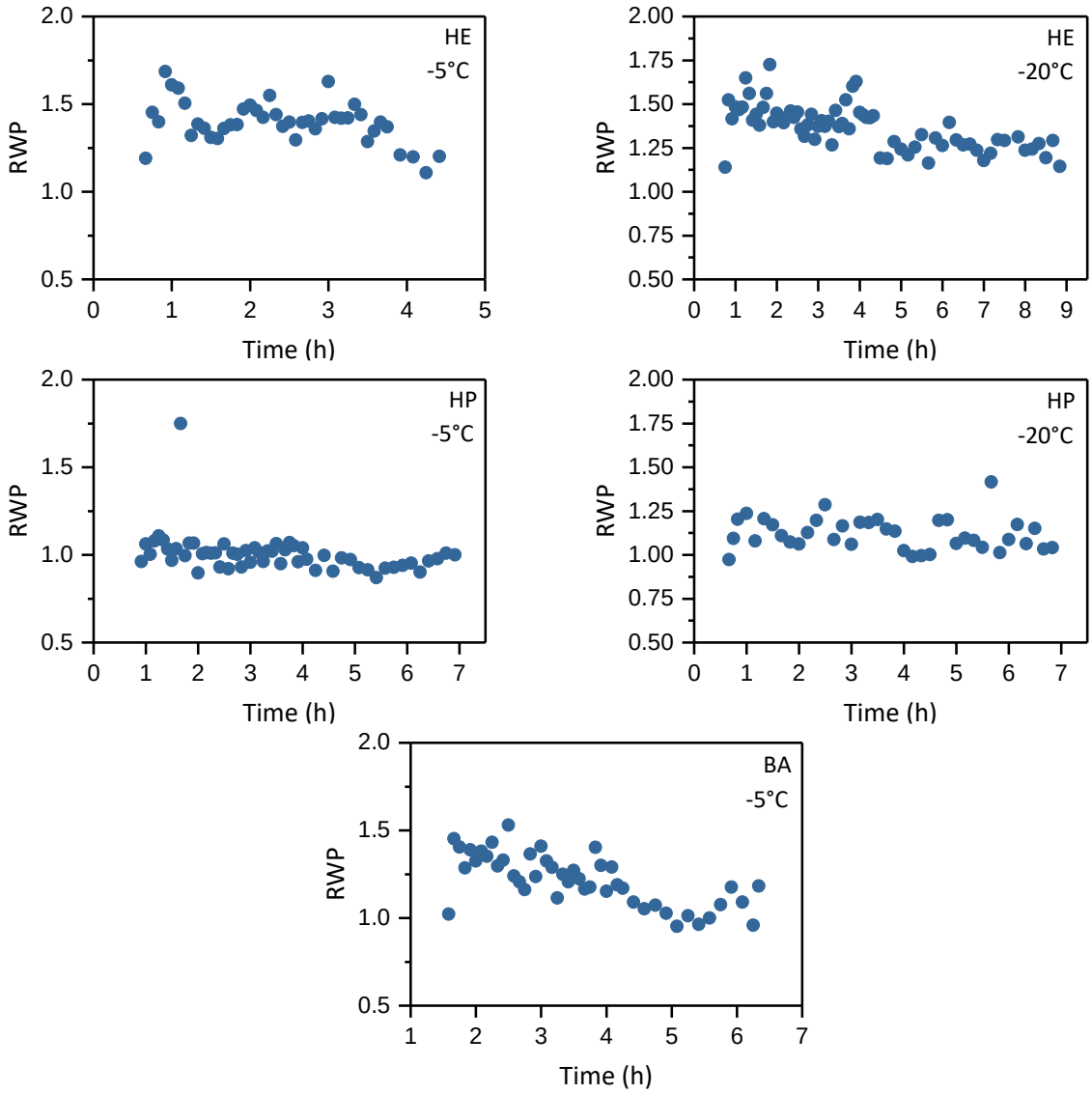

Figure 117 RWP of Pawley fits for HE, BA, and HP measurements at -20 °C to -5 °C. Time equal zero marks the beginning of the recording. The depicted data covers the whole duration of the measurements including pause, discharge, and relaxation.

8.3.5.2 FWHM

Figure 118 shows the FWHM of the Pawley fit phases for HE, BA and HP measurements at -20 °C to -5 °C. The depicted data covers the whole duration of the measurements including pause, discharge, and relaxation. Since the FWHM was set equal for all phases as a boundary condition to improve fit stability, there is only a single FWHM for each measurement independent of the number of phases.

In opposite to the R_{WP} values, the FWHM shows systematic change over time. During pause and at the end of the relaxation process the FWHM value is approx. 0.7. During discharge and at the beginning of relaxation the FWHM increases up to 1.2 and subsequently decreases. This indicates, that the number of phases present is greater than the number of phases fitted, which is counterbalanced with peak width. The Pawley fit analysis thus underestimates broadness of phase split due to suppressing intermediate phases. The disparity is greatest for the HE -5 °C and BA -5 °C data. For the HE -20 °C sample with stronger phase separation due to the lower temperature and more phases fitted, the FWHM only increases slightly to less than 0.8. The analysis shows the limits of data quality for the phase analysis. Pawley fit with additional phases was tried but discarded, since this strongly decreased fit stability and the signal to noise ratio is too low to clearly identify these phase contributions.

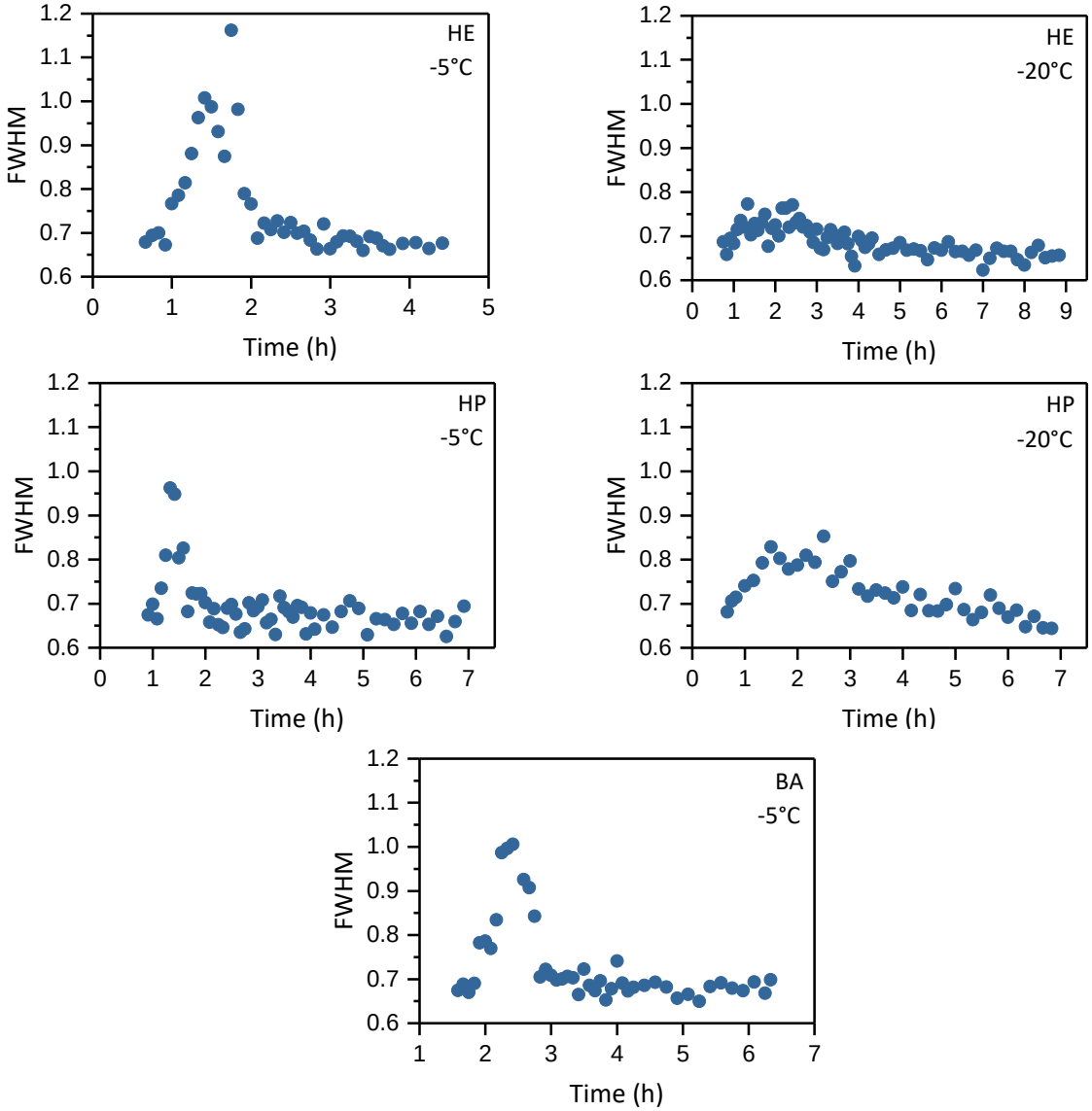

Figure 118 FWHM of peak fits for HE, BA and HP measurements at -20 °C to -5 °C. Time equal zero marks the beginning of the recording. The depicted data covers the whole duration of the measurements including pause, discharge, and relaxation.

8.3.5.3 Background

The background was determined in Highscore with the Search Peaks method. All fits were analyzed using a consistent standard set of parameters given in Table 36. In few cases the background was reworked with different fit parameters or manual background determination.

Table 36 Highscore Background determination.

Method	Search Peaks
Minimum significance	6
Minimum tip width gonio	0.01
Maximum tip width gonio	1.00
Peak base width with gonio	5.00

Figure 119 shows a comparison of the background for HE, BA and HP samples during pause, discharge, and relaxation. For the comparison the background beneath the reflection closest to the 35 °2θ position as fitted by Highscore is selected. The figure shows, with the exception of the BA sample the background is time independent. The standard deviation for the time averaged background counts is below 0.5 %. The background is independent from the state of the battery (pause, discharge, relaxation). The BA sample shows a slight variation in the background with higher values during the discharge phase and decreasing values during the relaxation process. However, the deviation is small and the standard deviation is still below 1 %.

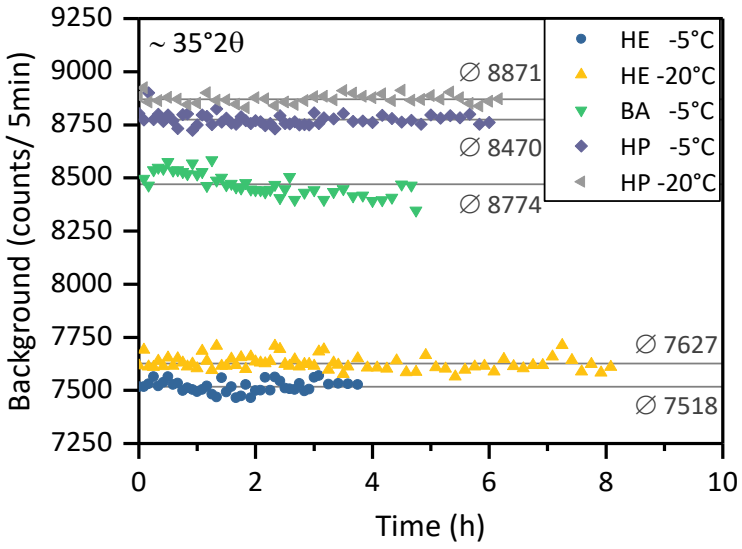

Figure 119 Background for all samples shown for the full measurement duration containing pause, discharge, relaxation and heating. Time equal zero marks the beginning of the data acquisition. The grey lines mark the time-averaged background.

The results show, that the background produced by the Search Peaks method and the used parameter set is consistent. The FWHM broadening observed for the Pawley fits is result of the phase distribution in the cell and not a variation of the background slopes.

8.4 Summary and comparison

The results of the two ND experiments show similarities and differences. To explore the origin of these differences, the experimental setup, sample properties, and data analysis and results are summarized, analyzed, and interpreted.

Setup

Since both experiments were conducted at the same facility, the experimental setup was overall the same. A different cryostat was used for the second experiment, but it was identical in build. The same X-Y table, detector, and neutron source were used and calibrated with the identical procedure. The same sample holder was used in both experiments. The temperature control and sensors were the same in both experiments.

Data analysis and quality

The raw data was converted with the same software and same version of the software. The first data set was fitted with MATLAB. The second data set was fitted with Highscore. In both cases a Pawley fit routine was used with FWHM coupling for overlapping features. The MATLAB routine fitted the background linearly. In the second experiment the peak finding function of Highscore was used for background determination. The signal to noise ratio of the custom-made cells was lower than for the commercial cell for all loadings. This is presumably due to larger amount of strongly damping electrolyte in the manually filled custom-made cells compared to the automatically filled commercial cells.

Samples

Both experiments included a high-power cell with thin graphite coating. The cathode material used was LCO in the first experiment and NCM for all cells in the second. In both experiments EC/DMC 1:1 electrolyte was used with 1M $LiPF_6$. The particle shape of the anode graphite material was spherical or potato shaped for both types of cells and the tortuosity of the coating was good in either case with close to ideal Bruggeman exponent values for spheres, as determined by 3D reconstruction. However, the average particle size was smaller for the custom-built cells (9.4 µm), than for the commercial pouch cell (16.4 µm). Another difference between experiments was, that the pouch cell of the first experiment was newly bought from a store, but the calendar age of the cells during storage at the store is unknown since the information was not given. The custom-made cells however were newly built.

Experiment

A one for one comparison between experiments cannot be made, since the measurement goal and procedure of the first and second experiment differed. The coating variation in the second experiment was an extension to the parameter variation of the first experiment with a single sample cell. The C-rate and temperature were kept constant for each HE, BA and HP comparison. The parameter variation of the first experiment could not be repeated due to the measurement time limitations of the proposal. 1C was used as standard C-rate for the second experiment, however odd C-rates such as 0.9C were used for the first experiment since the target current was initially set based on the current density 1.25 mA/cm^2 chosen for comparison with a particular electrochemical simulation model. Also, the anode lithiation targeted during discharge was close but not identical, since the concept to choose a fixed anode *dV/dQ* minimum evolved from the first experiment, where the target criteria was more broadly; center of the graphite 2θ phase shift.

Results

Overall, the results of the ND layer experiment agree with the previous relaxation experiment, but strong differences are observed in some aspects.

In both cases the anode shows Li_xC_6 phase splitting during discharge at low temperatures as a result of transport limitations. During the subsequent relaxation process, the multiple coexisting phases equalize towards a single or two phases close to mean lithium content is equally present. The relaxation process is faster for the second experiment, but the timescale is of the order of hours at 0 °C in both cases. The average particle diameter is slightly smaller for the custom-made cells. the calculated graphite effective diffusion constant for large particles is $D = 1.7 \cdot 10^{-11}\ \mathrm{cm^2\ s^{-1}}$ at -5 °C for the HP custom cell and $D = 2.8 \cdot 10^{-11}\ \mathrm{cm^2\ s^{-1}}$ at 0 °C for the commercial pouch and is therefore similar for both experiments despite the faster relaxation process observed for the second experiment.

The experiments differ strongly in the degree of the phase separation observed (Figure 83 and Figure 106). Phase separation during discharge is less pronounced for the custom-made cells, despite a slightly lower temperature of -5 °C compared to the 0 °C at the first experiment and a slightly higher discharge rate of 1C compared to 0.9C. This is true for the comparison of the commercial pouch cell with the HP custom cell, but also true for the comparison with the HE custom cell with approx. three times the graphite electrode width. The *dV/dt* plateau (Figure 82) observed consistently in the temperature and rate variations of the first experiment is not observed for either of the investigated loadings in the second experiment (Figure 105). However, this is not necessarily a contradiction to the first experiment. Rather, the lack of potential features can be attributed to the weakness of the observed phase splitting.

The comparison of the HE, BA, and HP cells with each other shows that the layer width does have a small effect on the initial phase separation. The cell with the thickest coating, HE, shows greater phase separation with equal intensities for the split LiC_{18} and $Li_{1-x}C_{54}$ phases at the beginning of the relaxation, compared to the BA and HP samples where the lower lithiated are less abundant and consequently contribute less intensity (Figure 106). The relaxation times however do not differ strongly between these cells despite the difference in initial phase separation. Here it needs to be noted that the relaxation analysis suffers from the speed of the relaxation and the data quality compared to the first experiment. Phases with lower intensity are more easily subsumed in the Pawley fit since the signal-to-noise ratio does not allow to fit broadened peaks with all features. Nonetheless, the contrast is sharp with previous experiment, and small between different anode coatings. At -20 °C the HE sample again shows greater phase separation and also a cell voltage drop to 2.8 V at less than 30 % DoD caused by the graphite particle shells being strongly delithiated (Figure 111). The HP cell does not show an equally strong phase separation and consistently does also not show the sharp voltage drop.

The results of the layer height variation experiment are consistent with the core shell interpretation of graphite delithiation from the first ND experiment. The process is faster, but the particle diameters are smaller and the calculated diffusion constants are similar. However, the layer experiment also shows that graphite inhomogeneity cannot be reduced to the particle effects alone, since greater anode coating thickness increases graphite charge inhomogeneity. While this is an expected result, given that the rate limiting effect of larger coatings is a well-known limitation in cell design, it also shows that multiple inhomogeneity causing effects are present in the sample despite the design choices for low potential and temperature gradients. The great difference in phase separation between the commercial pouch cell and the HP custom-made cells indicates unknown cell properties, such as graphite surface, particle morphology, SEI composition, or electrolyte additives had a strong impact on phase inhomogeneity despite similar electrode width and low tortuosity. The presence of differences in electrode design is visible in the comparison of the SEM images for both electrodes that show

qualitatively different particle morphology and electrode additive amounts. Electrolyte freezing in the HE sample but not in the HP sample at nearly equal low temperature could be interpreted as a result of lithium concentration gradients. This would strongly influence the vertical lithiation distribution in the electrode layers.

In conclusion, the analysis and comparison of the ND experiments shows that the core shell interpretation of graphite delithiation as main cause of the observed phase inhomogeneity remains plausible. However, other causes or contributions cannot be excluded based on thermal and potential homogeneity in the cell alone and must be considered in the interpretation. The isolation of the single parameter coating thickness was successful, but other parameters, such as particle morphology, electrolyte, and SEI properties, need to be isolated to locate the graphite inhomogeneity.

9 Conclusion

Two distinct phenomena have been investigated with in situ and ex situ diffraction in this thesis. First, the origin of the capacity recovery effect after long term storage. Second, the origin of lithiation gradients during discharge and relaxation cause a capacity reduction.

Capacity recovery

The capacity recovery effect, as first published by Dahn et al. 2015, was observed in experiments with small custom-made pouch cells with few mm wide overhang areas and relied on qualitative color analysis for the assessment of the overhang lithiation. This work extends the investigation to a 18650-type cylindrical cell and shows that the influence of the overhang on cell capacity is significant and of practical relevance for CE and SoH determination for commercial cells. For the first time, the lithiation of the overhang was proven with the XRD method that measures the bulk graphite state in addition to the surface only color method. The observed lithiation extended up to several cm into the overhang area, significantly further than previously reported. To minimize the effect of overhang areas on measurements, the author suggests the following procedure:

- Measure overhang areas of cells to assess the maximum recoverable capacity.
- Avoid long-term high temperature storage.
- Precondition cells before capacity tests by cycling. Use last cycle for capacity determination.
- Overhang areas can be drained by prolonged storage at low SoC and high temperatures.

A second set of experiments with laboratory cells has shown that the capacity recovery effect is not limited to overhang at the sides of the electrodes. Coatings on the electrode backsides can also be lithiated if they are in contact with the electrolyte. The presence of backside coatings is a typical practical problem in the analysis of harvested electrode material gained from post mortem of commercial cells. These experiments have demonstrated that the strong capacity contribution and alteration of the OCV necessitate the removal of the backside coating. High C-rates diminish the backside lithiation but are not sufficient to prevent it. The results suggest that a CE and SoH altering overhang effect as observed for the cylindrical cells may also be present in commercial pouch cells with double-coated electrodes at the top and bottom of the cell stack.

In situ ND of lithiation inhomogeneity

The experiments presented in this work were the first application of ND to specifically monitor graphite phase splitting during discharge and equalization during relaxation for commercial pouch cells. They demonstrate that neutron diffraction is a viable method to analyze phase coexistence and relaxation by showing that sufficient time resolution can be achieved with a high flux source and an optimized 2θ observation window. With this approach, the graphite phase splitting during discharge was quantified and the SoC inhomogeneity was measured in situ for challenging discharge conditions such as low temperature and high rates. The work presents a lithium distribution model for the observed SoC inhomogeneity and relaxation times as a result of solid diffusion transport limitations, which is based on the shrinking annuli mechanism. By analysis of the relaxation times, effective solid diffusion constants could be derived and matched between experiments and literature values. The slow lithium transport is attributed to transport limitations caused by grain boundaries between different phase domains or crystallites within the particles rather than in-plane transport. However, contributions to SoC inhomogeneity by other effects cannot be excluded, as indicated by the stronger initial phase separation observed for high loading cells compared to cells with thinner electrode width.

9.1 Outlook

To further test and validate the model approach, additional potential contributions, such as electrolyte transport limitations or particle size distribution, need to be evaluated in follow-up experiments. Based on the findings of this work the following focus points for future investigations are recommended.

Overhang areas in modern cell formats

The overhang experiment shows that the investigated capacity recovery effect is sufficiently large to be of practical relevance for the investigated 18650 cell and possibly other commercial cell formats. It should be of great interest for every researcher or engineer who performs CE or SoH measurements with today's commercial cells, whether the cell of choice exhibits similar overhang areas in order to approximate the extent of the effect or to prevent it through conditioning of the samples before measurement. Therefore, this investigation should be expanded to modern cell formats such as the 21700 cylindrical cells and large prismatic cells for BEV to assess whether the recovery effect is of similar practical relevance for these formats too.

Implications for BMS

It is also conceivable that the recovery effect impairs the battery management systems. Since it is typically not expected that a cell can improve its SoH and such a behavior may not be implemented in the software, this can interfere with SoC approximation or cell balancing.

Extended 2D overhang simulation

Further investigation of recovery effects would greatly benefit from a full scale 2D electrochemical model of an anode overhang area. With this, the influence of storage temperature and electrode potential can be quantitatively determined. The time and temperature dependent lithiation distribution of the overhang could be approximated from electrode geometry without comprehensive and costly aging and post mortem studies.

Recovery effect after partial cycling

Experiments at the EES institute found inhomogeneous LFP lithiation and a similar capacity recovery after partial cycling of commercial LFP cells. The effect is currently under investigation and appears to be linked to the anode overhang areas.

In situ neutron diffraction during discharge and equilibration processes provides lower and upper limits on graphite phase inhomogeneity. This approach can be applied to investigate the effectiveness of novel methods for electrode optimization, such as electrode structuring, in a complete cell system.

Electrode structuring

Electrode structuring, for example by means of laser ablation, is proposed as a potential method to maintain moderate rate capability of extremely thick electrode coatings to achieve very high energy densities on cell level. Monitoring the graphite lithiation during discharge and relaxation can visualize the impact of structuring through comparison of the observed phase splitting with a non-structured reference sample. The information on phase splitting may help to find ideal structuring parameters or can be used to validate SoC predictions by 3D electrochemical simulations.

Particle size effect

The extent of inhomogeneity between particles of different sizes and surface areas can be investigated by comparing cells with different graphite active materials. For this, a follow-up ND experiment with self-manufactured cells utilizing graphite powders of different size distributions has been proposed to the MLZ by Dr. S. Seidlmayer under the proposal 14942 and was granted 3 days of measurement time.

The results of this work highlight the prolificacy and necessity to use different and complementary techniques to investigate effects and processes in complex systems such as lithium-ion batteries. Such a comprehensive approach relies on the collaboration of different research facilities contributing with their expertise and knowledge. This was achieved in the collaboration of partners in physics, mechanical engineering, and electrochemistry in the framework of the ExZellTUM project.

Appendix

The following appendix contains additional information on the Overhang simulation (A), the XRD experiment (B), and the ND experiments (C).

A.1 2D-p2D Newman model

The 2D-p2D model presented in Figure 50 was built from two intermediate models of a graphite half-cell; the classical Newman approach, and a 2D representation without backside coating. The starting point of the model parametrization is the parametrization of the classical p2D Newman model. The full set of parameters and model equations is given in Table A.1 and Table A.2.

Geometric parameters such as particle radii r_{p}, active material volume ε_{s} and porosity ε_{l} were measured and calculated. The equilibrium voltage E_{eq} was measured and the Temperture T set to room temperature. Analytical expressions for the temperature and lithium-concentration dependence of the electrolyte diffusivity (eq. (80)) the ionic conductivity (81), and the activity coefficient (82) are implemented based on Valoen et al. [25]. The Bruggeman exponent α was derived from measurement. The parametrization was validated with the simulation of a rated capacity test. The best fit was achieved with the critical transport parameters electrolyte diffusivity $D_{\mathrm{l}}(c,T)$, graphite diffusion constant $D_{\mathrm{s,C6}}$ and reaction rate constant k_{C6} set to the values given in Table 37.

Table 37 Best fit model parameters. Data from [158].

Parameter	D_{l}	$D_{\mathrm{s,C6}}(\frac{\mathrm{m}^2}{\mathrm{s}})$	$k_{\mathrm{C6}}\ (\frac{\mathrm{m}}{\mathrm{s}})$
Value	$2 * \mathrm{Term}$	$8 * 10^{-14}$	$2 * 10^{-9}$

shows the experimental rated capacity data for a single-coated graphite – Li/ Li^+ half-cell with the classical Newman model best fit parameter results. While the cell capacity is reproduced well for the OCV at C/100, the model underestimates the capacity loss at higher rates. The shape of the discharge voltage curve as well as the voltage drop due to higher overvoltages at higher discharge rate are reproduced in a satisfying way by the Newman model.

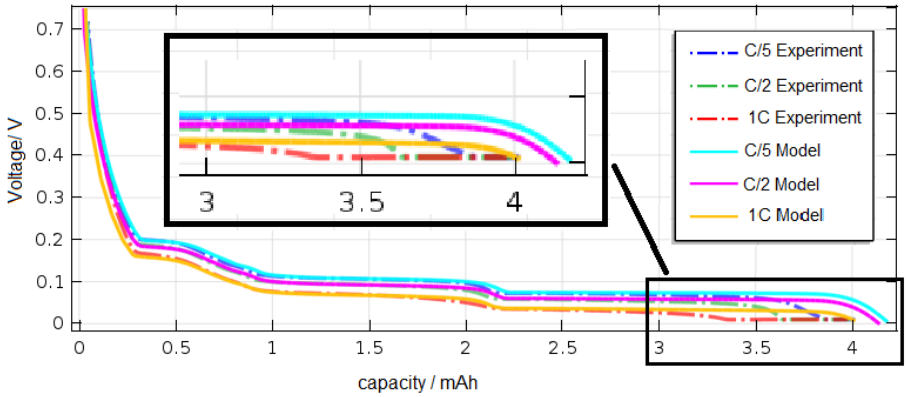

Figure 120 Half-cell voltage vs. discharged capacity for the classical p2D model of a graphite electrode (solid lines) and measured graphite half-cell profiles (dash-dotted lines). Image reprinted from [158].

Identical parameter sets are used for the model comparison of the extended 2D-model simulation as for the classical newsman model. Both models show excellent agreement in the rated capacity test shown in Figure 120. The model was successfully converted to 2D geometry. Since fundamentally

different results are expected for the final model due to the inclusion of the backside coating, no further consistency tests were performed between the two types of 2D models. The parameter set used for the preceding models is also used for the backside model. The only parameter changed is the coating thickness t_{c6}. It is changed from $t_{c6,1s} = 92.2\ \mu m$ for the single-sided electrode to $t_{c6,2s} = 80.64\ \mu m$ for the double-sided electrodes. The validation and simulation results of the backside model are presented with in the experimental results in the following section.

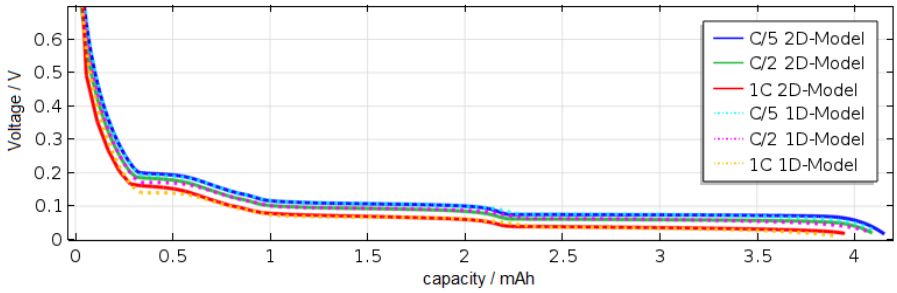

Figure 121 Half-cell voltage vs. discharged capacity for the classical p2D model of a graphite electrode (dotted lines) and the 2D implementation (solid lines). Image reprinted from [158].

A.2 2D-p2D Newman model equations

Table A.1 summarizes the p2D Newman model equations and boundary conditions utilized in the backside coating simulation model.

Table A.1 Newman p2D model equations and boundary conditions. Model description and fundamental equations listed in [86].

Domain	Expression	Boundary conditions	
Particle	$\frac{\partial c_s}{\partial t} = \nabla(D_s \nabla c_s) = D_s\left(\frac{\partial^2 c_s}{\partial r} + \frac{2}{r}\frac{\partial c_s}{\partial r}\right)$	$-D_s \frac{\partial c_s}{\partial r}\Big\vert_{r=0} = 0$	(70)
		$-D_s \frac{\partial c_s}{\partial r}\Big\vert_{r=r_p} = j_n$	
Electrode-Electrolyte-Interface	$i_n = i_0\left(e^{\frac{a_A F}{RT}\eta} - e^{\frac{a_C F}{RT}\eta}\right)$		(71)
	$i_0 = F k_C^{a_A} k_A^{a_A} \left(c_{s,max} - c_s\vert_{r=r_p}\right)^{a_A} \left(c_s\vert_{r=r_p}\right)^{a_C} \left(\frac{c_l}{1\ \mathrm{mol/m^3}}\right)^{a_A}$		(72)
	$\eta = \Phi_s - \Phi_l - E_{eq}$		(73)
Porous electrode	$\varepsilon_l \frac{\partial c_l}{\partial t} = \nabla\left(D_{l,eff} \nabla c_l\right) + a_s j_n (1 - t_+)$	$\nabla c_l\vert_{x=0,x=t_{cell}} = 0$	(74)
	$i_l = -\kappa_{eff}\ \nabla\Phi_l + \left(\frac{2\kappa_{eff} RT}{F}\right)\left(1 + \frac{\partial \ln f}{\partial \ln c_l}\right)(1 - t_+)\nabla \ln c_l$	$\nabla\Phi_l\vert_{x=0,x=L} = 0$	(75)
	$i_s = -\sigma_{eff} \nabla\Phi_s$	$\nabla\Phi_s\vert_{x=l_{neg},x=l_{neg}+l_{sep}} = 0$	(76)
	$\nabla \cdot \mathbf{I_l} + \nabla \cdot \mathbf{I_s} = 0$	$-\boldsymbol{n} \cdot \boldsymbol{i}_{\mathrm{CC}}\vert_{\partial\Omega_{\mathrm{CC}}} = 0$	(77)
		$-\boldsymbol{n} \cdot \boldsymbol{i}_{\mathrm{CC}}\vert_{\mathrm{tab}} = I_{\mathrm{app}}$	
Separator	$\varepsilon_l \frac{\partial c_l}{\partial t} = \nabla\left(D_{l,eff} \nabla c_l\right)$		(78)
	$\nabla \cdot \mathbf{I_l} = 0$		(79)
Electrolyte diffusivity	$D_l(c,T) = 10^{-4.43 - \frac{54}{T - 229 + 5c} - 0.22\,c} * 10^{-4}$		(80)
Ionic conductivity	$\kappa(c,T) = c * (-10.5 + 0.074\,T - 6.96 * 10^{-5}\,T^2 + 0.668\,c - 0.0178 * c\,T + 2.8 * 10^{-5}\,c\,T^2 + 0.494\,c^2 - 8.86 * 10^{-4}\,c^2\,T)^2 * 0.1$		(81)
Activity coefficient	$\frac{\partial \ln f \pm}{\partial \ln c} = \frac{0.601 - 0.24\,c^{0,5} + 0.982 * (1 - 0.0052 * (T - 298.15)) * c^{1,5}}{1 - t_+} - 1$		(82)

A.3 2D-p2D Newman model parameters

Table A.2 summarizes the Newman p2D model parameters for the 2-sided electrode model. Values obtained through measurement are marked with m and marked with c for calculated values. References are given for literature values.

Table A.2 Newman p2D model parameters for the 2-sided electrode model. Data from [191].

P2D Model			1S-C6	2S-C6	
Geometry	Symbol	Unit	LiC_6	LiC_6	Separator
Coating thickness	t	µm	92.2^m	70.1^m	
Current Collector		µm	14.9^m	14.9^m	381.3^m
Particle radii	r_p	µm	8^m	8^m	
Active material Volume	ε_s	%	40^c	40^c	
Porosity	ε_l	%	59.9^c	59.9^c	50
Physicochemical					Lithium foil
Equilibrium voltage	E_{eq}		measurement	measurement	
Lithiation window			$0-0.8^c$	$0-0.8^c$	
Max. lithium concentration	$c_{s,max}$	$\frac{mol}{m^3}$	31370^c	31370^c	
Temperature	T	K	298.15	298.15	298.15
Reaction rate	k	$\frac{m}{s}$	$2*10^{-11}$	$2*10^{-11}$	$1*10^{-10}$
Transfer number			0.5 [21]	0.5 [21]	
Solid diffusivity	D_s	$\frac{m^2}{s}$	$6*10^{-13}$	$6*10^{-13}$	
Electrical conductivity	σ	$\frac{S}{m}$	100	100	$1*10^7$
Bruggeman exponent	α		1.8	1.8	
Electrolyte	Symbol	Unit			
Diffusivity	D_l	$\frac{m^2}{s}$	$4*10^{-10}$ [19]		
Ionic conductivity	κ	$\frac{S}{m}$	1.07 [19]		
Activity factor	$\frac{\partial \ln f\pm}{\partial \ln c_l}$		analytical function [19]		
Transport number	t_+		0.38 [19]		

B.1 XRD phases literature values

Table B.1 to Table B.5 summarize the starting parameters for the current collector (Al, Cu) materials and the graphite phases (graphite, LiC_{12}, LiC_6) for the refinement of the XRD overhang samples. Table B.6 gives additional information on the XRD setup.

Al ICSD #-43423. [193]* Space group: $F\,m\,\bar{3}\,m$ (No. 225) a = 4.04497(0) Å V = 66.42(0) Å^3 Z = 4						
Atom	**Wyckoff position**	**occupancy**	**fractional coordinates** *x*	*y*	*z*	**isotropic displacement parameter B_{iso}[Å^2]***
Al	4*a*	1	0	0	0	-

Table B.1 Al Phase starting parameters. [138]

Cu ICSD #-43493. [168]* Space group: $F\,m\,\bar{3}\,m$ (No. 225) a = 3.6151(1) Å V = 47.24(0) Å^3 Z = 4						
Atom	**Wyckoff position**	**occupancy**	**fractional coordinates** *x*	*y*	*z*	**isotropic displacement parameter B_{iso}[Å^2]***
Cu	4*a*	1	0	0	0	-

Table B.2 Cu Phase starting parameters. [138]

Graphite ICSD #-617290. [169]* Space group: $P\,6_3/m\,m\,c$ (No. 194) a,b = 2.4630 Å c = 6.7220(1) Å V = 35.31 Å^3 Z = 1						
Atom	**Wyckoff position**	**occupancy**	**fractional coordinates** *x*	*y*	*z*	**isotropic displacement parameter B_{iso}[Å^2]***
C	2b	1	0	0	¼	1.62
C	2b	1	⅓	⅔	¼	1.62

Table B.3 Graphite Phase starting parameters. [138]

LiC_{12} ICSD #-193440. [170, 171]* Space group: $P\,6/m\,m\,m$ (No. 191) a, b = 4.2686(9) Å c = 7.0229(6)) Å V = 110.82(5) Å^3 Z = 1						
Atom	**Wyckoff position**	**occupancy**	**fractional coordinates** *x*	*y*	*z*	**isotropic displacement parameter B_{iso}[Å^2]***
Li	*1a*	1	0	0	0	-
C1	12n	1	⅓	0	¼	-

Table B.4 LiC_{12} Phase starting parameters. [138]

LiC_6 ICSD #-193441. [171]* Space group: $P\ 6/m\ m\ m$ (No. 191) a, b = 4.3008(1) Å c = 3.687(2)Å V = 59.72 Å^3 Z = 1						
Atom	**Wyckoff position**	**occupancy**	**fractional coordinates**			**isotropic displacement parameter B_{iso}[Å^2]***
			x	***y***	***z***	
Li	*1a*	1	0	0	0	-
C	6k	1	⅓	0	½	-

Table B.5 LiC_6 Phase starting parameters. [138]

Experimental setup	
Method	XRD
Instrument setup geometry	Transmission
Wavelength [Å]	0.70932
S/L Asymmetry	0.0022 (2)
D/L Asymmetry	0.0012 (4)
Step size	0.008
$K_{\alpha_2}/K_{\alpha_1}$ ratio[1]	0.3113 (3)

Table B.6 General information on XRD experimental setup. [138]

B.2 XRD refinement data

The following tables contain a complete list of refined parameter values of the diffraction data used in the XRD Overhang experiment. All refinements were carried out starting with the reference data sets as given in Table B.1 to B.5.

	S95-Q1	S95-Q2	S95-Q3	S95-Q4	S95-Q5	S95-Q6	S95-Q7
general parameters							
Exposure time	01:14:37	02:29:53	02:29:53	01:14:37	02:29:53	01:14:37	01:14:37
2θ-range [°2θ]	7 – 37	7 – 37	7 – 37	7 – 37	7 – 37	7 – 37	7 – 37
Zero Shift [°2θ]	-0.0072(5)	-0.0081(4)	-0.0058(4)	-0.0023(6)	-0.0009(4)	-0.0083(5)	-0.0108(5)
Sample displacement [mm]	-0.717(6)	-0.072(4)	-0.282(4)	-0.156(6)	-0.087(4)	-0.198(6)	-0.311(6)
Al parameters							
Al1 Cell axis a [Å]	4.04655(6)	4.04688(5)	4.04644(4)	4.0474(9)	4.04654(6)	4.0455(5)	4.04716(5)
Al2 Cell axis a [Å]	4.05187(7)	4.05100(5)	4.05139(4)	4.0510(1)	4.05032(5)	4.05044(6)	4.05188(5)
TCH-Profile *U*	0.025(2)	0.0159(9)	0.0104(7)	0.010(1)	0.015(1)	0.023(1)	0.0085(9)
TCH-Profile *W*	0.00117(5)	0.00136(3)	0.0016(3)	0.00195(4)	0.00158(3)	0.00062(5)	0.00147(4)
TCH-Profile Peak Shape	0.32(2)	0.358(8)	0.327(9)	0.416(9)	0.432(8)	0.14(1)	0.38(1)
Cu parameters							
Scale Factor	0.000316(4)	0.000532(5)	0.00041(1)	0.000213(3)	0.00047(4)	0.000269(3)	0.000244(3)
March-Dollase Factor (Pref. Orient. (0 2 0))	1.025(3)	0.984(2)	0.935(6)	0.989(3)	0.913(4)	0.998(3)	0.979(3)
Iso. displacement parameter B_{iso} [Å^2]	1.53(5)	0.63(4)	0.29(6)	0.11(5)	0.90(6)	0.8(5)	0.86(5)
TCH-Profile *U*	0.024(2)	0.0103(9)	0.0165(10)	0.015(2)	0.0116(9)	0.018(1)	0.016(1)
TCH-Profile *W*	0.00248(6)	0.00252(4)	0.00214(4)	0.00229(7)	0.00238(4)	0.00213(6)	0.00217(6)
TCH-Profile Peak Shape	0.52(1)	0.609(8)	0.679(7)	0.70(1)	0.637(8)	0.66(1)	0.59(1)
R values							
R_{Bragg} (Cu)	1.19	1.23	1.17	1.48	1.27	1.36	1.07
R_{Bragg} (Al1 // Al2)	0.41 // 2.42	0.6 // 2.70	0.40 // 2.49	0.94 // 3.24	0.74 // 2.60	1.56 // 2.63	0.37
R_{Bragg} (Graphite)	-	-	-	-	-	-	-
R_{Bragg} (LiC6)	-	-	-	1.94	2.01	1.86	2.38
R_{Bragg} (LiC12)	2.56	2.22	1.57	1.72	1.58	2.67	2.08
R_{Bragg} (LiC18 – LiC≥24)	-	-	-	-	-	-	-
R_{wp}	10.5571	9.6567	9.8672	13.84155	10.8514	12.3272	11.6848
Mass fraction							
m (Cu) [%]	40(2)	39(2)	36(2)	31(3)	32(2)	38(3)	32(3)
m (Graphite) [%]	-	-	-	-	-	-	-
m (LiC18 – LiC≥24) [%]	-	-	-	-	-	-	-
m (LiC12) [%]	60(7)	61(4)	64(5)	62(8)	49(4)	46(6)	52(7)
m (LiC6) [%]	-	-	-	7(3)	19(2)	16(2)	15(3)
Mass fraction (recalculated)							
m (LiC12) [%]	100(12)	100(7)	100(8)	90(12)	72(6)	74(10)	78(10)
m (LiC6) [%]	-	-	-	10(4)	28(3)	26(3)	22(4)
Refined LiC_6							
Scale Factor	-	-	-	0.00012(5)	0.00071(6)	0.0003(4)	0.0003(4)
Cell axis *a* [Å]	-	-	-	4.305(4)	4.3079(8)	4.307(2)	4.31(2)
Cell axis *c* [Å]	-	-	-	3.677(4)	3.67(2)	3.667(2)	3.669(2)
Spherical Harm. Coeff. Y20	-	-	-	7(7)	9(1)	4(1)	5(2)
Y40	-	-	-	4(4)	3.1(7)	0.1(10)	0.5(12)
Y60	-	-	-	2(3)	-	-	-
B overall	-	-	-	3.5(3)	3.9(2)	2.9(3)	4.9(3)
TCH-Profile *U*	-	-	-	0.02(2)	-0.01(1)	0.05(2)	-0.02(1)
TCH-Profile W	-	-	-	0.0089(9)	0.0082(6)	0.0072(8)	0.0072(7)
TCH-Profile Peak Shape	-	-	-	1.06(5)	1.08(4)	1.07(6)	1.07(6)
Refined LiC_{12}							
Scale Factor	0.00033(3)	0.00059(3)	0.00052(3)	0.0003(3)	0.00052(4)	0.00023(3)	0.00028(3)
Cell axis *a* [Å]	4.2888(3)	4.2886(2)	4.2881(2)	4.2889(4)	4.2881(3)	4.2886(4)	4.289(3)
Cell axis *c* [Å]	7.0573(7)	7.0563(5)	7.0566(5)	7.0584(8)	7.0607(5)	7.0599(8)	7.0599(8)
Spherical Harm. Coeff. Y20	8(1)	8.5(6)	9.0(6)	6.5(7)	8.7(7)	10.3(10)	10(1)
Y40	9.5(7)	9.7(4)	9.6(4)	9.3(6)	9.8(5)	9.1(7)	9.9(8)
Y60	5.1(4)	5.0(2)	4.4(2)	5.9(4)	4.8(3)	3.2(4)	4.3(4)
B overall	6.6(4)	4.4(2)	3.4(2)	3.5(3)	3.9(2)	2.9(3)	4.9(3)
TCH-Profile *U*	-0.1(1)	-0.056(7)	-0.011(9)	0.02(2)	-0.01(1)	0.05(2)	-0.02(1)
TCH-Profile W	0.0121(7)	0.0093(4)	0.008(5)	0.0089(9)	0.0082(6)	0.0072(8)	0.0072(7)
TCH-Profile Peak Shape	0.48(5)	0.66(4)	0.78(4)	1.06(5)	1.08(4)	1.07(6)	1.07(6)

Table B.7 Standard uncertainty values are given in parentheses as refined by Highscore without multiplying the values with the R_{wp}-value of the fit. [138]

	S95-Q8	S95-Q9	S95-Q10	CCCV100-E1	CCCV100-E2	CCCV100-E3	CCCV100-E4
general parameters							
Exposure time	01:14:37	01:14:37	85:55:57	01:14:37	01:14:37	12:29:26	11:51:58
2θ-range [°2θ]	7 – 37	7 – 37	7 – 37	7 – 37	7 – 37	7 – 37	7 – 37
Zero Shift [°2θ]	0.0024(5)	-0.01(5)	-0.00617(2)	-0.0045(5)	-0.0046(6)	-0.0015(2)	-0.0047(2)
Sample displacement [mm]	-0.254(6)	-0.256(6)	-0.1823(3)	-0.189(5)	-0.211(7)	-0.182(2)	-0.26(2)
Al parameters							
Al1 Cell axis a [Å]	4.04685(5)	4.04648(7)	4.048614(2)	4.04867(3)	4.0467(2)	4.0462(3)	4.04632(4)
Al2 Cell axis a [Å]	4.05204(6)	4.05067(7)	-	4.0588(1)	4.0494(1)	4.05099(3)	4.05100(7)
TCH-Profile *U*	0.016(1)	0.036(2)	0.02792(9)	0.028(2)	-0.004(2)	0.0195(7)	0.062(2)
TCH-Profile *W*	0.00138(5)	0.00048(6)	0.001455(3)	0.00179(7)	0.00258(5)	0.00092(2)	0.00037(5)
TCH-Profile Peak Shape	0.34(1)	0.52(1)	0.5155(7)	0.002(20)	0.411(9)	0.245(7)	0.325(5)
Cu parameters							
Scale Factor	0.000273(4)	0.000271(3)	0.01221(1)	0.000243(3)	0.00029(3)	0.00287(1)	0.00296(1)
March-Dollase Factor (Pref. Orient. (0 2 0))	0.978(3)	1.029(3)	0.9806(3)	0.981(3)	1.041(3)	1.0246(9)	1.06(1)
isotropic displacem. parameter B_{iso} [Å^2]	1.36(5)	0.38(4)	0.585(2)	0.88(5)	1.16(5)	1.47(2)	1.66(2)
TCH-Profile *U*	0.025(2)	0.011(1)	0.01565(8)	0.02(2)	0.027(2)	0.0255(5)	0.0161(5)
TCH-Profile *W*	0.00179(6)	0.00227(5)	0.002082(4)	0.0019(6)	0.00174(6)	0.00154(2)	0.00209(2)
TCH-Profile Peak Shape	0.63(1)	0.698(9)	0.6862(10)	0.7(1)	0.67(1)	0.658(3)	0.606(4)
R values							
R_{Bragg} (Cu)	1.81	1.44	1.77	1.6	1.25	1.25	1.26
R_{Bragg} (Al1 // Al2)	1.19 // 3.38	0.88 /7 2.57	3.52	0.61 // 3.03	1.34 // 2.66	0.91 // 2.71	0.43 // 2.44
R_{Bragg} (Graphite)	-	-	-	-	-	-	-
R_{Bragg} (LiC6)	1.9	-	-	-	-	2.06	2.31
R_{Bragg} (LiC12)	2.11	2.38	2.04	2.64	3.5	2.35	2.64
R_{Bragg} (LiC18 – LiC≥24)	-	-	-	3.23	-	-	-
R_{wp}	12.9758	13.0244	13.7919	11.2161	14.3634	9.6281	9.4076
Mass fraction							
m (Cu) [%]	54(7)	39(2)	30(1)	46(5)	41(29	39(1)	45(1)
m (Graphite) [%]	-	-	-	-	-	-	-
m (LiC18 – LiC≥24) [%]	-	-	-	43(8)	-	-	-
m (LiC12) [%]	54(11)	61(5)	70(1)	11(3)	59(5)	49(2)	28(2)
m (LiC6) [%]	7(2)	-	-	-	-	12(1)	27(1)
Mass fraction (recalculated)							
m (LiC12) [%]	83(11)	100(8)	100(1)	80(15)	100(9)	80(3)	51(4)
m (LiC6) [%]	17(3)	-	-	20(6)	-	20(2)	49(2)
Refined LiC_6							
Scale Factor	0.00023(4)	-	-	0.00004(1)	-	0.0022(1)	0.0046(2)
Cell axis *a* [Å]	4.305(2)	-	-	4.289(3)	-	4.3065(9)	4.3075(3)
Cell axis *c* [Å]	3.663(2)	-	-	7.057(8)	-	3.657(2)	3.6614(5)
Spherical Harm. Coeff. Y20	5(2)	-	-	9(1)	-	4.81(3)	8.7(4)
Y40	1(2)	-	-	8.2(8)	-	9.5(2)	3.4(3)
Y60	-	-	-	2.7(5)	-	4.4(1)	-
B overall	5(3)	-	-	3.1(4)	-	4.0(1)	3.8(1)
TCH-Profile *U*	-0.052(10)	-	-	-0.04(4)	-	0.000(6)	-0.104(9)
TCH-Profile W	0.0079(7)	-	-	0.017(2)	-	0.0098(3)	0.0195(6)
TCH-Profile Peak Shape	1.07(5)	-	-	0.65(7)	-	0.82(2)	0.71(2)
Refined LiC_{12}							
Scale Factor	0.0003(3)	0.0003(2)	0.0198(1)	0.00017(3)	0.00029(2)	0.00251(8)	0.00128(7)
Cell axis *a* [Å]	4.2885(3)	4.2893(3)	4.28803(3)	4.2749(7)	4.288(2)	4.2882(1)	4.2886(2)
Cell axis *c* [Å]	7.0605(7)	7.0578(7)	7.05778(8)	7.03(2)	7.0547(7)	7.0603(3)	7.0641(4)
Spherical Harm. Coeff. Y20	10(1)	9.1(9)	9.4(1)	9(1)	10.2(8)	9.1(3)	7.8(6)
Y40	10.2(7)	9.4(9)	8.88(7)	8.2(8)	9.5(5)	9.5(2)	11.8(6)
Y60	4.6(4)	4.3(6)	3.95(4)	2.7(4)	3.8(3)	4.4(1)	6.3(3)
B overall	5(3)	3.9(2)	5.74(3)	3.1(4)	3.7(2)	4.0(1)	3.8(1)
TCH-Profile *U*	-0.052(10)	-0.03(1)	-	-0.04(4)	-0.02(1)	0.000(6)	-0.104(9)
TCH-Profile W	0.0079(7)	0.0089(8)	0.00719(6)	0.017(2)	0.0083(6)	0.0098(3)	0.0195(6)
TCH-Profile Peak Shape	1.07(5)	0.97(5)	1.05(6)	0.65(7)	0.75(5)	0.82(2)	0.71(2)

Table B.8 Standard uncertainty values are given in parentheses as refined by Highscore without multiplying the values with the R_{wp}-value of the fit. [138]

	S00-A1	S00-A2	S00-A3	S00-A4	S00-A5	S00-A6	S00-A7
general parameters							
Exposure time	01:14:37	01:14:37	01:14:37	01:14:37	01:14:37	01:14:37	01:14:37
2θ-range [°2θ]	7 – 37	7 – 37	7 – 37	7 – 37	7 – 37	7 – 37	7 – 37
Zero Shift [°2θ]	-0.0127(6)	-0.0099(6)	-0.0045(6)	-0.00348(6)	-0.0045(6)	-0.0071(6)	-0.0012(7)
Sample displacement [mm]	-0.331(6)	-0.327(6)	-0.200(7)	-0.2482(6)	-0.212(7)	-0.302(7)	-0.315(7)
Al parameters							
Al1 Cell axis a [Å]	4.0455(4)	4.04766(4)	4.0472(1)	4.04675(1)	4.04827(7)	4.04736(8)	4.047(6)
Al2 Cell axis a [Å]	4.05226(5)	4.0553(2)	4.0516(1)	4.0510(8)	4.0530(1)	4.0520(1)	4.0520(1)
TCH-Profile *U*	0.03(2)	0.017(2)	0.021(4)	0.0076(1)	0.0004(2)	0.037(2)	0.016(2)
TCH-Profile *W*	0.00044(6)	0.00141(7)	0.0012(1)	0.001721(9)	0.00178(6)	0.0006(7)	0.00105(7)
TCH-Profile Peak Shape	0.26(1)	0.23(1)	0.37(2)	0.371(2)	0.39(2)	0.37(1)	0.21(2)
Cu parameters							
Scale Factor	0.000252(3)	0.000207(3)	0.000277(3)	0.00876(2)	0.000342(4)	0.000368(5)	0.000279(5)
March-Dollase Factor (Pref. Orient. (0 2 0))	1.038(3)	0.976(3)	1.009(3)	1.0086(5)	1.012(3)	1.076(3)	1.003(4)
isotropic displacem. parameter B_{iso} [Å^2]	0.74(5)	0.49(5)	0.67(5)	1.016(4)	1.92(5)	1.97(5)	1.23(6)
TCH-Profile *U*	0.014(2)	0.018(2)	0.03(2)	0.0242(1)	0.031(2)	0.03(2)	0.052(2)
TCH-Profile *W*	0.00307(7)	0.0025(7)	0.00203(6)	0.002108(8)	0.00185(7)	0.00187(7)	0.00145(8)
TCH-Profile Peak Shape	0.51(1)	0.63(1)	0.59(1)	0.548(2)	0.58(1)	0.60(1)	0.59(1)
R values							
R_{Bragg} (Cu)	3.3	1.47	1.51	3.33	1.11	1.13	1.55
R_{Bragg} (Al1 // Al2)	1.55 // 4.99	0.58 // 2.90	0.43 // 2.35	0.34 // 2.59	1.12 // 3.58	0.52 // 2.64	0.50 // 3.41
R_{Bragg} (Graphite)	2.42	1.97	2.17	3.68	3.34	3.25	3.14
R_{Bragg} (LiC6)	-	-	-	-	-	-	2.66
R_{Bragg} (LiC12)	-	-	-	-	-	-	-
R_{Bragg} (LiC18 – LiC≥24)	-	-	-	2.82	-	-	-
R_{wp}	16.3568	11.0126	10.8812	9.9372	11.4061	10.9191	12.3537
Mass fraction							
m (Cu) [%]	36(3)	31(3)	54(4)	34(1)	60(7)	32(4)	25(3)
m (Graphite) [%]	64(10)	69(12)	46(8)	52(2)	40(11)	68(13)	68(10)
m (LiC18 – LiC≥24) [%]	-	-	-	14(1)	-	-	7(3)
m (LiC12) [%]	-	-	-	-	-	-	-
m (LiC6) [%]	-	-	-	-	-	-	-
Mass fraction (recalculated)							
m (Graphite) [%]	100(16)	100(17)	100(17)	83(3)	100(28)	100(19)	91(13)
m (LiC18 – LiC≥24) [%]	-	-	-	17(1)	-	-	9(4)
Refined LiC_{18} – $LiC_{\geq 24}$							
Scale Factor	-	-	-	0.0028(1)	-	-	0.00006(3)
Cell axis *a* [Å]	-	-	-	4.2649(1)	-	-	4.267(2)
Cell axis *c* [Å]	-	-	-	6.79951(8)	-	-	6.800(3)
Spherical Harm. Coeff. Y20	-	-	-	9.1(6)	-	-	6(5)
Y40	-	-	-	6.6(4)	-	-	6(6)
Y60	-	-	-	2.7(3)	-	-	3(5)
B overall	-		-	4.34(7)	-	-	4.8(3)
TCH-Profile *U*	-	-	-	-0.028(2)	-	-	0.01(2)
TCH-Profile W	-	-	-	0.0068(2)	-	-	0.0059(9)
TCH-Profile Peak Shape	-	-	-	0.79(2)	-	-	0.94(9)
Refined Graphite							
Scale Factor	0.0032(4)	0.0033(5)	0.0017(3)	0.092(2)	0.0016(4)	0.0057(9)	0.0054(6)
Cell axis *a* [Å]	2.4602(2)	2.4603(2)	2.4602(2)	2.45949(2)	2.4604(2)	2.4606(1)	2.4594(2)
Cell axis *c* [Å]	6.732(1)	6.740(1)	6.738(1)	6.73815(4)	6.749(1)	6.745(1)	6.727(1)
Spherical Harm. Coeff. Y20	8.6(6)	7.0(6)	7.8(6)	8.8(1)	3.5(8)	3.8(7)	6.5(5)
Y40	7.1(4)	9.5(4)	8.5(5)	7.31(8)	17(1)	14.5(6)	6.4(4)
Y60	3.4(5)	6.3(5)	4.8(5)	3.5(1)	14.6(8)	12.6(7)	4.3(5)
B overall	3.4(4)	4.0(4)	1.4(5)	4.34(7)	3.2(8)	6.7(5)	4.8(3)
TCH-Profile *U*	-0.021(9)	-0.05(1)	0.01(2)	-0.028(2)	-0.09(2)	-0.09(2)	0.01(2)
TCH-Profile W	0.0053(9)	0.008(1)	0.007(1)	0.0068(2)	0.011(2)	0.012(2)	0.0059(9)
TCH-Profile Peak Shape	1.50(7)	1.18(9)	1.13(9)	0.79(2)	0.90(1)	0.82(10)	0.94(9)

Table B.9 Standard uncertainty values are given in parentheses as refined by Highscore without multiplying the values with the R_{wp}-value of the fit. [138]

	S00-A8	S00-E1	S00-E2	S00-E3	S90-A1	S90-E1
general parameters						
Exposure time	01:14:37	01:14:37	01:14:37	01:14:37	15:28:32	01:14:28
2θ-range [°2θ]	7 – 37	7 – 37	7 – 37	7 – 37	7 – 55	7 – 37
Zero Shift [°2θ]	-0.0125(5)	-0.012(5)	-0.0139(6)	-0.0101(5)	-0.0199(5)	-0.0108(9)
Sample displacement [mm]	-0.328(6)	-0.328(5)	-0.424(7)	-0.395(6)	-0.048(5)	-0.24(1)
Al parameters						
Al1 Cell axis a [Å]	4.04852(3)	4.04786(3)	4.04767(5)	4.04827(3)	4.04719(8)	4.04486(6)
Al2 Cell axis a [Å]	4.0565(1)	4.05405(8)	4.0586(1)	4.0565(1)	4.05066(8)	4.05079(1)
TCH-Profile *U*	0.026(3)	0.018(2)	0.028(4)	0.04(3)	0.006(1)	0.014(3)
TCH-Profile *W*	0.00123(8)	0.00211(7)	0.0015(1)	0.00134(9)	0.00229(4)	0.00122(9)
TCH-Profile Peak Shape	0.15(2)	0.25(1)	0.491(8)	0.332(10)	0.24(2)	0.23(3)
Cu parameters						
Scale Factor	0.000289(4)	0.000286(3)	0.000339(4)	0.000266(3)	0.00322(3)	0.00063(1)
March-Dollase Factor (Pref. Orient. (0 2 0))	1.019(3)	1.07(3)	1.009(3)	0.969(2)	0.984(4)	1.027(5)
isotropic displacem. parameter B_{iso} [Å^2]	0.93(5)	0.5(5)	2.16(5)	1.08(5)	0.8(3)	1.4(9)
TCH-Profile *U*	0.017(2)	0.01(1)	0.009(2)	0.015(1)	0.024(1)	0.04(4)
TCH-Profile *W*	0.00258(6)	0.0029(7)	0.00272(6)	0.00218(6)	0.00285(7)	0.0023(1)
TCH-Profile Peak Shape	0.66(10)	0.628(10)	0.659(9)	0.686(9)	0.53(1)	0.62(2)
R values						
R_{Bragg} (Cu)	1.24	1.09	0.97	1.26	2.67	1.35
R_{Bragg} (Al1 // Al2)	1.83 // 3.53	0.48 // 3.07	1.40 // 4.06	1.20 // 3.10	1.17 // 2.83	0.69 // 0.89
R_{Bragg} (Graphite)	3.47	1.89	2.66	3.16	1.67	1.61
R_{Bragg} (LiC6)	-	-	-	-	-	-
R_{Bragg} (LiC12)	-	-	-	-	-	-
R_{Bragg} (LiC18 – LiC≥24)	1.56	1.83	2.64	2.76	0.71	0.66
R_{wp}	12.41575	11.7729	14.8616	13.2509	10.9265	8.3461
Mass fraction						
m (Cu) [%]	48(6)	50(5)	53(5)	49(5)	35(8)	34(7)
m (Graphite) [%]	50(12)	43(3)	42(9)	42(9)	39(16)	59(21)
m (LiC18 – LiC≥24) [%]	3(3)	6(1)	5(1)	9(2)	26(10)	7(3)
m (LiC12) [%]	-	-	-	-	-	-
m (LiC6) [%]	-	-	-	-	-	-
Mass fraction (recalculated)						
m (Graphite) [%]	98(25)	89(19)	82(18)	88(18)	60(25)	89(32)
m (LiC18 – LiC≥24) [%]	2(6)	11(2)	18(4)	12(2)	40(15)	11(5)
Refined LiC_{18} – $LiC_{≥24}$						
Scale Factor	0.00001(1)	0.000026(5)	0.000025(5)	0.000037(7)	0.0018(5)	0.0001(3)
Cell axis *a* [Å]	4.26(2)	4.261(5)	4.263(5)	4.265(2)	4.2863(8)	4.264(5)
Cell axis *c* [Å]	6.793(4)	6.806(4)	6.807(4)	6.781(4)	7.036(3)	6.854(7)
Spherical Harm. Coeff. Y20	3(30)	5.1(9)	7(1)	7(1)	9(3)	6.(1)
Y40	7(41)	13.9(9)	14(1)	14(1)	8(2)	7.8(7)
Y60	2(29)	10.1(8)	9(1)	9.0(8)	4.0(9)	5.1(8)
B overall	3.0(5)	4.3(5)	5.5(6)	4.3(5)	5.0(9)	5.1(9)
TCH-Profile *U*	-0.03(2)	-0.04(1)	-0.04(2)	-0.04(2)	0.00(2)	-0.1(2)
TCH-Profile W	0.009(1)	0.0101(8)	0.0094(9)	0.0089(10)	0.006(1)	0.018(2)
TCH-Profile Peak Shape	0.5(1)	0.4(7)	0.78(7)	0.77(7)	0.7(2)	0.4(1)
Refined Graphite						
Scale Factor	0.0023(5)	0.0017(3)	0.0019(4)	0.0016(3)	0.025(9)	0.008(2)
Cell axis *a* [Å]	2.4607(2)	2.4605(4)	2.4609(5)	2.4607(3)	2.4606(5)	2.4595(4)
Cell axis *c* [Å]	6.734(1)	6.731(7)	6.7336(7)	6.7316(9)	6.746(3)	6.740(1)
Spherical Harm. Coeff. Y20	2.1(5)	5.1(9)	7(1)	7(1)	9(2)	67(1)
Y40	12.8(6)	13.9(9)	14(1)	14(1)	8(1)	7.8(7)
Y60	12.1(6)	10.1(8)	9(1)	9.0(8)	4(2)	5.1(8)
B overall	3.0(5)	4.3(5)	5.5(6)	4.3(5)	5.0(9)	5.1(9)
TCH-Profile *U*	-0.03(2)	-0.04(1)	-0.04(2)	-0.04(2)	0.00(2)	-0.1(2)
TCH-Profile W	0.009(1)	0.0101(8)	0.0094(9)	0.0089(10)	0.006(1)	0.018(2)
TCH-Profile Peak Shape	0.5(1)	0.4(7)	0.78(7)	0.77(7)	0.7(2)	0.4(1)

Table B.10 Standard uncertainty values are given in parentheses as refined by Highscore without multiplying the values with the R_{wp}-value of the fit. [138]

	S95-L1	S95-L2	S95-L3	S95-L4	S95-L5	S95-L6	S95-L7
general parameters							
Exposure time	01:14:37	01:14:37	01:14:37	01:14:37	01:14:37	01:14:37	14:14:13
2θ-range [°2θ]	7 – 37	7 – 37	7 – 37	7 – 37	7 – 37	7 – 37	5 – 55
Zero Shift [°2θ]	-0.0096(6)	-0.0067(6)	-0.01(6)	-0.0026(7)	-0.0147(6)	-0.0049(7)	-0.0107(9)
Sample displacement [mm]	-0.283(6)	-0.25(6)	-0.11(7)	-0.346(7)	-0.471(6)	-0.001(7)	-0.3142(9)
Al parameters							
Al1 Cell axis a [Å]	4.04624(6)	4.04674(5)	4.04655(6)	4.0472(4)	4.04622(3)	4.04703(9)	4.04677(1)
Al2 Cell axis a [Å]	4.05127(8)	4.052(1)	4.0515(1)	4.0495(4)	4.05299(6)	4.051(1)	4.050599(9)
TCH-Profile *U*	0.007(2)	0.014(2)	0.027(2)	0.031(5)	0.023(3)	0.005(2)	0.00379(10)
TCH-Profile *W*	0.00131(8)	0.00116(7)	0.00071(7)	0.00122(10)	0.00087(8)	0.00157(7)	0.001545(8)
TCH-Profile Peak Shape	0.51(1)	0.3(1)	0.33(1)	0.33(2)	0.355(9)	0.46(2)	0.563(3)
Cu parameters							
Scale Factor	0.00029(3)	0.000258(3)	0.000354(4)	0.000265(3)	0.000247(3)	0.000278(3)	0.004487(7)
March-Dollase Factor (Pref. Orient. (0 2 0))	0.986(3)	0.992(2)	1.044(3)	0.995(3)	0.963(3)	0.994(3)	1.0163(6)
isotropic displacem. parameter B_{iso} [Å^2]	1.22(5)	0.81(5)	1.91(5)	1.17(5)	0.87(5)	1.51(5)	0.715(4)
TCH-Profile *U*	0.025(1)	0.021(2)	0.023(2)	0.031(2)	0.023(2)	0.037(2)	0.0237(2)
TCH-Profile *W*	0.00198(6)	0.00238(6)	0.00236(6)	0.00221(7)	0.00252(7)	0.00194(7)	0.00236(1)
TCH-Profile Peak Shape	0.613(9)	0.62(1)	0.57(1)	0.58(1)	0.6(1)	0.58(1)	0.649(2)
R values							
R_{Bragg} (Cu)	1.55	1.49	1.26	1.5	1.38	1.55	2.61
R_{Bragg} (Al1 // Al2)	2.23 // 3.66	0.61 // 3.54	0.73 // 3.75	1.35 // 2.71	0.23 // 3.67	0.99 // 3.45	1.88 // 3.7
R_{Bragg} (Graphite)	-	-	-	-	-	-	-
R_{Bragg} (LiC6)	-	-	-	-	-	-	-
R_{Bragg} (LiC12)	2.24	2.01	3.38	2.48	1.93	2.42	1.78
R_{Bragg} (LiC18 – LiC≥24)	-	2.94	1.63	3.41	-	-	-
R_{wp}	13.5699	12.0853	10.8706	12.1361	12.1545	13.0257	10.85644
Mass fraction							
m (Cu) [%]	43(3)	38(3)	48(4)	35(3)	38(2)	40(3)	32(5)
m (Graphite) [%]	-	-	-	-	-	-	-
m (LiC18 – LiC≥24) [%]	-	11(2)	9(2)	11(3)	-	-	-
m (LiC12) [%]	57(7)	51(7)	43(6)	54(6)	62(6)	60(7)	68(2)
m (LiC6) [%]	-	-	-	-	-	-	-
Mass fraction (recalculated)							
m (LiC18 – LiC≥24) [%]	-	18(3)	17(4)	17(5)	100(10)	100(12)	100(3)
m (LiC12) [%]	100(12)	82(11)	83(12)	83(9)	-	-	-
Refined LiC_{12}							
Scale Factor	0.00027(3)	0.00025(3)	0.00023(3)	0.0003(2)	0.00029(2)		
Cell axis *a* [Å]	4.2881(2)	4.2883(3)	4.288(3)	4.288(2)	4.2886(2)	-	-
Cell axis *c* [Å]	7.054(1)	7.053(1)	7.047(1)	7.071(2)	7.057(1)	-	-
Spherical Harm. Coeff. Y20	9.7(9)	3.9(4)	10(1)	9.6(8)	9.3(7)	-	-
Y40	9.2(5)	10.0(9)	6.8(5)	7.7(4)	9.3(4)	-	-
Y60	4.4(3)	6.8(5)	2.2(4)	3.4(3)	4.8(2)	-	-
B overall	3.7(3)	2.2(4)	4.0(4)	4.0(3)	3.6(3)	-	-
TCH-Profile *U*	0.03(1)	0.00(1)	0.01(1)	0.013(8)	0.00(1)	-	-
TCH-Profile W	0.0042(6)	0.0045(7)	0.0039(6)	0.0024(4)	0.0058(5)	-	-
TCH-Profile Peak Shape	0.91(7)	1.08(8)	1.08(9)	1.08(7)	0.63(7)	-	-
Refined LiC_{18} – $LiC_{\geq 24}$							
Scale Factor	-	0.000055(9)	0.000051(8)	0.00006(2)	-	0.0003(3)	0.0067(1)
Cell axis *a* [Å]	-	4.275(1)	4.274(1)	4.2721(9)	-	4.2883(2)	4.28878(6)
Cell axis *c* [Å]	-	6.991(5)	6.987(5)	7.035(2)	-	7.066(1)	7.0574(3)
Spherical Harm. Coeff. Y20	-	10.0(9)	10(1)	3.9(2)	-	9.5(9)	9.7(2)
Y40	-	6.8(5)	6.8(5)	-	-	9.4(9)	8.22(9)
Y60	-	2.2(4)	2.2(4)	-	-	4.7(6)	3.75(5)
B overall	-	4.0(4)	4.0(4)	3(1)	-	4.9(3)	4.52(7)
TCH-Profile *U*	-	0(1)	0.01(1)	0.013(8)	-	-0.01(1)	-0.007(3)
TCH-Profile W	-	0.0045(7)	0.0039(6)	0.0024(4)	-	0.0063(6)	0.0052(2)
TCH-Profile Peak Shape	-	1.08(8)	1.08(9)	1.08(7)	-	0.65(8)	1.2(2)

Table B.11 Standard uncertainty values are given in parentheses as refined by Highscore without multiplying the values with the R_{wp}-value of the fit. [138]

	S95-L8	S95-L9	S95-L10	S95-L11	S95-L12	S95-L13	S95-L14
general parameters							
Exposure time	01:14:37	02:17:16	02:29:14	02:29:14	02:02:02	08:44:14	15:15:14
2θ-range [°2θ]	7 – 37	9.5 – 36.5	7 – 37	7 – 37	5 – 55	7 – 37	5 – 55
Zero Shift [°2θ]	-0.0071(6)	-0.0016(2)	-0.0001(6)	-0.0046(4)	-0.0097(3)	-0.0131(2)	-0.0118(1)
Sample displacement [mm]	-0.361(7)	-0.036(3)	-0.144(7)	-0.167(5)	-0.35(3)	-0.21(3)	-0.198(1)
Al parameters							
Al1 Cell axis a [Å]	4.0471(1)	4.04762(2)	4.04678(3)	4.04669(8)	4.04627(9)	4.04608(3)	4.04742(2)
Al2 Cell axis a [Å]	4.0505(2)	4.05667(7)	4.05436(7)	4.051(2)	4.04944(6)	4.051(3)	4.05098(3)
TCH-Profile *U*	0.015(3)	0.0167(8)	0.057(3)	0.010(3)	0.0115(9)	0.047(2)	0.0055(3)
TCH-Profile *W*	0.00129(10)	0.00179(3)	0.00016(7)	0.00172(9)	0.00153(4)	0.00031(8)	0.00257(1)
TCH-Profile Peak Shape	0.38(2)	0.165(6)	0.29(1)	0.25(1)	0.46(1)	0.443(6)	0.328(3)
Cu parameters							
Scale Factor	0.000254(3)	0.001201(7)	0.000277(3)	0.000537(5)	0.000299(2)	0.001616(8)	0.00198(5)
March-Dollase Factor (Pref. Orient. (0 2 0))	0.983(3)	0.994(1)	1.004(3)	0.984(2)	1.026(2)	1.016(1)	0.989(8)
isotropic displacem. parameter B_{iso} [Å^2]	0.89(5)	1.14(2)	1.60(5)	0.96(4)	0.87(2)	0.21(2)	0.671(6)
TCH-Profile *U*	0.023(2)	0.0433(9)	0.032(2)	0.033(1)	0.0248(8)	0.0253(7)	0.0211(3)
TCH-Profile *W*	0.00247(7)	0.00184(3)	0.0022(8)	0.00189(5)	0.00205(4)	0.00253(3)	0.00277(2)
TCH-Profile Peak Shape	0.58(1)	0.523(5)	0.61(1)	0.641(8)	0.605(8)	0.632(5)	0.61(3)
R values							
R_{Bragg} (Cu)	1.33	1.81	1.53	1.29	5.42	0.92	1.78
R_{Bragg} (Al1 // Al2)	0.55 // 2.32	1.03 // 3.25	0.49 // 3.84	0.36 // 2.67	0.60 // 1.66	0.42 // 2.40	0.54 // 3.87
R_{Bragg} (Graphite)	-	-		-	-	-	-
R_{Bragg} (LiC6)	-	2.5	2.04	3.88	2.75	1.33	2.81
R_{Bragg} (LiC12)	1.58	1.25	1.8	3.59	3.04	1.61	1.94
R_{Bragg} (LiC18 – LiC≥24)	-	-		-	-	-	-
R_{wp}	11.1524	10.35491	12.6308	11.252	12.8535	12.5219	10.52261
Mass fraction							
m (Cu) [%]	36(3)	42(1)	33(3)	39(2)	32(2)	34(1)	42(1)
m (Graphite) [%]	-	-		-	-	-	-
m (LiC18 – LiC≥24) [%]	-	-		-	-	-	-
m (LiC12) [%]	64(8)	54(3)	51(7)	46(5)	50(7)	48(3)	45(2)
m (LiC6) [%]	-	4(1)	16(2)	15(2)	18(2)	17(1)	13(1)
Mass fraction (recalculated)							
m (LiC12) [%]	100(13)	93(5)	76(10)	75(8)	74(10)	74(5)	78(3)
m (LiC6) [%]	-	7(2)	24(3)	25(3)	26(3)	26(2)	22(2)
Refined LiC_6							
Scale Factor	-	0.00031(6)	0.00035(4)	0.00052(5)	0.00043(5)	0.0021(1)	0.00162(9)
Cell axis *a* [Å]	-	4.308(6)	4.307(1)	4.307(1)	4.307(2)	4.3062(5)	4.3071(4)
Cell axis *c* [Å]	-	3.601(2)	3.657(3)	3.685(3)	3.662(4)	3.665(1)	3.678(1)
Spherical Harm. Coeff. Y20	-	22(3)	5(1)	7(1)	6(1)	8.2(5)	16.7(8)
Y40	-	13(2)	0.4(9)	1.1(7)	0.5(9)	2.5(4)	8.8(6)
Y60	-	-	3.8(4)	-	-	-	-
B overall	-	1.4(5)	5.2(3)	2.7(2)	4.7(3)	3.3(1)	3.3(1)
TCH-Profile *U*	-	-0.005(7)	-0.01(1)	0.04(1)	0.06(3)	0.029(7)	0.007(6)
TCH-Profile W	-	0.0061(4)	0.0059(8)	0.0061(7)	0.006(1)	0.0055(3)	0.0067(3)
TCH-Profile Peak Shape	-	1.02(4)	0.96(8)	0.96(6)	1.02(8)	1.02(3)	0.94(3)
Refined LiC_{12}							
Scale Factor	0.00031(3)	0.0011(5)	0.00031(3)	0.00045(4)	0.00033(4)	0.0016(7)	0.00152(6)
Cell axis *a* [Å]	4.2892(3)	4.2885(2)	4.2882(3)	4.2877(2)	4.2882(4)	4.2882(1)	4.2886(1)
Cell axis *c* [Å]	7.064(1)	7.0634(6)	7.065(1)	7.063(1)	7.065(1)	7.0617(5)	7.0618(5)
Spherical Harm. Coeff. Y20	9.5(9)	9.7(6)	10(1)	9.9(6)	10(1)	9.6(4)	10.5(4)
Y40	8.7(5)	9.2(4)	8.4(6)	9(4)	7.4(9)	8.5(2)	10.9(3)
Y60	4.2(3)	4.4(2)	3.8(4)	4.1(3)	2.6(6)	3.9(1)	5.3(1)
B overall	4.7(3)	4.5(2)	5.2(3)	2.7(2)	4.7(3)	3.3(1)	3.3(1)
TCH-Profile *U*	-0.01(1)	-0.005(7)	-0.01(1)	0.04(1)	0.06(3)	0.029(7)	0.007(6)
TCH-Profile W	0.007(8)	0.0061(4)	0.0059(8)	0.0061(7)	0.006(1)	0.0055(3)	0.0067(3)
TCH-Profile Peak Shape	0.86(7)	1.02(4)	0.96(8)	0.96(6)	1.02(8)	1.02(3)	0.94(3)

Table B.12 Standard uncertainty values are given in parentheses as refined by Highscore without multiplying the values with the R_{wp}-value of the fit. [138]

	S95-L15	S95-L16	S95-L17	S95-L18	S95-L19	S95-L20	S95-Tab
general parameters							
Exposure time	01:08:38	01:08:38	01:08:38	01:08:38	01:08:38	01:08:38	14:47:56
2θ-range [°2θ]	9.5 – 36.5	9.5 – 36.5	9.5 – 36.5	9.5 – 36.5	9.5 – 36.5	9.5 – 36.5	5 – 55
Zero Shift [°2θ]	-0.0058(6)	-0.0096(6)	0.0013(6)	-0.008(6)	-0.0073(6)	-0.0145(6)	-0.0093(2)
Sample displacement [mm]	-0.012(7)	-0.15(6)	-0.181(7)	0.016(7)	-0.107(7)	-0.282(6)	-0.112(2)
Al parameters							
Al1 Cell axis a [Å]	4.04603(5)	4.04767(5)	4.04715(6)	4.0471(4)	4.0472(1)	4.04735(8)	4.04641(4)
Al2 Cell axis a [Å]	4.05096(7)	4.054(2)	4.052(10)	4.0500(3)	4.051(2)	4.0516(1)	4.0517(4)
TCH-Profile *U*	0.033(3)	0.026(2)	0.023(2)	0.038(5)	0.021(4)	0.01(2)	0.0207(7)
TCH-Profile *W*	0.0004(1)	0.00105(7)	0.00091(6)	0.0015(1)	0.0012(1)	0.00136(8)	0.0019(6)
TCH-Profile Peak Shape	0.58(1)	0.27(2)	0.37(1)	0.37(1)	0.46(2)	0.44(2)	0.20(1)
Cu parameters							
Scale Factor	0.000266(3)	0.000283(3)	0.000291(4)	0.000348(3)	0.000384(4)	0.00032(4)	0.000804(4)
March-Dollase Factor (Pref. Orient. (0 2 0))	0.955(2)	1.017(3)	1.001(3)	1.046(2)	1.07(3)	1.053(3)	1.054(2)
isotropic displacem. parameter B_{iso} [Å^2]	1.06(5)	0.78(5)	1.18(5)	1.35(5)	1.90(5)	1.28(5)	0.77(1)
TCH-Profile *U*	0.019(1)	0.028(2)	0.023(2)	0.03(2)	0.033(2)	0.01(1)	0.0208(5)
TCH-Profile *W*	0.00236(6)	0.00208(6)	0.00232(6)	0.00207(6)	0.00177(6)	0.00284(6)	0.00254(3)
TCH-Profile Peak Shape	0.632(10)	0.626(10)	0.62(1)	0.637(9)	0.632(10)	0.6(1)	0.604(6)
R values							
R_{Bragg} (Cu)	1.21	1.15	1.54	1.28	1.24	1.11	0.94
R_{Bragg} (Al1 // Al2)	0.66 // 2.84	0.91 // 3.42	0.77 // 4.28	1.08 // 1.86	0.36 // 2.41	1.30 // 3.02	2.51 // 0.78
R_{Bragg} (Graphite)	-	-	-	-	-	-	-
R_{Bragg} (LiC6)	1.43	2.95	2.87	3.35	2.75	2.94	-
R_{Bragg} (LiC12)	2.15	2.1	1.9	2.87	2.58	2.43	1.39
R_{Bragg} (LiC18 – LiC≥24)	-	-	-	-	-	-	-
R_{wp}	13.15	12.8055	12.131	12.1165	13.8088	12.2155	13.0148
Mass fraction							
m (Cu) [%]	39(3)	40(3)	37(3)	41(3)	45(3)	45(3)	37(1)
m (Graphite) [%]	-	-	-	-	-	-	-
m (LiC18 – LiC≥24) [%]	-	-	-	-	-	-	63(4)
m (LiC12) [%]	47(6)	47(7)	50(6)	44(6)	43(6)	43(6)	-
m (LiC6) [%]	14(2)	13(2)	13(2)	15(3)	12(2)	12(2)	-
Mass fraction (recalculated)							
m (LiC12) [%]	77(10)	78(12)	79(10)	75(10)	78(11)	78(11)	100(6)
m (LiC6) [%]	23(3)	22(3)	21(3)	25(3)	22(4)	22(4)	-
Refined LiC_6							
Scale Factor	0.00026(4)	0.00025(4)	0.00026(4)	0.00032(3)	0.00025(4)	0.00022(3)	0.00097(5)
Cell axis *a* [Å]	4.3061(9)	4.307(1)	4.307(1)	4.3054(9)	4.307(1)	4.309(1)	4.2883(1)
Cell axis *c* [Å]	3.674(4)	3.69(5)	3.689(3)	3.703(2)	3.687(4)	3.665(5)	7.0584(7)
Spherical Harm. Coeff. Y20	17(2)	14(2)	14(2)	11(1)	11(2)	12(2)	9.3(6)
Y40	9(2)	6(2)	6(2)	4.3(9)	4(1)	5(2)	11.3(7)
Y60	-	-	-	-	-	-	6.4(5)
B overall	4.1(3)	4.4(4)	4.2(3)	4.1(3)	4.1(4)	4.1(4)	5.4(2)
TCH-Profile *U*	-0.01(1)	-0.01(2)	-0.01(1)	0(0.01)	0(0.01)	0(0.01)	-0.019(6)
TCH-Profile W	0.0061(8)	0.0068(9)	0.0064(8)	0.0064(8)	0.0064(9)	0.0064(9)	0.0068(3)
TCH-Profile Peak Shape	0.94(8)	0.94(9)	0.95(8)	0.72(9)	0.97(9)	0.91(9)	0.67(4)
Refined LiC_{12}							
Scale Factor	0.00023(3)	0.00024(3)	0.00028(3)	0.00027(3)	0.00026(3)	0.00022(3)	-
Cell axis *a* [Å]	4.2889(3)	4.2889(3)	4.2886(3)	4.2885(3)	4.289(3)	4.2888(3)	-
Cell axis *c* [Å]	7.062(1)	7.071(1)	7.072(1)	7.064(1)	7.063(1)	7.069(1)	-
Spherical Harm. Coeff. Y20	10(1)	10(1)	11(1)	8.7(9)	8.7(10)	10(1)	-
Y40	10.9(8)	10.6(8)	10.6(7))	7.5(5)	8.4(6)	9.6(8)	-
Y60	5.3(4)	4.9(4)	5(4)	3.6(3)	4.4(4)	5.0(4)	-
B overall	4.1(3)	4.4(4)	4.2(3)	4.1(3)	4.1(4)	4.1(4)	-
TCH-Profile *U*	-0.01(1)	-0.01(2)	-0.01(1)	0(0.01)	0(0.02)	0(0.02)	-
TCH-Profile W	0.0061(8)	0.0068(9)	0.0064(8)	0.0064(8)	0.0064(9)	0.0064(9)	-
TCH-Profile Peak Shape	0.94(8)	0.94(9)	0.95(8)	0.72(9)	0.97(9)	0.91(9)	-

Table B.13 Standard uncertainty values are given in parentheses as refined by Highscore without multiplying the values with the R_{wp}-value of the fit. [138]

	S50-25-A1	S50-25-A2	S50-25-A3	S50-25-A4	S50-25-A5	S50-25-A6	S50-25-A7
general parameters							
Exposure time	01:14:37	01:14:37	03:07:22	13:44:23	01:14:37	01:14:37	01:14:37
2θ-range [°2θ]	7 – 37	7 – 37	7 – 37	7 – 37	7 – 37	7 – 37	7 – 37
Zero Shift [°2θ]	-0,0129(6)	-0.0135(4)	-0.018(7)	-0.0069(2)	0.0002(6)	-0,0107(7)	-0,008(1)
Sample displacement [mm]	-0,236(7)	-0.192(5)	-0.444(7)	-0.001(2)	-0.032(7)	-0,317(8)	-0,33(2)
Al parameters							
Al1 Cell axis a [Å]	4,0472(4)	4.04843(3)	4.0468(1)	4.045(3)	4.041(2)	4,0466(3)	4,046(1)
Al2 Cell axis a [Å]	4,0500(5	4.0583(1)	4.0500(1)	4.04896(2)	4.04831(4)	4,0499(4)	4,0500(2)
TCH-Profile *U*	0,064(8)	0.028(2)	-0.008(2)	-0.0007(4)	0.100(6)	0,038(7)	0,01(1)
TCH-Profile *W*	0,0004(1)	0.00127(6)	0.00217(6)	0.00175(2)	0.0002(2)	0,001(1)	0,0013(3)
TCH-Profile Peak Shape	0,19(3)	0.23(1)	0.39(2)	0.562(5)	0.32(1)	0(2)	0,16(4)
Cu parameters							
Scale Factor	0,000233(3)	0.000219(3)	0.000257(4)	0.00314(1)	0.000261(3)	0,000301(3)	0,000283(3)
March-Dollase Factor (Pref. Orient. (0 2 0))	1,028(3)	0.979(3)	1.022(3)	1.0484(9)	0.979(2)	0,987(3)	0,985(2)
isotropic displacem. parameter B_{iso} [Å^2]	0,24(5)	0.31(5)	0.74(5)	1.06(2)	0.93(5)	1,55(5)	1,56(5)
TCH-Profile *U*	0,017(2)	0.020(2)	0.038(2)	0.0219(5)	0.041(2)	0,038(2)	0,03(2)
TCH-Profile *W*	0,00296(7)	0.00226(6)	0.00224(8)	0.00239(2)	0.00172(7)	0,00207(7)	0,00217(7)
TCH-Profile Peak Shape	0,49(1)	0.58(1)	0.57(1)	0.561(4)	0.62(1)	0,55(1)	0,58(1)
R values							
R_{Bragg} (Cu)	1,38	1.19	1.18	1.3	1.81	1,33	1,42
R_{Bragg} (Al1 // Al2)	0.62 // 2.44	0.99 // 2.81	2.29 // 4.43	0.92 // 3.88	0.93 // 2.1	0.35 // 1.91	1.25 // 3.27
R_{Bragg} (Graphite)	-	-	-	-	-	-	-
R_{Bragg} (LiC6)	-	-	-	-	-	-	-
R_{Bragg} (LiC12)	-	-	1.13	3.14	-	2,27	1,97
R_{Bragg} (LiC18 – LiC≥24)	2,93	1.34	2.67	1.37	1.72	2,88	2,28
R_{wp}	11,0685	12.35767	14.1927	13.8973	15.2651	12,1817	12,6921
Mass fraction							
m (Cu) [%]	56(6)	48(5)	49(7)	64(2)	43(3)	49(6)	48(6)
m (Graphite) [%]	-	-	-	-	-	-	-
m (LiC18 – LiC≥24) [%]	44(11)	52(12)	45(11)	32(2)	57(9)	41(10)	37(9)
m (LiC12) [%]	-	-	6(4)	5(1)	-	10(4)	15(4)
m (LiC6) [%]	-	-	-	-	-	-	-
Mass fraction (recalculated)							
m (LiC18 – LiC≥24) [%]	100(25)	100(23)	88(22)	86(5)	100(16)	80(20)	71(17)
m (LiC12) [%]	-	-	12(8)	14(3)	-	20(8)	29(8)
Refined LiC_{12}							
Scale Factor	-	-	0.00002(1)	0.00017(3)	-	0,00004(2)	0,00006(2)
Cell axis *a* [Å]	-	-	4.285(2)	4.2894(5)	-	4,28(4)	4,285(3)
Cell axis *c* [Å]	-	-	7.07(2)	7.050(2)	-	7,07(2)	7,065(10)
Spherical Harm. Coeff. Y20	-	-	6(9)	2(2)	-	10,1(9)**	10(9)**
Y40	-	-	20(13)	20(4)	-	6,0(5)	6,0(4)
Y60	-	-	15(8)	16(3)	-	1,4(4)	1,5(4)
B overall	-	-	3.1(6)	1.6(2)	-	2,4(5)	2,6
TCH-Profile *U*	-	-	-0.14(3)	-0.071(8)	-	-*	-*
TCH-Profile W	-	-	0.019(3)	0.0134(7)	-	0,021(3)	0,0206(4)
TCH-Profile Peak Shape	-	-	0.8(1)	0.80(3)	-	0,6(1)	0,30
Refined LiC_{18} – $LiC_{\geq 24}$							
Scale Factor	0,00013(3)	0.00018(4)	0.00017(4)	0.00113(7)	0.00026(3)	0,00018(4)	0,00016(4)
Cell axis *a* [Å]	4,2725(5)	4.2749(4)	4.274(4)	4.2733(1)	4.2727(4)	4,2727(9)	4,274(1)
Cell axis *c* [Å]	7,005(2)	7.015(3)	7.007(4)	6.997(1)	7.025(2)	7,000(5)	7,016(5)
Spherical Harm. Coeff. Y20	9,4(10)	10(1)	9(1)	10.0(4)	10(1)	10,1(9)**	10,0(9)**
Y40	9,9(9)	13(1)	10(1)	11.0(4)	11(1)	6,0(5)	6,0(4)
Y60	5,0(5)	7.0(6)	5.3(6)	5.5(2)	5.5(7)	1,4(4)	1,5(4)
B overall	2,0(6)	3.0(6)	3.1(6)	1.6(2)	4.6(4)	2,4(5)	2,6
TCH-Profile *U*	-*	-0.23(4)	-0.14(3)	-0.071(8)	-0.38(4)	-*	-*
TCH-Profile W	0,019(2)	0.038(3)	0.019(3)	0.0134(7)	0.045(3)	0,021(3)	0,0206(4)
TCH-Profile Peak Shape	0,2(1)	0.3(1)	0.8(1)	0.80(3)	0.37(9)	0,6(1)	0,3(5)

Table B.14 Standard uncertainty values are given in parentheses as refined by Highscore without multiplying the values with the R_{wp}-value of the fit. *The TCH-profile parameter *U* was not fitted. **SPH parameters constrained between LiC_{12} and LiC_{18} – $LiC_{\geq 24}$. [138]

	S50-25-A8	S55-E1	S55-E2	S55-E3	S95-E1	S95-E2	S95-E3
general parameters							
Exposure time	01:14:37	01:14:37	01:14:37	01:14:37	01:14:37	01:14:37	01:14:37
2θ-range [°2θ]	7 – 37	7 – 37	7 – 37	7 – 37	7 – 37	7 – 37	7 – 37
Zero Shift [°2θ]	-0.0046(7)	-0.0075(6)	-0.0142(5)	-0.0073(5)	-0.0089(5)	-0.0156(6)	-0.01(5)
Sample displacement [mm]	-0.13(7)	-0.357(6)	-0.502(5)	-0.46(6)	-0.381(6)	-0.49(7)	-0.442(6)
Al parameters							
Al1 Cell axis a [Å]	4.046(5)	4.04707(6)	4.04689(4)	4.04537(5)	4.04604(3)	4.04696(10)	4.04707(3)
Al2 Cell axis a [Å]	4.0492(1)	4.0520(2)	4.05169(5)	4.05061(4)	4.0516(1)	4.0516(1)	4.05558(9)
TCH-Profile *U*	0.056(4)	0.017(1)	-0.0005(6)	0.0007(7)	0.044(2)	0.01(4)	0.029(3)
TCH-Profile *W*	0.0012(1)	0.00179(4)	0.00204(4)	0.00227(3)	0.00096(7)	0.0016(1)	0.00109(9)
TCH-Profile Peak Shape	0.31(1)	0.29(1)	0.337(9)	0.356(10)	0.22(1)	0.45(2)	0.37(2)
Cu parameters							
Scale Factor	0.000314(3)	0.000246(3)	0.000251(3)	0.000234(3)	0.000301(4)	0.000278(3)	0.000229(3)
March-Dollase Factor (Pref. Orient. (0 2 0))	1.056(3)	0.989(3)	1.009(3)	0.939(3)	1.037(3)	0.955(3)	0.963(3)
isotropic displacem. parameter B_{iso} [Å^2]	1.20(5)	0.47(5)	0.26(5)	1.00(5)	1.49(5)	1.72(5)	0.19(5)
TCH-Profile *U*	0.019(2)	0.024(2)	0.009(1)	0.015(2)	0.019(2)	0.027(2)	0.013(1)
TCH-Profile *W*	0.00273(7)	0.00241(7)	0.00244(5)	0.00263(7)	0.00244(7)	0.0019(6)	0.00234(5)
TCH-Profile Peak Shape	0.61(1)	0.58(1)	0.65(1)	0.61(1)	0.55(1)	0.61(1)	0.6(1)
R values							
R_{Bragg} (Cu)	1.37	1.45	1.26	1.05	1.41	1.39	1.34
R_{Bragg} (Al1 // Al2)	1.14 // 1.95	1.34 // 4.7	0.57 // 3.28	1.28 // 2.73	0.25 // 3.32	1.28 // 2.87	1.00 // 3.22
R_{Bragg} (Graphite)	-	-	-	-	-	-	-
R_{Bragg} (LiC6)	-	-	-	-	-	-	-
R_{Bragg} (LiC12)	2.19	1.44	3.52	2.53	2.5	2.76	2.8
R_{Bragg} (LiC18 – LiC≥24)	2.69	1.66	3.2	1.53	-	-	-
R_{wp}	11.9083	13.1026	12.2016	12.0847	11.1809	12.4627	11.7926
Mass fraction							
m (Cu) [%]	42(3)	63(5)	64(5)	62(5)	43(2)	41(2)	39(2)
m (Graphite) [%]	-	-	-	-	-	-	-
m (LiC18 – LiC≥24) [%]	49(8)	30(5)	17(4)	17(3)	-	-	-
m (LiC12) [%]	9(1)	7(2)	19(4)	20(4)	57(6)	59(6)	61(7)
m (LiC6) [%]	-	-	-	-	-	-	-
Mass fraction (recalculated)							
m (LiC18 – LiC≥24) [%]	84(14)	81(14)	47(11)	46(8)	-	-	-
m (LiC12) [%]	16(2)	19(5)	53(11)	54(11)	100(10)	100(12)	100(11)
Refined LiC_{12}							
Scale Factor	0.00005	0.000018(6)	0.00005(1)	0.000055(9)	0.00029(2)	0.00028(2)	0.00025(2)
Cell axis *a* [Å]	4.287(5)	4.276(2)	4.2871(5)	4.2871(5)	4.287(2)	4.2883(2)	4.2884(2)
Cell axis *c* [Å]	7.06(9)	7.060(7)	7.045(3)	7.048(2)	7.0532(6)	7.054(7)	7.0569(7)
Spherical Harm. Coeff. Y20	8(6)	7(1)	7(1)	7(1)	10(1)	8.8(9)	9(1)
Y40	5(5)	11(1)	11(2)	11(1)	11.2(8)	10.7(6)	11.4(8)
Y60	2(3)	5.4(7)	5(1)	5.4(7)	5.4(4)	5.6(3)	5.7(4)
B overall	3.5(4)	2.0(5)	1.5(6)	1.5(5)	4.9(3)	4.5(3)	4.8(3)
TCH-Profile *U*	0.07(7)	-0.16(2)	-0.13(2)	-0.12(2)	-0.044(8)	-0.02(1)	-0.06(1)
TCH-Profile W	0.019(3)	0.019(2)	0.016(2)	0.015(2)	0.0073(6)	0.0077(6)	0.0096(7)
TCH-Profile Peak Shape	0.4(1)	0.56(7)	0.57(7)	0.57(7)	0.93(5)	0.76(5)	0.67(5)
Refined LiC_{18} – $LiC_{\geq 24}$							
Scale Factor	0.00027(4)	0.00008(1)	0.000048(9)	0.000047(7)			
Cell axis *a* [Å]	4.2756(9)	4.2723(4)	4.2749(5)	4.2740(5)	-	-	-
Cell axis *c* [Å]	7.03(7)	7.016(2)	7.026(3)	7.029(2)	-	-	-
Spherical Harm. Coeff. Y20	7(1)	7(1)	7(1)	7(1)	-	-	-
Y40	5.0(1)	11(1)	11(2)	11(1)	-	-	-
Y60	2.3(7)	5.4(7)	5(1)	5.4(7)	-	-	-
B overall	3.5(4)	2.0(5)	1.5(6)	1.5(5)	-	-	-
TCH-Profile *U*	0.07(7)	-0.16(2)	-0.13(2)	-0.12(2)	-	-	-
TCH-Profile W	0.019(3)	0.019(2)	0.016(2)	0.015(2)	-	-	-
TCH-Profile Peak Shape	0.4(1)				-	-	-

Table B.15 Standard uncertainty values are given in parentheses as refined by Highscore without multiplying the values with the R_{wp}-value of the fit. [138]

	S55-A1	S55-A2	S55-A3	S55-A4	S55-A5	S55-A6	S55-A7
general parameters							
Exposure time	01:14:28	01:14:28	03:06:10	13:39:08	01:14:28	01:14:28	01:14:28
2θ-range [°2θ]	7 – 37	7 – 37	7 – 37	7 – 37	7 – 37	7 – 37	7 – 37
Zero Shift [°2θ]	-0.0083(5)	-0.0018(6)	-0.0053(4)	-0.013(2)	-0.0011(7)	-0.0094(7)	-0.006(7)
Sample displacement [mm]	-0.124(6)	-0.305(7)	-0.258(5)	-0.194(2)	-0.014(8)	-0.346(8)	-0.229(8)
Al parameters							
Al1 Cell axis a [Å]	4.0455(5)	4.0462(1)	4.0462(3)	4.0467(3)	4.0478(5)	4.0474(3)	4.04498(8)
Al2 Cell axis a [Å]	4.05054(5)	4.0500(1)	4.0491(2)	4.0510(3)	4.0500(4)	4.0500(2)	4.0500(1)
TCH-Profile *U*	0.014(2)	0.018(3)	0.025(3)	0.051(1)	0.016(6)	0.019(4)	0.023(3)
TCH-Profile *W*	0.00107(6)	0.00113(9)	0.0008(1)	0.00048(4)	0.0019(2)	0.00145(7)	0.00052(8)
TCH-Profile Peak Shape	0.40(2)	0.39(2)	0.16(2)	0.413(5)	0.28(2)	0.36(1)	0.22(3)
Cu parameters							
Scale Factor	0.000222(3)	0.000261(3)	0.00065(5)	0.00304(1)	0.000255(3)	0.000323(4)	0.000364(4)
March-Dollase Factor (Pref. Orient. (0 2 0))	0.97(3)	0.953(2)	1.032(2)	1.0083(8)	0.956(2)	1.016(3)	1.043(3)
isotropic displacem. parameter B_{iso} [Å^2]	0.26(5)	1.31(5)	0.75(3)	0.35(1)	1.05(5)	1.67(5)	1.98(5)
TCH-Profile *U*	0.011(1)	0.027(2)	0.025(1)	0.0315(5)	0.038(2)	0.03(2)	0.031(2)
TCH-Profile *W*	0.0028(6)	0.00194(6)	0.00255(5)	0.00211(2)	0.00197(7)	0.00232(7)	0.0025(8)
TCH-Profile Peak Shape	0.58(1)	0.65(1)	0.547(7)	0.614(3)	0.61(1)	0.59(1)	0.61(1)
R values							
R_{Bragg} (Cu)	1.71	1.64	1.3	0.9	1.61	1.63	1.2
R_{Bragg} (Al1 // Al2)	0.52 // 3.77	0.43 // 2.34	0.87 // 1.16	0.36 // 2.86	0.68 // 1.95	1.65 // 3.41	0.25 // 3.30
R_{Bragg} (Graphite)	-	-	-	-	-	-	-
R_{Bragg} (LiC6)	-	-	-	-	-	-	-
R_{Bragg} (LiC12)	-	2.39	2.22	2.68	-	2.31	3.15
R_{Bragg} (LiC18 – LiC≥24)	1.9	2.08	1.55	2.43	1.42	3.69	3.51
R_{wp}	12.5557	12.2764	8.9259	12.6921	14.5285	12.8295	12.2006
Mass fraction							
m (Cu) [%]	57(5)	36(7)	44(5)	60(2)	27(2)	50(5)	51(3)
m (Graphite) [%]	-	-	-	-	-	-	-
m (LiC18 – LiC≥24) [%]	43(9)	56(16)	51(10)	29(2)	73(9)	41(6)	27(3)
m (LiC12) [%]	-	8(9)	5(4)	11(1)	-	10(4)	23(3)
m (LiC6) [%]	-	-	-	-	-	-	-
Mass fraction (recalculated)							
m (LiC18 – LiC≥24) [%]	100(21)	88(25)	91(18)	73(5)	100(12)	80(12)	54(6)
m (LiC12) [%]	-	13(14)	9(7)	28(3)	-	20(8)	46(6)
Refined LiC_{12}							
Scale Factor	-	0.00004(4)	0.00005(4)	0.0004(4)	-	0.00004(2)	0.00011(1)
Cell axis *a* [Å]	-	4.280(6)	4.287(7)	4.2888(3)	-	4.290(3)	4.2872(6)
Cell axis *c* [Å]	-	7.060(7)	7.055(6)	7.065(2)	-	7.055(6)	7.065(9)
Spherical Harm. Coeff. Y20	-	7(7)	10(7)	9(1)	-	12(6)	12(2)
Y40	-	11(8)	9(7)	17(1)	-	8(3)	6.8(9)
Y60	-	6(5)	2(4)	11.0(9)	-	1(3)	1.2(7)
B overall	-	4.3(4)	2.7(3)	1.4(2)	-	3.4(3)	2.7(3)
TCH-Profile *U*	-	-0.21(6)	-0.03(4)	-0.044(8)	-	0.01(6)	-0.09(2)
TCH-Profile W	-	0.039(4)	0.027(3)	0.0118(7)	-	0.018(3)	0.017(2)
TCH-Profile Peak Shape	-	0.1(1)	0.3(8)	0.8(3)	-	0.3(1)	0.2(1)
Refined LiC_{18} – $LiC_{≥24}$							
Scale Factor	0.00012(2)	0.0003(6)	0.00055(8)	0.00108(7)	0.00051(5)	0.00019(2)	0.00014(2)
Cell axis *a* [Å]	4.2735(3)	4.274(1)	4.2736(9)	4.2742(1)	4.276(6)	4.275(1)	4.2742(5)
Cell axis *c* [Å]	7.023(2)	6.98(1)	7.000(6)	7.0161(1)	7.031(3)	6.993(6)	7.028(5)
Spherical Harm. Coeff. Y20	8(1))	8.2(9)	8.8(6)	8.6(4)	9.2(7)	8(1)	8(1)
Y40	13(1)	5.4(7)	5.0(4)	13.4(4)	5.5(3)	4.6(5)	5.9(6)
Y60	8.3(6)	2.4(5)	1.6(3)	8.1(2)	1.7(3)	1.7(5)	2.5(5)
B overall	2.0(6)	4.3(4)	2.7(3)	1.4(2)	4.5(3)	3.4(3)	2.7(3)
TCH-Profile *U*	-0.26(3)	-0.21(6)	-0.03(4)	-0.044(8)	-0.18(5)	0.01(6)	-0.09(2)
TCH-Profile W	0.031(3)	0.039(4)	0.027(3)	0.0118(7)	0.039(4)	0.018(3)	0.017(2)
TCH-Profile Peak Shape	0.2(1)	0.1(1)	0.3(8)	0.8(3)	0.81(7)	0.3(1)	0.2(1)

Table B.16 Standard uncertainty values are given in parentheses as refined by Highscore without multiplying the values with the R_{wp}-value of the fit. [138]

	S55-A8	S100-E1	S100-A1
general parameters			
Exposure time	01:14:28	01:14:28	01:14:28
2θ-range [°2θ]	7 – 37	7 – 37	7 – 37
Zero Shift [°2θ]	-0.0072(6)	-0.0124(8)	-0.0033(7)
Sample displacement [mm]	-0.299(6)	-0.147(9)	-0.151(8)
Al parameters			
Al1 Cell axis a [Å]	4.04500(6)	4.0472(2)	4.0463(3)
Al2 Cell axis a [Å]	4.0500(6)	4.0511(2)	4.0490(3)
TCH-Profile *U*	0.024(2)	0.027(6)	0.029(4)
TCH-Profile *W*	0.00036(6)	0.0006(2)	0.0011(1)
TCH-Profile Peak Shape	0.33(2)	0.26(2)	0.24(2)
Cu parameters			
Scale Factor	0.000247(3)	0.00056(1)	0.00558(9)
March-Dollase Factor (Pref. Orient. (0 2 0))	0.988(3)	1.004(5)	1.027(3)
isotropic displacem. parameter B_{iso} [Å^2]	0.64(5)	0.7(8)	0.69(6)
TCH-Profile *U*	0.023(2)	0.019(2)	0.025(2)
TCH-Profile *W*	0.0025(7)	0.00206(9)	0.00231(8)
TCH-Profile Peak Shape	0.61(1)	0.61(2)	0.58(2)
R values			
R_{Bragg} (Cu)	1.21	1.39	1.35
R_{Bragg} (Al1 // Al2)	1.27 // 2.54	1.07 // 1.77	0.69 // 0.89
R_{Bragg} (Graphite)	-	1.37	1.61
R_{Bragg} (LiC6)	-	-	-
R_{Bragg} (LiC12)	2.37	-	-
R_{Bragg} (LiC18 – LiC≥24)	2.33	1.9	0.66
R_{wp}	12.3543	9.5378	8.3461
Mass fraction			
m (Cu) [%]	51(8)	28(8)	28(3)
m (Graphite) [%]	-	61(29)	41(8)
m (LiC18 – LiC≥24) [%]	31(9)	11(6)	31(5)
m (LiC12) [%]	18(7)	-	-
m (LiC6) [%]	-	-	-
Mass fraction (recalculated)			
m (LiC18 – LiC≥24) [%]	63(18)	85(40)	57(11)
m (LiC12) [%]	37(14)	15(8)	43(7)
Refined LiC_{12}			
Scale Factor	0.00006(2)	0.00016(8)	0.0045(5)
Cell axis *a* [Å]	4.285(2)	4.265(4)	4.2884(4)
Cell axis *c* [Å]	7.055(4)	6.839(7)	7.050(3)
Spherical Harm. Coeff. Y20	6(3)	4(5)	10(2)
Y40	14(3)	5(6)	10(1)
Y60	10(3)	5(4)	4.9(7)
B overall	2.5(5)	5.1(10)	6.5(4)
TCH-Profile *U*	0.05(6)	-0.1(3)	-0.03(1)
TCH-Profile W	0.011(2)	0.018(2)	0.0067(9)
TCH-Profile Peak Shape	0.5(1)	0.4(1)	0.9(1)
Refined LiC_{18} – $LiC_{≥24}$			
Scale Factor	0.00011(3)	0.009(3)	0.058(9)
Cell axis *a* [Å]	4.277(2)	2.4609(5)	2.4598(3)
Cell axis *c* [Å]	7.007(7)	6.738(1)	6.743(3)
Spherical Harm. Coeff. Y20	11(2)	3(1)	9(1)
Y40	8(1)	5.7(8)	9(1)
Y60	3(1)	5.3(9)	5(1)
B overall	2.5(5)	5(1)	6.5(4)
TCH-Profile *U*	0.05(6)	-0.1(3)	-0.03(1)
TCH-Profile W	0.011(2)	0.018(2)	0.0067(9)
TCH-Profile Peak Shape	0.5(1)	0.4(1)	0.9(1)

Table B.17 Standard uncertainty values are given in parentheses as refined by Highscore without multiplying the values with the R_{wp}-value of the fit. [138]

B.3 XRD electrode images

The following section provides additional images of the graphite anodes extracted from the batteries used in the calendar aging experiment.

The anode side facing away from the battery center is considered the front and marked by (F) for the following images. Photos were taken of the outermost part of the electrode (1), the center region (2) and the innermost part of the jelly roll (3). The anode side facing to the battery center is considered the backside and marked with (B). Additional close ups are provided for the electrode sides (F-S, B-S) and parts located opposite to the cathode tab (B-T, F-T).

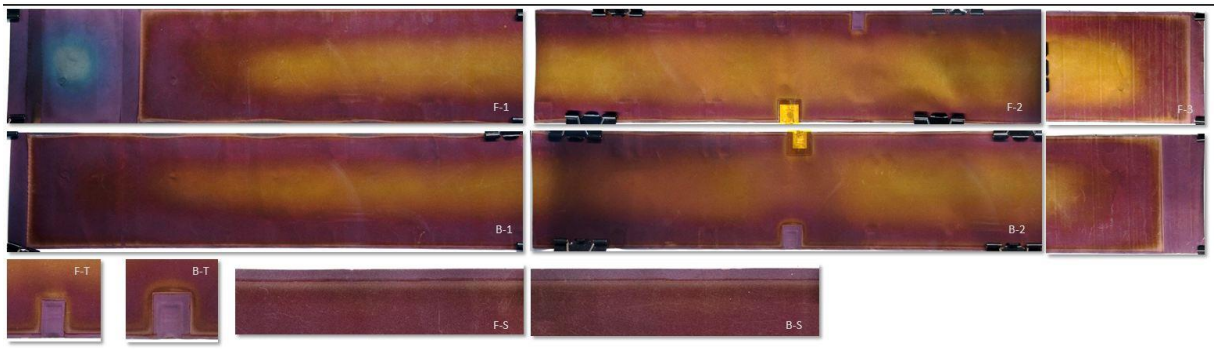

Figure B.1 Battery S95 stored at 40 C and 95% SoC. [138]

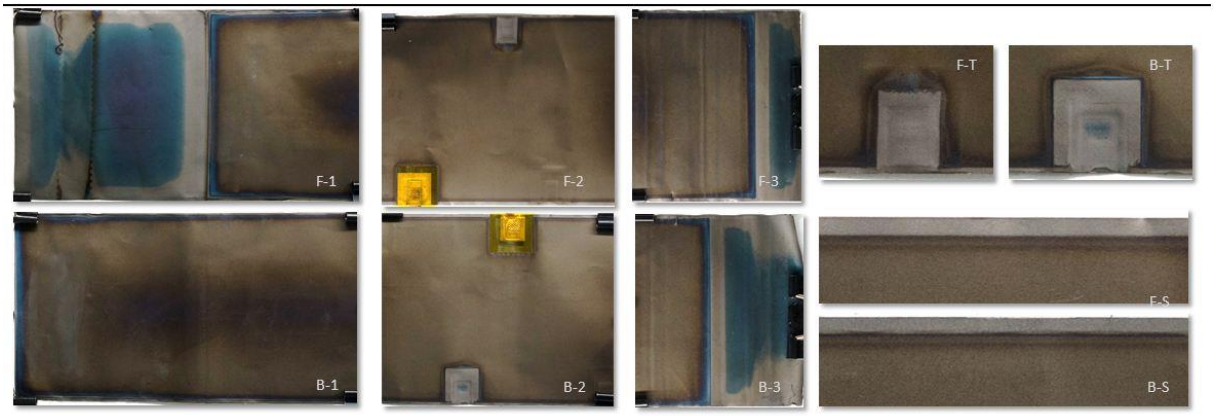

Figure B.2 Battery S100 was stored at 100 % SoC and 40 °C with subsequent C/4 CC cycling for 250h at 25 °C. The battery underwent additional five discharges (C/4, CCCV, I<0.05%, 10h pause between each discharge) at 50 °C to further deplete the overhang region. Disassembly was performed at fully discharged state. [138]

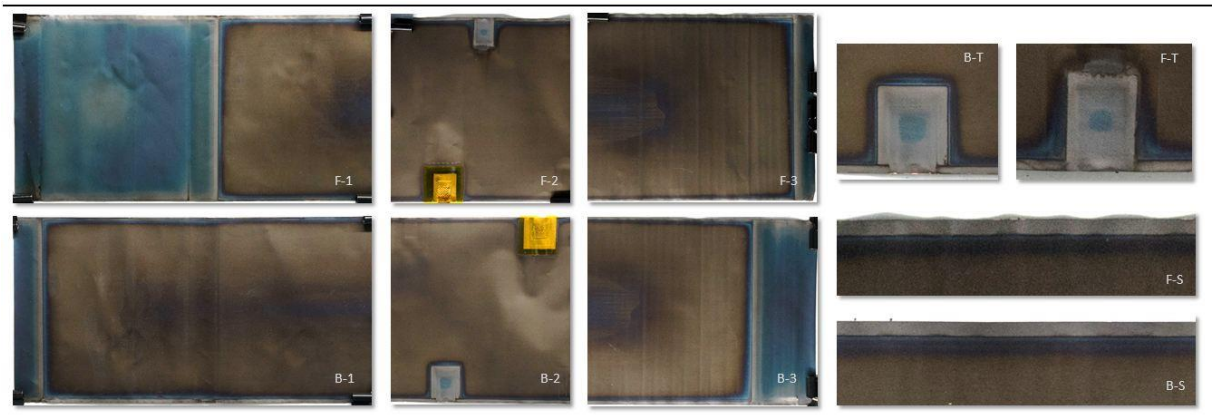

Figure B.3 Battery S90 was stored at 90 % SoC and 40 °C with subsequent C/4 CC cycling for 250 h at 25 °C. The battery was disassembled at fully discharged state. [138]

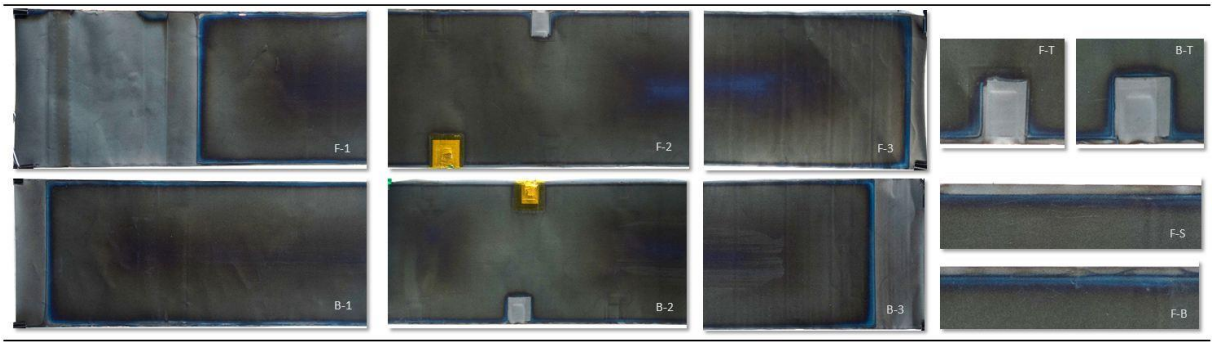

Figure B.4 Battery S80 was stored at 40 °C and 80 % SoC with subsequent C/4 CC cycling for 300 cycles at 25 °C. The battery was disassembled at a partially discharged state with 66 % SoC (0.6 Ah). [138]

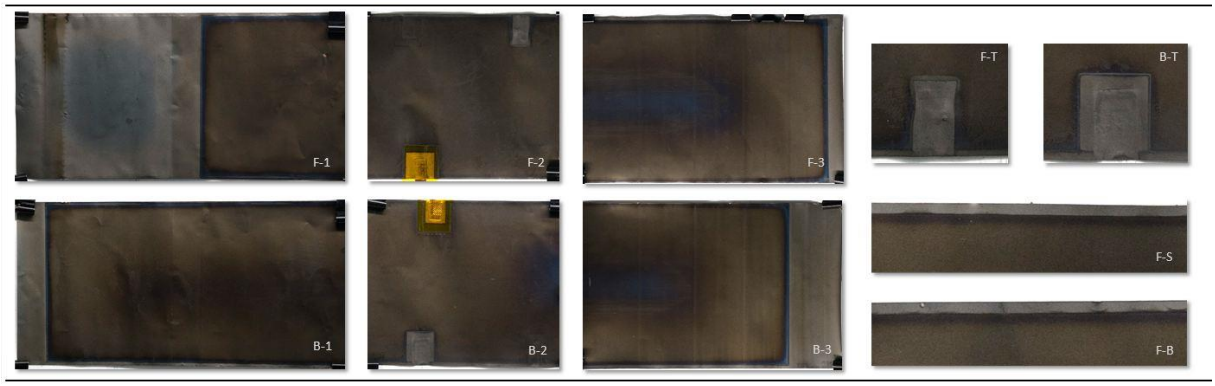

Figure B.5 Battery S60 was stored at 40 C and 60 % SoC with subsequent C/4 CC cycling for 250 h at 25°C. The battery underwent additional five discharges (C/4, CCCV, I < 0.05 %, 10 h pause between each discharge) at 50°C to further deplete the overhang region. The battery was disassembled at fully discharged state. [138]

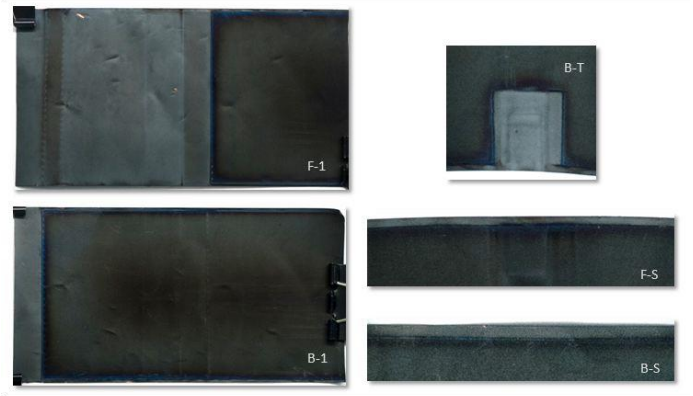

Figure B.6 Battery S55 stored at 40°C and 55 % SoC. Disassembly was performed at the storage SoC. [138]

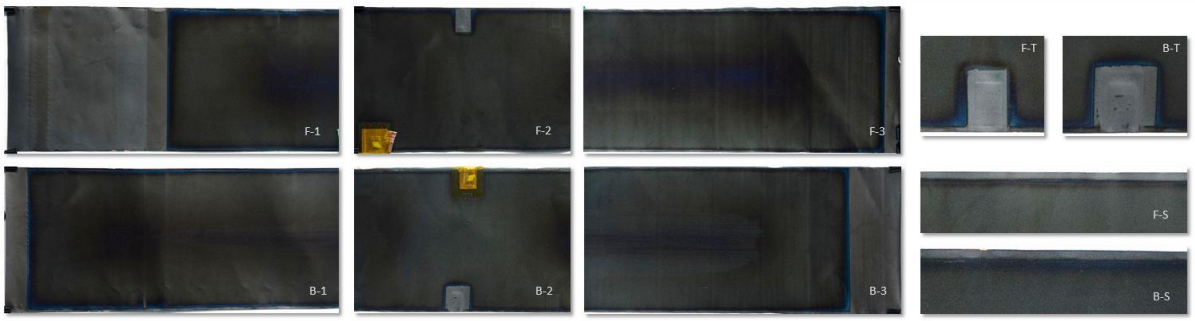

Figure B.7 Battery S40 was stored at 40 % SoC and 40°C with subsequent C/4 CC cycling for 300 cycles at 25°C. The battery was disassembled at fully discharged state. [138]

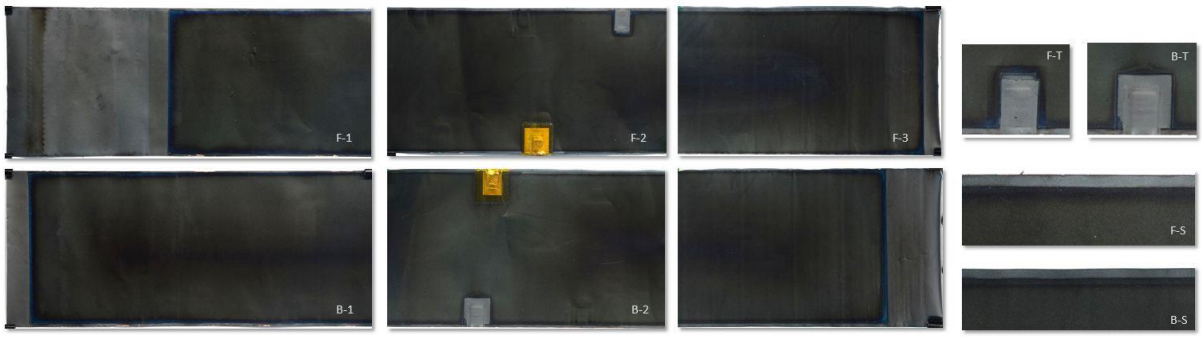

Figure B.8 Battery S20 was stored at 20 % SoC and 40 C with subsequent C/4 CC cycling for 300 cycles at 25°C. The battery was disassembled at a partially discharged state with 34 % SoC (0.3 Ah). [138]

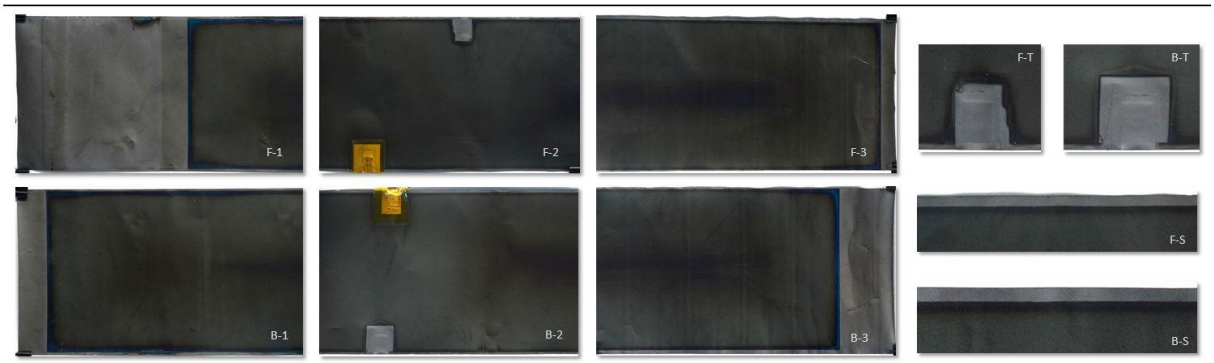

Figure B.9 Battery S10 was stored at 10 % SoC and 40°C with subsequent C/4 CC cycling for 300 cycles at 25°C. The battery was disassembled at a partially discharged state with 69 % SoC (0.7 Ah). [138]

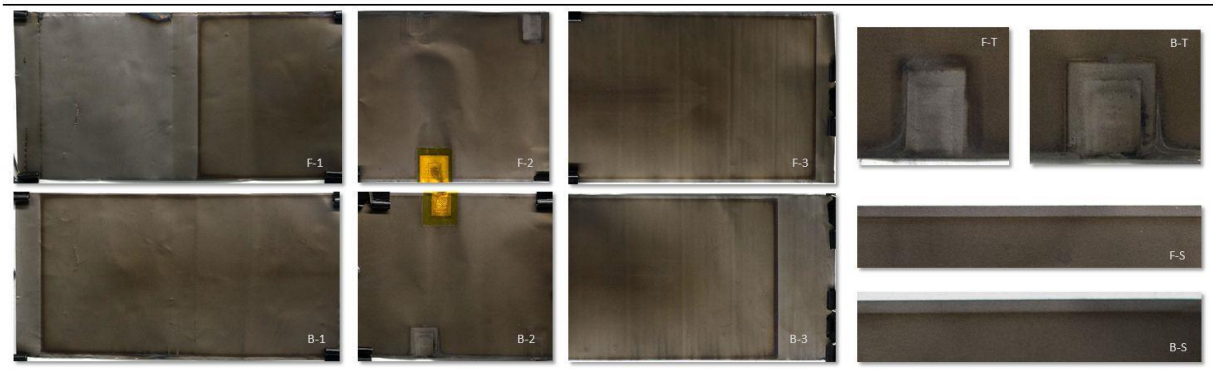

Figure B.10 Battery S05 stored at 5 % SoC and 40°C. Disassembly was performed at the storage SoC. [138]

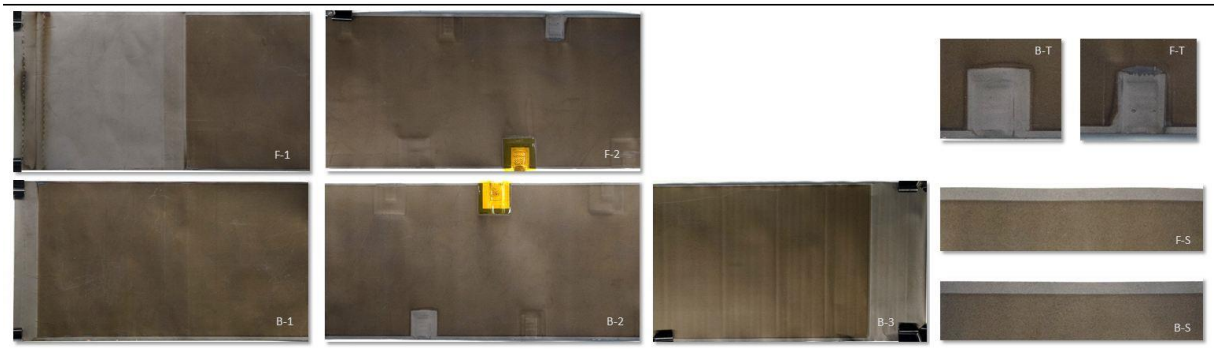

Figure B.11 Battery S00 stored at 0 % SoC and 40°C. Disassembly was performed at the storage SoC. [138]

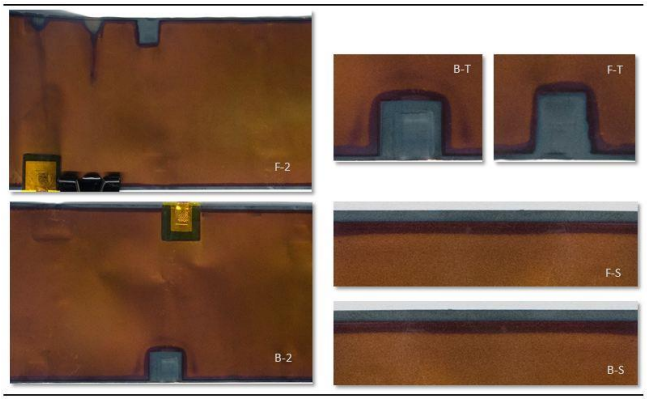

Figure B.12 Battery CCCV100 was a new cell not taking part in the 40°C calendar aging experiment. Battery disassembly was performed at a fully charged state (C/4, CCCV, I<0.05). [138]

C.1 ND-Data MATLAB fit routine

In the following the MATLAB fit routine for the analysis of the ND-data is given. Adapted from V. Zinth.

```
% Voigt Profile Fit routine

fitmode=1; %set 0 if you want only simulation
% i: final two digits of number in filename
fid=fopen('results_m283000-138-226.txt','wt');  %opens  file  for  writing
results
for i=138:226
    fv=sprintf('%01.0f',i);
    textvar=['m283000_' fv];
    textvar2=['m283000_' fv];
    A = importdata([textvar '.dat'],' ',13);
    aa=A.data;
    DirInfo = dir([textvar2 '.dat']);
    filedate = DirInfo.date


    % define starting values and whether they should be fitted (active 1)
    % or kept constant (active 0)
    initpa(1,1)=600;  active(1,1)=1;     % y0
    initpa(10,1)=0.9; active(10,1)=1;
    initpa(2,1)=0.5;  active(2,1)=0;     % eta
    initpa(3,1)=0;  active(3,1)=0;     % A0
    initpa(4,1)=35.07;     active(4,1)=0;    % be
    initpa(5,1)=0.65;    active(5,1)=1;      % FWHM
    initpa(6,1)=400;  active(6,1)=1;     % A0
    initpa(7,1)=35.9;     active(7,1)=1;    % be
    %initpa(8,1)=0.5959;    active(8,1)=1;      % FWHM1
    initpa(8,1)=0;  active(8,1)=0;     % A0
    initpa(9,1)=29.5;     active(9,1)=0;    % be
    %initpa(11,1)=0.5959;    active(8,1)=1;      % FWHM
    %initpa(8,1)=1400;  active(8,1)=0;     % x
    %initpa(9,1)=62.5;     active(9,1)=0;    % y

    % sets active params to be the initial fitting params initpa2
    ni=1;
    initpa2=zeros(1,sum(active));
    for ii=1:length(initpa)
        if active(ii)
            initpa2(ni)=initpa(ii);
            ni=ni+1;
        end
    end

    % define a function handle fh to be fed into the optimization procedure
    % nlinfit
    fh=@(fitpa,x)mypseudovoigt3(fitpa,x,active,initpa);
    if fitmode
        options=optimset('display','iter');
        [finalpa,r,J,COVB] = nlinfit(aa(:,1),aa(:,2),fh,initpa2,options);
        % calculate the confidence intervals of fitting params
        ci = nlparci(finalpa,r,'covar',COVB);
    else
        finalpa=initpa2;
    end
    % calculate final function
    yfinal=fh(finalpa,aa(:,1));
```

```
% prepare results to be exported
    ni=1;
    ciexp=zeros(length(initpa),2);
    for ii=1:length(initpa)
        if active(ii)
            initpa(ii)=finalpa(ni);
            ciexp(ii,:)=ci(ni,:);
            ni=ni+1;
        end
    end
    export=transpose([initpa ciexp active]);

    %Berechnung Fehler aus dem Konfidenzintervall
    fehler=(export(3,:)-export(2,:))./2;

  %Berechnung Integralintensität nach der Formel FWHM*Imax/0.939 (Gauss)
  %bzw. 0.637 (Lorenz) für Mischungsparam=0.5
        export2(:,1)=(export(:,3)).*(export(:,5).*1.3174);

export2(:,2)=sqrt(((fehler(:,3)/export(1,3)).^2)+((fehler(:,5)/export(1,5
)).^2)).*export2(:,1);
        export2(:,3)=(export(:,6)).*(export(:,5).*1.3174);

export2(:,4)=sqrt(((fehler(:,6)/export(1,6)).^2)+((fehler(:,5)/export(1,5
)).^2)).*export2(:,3);
        export2(:,5)=(export(:,8)).*(export(:,5).*1.3174);

export2(:,6)=sqrt(((fehler(:,8)/export(1,8)).^2)+((fehler(:,5)/export(1,5
)).^2)).*export2(:,5);

        export3=export2(1,:);
    % write results into file
   % fprintf(fid, [textvar '\n-------------- \n\n']);
    fprintf(fid, [filedate ' ' textvar ' '], export);
    fprintf(fid, ['%8.4f   -%8.4f   +%8.4f   %1.0f '], export);
    fprintf(fid, ['%8.4f ' ], export3);
    fprintf(fid,'\n');

    % make figure with handle h
    diff=(aa(:,2)-yfinal)
    h=figure(i);
    plot(aa(:,1),aa(:,2))
    hold on
    plot(aa(:,1),yfinal,'color','r')
    hold on
    plot(aa(:,1),diff,'color','black')
    % save figure h
    saveas(h,textvar,'fig')

end
```

C.2 ND-Data MATLAB Voigt profile implementation

The following function implements the pseudo Voigt profile in the MATLAB fit routine for ND analysis. The function implements the FWHM coupling discussed in section 4.9.2:

```
function f=mypseudovoigt(fitpa,x,active,initpa)
ni=1;
param=zeros(1,length(initpa));
for ii=1:length(initpa)
    if active(ii)
        param(ii)=fitpa(ni);
        ni=ni+1;
    else
        param(ii)=initpa(ii);
    end
end
f=param(1)+param(10)*x+param(3) * (param(2) * (1./(1+ ((x-
param(4)).^2/(param(5)/(2*sqrt(2*0.69314718)))^2) )) + (1-param(2)) *
exp(-((x-param(4)).^2/(param(5)/(2*sqrt(2*0.69314718)))^2)*0.5))+
param(6) * (param(2) * (1./(1+ ((x-
param(7)).^2/(param(5)/(2*sqrt(2*0.69314718)))^2) )) + (1-param(2)) *
exp(-((x-param(7)).^2/(param(5)/(2*sqrt(2*0.69314718)))^2)*0.5))+param(8)
* (param(2) * (1./(1+ ((x-
param(9)).^2/(param(5)/(2*sqrt(2*0.69314718)))^2) )) + (1-param(2)) *
exp(-((x-param(9)).^2/(param(5)/(2*sqrt(2*0.69314718)))^2)*0.5));
```

C.3 Neutron wavelength calibration

Neutron diffraction data and Rietveld refinement for the NIST Si-Standard powder to determine the neutron wavelength. Figure C.1 shows the calibration preliminary to the test series of proposal 10604. Figure C.2 shows the calibration preliminary to the test series of proposal 11536.

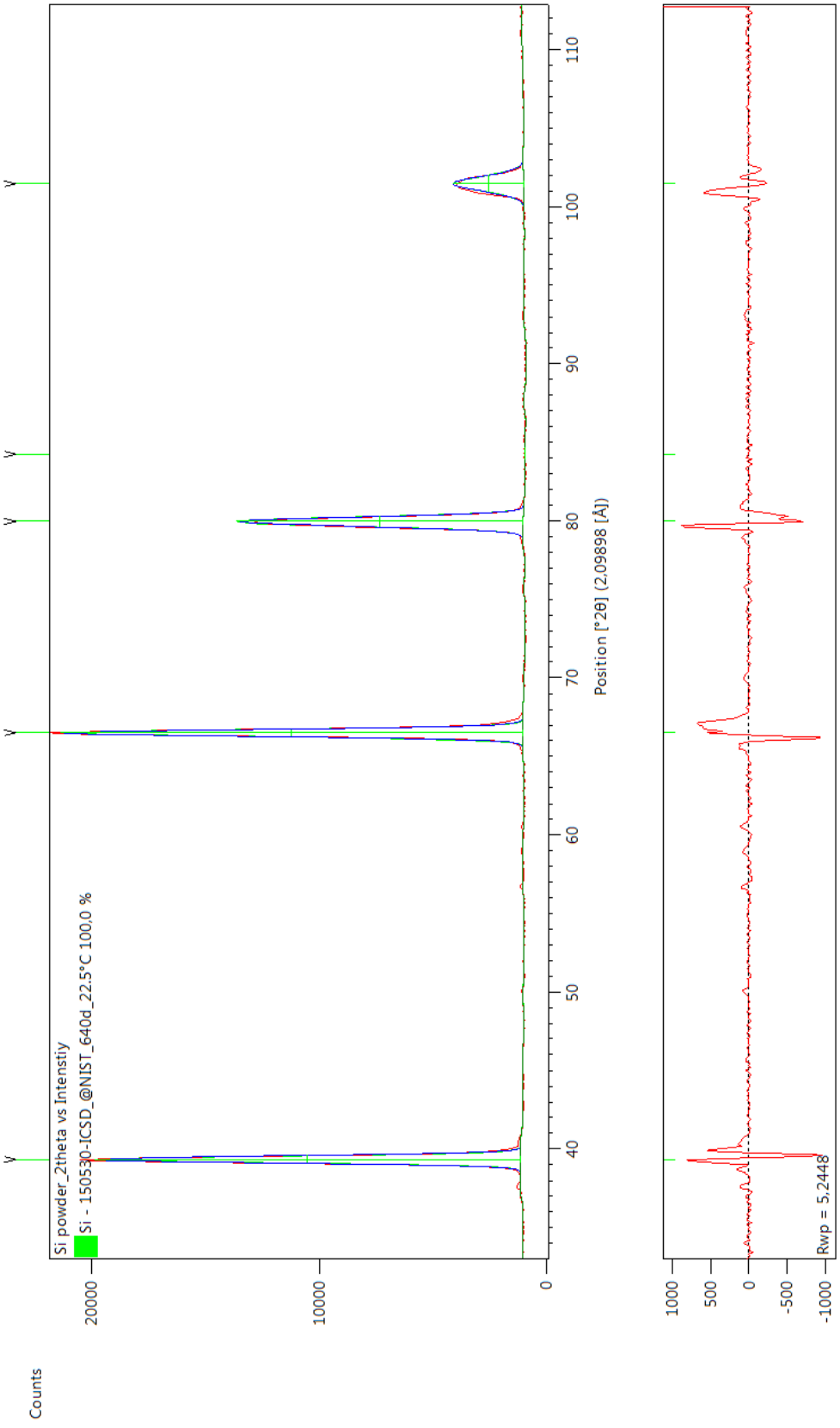

Figure C.1 NIST Si-Standard powder Rietveld refinement for the ND measurements of proposal 10604 Phase coexistence in Li-ion cells during high current discharge.

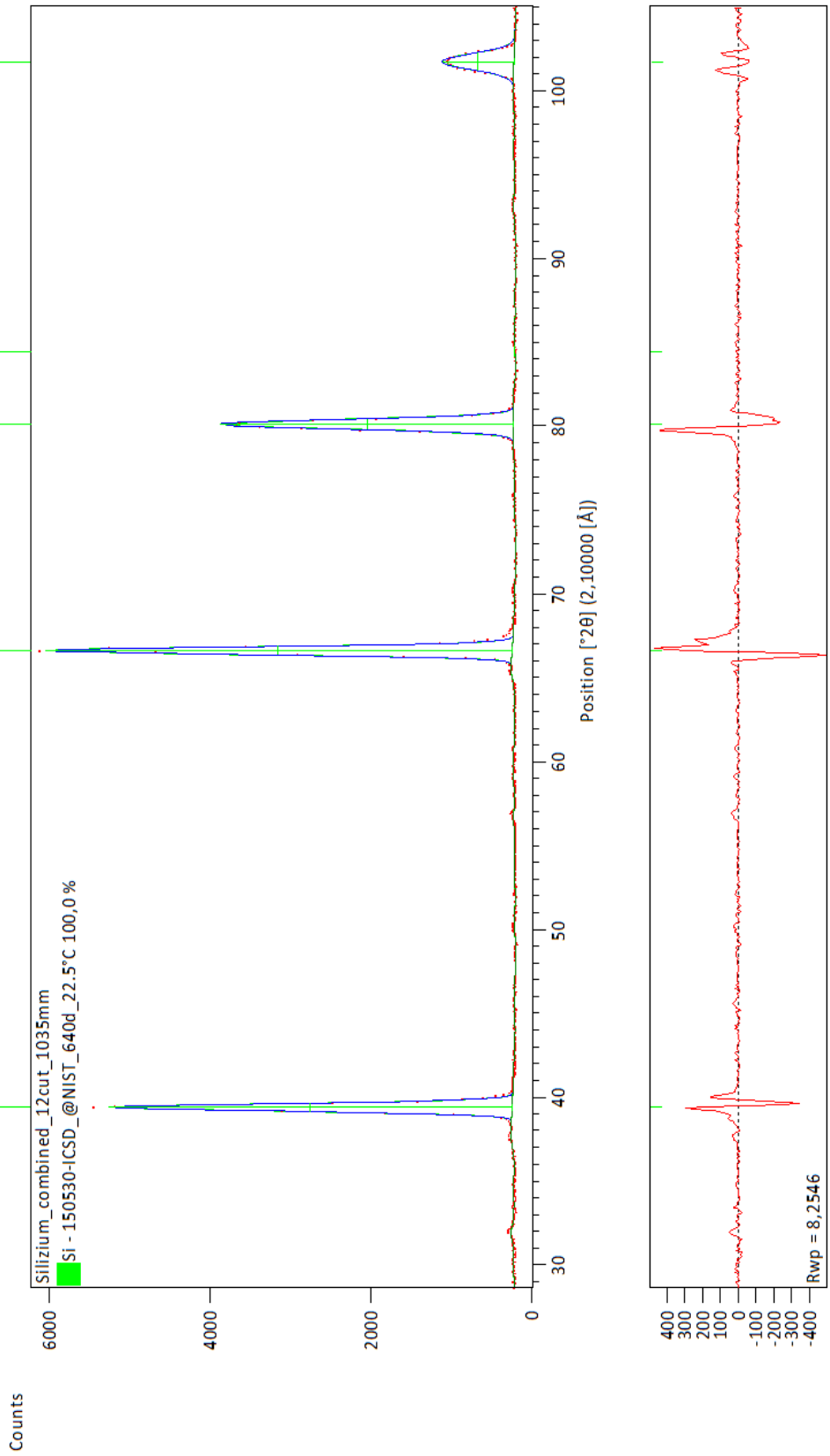

Figure C.2 NIST Si-Standard powder fit for the ND measurements of proposal 11536 Effect of anode coating thickness on low temperature relaxation in lithium ion batteries.

C.4 NCM Electrode SEM and particle data

Figure C.3 shows the NCM electrode top view and cross view SEM images for the HE, BA and HP samples. The corresponding particle radii probability distribution is shown in Figure C.4.

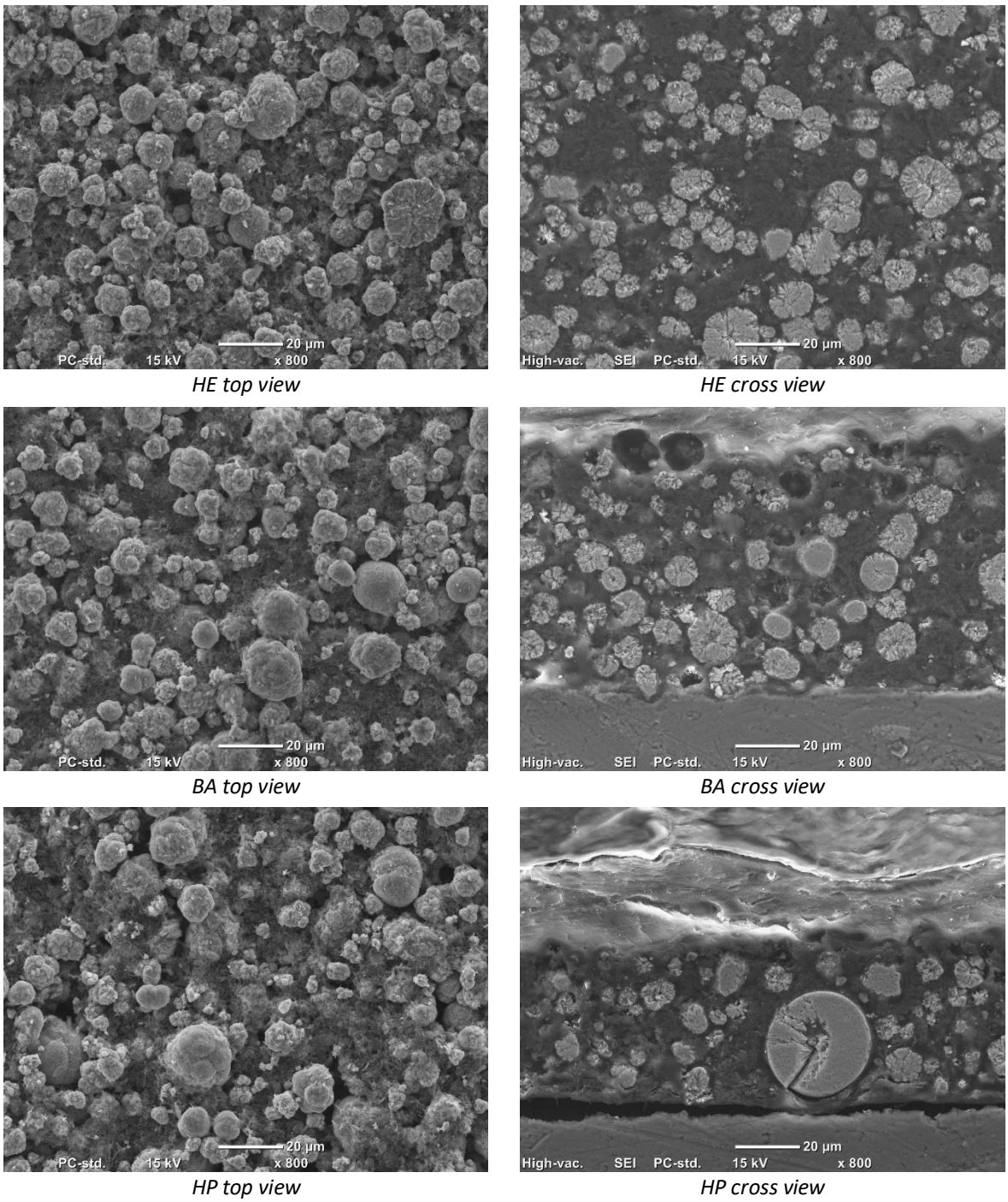

Figure C.3 Top view and cross view SEM images of NCM electrodes for the HE, BA and HP samples with 800x magnification. Images taken by J. Wilhelm. Image reprinted from [191].

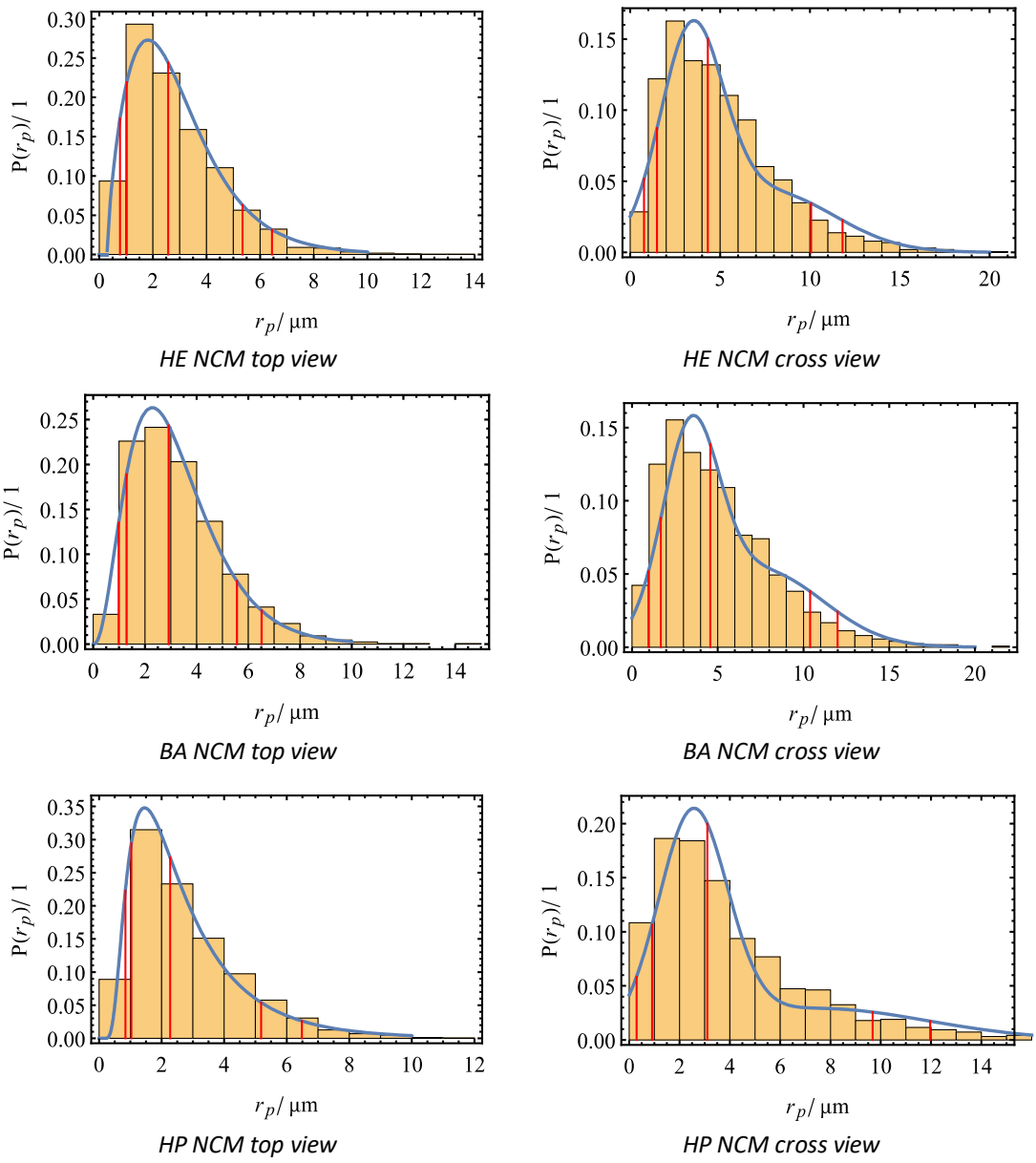

Figure C.4 Probability distribution for particle radii for top- and cross-section SEM images of the NCM cathode of the HE, BA and HP batteries. The blue line marks the best fit distribution. The red lines mark the percentile values where 5 %, 10 %, 50 %, 90 % and 95% of the particle population have a smaller radius than the marked value. Image reprinted from [191].

C.5 PEIS data

Figure C.5 to C.6 show the PEIS data for tortuosity analysis of the HE, BA, and HP electrodes.

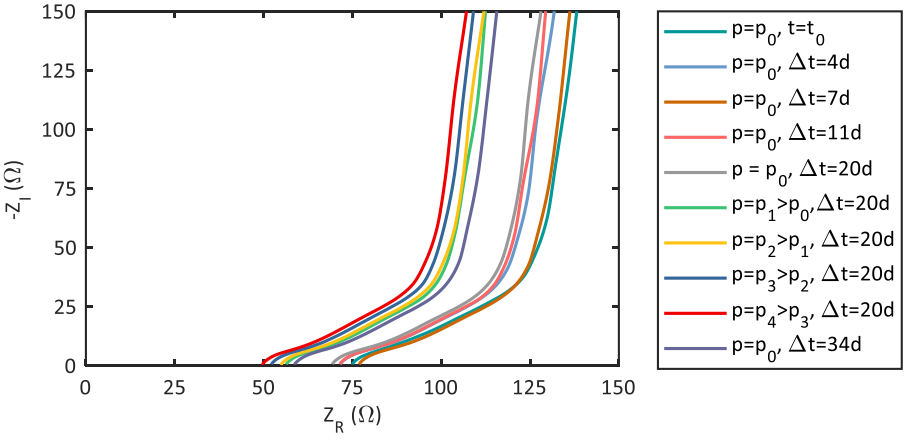

***(a)** HE graphite*

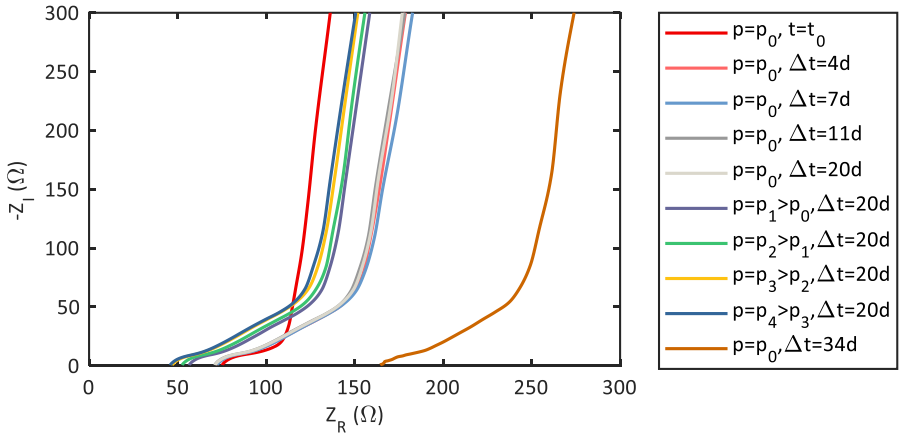

***(b)** BA graphite*

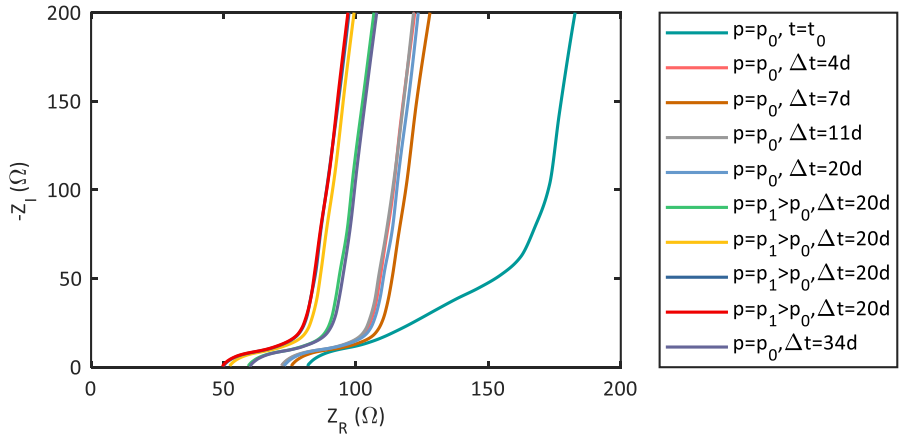

***(c)** HP graphite*

Figure C.5 Nyquist plot of PEIS data of (a) HE (b) BA and (c) HP type 1 symmetric graphite cells. Data from [191].

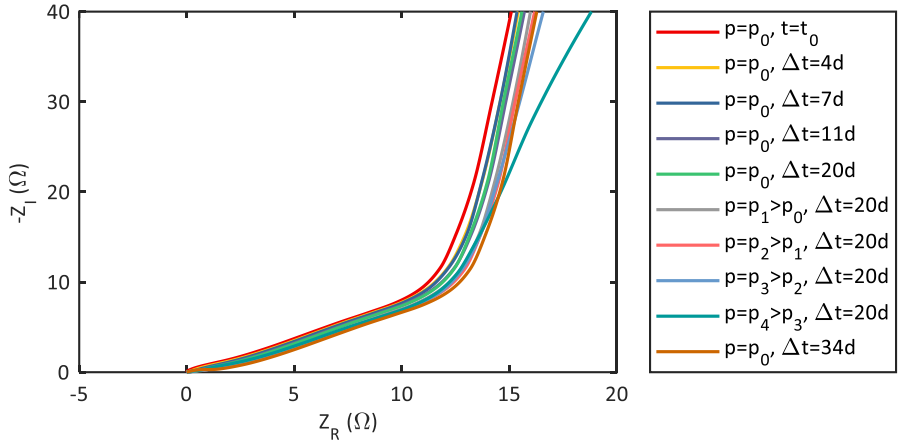

***(a)** HE graphite*

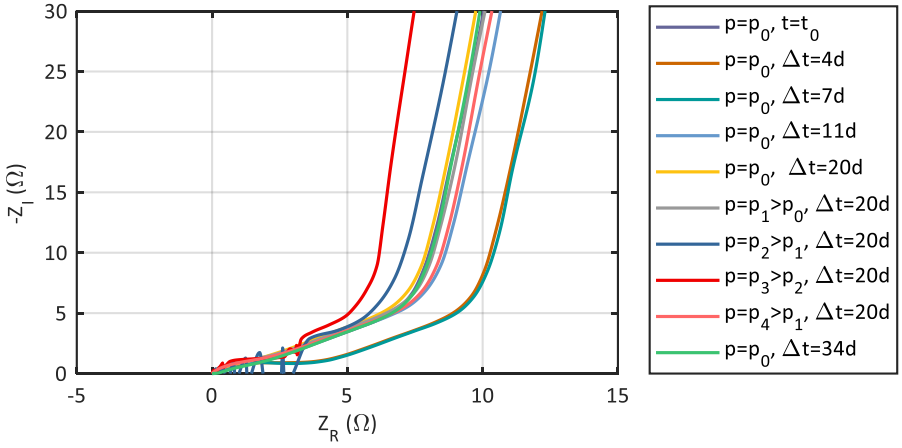

***(b)** BA graphite*

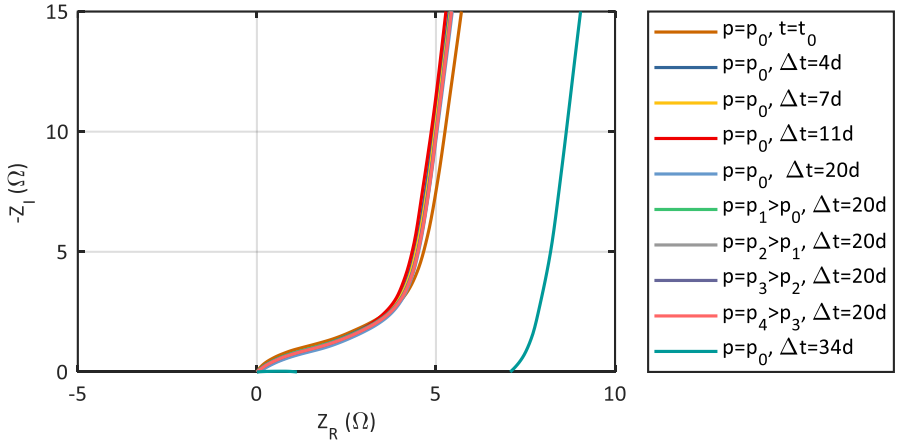

***(c)** HP graphite*

Figure C.6 Nyquist plot of PEIS data of (a) HE (b) BA and (c) HP type 2 symmetric graphite cells. Data from [191].

References

[1] Avicenne Energy (Christoph Pillot), "The Rechargeable Battery Market: Value Chain and Main Trends 2019-2030," in *Advanced Automotive Battery Conference 2021*.

[2] J. Jaguemont, L. Boulon, and Y. Dubé, "A comprehensive review of lithium-ion batteries used in hybrid and electric vehicles at cold temperatures," *Applied Energy*, vol. 164, pp. 99–114, 2016, doi: 10.1016/j.apenergy.2015.11.034.

[3] A. Barré, B. Deguilhem, S. Grolleau, M. Gérard, F. Suard, and D. Riu, "A review on lithium-ion battery ageing mechanisms and estimations for automotive applications," *Journal of Power Sources*, vol. 241, pp. 680–689, 2013, doi: 10.1016/j.jpowsour.2013.05.040.

[4] J. Zhang and J. Lee, "A review on prognostics and health monitoring of Li-ion battery," *Journal of Power Sources*, vol. 196, no. 15, pp. 6007–6014, 2011, doi: 10.1016/j.jpowsour.2011.03.101.

[5] P. Keil *et al.,* "Calendar Aging of Lithium-Ion Batteries," (in af), *J. Electrochem. Soc.*, vol. 163, no. 9, pp. A1872-A1880, 2016, doi: 10.1149/2.0411609jes.

[6] J. Belt, V. Utgikar, and I. Bloom, "Calendar and PHEV cycle life aging of high-energy, lithium-ion cells containing blended spinel and layered-oxide cathodes," *Journal of Power Sources*, vol. 196, no. 23, pp. 10213–10221, 2011, doi: 10.1016/j.jpowsour.2011.08.067.

[7] S. Grolleau *et al.,* "Calendar aging of commercial graphite/LiFePO4 cell – Predicting capacity fade under time dependent storage conditions," *Journal of Power Sources*, vol. 255, pp. 450–458, 2014, doi: 10.1016/j.jpowsour.2013.11.098.

[8] S. Käbitz *et al.,* "Cycle and calendar life study of a graphite|LiNi1/3Mn1/3Co1/3O2 Li-ion high energy system. Part A: Full cell characterization," *Journal of Power Sources*, vol. 239, pp. 572–583, 2013, doi: 10.1016/j.jpowsour.2013.03.045.

[9] M. Kassem, J. Bernard, R. Revel, S. Pélissier, F. Duclaud, and C. Delacourt, "Calendar aging of a graphite/LiFePO4 cell," (in af), *Journal of Power Sources*, vol. 208, pp. 296–305, 2012, doi: 10.1016/j.jpowsour.2012.02.068.

[10] I. Bloom *et al.,* "An accelerated calendar and cycle life study of Li-ion cells," *Journal of Power Sources*, vol. 101, no. 2, pp. 238–247, 2001, doi: 10.1016/S0378-7753(01)00783-2.

[11] M. Ecker *et al.,* "Calendar and cycle life study of Li(NiMnCo)O2-based 18650 lithium-ion batteries," *Journal of Power Sources*, vol. 248, pp. 839–851, 2014, doi: 10.1016/j.jpowsour.2013.09.143.

[12] M. Safari and C. Delacourt, "Aging of a Commercial Graphite/LiFePO4 Cell," (in af), *J. Electrochem. Soc.*, vol. 158, no. 10, pp. A1123, 2011, doi: 10.1149/1.3614529.

[13] S. B. Peterson, J. Apt, and J. F. Whitacre, "Lithium-ion battery cell degradation resulting from realistic vehicle and vehicle-to-grid utilization," *Journal of Power Sources*, vol. 195, no. 8, pp. 2385–2392, 2010, doi: 10.1016/j.jpowsour.2009.10.010.

[14] A. J. Smith, J. C. Burns, and J. R. Dahn, "A High Precision Study of the Coulombic Efficiency of Li-Ion Batteries," *Electrochem. Solid-State Lett.*, vol. 13, no. 12, pp. A177, 2010, doi: 10.1149/1.3487637.

[15] A. J. Smith, J. C. Burns, D. Xiong, and J. R. Dahn, "Interpreting High Precision Coulometry Results on Li-ion Cells," (in ca), *J. Electrochem. Soc.*, vol. 158, no. 10, pp. A1136, 2011, doi: 10.1149/1.3625232.

[16] A. J. Smith, J. C. Burns, S. Trussler, and J. R. Dahn, "Precision Measurements of the Coulombic Efficiency of Lithium-Ion Batteries and of Electrode Materials for Lithium-Ion Batteries," *J. Electrochem. Soc.*, vol. 157, no. 2, pp. A196, 2010, doi: 10.1149/1.3268129.

[17] J. C. Burns *et al.,* "Evaluation of Effects of Additives in Wound Li-Ion Cells Through High Precision Coulometry," *J. Electrochem. Soc.*, vol. 158, no. 3, pp. A255, 2011, doi: 10.1149/1.3531997.
[18] B. Gyenes, D. A. Stevens, V. L. Chevrier, and J. R. Dahn, "Understanding Anomalous Behavior in Coulombic Efficiency Measurements on Li-Ion Batteries," (in ca), *Journal of the Electrochemical Society*, vol. 162, no. 3, pp. A278-A283, 2014, doi: 10.1149/2.0191503jes.
[19] M. Tang, P. Albertus, and J. Newman, "Two-Dimensional Modeling of Lithium Deposition during Cell Charging," *J. Electrochem. Soc.*, vol. 156, no. 5, pp. A390, 2009, doi: 10.1149/1.3095513.
[20] M. Lewerenz, J. Münnix, J. Schmalstieg, S. Käbitz, M. Knips, and D. U. Sauer, "Systematic aging of commercial LiFePO4|Graphite cylindrical cells including a theory explaining rise of capacity during aging," *Journal of Power Sources*, vol. 345, pp. 254–263, 2017, doi: 10.1016/j.jpowsour.2017.01.133.
[21] R. Zhao, S. Zhang, J. Liu, and J. Gu, "A review of thermal performance improving methods of lithium ion battery: Electrode modification and thermal management system," *Journal of Power Sources*, vol. 299, pp. 557–577, 2015, doi: 10.1016/j.jpowsour.2015.09.001.
[22] V. Zinth *et al.,* "Lithium plating in lithium-ion batteries at sub-ambient temperatures investigated by in situ neutron diffraction," *Journal of Power Sources*, vol. 271, pp. 152–159, 2014, doi: 10.1016/j.jpowsour.2014.07.168.
[23] T. Waldmann, M. Wilka, M. Kasper, M. Fleischhammer, and M. Wohlfahrt-Mehrens, "Temperature dependent ageing mechanisms in Lithium-ion batteries – A Post-Mortem study," *Journal of Power Sources*, vol. 262, pp. 129–135, 2014, doi: 10.1016/j.jpowsour.2014.03.112.
[24] T. M. Bandhauer, S. Garimella, and T. F. Fuller, "A Critical Review of Thermal Issues in Lithium-Ion Batteries," (in af), *J. Electrochem. Soc.*, vol. 158, no. 3, pp. R1, 2011, doi: 10.1149/1.3515880.
[25] Lo Valoen and J. N. Reimers, "Transport properties of LiPF6-based Li-ion battery electrolytes," (in af), *Journal of the Electrochemical Society*, vol. 152, no. 5, pp. A882-A891, 2005, doi: 10.1149/1.1872737.
[26] E. J. Plichta and W. K. Behl, "A low-temperature electrolyte for lithium and lithium-ion batteries," *Journal of Power Sources*, vol. 88, no. 2, pp. 192–196, 2000.
[27] S. S. Zhang, K. Xu, and T. R. Jow, "Low temperature performance of graphite electrode in Li-ion cells," (in af), *Electrochimica Acta*, vol. 48, no. 3, pp. 241–246, 2002.
[28] T. L. Kulova, Am Skundin, E. A. Nizhnikovskii, and A. V. Fesenko, "Temperature effect on the lithium diffusion rate in graphite," *Russian Journal of Electrochemistry*, vol. 42, no. 3, pp. 259–262, 2006.
[29] M. Park, X. Zhang, M. Chung, G. B. Less, and A. M. Sastry, "A review of conduction phenomena in Li-ion batteries," (in af), *Journal of Power Sources*, vol. 195, no. 24, pp. 7904–7929, 2010, doi: 10.1016/j.jpowsour.2010.06.060.
[30] G. Nagasubramanian, "Two- and three-electrode impedance studies on 18650 Li-ion cells," *Journal of Power Sources*, vol. 87, 1-2, pp. 226–229, 2000.
[31] G. Nagasubramanian, "Electrical characteristics of 18650 Li-ion cells at low temperatures," *Journal of Applied Electrochemistry*, vol. 31, no. 1, pp. 99–104, 2001.
[32] S. S. Zhang, K. Xu, and T. R. Jow, "The low temperature performance of Li-ion batteries," *Journal of Power Sources*, vol. 115, no. 1, pp. 137–140, 2003, doi: 10.1016/S0378-7753(02)00618-3.
[33] DAHN, JR, "PHASE-DIAGRAM OF LIXC6," (in af), *Physical Review B*, vol. 44, no. 17, pp. 9170–9177, 1991, doi: 10.1103/PhysRevB.44.9170.
[34] T. Ohzuku, "Formation of Lithium-Graphite Intercalation Compounds in Nonaqueous Electrolytes and Their Application as a Negative Electrode for a Lithium Ion (Shuttlecock) Cell," *J. Electrochem. Soc.*, vol. 140, no. 9, p. 2490, 1993, doi: 10.1149/1.2220849.
[35] C. S. Wang, A. J. Appleby, and F. E. Little, "Low-temperature characterization of lithium-ion carbon anodes via microperturbation measurement," (in af), *Journal of the Electrochemical Society*, vol. 149, no. 6, pp. A754-A760, 2002, doi: 10.1149/1.1474427.

[36] S. R. Sivakkumar, J. Y. Nerkar, and A. G. Pandolfo, “Rate capability of graphite materials as negative electrodes in lithium-ion capacitors,” (in af), *Electrochimica Acta*, vol. 55, no. 9, pp. 3330–3335, 2010.

[37] S. Flandrois and B. Simon, “Carbon materials for lithium-ion rechargeable batteries,” (in da), *Carbon*, vol. 37, no. 2, pp. 165–180, 1999, doi: 10.1016/S0008-6223(98)00290-5.

[38] N. Takami, “Structural and Kinetic Characterization of Lithium Intercalation into Carbon Anodes for Secondary Lithium Batteries,” *J. Electrochem. Soc.*, vol. 142, no. 2, p. 371, 1995, doi: 10.1149/1.2044017.

[39] K. Persson *et al.,* “Lithium Diffusion in Graphitic Carbon,” (in af), *J. Phys. Chem. Lett.*, vol. 1, no. 8, pp. 1176–1180, 2010, doi: 10.1021/jz100188d.

[40] A. Funabiki, “Impedance Study on the Electrochemical Lithium Intercalation into Natural Graphite Powder,” *J. Electrochem. Soc.*, vol. 145, no. 1, p. 172, 1998, doi: 10.1149/1.1838231.

[41] J. Landesfeind, J. Hattendorff, A. Ehrl, W. A. Wall, and H. A. Gasteiger, “Tortuosity Determination of Battery Electrodes and Separators by Impedance Spectroscopy,” *J. Electrochem. Soc.*, vol. 163, no. 7, pp. A1373-A1387, 2016, doi: 10.1149/2.1141607jes.

[42] M. Ebner and V. Wood, “Tool for Tortuosity Estimation in Lithium Ion Battery Porous Electrodes,” *Journal of the Electrochemical Society*, vol. 162, no. 2, pp. A3064-A3070, 2014, doi: 10.1149/2.0111502jes.

[43] G. Zhu *et al.,* “Materials insights into low-temperature performances of lithium-ion batteries,” *Journal of Power Sources*, vol. 300, pp. 29–40, 2015, doi: 10.1016/j.jpowsour.2015.09.056.

[44] G. Zhang, L. Cao, S. Ge, C.-Y. Wang, C. E. Shaffer, and C. D. Rahn, “In Situ Measurement of Radial Temperature Distributions in Cylindrical Li-Ion Cells,” (in af), *Journal of the Electrochemical Society*, vol. 161, no. 10, pp. A1499-A1507, 2014, doi: 10.1149/2.0051410jes.

[45] S. Zhang, K. Xu, and T. Jow, “A new approach toward improved low temperature performance of Li-ion battery,” *Electrochemistry Communications*, vol. 4, no. 11, pp. 928–932, 2002, doi: 10.1016/S1388-2481(02)00490-3.

[46] A. Senyshyn, O. Dolotko, M. J. Muhlbauer, K. Nikolowski, H. Fuess, and H. Ehrenberg, “Lithium Intercalation into Graphitic Carbons Revisited: Experimental Evidence for Twisted Bilayer Behavior,” *Journal of the Electrochemical Society*, vol. 160, no. 5, pp. A3198-A3205, 2013, doi: 10.1149/2.031305jes.

[47] S. Taminato *et al.,* “Real-time observations of lithium battery reactions-operando neutron diffraction analysis during practical operation,” *Scientific reports*, vol. 6, p. 28843, 2016.

[48] I. A. Bobrikov *et al.,* “Structural evolution in LiFePO4-based battery materials: In-situ and ex-situ time-of-flight neutron diffraction study,” *Journal of Power Sources*, vol. 258, pp. 356–364, 2014, doi: 10.1016/j.jpowsour.2014.02.060.

[49] C. von Lüders *et al.,* “Lithium plating in lithium-ion batteries investigated by voltage relaxation and in situ neutron diffraction,” *Journal of Power Sources*, vol. 342, pp. 17–23, 2017, doi: 10.1016/j.jpowsour.2016.12.032.

[50] N. Sharma and V. K. Peterson, “Current-dependent electrode lattice fluctuations and anode phase evolution in a lithium-ion battery investigated by in situ neutron diffraction,” *Electrochimica Acta*, vol. 101, pp. 79–85, 2013, doi: 10.1016/j.electacta.2012.09.101.

[51] N. Sharma, D. H. Yu, Y. Zhu, Y. Wu, and V. K. Peterson, “In operando neutron diffraction study of the temperature and current rate-dependent phase evolution of LiFePO 4 in a commercial battery,” *Journal of Power Sources*, vol. 342, pp. 562–569, 2017, doi: 10.1016/j.jpowsour.2016.12.048.

[52] P. Maire, A. Evans, H. Kaiser, W. Scheifele, and P. Novák, “Colorimetric Determination of Lithium Content in Electrodes of Lithium-Ion Batteries,” (in af), *J. Electrochem. Soc.*, vol. 155, no. 11, pp. A862, 2008, doi: 10.1149/1.2979696.

[53] S. J. Harris, A. Timmons, D. R. Baker, and C. Monroe, “Direct in situ measurements of Li transport in Li-ion battery negative electrodes,” (in af), *Chemical Physics Letters*, vol. 485, 4-6, pp. 265–274, 2010, doi: 10.1016/j.cplett.2009.12.033.

[54] D. Manka and E. Ivers-Tiffée, “Electro-optical measurements of lithium intercalation/de-intercalation at graphite anode surfaces,” (in da), *Electrochimica Acta*, vol. 186, pp. 642–653, 2015, doi: 10.1016/j.electacta.2015.10.072.

[55] J. Liu, M. Kunz, K. Chen, N. Tamura, and T. J. Richardson, “Visualization of Charge Distribution in a Lithium Battery Electrode,” (in af), *J. Phys. Chem. Lett.*, vol. 1, no. 14, pp. 2120–2123, 2010, doi: 10.1021/jz100634n.

[56] V. Zinth *et al.,* “Inhomogeneity and relaxation phenomena in the graphite anode of a lithium-ion battery probed by in situ neutron diffraction,” *Journal of Power Sources*, vol. 361, pp. 54–60, 2017, doi: 10.1016/j.jpowsour.2017.06.060.

[57] J. N. Reimers, “Analytic theory for foil impedance in spiral wound cell geometries,” *Journal of Power Sources*, vol. 262, pp. 429–443, 2014, doi: 10.1016/j.jpowsour.2014.03.018.

[58] W. Zhao, G. Luo, and C.-Y. Wang, “Effect of tab design on large-format Li-ion cell performance,” (in ca), *Journal of Power Sources*, vol. 257, pp. 70–79, 2014, doi: 10.1016/j.jpowsour.2013.12.146.

[59] P. J. Osswald, S. V. Erhard, J. Wilhelm, H. E. Hoster, and A. Jossen, “Simulation and Measurement of Local Potentials of Modified Commercial Cylindrical Cells I. Cell Preparation and Measurements,” *Journal of the Electrochemical Society*, vol. 162, no. 10, pp. A2099-A2105, 2015, doi: 10.1149/2.0561510jes.

[60] S. V. Erhard, P. J. Osswald, J. Wilhelm, A. Rheinfeld, S. Kosch, and A. Jossen, “Simulation and Measurement of Local Potentials of Modified Commercial Cylindrical Cells,” *Journal of the Electrochemical Society*, vol. 162, no. 14, pp. A2707-A2719, 2015, doi: 10.1149/2.0431514jes.

[61] S. J. Drake, D. A. Wetz, J. K. Ostanek, S. P. Miller, J. M. Heinzel, and A. Jain, “Measurement of anisotropic thermophysical properties of cylindrical Li-ion cells,” (in af), *Journal of Power Sources*, vol. 252, pp. 298–304, 2014, doi: 10.1016/j.jpowsour.2013.11.107.

[62] M. Fleckenstein, O. Bohlen, M. A. Roscher, and B. Bäker, “Current density and state of charge inhomogeneities in Li-ion battery cells with LiFePO4 as cathode material due to temperature gradients,” *Journal of Power Sources*, vol. 196, no. 10, pp. 4769–4778, 2011, doi: 10.1016/j.jpowsour.2011.01.043.

[63] D. A. H. McCleary, J. P. Meyers, and B. Kim, “Three-Dimensional Modeling of Electrochemical Performance and Heat Generation of Spirally and Prismatically Wound Lithium-Ion Batteries,” *Journal of the Electrochemical Society*, vol. 160, no. 11, pp. A1931-A1943, 2013, doi: 10.1149/2.023311jes.

[64] K.-J. Lee, K. Smith, A. Pesaran, and G.-H. Kim, “Three dimensional thermal-, electrical-, and electrochemical-coupled model for cylindrical wound large format lithium-ion batteries,” *Journal of Power Sources*, vol. 241, pp. 20–32, 2013, doi: 10.1016/j.jpowsour.2013.03.007.

[65] A. Senyshyn, M. J. Mühlbauer, O. Dolotko, M. Hofmann, and H. Ehrenberg, “Homogeneity of lithium distribution in cylinder-type Li-ion batteries,” *Scientific reports*, vol. 5, p. 18380, 2015, doi: 10.1038/srep18380.

[66] S. V. Erhard *et al.,* “Simulation and Measurement of the Current Density Distribution in Lithium-Ion Batteries by a Multi-Tab Cell Approach,” *J. Electrochem. Soc.*, vol. 164, no. 1, pp. A6324-A6333, 2017, doi: 10.1149/2.0551701jes.

[67] G. E. Blomgren, “The Development and Future of Lithium Ion Batteries,” *J. Electrochem. Soc.*, vol. 164, no. 1, pp. A5019-A5025, 2017, doi: 10.1149/2.0251701jes.

[68] A. Jossen and W. Weydanz, *Moderne Akkumulatoren richtig einsetzen,* 2nd ed. Göttingen: Cuvillier Verlag, 2019.

[69] J. B. Goodenough and K.-S. Park, “The Li-ion rechargeable battery: a perspective,” *Journal of the American Chemical Society*, vol. 135, no. 4, pp. 1167–1176, 2013, doi: 10.1021/ja3091438.

[70] C. Daniel and J. O. Besenhard, *Handbook of Battery Materials,* 2nd ed. Weinheim: Wiley-VCH Verlag, 2011.

[71] S. F. Lux, F. Schappacher, A. Balducci, S. Passerini, and M. Winter, "Low Cost, Environmentally Benign Binders for Lithium-Ion Batteries," (in da), *J. Electrochem. Soc.*, vol. 157, no. 3, pp. A320, 2010, doi: 10.1149/1.3291976.

[72] M. Winter, J. O. Besenhard, M. E. Spahr, and P. Novák, "Insertion Electrode Materials for Rechargeable Lithium Batteries," (in da), *Adv. Mater.*, vol. 10, no. 10, pp. 725–763, 1998, doi: 10.1002/(SICI)1521-4095(199807)10:10<725::AID-ADMA725>3.0.CO;2-Z.

[73] P. G. Balakrishnan, R. Ramesh, and T. Prem Kumar, "Safety mechanisms in lithium-ion batteries," (in af), *Journal of Power Sources*, vol. 155, no. 2, pp. 401–414, 2006, doi: 10.1016/j.jpowsour.2005.12.002.

[74] B. P. Miller, "Automotive Lithium-Ion Batteries," *johnson matthey technol rev*, vol. 59, no. 1, pp. 4–13, 2015, doi: 10.1595/205651315x685445.

[75] J. N. Reimers, "Predicting current flow in spiral wound cell geometries," (in af), *Journal of Power Sources*, vol. 158, no. 1, pp. 663–672, 2006, doi: 10.1016/j.jpowsour.2005.08.042.

[76] H. Li and H. Zhou, "Enhancing the performances of Li-ion batteries by carbon-coating: present and future," *Chemical communications (Cambridge, England)*, vol. 48, no. 9, pp. 1201–1217, 2012, doi: 10.1039/c1cc14764a.

[77] M. B. DeGostin, A. Nakajo, B. N. Cassenti, A. A. Peracchio, G. J. Nelson, and W. K. Chiu, "Geometric sensitivity of electrochemical fin shape on three dimensional microstructure network conductivity analysis," *Journal of Power Sources*, vol. 291, pp. 181–194, 2015, doi: 10.1016/j.jpowsour.2015.04.153.

[78] E. Peled, "Advanced Model for Solid Electrolyte Interphase Electrodes in Liquid and Polymer Electrolytes," *J. Electrochem. Soc.*, vol. 144, no. 8, pp. L208, 1997, doi: 10.1149/1.1837858.

[79] S.-P. Kim, A. C. van Duin, and V. B. Shenoy, "Effect of electrolytes on the structure and evolution of the solid electrolyte interphase (SEI) in Li-ion batteries: A molecular dynamics study," *Journal of Power Sources*, vol. 196, no. 20, pp. 8590–8597, 2011, doi: 10.1016/j.jpowsour.2011.05.061.

[80] J. Vetter *et al.,* "Ageing mechanisms in lithium-ion batteries," (in af), *Journal of Power Sources*, vol. 147, 1-2, pp. 269–281, 2005, doi: 10.1016/j.jpowsour.2005.01.006.

[81] M. Yoshio, R. J. Brodd, and A. Kozawa, *Lithium-Ion Batteries*. New York, NY: Springer New York, 2009.

[82] Y. NuLi, J. Yang, and Z. Jiang, "Intercalation of lithium ions into bulk and powder highly oriented pyrolytic graphite," *Journal of Physics and Chemistry of Solids*, vol. 67, no. 4, pp. 882–886, 2006, doi: 10.1016/j.jpcs.2005.11.003.

[83] S. Cui *et al.,* "Optimized Temperature Effect of Li-Ion Diffusion with Layer Distance in Li(Ni x Mn y Co z)O 2 Cathode Materials for High Performance Li-Ion Battery," *Adv. Energy Mater.*, vol. 6, no. 4, p. 1501309, 2016, doi: 10.1002/aenm.201501309.

[84] S. Thinius, M. M. Islam, P. Heitjans, and T. Bredow, "Theoretical Study of Li Migration in Lithium–Graphite Intercalation Compounds with Dispersion-Corrected DFT Methods," *J. Phys. Chem. C*, vol. 118, no. 5, pp. 2273–2280, 2014.

[85] H.-C. Yu, A. van der Ven, and K. Thornton, "Theory of grain boundary diffusion induced by the Kirkendall effect," *Appl. Phys. Lett.*, vol. 93, no. 9, p. 91908, 2008, doi: 10.1063/1.2978161.

[86] J. S. Newman and K. E. Thomas-Alyea, *Electrochemical Systems,* 3rd ed. Hoboken, N.J: J. Wiley, 2004.

[87] S.-C. Chen, Y.-Y. Wang, and C.-C. Wan, "Thermal Analysis of Spirally Wound Lithium Batteries," (in af), *J. Electrochem. Soc.*, vol. 153, no. 4, pp. A637, 2006, doi: 10.1149/1.2168051.

[88] F. P. Incropera, *Fundamentals of heat and mass transfer,* 6th ed. Hoboken, N.J.: John Wiley & Sons, 2007.

[89] A. Senyshyn, M. J. Mühlbauer, O. Dolotko, and H. Ehrenberg, “Low-temperature performance of Li-ion batteries: The behavior of lithiated graphite,” *Journal of Power Sources*, vol. 282, pp. 235–240, 2015.

[90] S. S. Zhang, “A review on electrolyte additives for lithium-ion batteries,” *Journal of Power Sources*, vol. 162, no. 2, pp. 1379–1394, 2006, doi: 10.1016/j.jpowsour.2006.07.074.

[91] M. C. Smart, “Electrolytes for Low-Temperature Lithium Batteries Based on Ternary Mixtures of Aliphatic Carbonates,” *J. Electrochem. Soc.*, vol. 146, no. 2, p. 486, 1999, doi: 10.1149/1.1391633.

[92] K. Zaghib, F. Brochu, A. Guerfi, and K. Kinoshita, “Effect of particle size on lithium intercalation rates in natural graphite,” *Journal of Power Sources*, vol. 103, no. 1, pp. 140–146, 2001, doi: 10.1016/S0378-7753(01)00853-9.

[93] K. Zaghib, X. Song, A. Guerfi, R. Kostecki, and K. Kinoshita, “Effect of particle morphology on lithium intercalation rates in natural graphite,” *Journal of Power Sources*, vol. 124, no. 2, pp. 505–512, 2003, doi: 10.1016/S0378-7753(03)00801-2.

[94] M. C. Smart and B. V. Ratnakumar, “Effects of Electrolyte Composition on Lithium Plating in Lithium-Ion Cells,” *J. Electrochem. Soc.*, vol. 158, no. 4, pp. A379, 2011, doi: 10.1149/1.3544439.

[95] M. Umeda, K. Dokko, Y. Fujita, M. Mohamedi, I. Uchida, and J. Selman, “Electrochemical impedance study of Li-ion insertion into mesocarbon microbead single particle electrode,” *Electrochimica Acta*, vol. 47, no. 6, pp. 885–890, 2001, doi: 10.1016/S0013-4686(01)00799-X.

[96] M. D. Levi, E. Markevich, and D. Aurbach, “Comparison between Cottrell diffusion and moving boundary models for determination of the chemical diffusion coefficients in ion-insertion electrodes,” *Electrochimica Acta*, vol. 51, no. 1, pp. 98–110, 2005, doi: 10.1016/j.electacta.2005.04.007.

[97] J. S. Newman and C. W. Tobias, “Theoretical Analysis of Current Distribution in Porous Electrodes,” (in af), *J. Electrochem. Soc.*, vol. 109, no. 12, p. 1183, 1962, doi: 10.1149/1.2425269.

[98] J. Newman, “Potential and Current Distribution in Electrochemical Cells,” *J. Electrochem. Soc.*, vol. 140, no. 7, p. 1961, 1993, doi: 10.1149/1.2220746.

[99] H. Buqa, D. Goers, M. Holzapfel, M. E. Spahr, and P. Novák, “High Rate Capability of Graphite Negative Electrodes for Lithium-Ion Batteries,” *J. Electrochem. Soc.*, vol. 152, no. 2, pp. A474, 2005, doi: 10.1149/1.1851055.

[100] S.-H. Ng, F. La Mantia, and P. Novák, “A Multiple Working Electrode for Electrochemical Cells: A Tool for Current Density Distribution Studies,” (in da), *Angew. Chem. Int. Ed.*, vol. 48, no. 3, pp. 528–532, 2009, doi: 10.1002/anie.200803981.

[101] S. Klink, W. Schuhmann, and F. La Mantia, “Vertical distribution of overpotentials and irreversible charge losses in lithium ion battery electrodes,” *ChemSusChem*, vol. 7, no. 8, pp. 2159–2166, 2014, doi: 10.1002/cssc.201400056.

[102] F. M. Kindermann *et al.,* “Measurements of lithium-ion concentration equilibration processes inside graphite electrodes,” (in af), *Journal of Power Sources*, vol. 342, pp. 638–643, 2017, doi: 10.1016/j.jpowsour.2016.12.093.

[103] S. C. Nagpure, R. G. Downing, B. Bhushan, S. S. Babu, and L. Cao, “Neutron depth profiling technique for studying aging in Li-ion batteries,” *Electrochimica Acta*, vol. 56, no. 13, pp. 4735–4743, 2011, doi: 10.1016/j.electacta.2011.02.037.

[104] Oudenhoven, J. F. M., F. Labohm, M. Mulder, Niessen, R. A. H., F. M. Mulder, and Notten, P. H. L., “In Situ Neutron Depth Profiling: A Powerful Method to Probe Lithium Transport in Micro-Batteries,” *Adv. Mater.*, vol. 23, no. 35, pp. 4103–4106, 2011, doi: 10.1002/adma.201101819.

[105] S. Whitney, S. R. Biegalski, Y. H. Huang, and J. B. Goodenough, “Neutron Depth Profiling Applications to Lithium-Ion Cell Research,” (in da), *J. Electrochem. Soc.*, vol. 156, no. 11, pp. A886, 2009, doi: 10.1149/1.3216033.

[106] Y. He, R. G. Downing, and H. Wang, “3D mapping of lithium in battery electrodes using neutron activation,” (in af), *Journal of Power Sources*, vol. 287, pp. 226–230, 2015, doi: 10.1016/j.jpowsour.2015.03.176.

[107] A. Lasia, *Electrochemical impedance spectroscopy and its applications*. New York, N.Y.: Springer, 2014.

[108] J. Nanda *et al.,* “Local State-of-Charge Mapping of Lithium-Ion Battery Electrodes,” *Adv. Funct. Mater.*, vol. 21, no. 17, pp. 3282–3290, 2011, doi: 10.1002/adfm.201100157.

[109] Z. Li *et al.,* “Examining temporal and spatial variations of internal temperature in large-format laminated battery with embedded thermocouples,” *Journal of Power Sources*, vol. 241, pp. 536–553, 2013, doi: 10.1016/j.jpowsour.2013.04.117.

[110] G. Zhang, C. E. Shaffer, C.-Y. Wang, and C. D. Rahn, “In-Situ Measurement of Current Distribution in a Li-Ion Cell,” (in af), *Journal of the Electrochemical Society*, vol. 160, no. 4, pp. A610-A615, 2013, doi: 10.1149/2.046304jes.

[111] A. Senyshyn, M. J. Mühlbauer, K. Nikolowski, T. Pirling, and H. Ehrenberg, “In-operando - Neutron scattering studies on Li-ion batteries,” (in ca), *Journal of Power Sources*, vol. 203, pp. 126–129, 2012, doi: 10.1016/j.jpowsour.2011.12.007.

[112] A. Senyshyn, M. J. Mühlbauer, O. Dolotko, M. Hofmann, T. Pirling, and H. Ehrenberg, “Spatially resolved in operando neutron scattering studies on Li-ion batteries,” (in ca), *Journal of Power Sources*, vol. 245, pp. 678–683, 2014, doi: 10.1016/j.jpowsour.2013.06.158.

[113] H. Zhou *et al.,* “Probing Multiscale Transport and Inhomogeneity in a Lithium-Ion Pouch Cell Using In Situ Neutron Methods,” *ACS Energy Lett.*, vol. 1, no. 5, pp. 981–986, 2016, doi: 10.1021/acsenergylett.6b00353.

[114] W. B. Gu and C. Y. Wang, “Thermal-Electrochemical Modeling of Battery Systems,” (in af), *J. Electrochem. Soc.*, vol. 147, no. 8, p. 2910, 2000, doi: 10.1149/1.1393625.

[115] M. Lewerenz, A. Warnecke, and D. U. Sauer, “Introduction of capacity difference analysis (CDA) for analyzing lateral lithium-ion flow to determine the state of covering layer evolution,” *Journal of Power Sources*, vol. 354, pp. 157–166, 2017, doi: 10.1016/j.jpowsour.2017.04.043.

[116] Z. Q. Li, C. J. Lu, Z. P. Xia, Y. Zhou, and Z. Luo, “X-ray diffraction patterns of graphite and turbostratic carbon,” *Carbon*, vol. 45, no. 8, pp. 1686–1695, 2007, doi: 10.1016/j.carbon.2007.03.038.

[117] Y. Imai and A. Watanabe, “Energetic evaluation of possible stacking structures of Li-intercalation in graphite using a first-principle pseudopotential calculation,” *Journal of Alloys and Compounds*, vol. 439, 1-2, pp. 258–267, 2007, doi: 10.1016/j.jallcom.2006.08.061.

[118] S. Konar, U. Häusserman, and G. Svensson, “Intercalation Compounds from LiH and Graphite: Relative Stability of Metastable Stages and Thermodynamic Stability of Dilute Stage I d,” *Chem. Mater.*, vol. 27, no. 7, pp. 2566–2575, 2015, doi: 10.1021/acs.chemmater.5b00235.

[119] O. Y. M. Wakihara, *Lithium Ion Batteries: Fundamentals and Performance*. Tokyo: Kodansha Ltd., 1998.

[120] I. L. Spain and D. J. Nagel, “The electronic properties of lamellar compounds of graphite — An introduction,” *Materials Science and Engineering*, vol. 31, pp. 183–193, 1977, doi: 10.1016/0025-5416(77)90034-9.

[121] J. W. Cahn and J. E. Hilliard, “Free Energy of a Nonuniform System. I. Interfacial Free Energy,” *The Journal of Chemical Physics*, vol. 28, no. 2, pp. 258–267, 1958, doi: 10.1063/1.1744102.

[122] S. A. Safran, “Phase Diagrams for Staged Intercalation Compounds,” (in da), *Phys. Rev. Lett.*, vol. 44, no. 14, pp. 937–940, 1980, doi: 10.1103/PhysRevLett.44.937.

[123] S. A. Safran, “Stage Ordering in Intercalation Compounds,” in *Solid State Physics*: Elsevier, 1987, pp. 183–246.

[124] N. Daumas and Albert Herold, “Relations between phase concept and reaction mechanics in graphite insertion compounds,” *Comptes Rendus Hebdomadaires Des Seances De L Academie Des Sciences Serie C*, vol. 268, no. 5, pp. 373–375, 1969.

[125] S. Krishnan *et al.,* “Revisiting the domain model for lithium intercalated graphite,” *Appl. Phys. Lett.*, vol. 103, no. 25, p. 251904, 2013, doi: 10.1063/1.4850877.

[126] P. Hawrylak and K. R. Subbaswamy, “Kinetic Model of Stage Transformation and Intercalation in Graphite,” *Phys. Rev. Lett.*, vol. 53, no. 22, pp. 2098–2101, 1984, doi: 10.1103/PhysRevLett.53.2098.

[127] Kirczenow, “Kinetics of stage ordering and stage transitions,” *Physical review letters*, vol. 55, no. 25, pp. 2810–2813, 1985, doi: 10.1103/PhysRevLett.55.2810.

[128] S. A. Safran and D. R. Hamann, “Electrostatic interactions and staging in graphite intercalation compounds,” *Phys. Rev. B*, vol. 22, no. 2, pp. 606–612, 1980, doi: 10.1103/PhysRevB.22.606.

[129] R. Clarke, N. Wada, and S. A. Solin, “Pressure-Induced Staging Transition in K C24,” (in af), *Phys. Rev. Lett.*, vol. 44, no. 24, pp. 1616–1619, 1980, doi: 10.1103/PhysRevLett.44.1616.

[130] J. M. Thomas, G. R. Millward, R. F. Schlögl, and H. P. Boehm, “Direct imaging of a graphite intercalate: Evidence of interpenetration of ‘stages’ in graphite: Ferric chloride,” (in af), *Materials Research Bulletin*, vol. 15, no. 5, pp. 671–676, 1980, doi: 10.1016/0025-5408(80)90149-X.

[131] Y. Guo *et al.,* “Li Intercalation into Graphite: Direct Optical Imaging and Cahn-Hilliard Reaction Dynamics,” *The journal of physical chemistry letters*, vol. 7, no. 11, pp. 2151–2156, 2016, doi: 10.1021/acs.jpclett.6b00625.

[132] D. Billaud, F. X. Henry, M. Lelaurain, and P. Willmann, “Revisited structures of dense and dilute stage II lithium-graphite intercalation compounds,” *Journal of Physics and Chemistry of Solids*, vol. 57, 6-8, pp. 775–781, 1996, doi: 10.1016/0022-3697(95)00348-7.

[133] M. Heß and P. Novák, “Shrinking annuli mechanism and stage-dependent rate capability of thin-layer graphite electrodes for lithium-ion batteries,” *Electrochimica Acta*, vol. 106, pp. 149–158, 2013, doi: 10.1016/j.electacta.2013.05.056.

[134] X.-C. Tang, C.-Y. Pan, L.-P. He, L.-Q. Li, and Z.-Z. Chen, “A novel technique based on the ratio of potentio-charge capacity to galvano-charge capacity (RPG) for determination of the diffusion coefficient of intercalary species within insertion-host materials: Theories and experiments,” *Electrochimica Acta*, vol. 49, no. 19, pp. 3113–3119, 2004, doi: 10.1016/j.electacta.2004.02.025.

[135] M. D. Levi, C. Wang, E. Markevich, D. Aurbach, and Z. Chvoj, “Noteworthy electroanalytical features of the stage 4 to stage 3 phase transition in lithiated graphite,” *Journal of Solid State Electrochemistry*, vol. 8, no. 1, pp. 40–43, 2003, doi: 10.1007/s10008-003-0404-x.

[136] T. Tran and K. Kinoshita, “Lithium intercalation/deintercalation behavior of basal and edge planes of highly oriented pyrolytic graphite and graphite powder,” *Journal of Electroanalytical Chemistry*, vol. 386, 1-2, pp. 221–224, 1995, doi: 10.1016/0022-0728(95)03907-X.

[137] S. Rodrigues, N. Munichandraiah, and A. K. Shukla, “A review of state-of-charge indication of batteries by means of a.c. impedance measurements,” *Journal of Power Sources*, vol. 87, 1-2, pp. 12–20, 2000, doi: 10.1016/S0378-7753(99)00351-1.

[138] J. Wilhelm *et al.,* “Cycling capacity recovery effect: A coulombic efficiency and post-mortem study,” *Journal of Power Sources*, vol. 365, pp. 327–338, 2017, doi: 10.1016/j.jpowsour.2017.08.090.

[139] T. M. Bond, J. C. Burns, D. A. Stevens, H. M. Dahn, and J. R. Dahn, “Improving Precision and Accuracy in Coulombic Efficiency Measurements of Li-Ion Batteries,” *Journal of the Electrochemical Society*, vol. 160, no. 3, pp. A521-A527, 2013, doi: 10.1149/2.014304jes.

[140] Allen J. Bard, Larry R. Faulkner, *Electrochemcial Methods: Fundamentals and Applications,* 2nd ed.: John Wiley & Sons.

[141] J. O. Bockris, B. E. Conway, J. O. Bockris, and R. E. White, *Modern Aspects of Electrochemistry*. New York, Boston, MA: Kluwer Academic/Plenum Publishers; Springer US, 2002.

[142] N. Ogihara, S. Kawauchi, C. Okuda, Y. Itou, Y. Takeuchi, and Y. Ukyo, “Theoretical and Experimental Analysis of Porous Electrodes for Lithium-Ion Batteries by Electrochemical Impedance Spectroscopy Using a Symmetric Cell,” *J. Electrochem. Soc.*, vol. 159, no. 7, pp. A1034-A1039, 2012, doi: 10.1149/2.057207jes.

[143] D. Meschede, *Gerthsen Physik*. Berlin, Heidelberg: Springer Berlin Heidelberg, 2015.

[144] S. S. Antman, L. Sirovich, J. E. Marsden, S. Wiggins, and S. Torquato, *Random Heterogeneous Materials*. New York, NY: Springer New York, 2002.

[145] H. M. Dahn, A. J. Smith, J. C. Burns, D. A. Stevens, and J. R. Dahn, “User-Friendly Differential Voltage Analysis Freeware for the Analysis of Degradation Mechanisms in Li-Ion Batteries,” *J. Electrochem. Soc.*, vol. 159, no. 9, pp. A1405-A1409, 2012, doi: 10.1149/2.013209jes.

[146] I. Bloom *et al.,* “Differential voltage analyses of high-power, lithium-ion cells,” *Journal of Power Sources*, vol. 139, 1-2, pp. 295–303, 2005, doi: 10.1016/j.jpowsour.2004.07.021.

[147] I. Bloom, J. Christophersen, and K. Gering, “Differential voltage analyses of high-power lithium-ion cells,” *Journal of Power Sources*, vol. 139, 1-2, pp. 304–313, 2005, doi: 10.1016/j.jpowsour.2004.07.022.

[148] I. Bloom, J. P. Christophersen, D. P. Abraham, and K. L. Gering, “Differential voltage analyses of high-power lithium-ion cells,” *Journal of Power Sources*, vol. 157, no. 1, pp. 537–542, 2006, doi: 10.1016/j.jpowsour.2005.07.054.

[149] Peter Keil, “Aging of Lithium-Ion Batteries in Electric Vehicles,” Dissertation, Technical University Munich, München, 2017.

[150] W. Friedrich, P. Knipping, and M. Laue, “Interferenzerscheinungen bei Röntgenstrahlen,” (in de), *Ann. Phys.*, vol. 346, no. 10, pp. 971–988, 1913, doi: 10.1002/andp.19133461004.

[151] J. I. Langford and A. J. C. Wilson, “Scherrer after sixty years: A survey and some new results in the determination of crystallite size,” *J Appl Crystallogr*, vol. 11, no. 2, pp. 102–113, 1978, doi: 10.1107/s0021889878012844.

[152] U. Holzwarth and N. Gibson, “The Scherrer equation versus the 'Debye-Scherrer equation',” *Nature nanotechnology*, vol. 6, no. 9, p. 534, 2011, doi: 10.1038/nnano.2011.145.

[153] M. Hofmann *et al.,* “The New Materials Science Diffractometer STRESS-SPEC at FRM-II,” *MSF*, 524-525, pp. 211–216, 2006, doi: 10.4028/www.scientific.net/MSF.524-525.211.

[154] T. Degen, M. Sadki, E. Bron, U. König, and G. Nénert, “The HighScore suite,” *Powder Diffr.*, vol. 29, S2, pp. S13-S18, 2014, doi: 10.1017/S0885715614000840.

[155] W. A. Dollase, “Correction of intensities for preferred orientation in powder diffractometry: Application of the March model,” *J Appl Crystallogr*, vol. 19, no. 4, pp. 267–272, 1986, doi: 10.1107/S0021889886089458.

[156] M. Järvinen, “Application of symmetrized harmonics expansion to correction of the preferred orientation effect,” *J Appl Crystallogr*, vol. 26, no. 4, pp. 525–531, 1993, doi: 10.1107/S0021889893001219.

[157] B. H. Toby, “R factors in Rietveld analysis: How good is good enough?,” *Powder Diffr.*, vol. 21, no. 01, pp. 67–70, 2006, doi: 10.1154/1.2179804.

[158] Korbinian Wachutka, “Untersuchung und Modellierung des Einflusses mehrseitig beschichteter Elektroden auf die Eigenschaften von Knopfzellen,” Master thesis, Institute for Electrical Energy Storage Technology EES (Prof. Jossen), Technical University Munich.

[159] T. Marks, S. Trussler, A. J. Smith, D. Xiong, and J. R. Dahn, “A Guide to Li-Ion Coin-Cell Electrode Making for Academic Researchers,” *J. Electrochem. Soc.*, vol. 158, no. 1, pp. A51, 2011, doi: 10.1149/1.3515072.

[160] Y. Lee, B. Son, J. Choi, J. H. Kim, M.-H. Ryou, and Y. M. Lee, “Effect of back-side-coated electrodes on electrochemical performances of lithium-ion batteries,” *Journal of Power Sources*, vol. 275, pp. 712–719, 2015, doi: 10.1016/j.jpowsour.2014.11.029.

[161] J. Feinauer *et al.,* "MULTIBAT: Unified workflow for fast electrochemical 3D simulations of lithium-ion cells combining virtual stochastic microstructures, electrochemical degradation models and model order reduction," *Journal of Computational Science*, vol. 31, pp. 172–184, 2019, doi: 10.1016/j.jocs.2018.03.006.

[162] R. Malik, A. Abdellahi, and G. Ceder, "A Critical Review of the Li Insertion Mechanisms in LiFePO4 Electrodes," *Journal of the Electrochemical Society*, vol. 160, no. 5, pp. A3179-A3197, 2013, doi: 10.1149/2.029305jes.

[163] G. X. Wang, L. Yang, S. L. Bewlay, Y. Chen, H. K. Liu, and J. H. Ahn, "Electrochemical properties of carbon coated LiFePO4 cathode materials," (in af), *Journal of Power Sources*, vol. 146, 1-2, pp. 521–524, 2005, doi: 10.1016/j.jpowsour.2005.03.201.

[164] P. Thompson, D. E. Cox, and J. B. Hastings, "Rietveld refinement of Debye–Scherrer synchrotron X-ray data from Al 2 O 3," (in af), *J Appl Crystallogr*, vol. 20, no. 2, pp. 79–83, 1987, doi: 10.1107/S0021889887087090.

[165] H. M. Rietveld, "A profile refinement method for nuclear and magnetic structures," *J Appl Crystallogr*, vol. 2, no. 2, pp. 65–71, 1969, doi: 10.1107/S0021889869006558.

[166] G. S. Pawley, "Unit-cell refinement from powder diffraction scans," *J Appl Crystallogr*, vol. 14, no. 6, pp. 357–361, 1981, doi: 10.1107/S0021889881009618.

[167] A. S. Cooper, "Precise lattice constants of germanium, aluminum, gallium arsenide, uranium, sulphur, quartz and sapphire," *Acta Cryst*, vol. 15, no. 6, pp. 578–582, 1962, doi: 10.1107/S0365110X62001474.

[168] H. M. Otte, "Lattice Parameter Determinations with an X-Ray Spectrogoniometer by the Debye-Scherrer Method and the Effect of Specimen Condition," *Journal of Applied Physics*, vol. 32, no. 8, pp. 1536–1546, 1961, doi: 10.1063/1.1728392.

[169] O. Dolotko, A. Senyshyn, M. J. Muehlbauer, K. Nikolowski, F. Scheiba, and H. Ehrenberg, "Fatigue Process in Li-Ion Cells: An In Situ Combined Neutron Diffraction and Electrochemical Study," *Journal of the Electrochemical Society*, vol. 159, no. 12, pp. A2082-A2088, 2012, doi: 10.1149/2.080212jes.

[170] D. Guerard and A. Herold, "Intercalation of lithium into graphite and other carbons," *Carbon*, vol. 13, no. 4, pp. 337–345, 1975, doi: 10.1016/0008-6223(75)90040-8.

[171] B. Vadlamani, K. An, M. Jagannathan, and K. S. R. Chandran, "An In-Situ Electrochemical Cell for Neutron Diffraction Studies of Phase Transitions in Small Volume Electrodes of Li-Ion Batteries," *Journal of the Electrochemical Society*, vol. 161, no. 10, pp. A1731-A1741, 2014, doi: 10.1149/2.0951410jes.

[172] W. Waag, S. Käbitz, and D. U. Sauer, "Experimental investigation of the lithium-ion battery impedance characteristic at various conditions and aging states and its influence on the application," *Applied Energy*, vol. 102, pp. 885–897, 2013, doi: 10.1016/j.apenergy.2012.09.030.

[173] P. B. Balbuena and Y. Wang, *Lithium-ion batteries: Solid-electrolyte interphase*: Imperial College Press, London, 2004.

[174] M. Klett *et al.,* "Non-uniform aging of cycled commercial LiFePO4//graphite cylindrical cells revealed by post-mortem analysis," *Journal of Power Sources*, vol. 257, pp. 126–137, 2014, doi: 10.1016/j.jpowsour.2014.01.105.

[175] M. Klett *et al.,* "Uneven Film Formation across Depth of Porous Graphite Electrodes in Cycled Commercial Li-Ion Batteries," (in af), *J. Phys. Chem. C*, vol. 119, no. 1, pp. 90–100, 2015, doi: 10.1021/jp509665e.

[176] J. Wilhelm, S. Seidlmayer, S. Erhard, M. Hofmann, R. Gilles, and A. Jossen, "In Situ Neutron Diffraction Study of Lithiation Gradients in Graphite Anodes during Discharge and Relaxation," *J. Electrochem. Soc.*, vol. 165, no. 9, pp. A1846-A1856, 2018, doi: 10.1149/2.1231809jes.

[177] M. Hofmann, W. Gan, and J. Rebelo-Kornmeier, "STRESS-SPEC: Materials science diffractometer," (in fr), *JLSRF*, vol. 1, 2015, doi: 10.17815/jlsrf-1-25.

[178] C. Randau, U. Garbe, and H.-G. Brokmeier, “StressTextureCalculator: A software tool to extract texture, strain and microstructure information from area-detector measurements,” *J Appl Crystallogr*, vol. 44, no. 3, pp. 641–646, 2011, doi: 10.1107/S0021889811012064.

[179] O. Dolotko, A. Senyshyn, M. J. Mühlbauer, K. Nikolowski, and H. Ehrenberg, “Understanding structural changes in NMC Li-ion cells by in situ neutron diffraction,” (in af), *Journal of Power Sources*, vol. 255, pp. 197–203, 2014, doi: 10.1016/j.jpowsour.2014.01.010.

[180] P. TRUCANO and R. CHEN, “Structure of graphite by neutron diffraction,” (in af), *Nature*, vol. 258, no. 5531, pp. 136–137, 1975, doi: 10.1038/258136a0.

[181] H. He, C. Huang, C.-W. Luo, J.-J. Liu, and Z.-S. Chao, “Dynamic study of Li intercalation into graphite by in situ high energy synchrotron XRD,” *Electrochimica Acta*, vol. 92, pp. 148–152, 2013, doi: 10.1016/j.electacta.2012.12.135.

[182] C. Huang, S. Zhuang, and F. Tu, “Electrode/Electrolyte Interfacial Behaviors of LiCoO2/Mixed Graphite Li-Ion Cells during Operation and Storage,” *Journal of the Electrochemical Society*, vol. 160, no. 2, pp. A376-A382, 2012, doi: 10.1149/2.009303jes.

[183] H. C. Shiao, D. Chua, H. P. Lin, S. Slane, and M. Salomon, “Low temperature electrolytes for Li-ion PVDF cells,” (in ca), *Journal of Power Sources*, vol. 87, 1-2, pp. 167–173, 2000.

[184] M. Bauer *et al.,* “Multi-phase formation induced by kinetic limitations in graphite-based lithium-ion cells: Analyzing the effects on dilation and voltage response,” *Journal of Energy Storage*, vol. 10, pp. 1–10, 2017, doi: 10.1016/j.est.2016.11.006.

[185] J. Rossat-Mignod, A. Wiedenmann, K. C. WOO, J. W. Milliken, and J. E. FISCHER, “First-order phase transition in the graphite compound LiC6,” *Solid State Communications*, vol. 44, no. 8, pp. 1339–1342, 1982, doi: 10.1016/0038-1098(82)91118-8.

[186] J. K. W. Polifke, *Wärmeübertragung: Grundlagen, analytische und numerische Methoden,* 2nd ed. München, Boston [u.a.]: Pearson Studium, 2009.

[187] H. Yang, H. J. Bang, and J. Prakash, “Evaluation of Electrochemical Interface Area and Lithium Diffusion Coefficient for a Composite Graphite Anode,” *J. Electrochem. Soc.*, vol. 151, no. 8, pp. A1247, 2004, doi: 10.1149/1.1763139.

[188] M. D. Levi, E. Markevich, and D. Aurbach, “The effect of slow interfacial kinetics on the chronoamperometric response of composite lithiated graphite electrodes and on the calculation of the chemical diffusion coefficient of Li ions in graphite,” *The journal of physical chemistry. B*, vol. 109, no. 15, pp. 7420–7427, 2005, doi: 10.1021/jp0441902.

[189] S. Seidlmayer, J. Hattendorff, I. Buchberger, L. Karge, H. A. Gasteiger, and R. Gilles, “In Operando Small-Angle Neutron Scattering (SANS) on Li-Ion Batteries,” (in ca), *Journal of the Electrochemical Society*, vol. 162, no. 2, pp. A3116-A3125, 2014, doi: 10.1149/2.0181502jes.

[190] D. A. G. Bruggeman, “Berechnung verschiedener physikalischer Konstanten von heterogenen Substanzen. I. Dielektrizitätskonstanten und Leitfähigkeiten der Mischkörper aus isotropen Substanzen,” (in de), *Ann. Phys.*, vol. 416, no. 7, pp. 636–664, 1935, doi: 10.1002/andp.19354160705.

[191] Maximilian Drexl, “Relaxationsverhalten von Konzentrationsgradienten in Lithium-Ionen-Zellen im Tieftemperaturbereich,” Master thesis, Institute for Electrical Energy Storage Technology EES (Prof. Jossen), Technical University Munich, 2017.

[192] M. Doyle, “Modeling of Galvanostatic Charge and Discharge of the Lithium/Polymer/Insertion Cell,” *J. Electrochem. Soc.*, vol. 140, no. 6, p. 1526, 1993, doi: 10.1149/1.2221597.

[193] A. S. Cooper, “Precise lattice constants of germanium, aluminum, gallium arsenide, uranium, sulphur, quartz and sapphire,” *Acta Cryst*, vol. 15, no. 6, pp. 578–582, 1962, doi: 10.1107/S0365110X62001474.